UNIVERSITY OF CALIFORNIA

San Diego

Dynamic Green's Functions for Layered Media and Applications to Boundary-Value Problems

A dissertation submitted in partial satisfaction of the requirements for the degree of Doctor of Philosophy in Applied Mechanics

by

Randy Jay Apsel

Committee in charge:

Professor J. Enrique Luco, Chairman
Professor James N. Brune
Professor Gilbert A. Hegemier
Professor Eric Reissner
Professor John A. Tragenstein
Doctor Gerald A. Frazier

1979

50272-101

REPORT DOCUMENTATION PAGE	1. REPORT NO. NSF/RA-790596	2.	3. Recipient's Accession No. PB81 178204

4. Title and Subtitle
Dynamic Green's Functions for Layered Media and Applications to Boundary-Value Problems

5. Report Date
1979

6.

7. Author(s)
R. J. Apsel

8. Performing Organization Rept. No.

9. Performing Organization Name and Address
University of California/San Diego
Department of Applied Mechanics
La Jolla, CA 92093

10. Project/Task/Work Unit No.

11. Contract(C) or Grant(G) No.
(C)
(G) PFR7900006

12. Sponsoring Organization Name and Address
Office of Planning and Resources Management (OPRM)
National Science Foundation
1800 G Street, N.W.
Washington, D.C. 20550

13. Type of Report & Period Covered
Ph.D. Dissertation

14.

15. Supplementary Notes

16. Abstract (Limit: 200 words)

Motivated by increasing demands on earthquake engineering and theoretical seismology, a method to calculate the three-dimensional dynamic Green's functions for layered viscoelastic media is developed. In seismology, Green's functions are used to synthesize theoretical seismograms for an extended source including the propagational effects of geologic layering. In earthquake engineering, Green's functions are used to determine the response of foundations to external forces and incoming seismic waves when embedded in realistic geologic structures. Part I of the study presents the formulation of the method and the subsequent application to problems in theoretical seismology. The formulation of an integral equation approach using Green's functions to assess boundary-value problems and the subsequent application to problems in earthquake engineering are presented in Part II.

17. Document Analysis a. Descriptors
Earthquakes
Seismology
Green's function
Wave propagation
Analysis (mathematics)
Dynamic response
Viscoelastic theory

b. Identifiers/Open-Ended Terms
Earthquake Hazards Mitigation

c. COSATI Field/Group

18. Availability Statement	19. Security Class (This Report)	21. No. of Pages
NTIS	20. Security Class (This Page)	22. Price

(See ANSI-Z39.18) *See Instructions on Reverse*

OPTIONAL FORM 272 (4-7)
(Formerly NTIS-35)
Department of Commerce

The dissertation of Randy Jay Apsel is approved, and it is acceptable in quality and form for publication on microfilm:

Gerald A. Frazier

Eric Reiss

Gilbert A. Bagnani

James M. Bruno

John A. Trangenstein

Juan Enrique Luco

Chairman

University of California, San Diego

1979

TO

OLGA

TABLE OF CONTENTS

LIST OF FIGURES
(Part I)

LIST OF FIGURES
(Part II)

LIST OF TABLES
(Part I)

LIST OF TABLES
(Part II)

ACKNOWLEDGEMENTS

Foremost, I wish to thank my advisor, Enrique Luco, for providing continuous guidance and stimulating ideas, without which the objectives of this work would have been insurmountable. I am especially grateful for his meticulous contributions to major parts of this dissertation.

I benefited greatly from innumerable discussions with Jerry Frazier on all aspects of this thesis. His interest provided much of the impetus and direction for the success of the work.

I wish to thank Ralph Wiggins as well as Jerry Frazier for the opportunity to collaborate on the method of integration used in Part I of this thesis. They both deserve considerable credit for the efficiency of the numerical procedure.

I am grateful to John Orcutt for introducing me to several interesting problems in theoretical seismology. I thank him for his interest in this work and for his frequent collaboration with specific problems.

I want to thank Steve Day, Steve Hartzell, Alan Olson, John Orcutt, Dave Wong, David Harkrider and Don Helmberger for their generous assistance in pursuing the validation comparisons in Chapter 5 of Part I. I also benefited from discussions with Jeff Fried on numerical techniques and their implementation.

I thank Enrique Luco for patiently providing financial support during several of my years at UCSD. Gilbert Hegemier, Jim Brune and John Orcutt also provided occasional support.

I am grateful to Adrienne Rose for the clarity and consistency of the manuscript, maintained by her expertise in typing. I thank Ted Velasquez, Don Betts and Evelyn Portilla for preparing the figures.

Finally, I thank my friend Olga, and my mother and father, for their patient support and genuine interest in my completion of this dissertation. I also thank my children, Michele and Jennifer, for understanding and sacrificing in behalf of this effort.

Apsel, R. J. Computation of complete theoretical seismograms in a multilayered viscoelastic half-space, Abstr. in EOS, Trans. Am. Geophys. Union, 58, p. 1192, December 1977.

Orcutt, J. A. and R. J. Apsel. Synthetic seismograms of sea floor earthquakes as observed by ocean bottom seismographs, Abstr. in EOS, Trans. Am. Geophys. Union, 58, p. 1191, December 1977.

FIELDS OF STUDY

Major Field: Applied Mechanics and Engineering Sciences

Studies in Elasticity/Anelasticity
Professor Eric Reissner
Professor Gilbert A. Hegemier

Studies in Structural Dynamics
Professor J. Enrique Luco

Studies in Mathematics
Professor Forman A. Williams
Professor John A. Tragenstein

ABSTRACT OF THE DISSERTATION

Dynamic Green's Functions for Layered Media
and Applications to Boundary-Value Problems

by

Randy Jay Apsel
Doctor of Philosophy in Applied Mechanics and Engineering Sciences
University of California, San Diego, 1979
Professor J. Enrique Luco, Chairman

Motivated by the increasing demands on earthquake engineering and theoretical seismology, a method to calculate the three-dimensional dynamic Green's functions for layered viscoelastic media is developed in this study. In seismology, these Green's functions may be used to synthesize theoretical seismograms for an extended source including the propagational effects of geologic layering. In earthquake engineering, these Green's functions may be used to determine the response of foundations to external forces and incoming seismic waves when embedded in realistic

geologic structures. The formulation of the method and the subsequent application to problems in theoretical seismology are presented in Part I of this work. The formulation of an integral equation approach involving the Green's functions used to study boundary-value problems and the subsequent application to problems in earthquake engineering are presented in Part II of this work.

The derivation of the method and the calculation of the three-dimensional Green's functions are conducted in the frequency domain by representing the complete response in terms of semi-infinite integrals with respect to wavenumber so as to automatically include all types of waves. If desired, time domain results are then generated through Fourier synthesis. Realistic attenuation for shear and compressional waves is introduced at the outset of the formulation. In addition, there is no frequency limitation, making the method particularly useful for earthquake engineering applications. The method is limited, however, to the case of horizontally parallel layers. The complete displacement and stress fields at multiple receiver points anywhere in the layered viscoelastic medium are efficiently evaluated for different types of sources.

The applications considered in Part I for theoretical seismology include studies of near-field as well as far-field ground motion (although certain earth-flattening approximations may be inappropriate at teleseismic distances); earthquake strong ground motion modeling; wave propagation in an oceanic crustal configuration; and sensitivity studies on earth parameters such as layer thickness and material attenuation. These applications are prefaced by an extensive set of validation tests and demonstrate the flexibility of the method.

In Part II, an integral equation formulation based on the dynamic Green's functions for a layered viscoelastic medium is developed for use as a tool in analyzing various radiation and scattering problems in elastodynamics. Possible studies include the generation of nonreflecting boundary conditions for use in properly modeling the extended earth with finite elements; the response of valleys, canyons and foundations to the action of incoming seismic waves and external forces; and equivalent source representation for propagation purposes.

The applications considered in Part II for earthquake engineering include the dynamic response of foundations embedded in layered viscoelastic media when excited by external forces and moments. The sensitivity to depth of foundation embedment, to degree of material attenuation and to type of lateral contact conditions between the foundation and the surrounding soil is also studied. Such an analysis resolves two prevailing shortcomings in the present state-of-the-art: 1) the practice of restricting the soil model to a homogeneous, non-dissipative, purely elastic half-space; and 2) the practice of constraining the analysis to the case of flat foundations.

CHAPTER 1

INTRODUCTION

1.1 OBJECTIVES AND SCOPE

The development of an efficient method to calculate the three-dimensional dynamic Green's functions for layered viscoelastic media can have significant implications in fields such as seismology, earthquake engineering and dynamic soil mechanics. In seismology, the Green's functions may be used to synthesize theoretical seismograms for an extended source. When compared with observed seismograms, the synthetic seismograms serve to increase our understanding of rupture physics as well as wave propagation in the real Earth. In earthquake engineering, the Green's functions may be used to determine the response of foundations when excited by external forces as well as by incoming seismic waves. In more general terms, the Green's functions coupled with integral equation formulations may be used to solve a variety of radiation and scattering problems in elastodynamics.

For the applications considered in this dissertation, it is necessary to develop the capability of calculating the complete displacement and stress fields at any point in a layered viscoelastic half-space due to different types of buried concentrated sources. It is also important that the method provide accurate solutions across the entire frequency band of interest. The final requirement is that the methodology remain cost-efficient and highly flexible.

The formulation of the method and the calculation of the three-dimensional Green's functions are conducted in the frequency domain. The complete response at a particular frequency is represented in terms of semi-infinite integrals with respect to wavenumber so as to automatically include all types of waves. Then, if desired, time domain results are synthesized through use of a discrete Fast Fourier Transform algorithm. The appearance of common terms is exploited to expedite the calculation when considering many source-receiver pairs simultaneously. Also, the flexibility of the method permits investigations involving sources such as multipoles and concentrated ring loads, fluid layers as well as solid layers, etc. The methodology is limited to a model consisting of a set of horizontally parallel viscoelastic layers overlying a viscoelastic half-space.

Before delving into the details of the present method, a review of the state-of-the-art is presented.

1.2 REVIEW OF THE LITERATURE

In recent years, it has become increasingly important to synthesize seismic signals. Two different, although related, tools have been developed for such studies: 1) Fourier synthesis of frequency dependent Fourier integrals over wavenumber in which the reflection/conversion/transmission properties of the layering are handled analytically as a function of frequency and wavenumber (hereafter referred to as the wavenumber integration method); and 2) geometrical ray techniques in which the time response is decomposed into an infinite set of ray contributions (hereafter referred to as the ray-theoretical method). In the

following two subsections, previous studies along these two lines are briefly reviewed.

1.2.1 Wavenumber Integration Method

In the wavenumber integration approach, the frequency-domain solutions to the equations of motion in cylindrical coordinates are written schematically as

$$\sum_{n} \begin{matrix} \cos(n\theta) \\ \sin(n\theta) \end{matrix} \int_0^\infty F_n(k, \omega, z, z_s, L)\, J_m(kr)\, dk \qquad (1.1)$$

in which the azimuthal dependence is represented by the Fourier series expansion, while the depth and radial dependence appear in the integrands, which correspond to solutions to the equations of motion in the frequency-wavenumber domain. The arguments k, ω, z, z_s, L in the function F show the dependence on wavenumber, frequency, receiver and source depth, and layer properties, respectively. The argument kr of the Bessel functions J_m reveals the dependence on radial observation distance. Eq. (1.1) is presented as a device to guide the following review of the contributions made by various authors.

The function F may be obtained as the solution to a set of linear algebraic equations together with the boundary conditions at the free surface, the continuity conditions at each layer interface and the Sommerfeld radiation condition in the underlying half-space. The system of equations grows linearly with the number of layers, but various matrix decompositions may be used to take advantage of the block diagonal form of the system.

The first such matrix decomposition was presented by Thomson (1950), who reformulated the problem in terms of the so-called layer matrices which transfer the components of motion from interface to interface in an elastic multilayered medium. Haskell (1953) used Thomson's matrix formalism in developing a systematic computational procedure to study surface-wave dispersion for an elastic multilayered half-space. In surface-wave dispersion computations, the surface-wave phase velocity is calculated as a function of frequency and layer properties essentially by finding the surface-wave poles of the function F. To construct the dispersion functions with the Thomson-Haskell technique, the response at the deepest layer interface is related to the response at the free surface by a product of layer matrices, the elements of which are used to find the dispersion function. Even though all the quantities necessary to form the functions F are included in Thomson's formulation, there was apparently no interest in doing so until Haskell (1960, 1962) evaluated the F functions at the free surface due to plane SH and plane P-SV waves incident at the base of the layered structure.

The Thomson-Haskell technique becomes unstable for short wavelengths due to the computation of squares of large exponential terms that must cancel identically (for functions F involving P-SV-Rayleigh waves). These large exponentials dominate the layer-matrices so that the final product consists entirely of the spurious remains of trying to numerically cancel the squared exponential terms.

Thrower (1965), Dunkin (1965) and Watson (1970) modified the Thomson-Haskell formulation using determinant matrix extensions (Pestel

and Leckie, 1963) in which the minors of the layer matrices are propagated from interface to interface so that the squared exponential terms never appear, thus controlling the loss of precision. Schwab (1970) points out that Watson's reduced determinant matrix extension (1970) of the original Thomson-Haskell formulation is the most efficient of the three extensions for surface-wave dispersion computations. However, Schwab (1970) also reveals that the more flexible approach of Knopoff (1964) also contains the loss-of-precision control feature without recourse to determinant matrix theory and is 38% faster than Watson's approach. Knopoff's approach is to immediately construct the solution to the set of linear algebraic equations for F in its full determinental form. Then the determinants are decomposed by means of Laplace's development by minors (Dickson, 1914) into products of interface matrices which transfer the amplitudes of up and downgoing waves from layer to layer across each interface. The general method of "propagator" matrices was introduced by Gilbert and Backus (1966) who formulate F in terms of the numerical solution of a set of linear, first order, ordinary differential equations (see also Richards, 1971 and Kennett, 1972). In the case of homogeneous layers, the product integral of the "propagator" matrices reduces to any of the aforementioned methods using minor propagator techniques.

The first attempts to synthesize seismic signals by evaluating integrals typified by Eq. (1.1) were by Haskell (1964) and Harkrider (1964). They limited their analyses to the surface-wave contributions of the free surface motion by calculating the residues at the Rayleigh and Love poles of the F functions (using Thomson-Haskell theory for F). The time domain response was obtained through Fourier synthesis after evaluating

the residues at a discrete number of frequencies. Later, Harkrider (1970) eliminated the instabilities in his surface-wave algorithm by employing the determinant matrix version of the original Thomson-Haskell formulation as discussed above.

Hudson (1969) extended the work of Haskell (1964) and Harkrider (1964) to synthesize seismic signals at teleseismic distances again using contour integration as described by Lapwood (1949) or Ewing, Jardetzky and Press (1957). Hudson's analysis is limited to large epicentral distances since terms decaying with distance faster than $r^{-1/2}$ are ignored. The remaining terms are evaluated by using the method of steepest descents for the first term in the asymptotic expansion of the Hankel functions. However, as shown by Herrmann (1978), the truncation of the terms with poles between the real axis and the steepest descents path leads to non-causal arrivals. Herrmann (1977) uses contour integration to study the complete SH-Love wave propagation problem in layered elastic media. Following the lead of Carpanter (1966), Hudson (1969) introduced attenuation factors for shear and compressional waves by multiplying the final results by an empirical factor that depends on the ray path from source to receiver.

More recently, the reflectivity method of Fuchs and Müller (1971) became the most widely used wavenumber integration approach. One achievement in this work was the introduction of attenuation into the layers in the form of complex velocities. This not only makes the multilayered medium more realistic (viscoelastic), but also has the desirable feature of shifting all the singularities of the F integrands off the contour of integration, thereby allowing the numerical integration to be performed

directly along the real k axis. Hence, the formidable task of searching for all of the poles of F is eliminated.

However, Fuchs and Müller introduce several approximations which limit the applicability of their method. First of all, their Earth model consists of a set of nonreflecting layers overlying a deep reflecting zone. Their source representation is an explosion applied at the surface of the layered half-space incapable of exciting any shear or surface-wave motion directly. The compressional waves are propagated down to the reflecting zone (using transmission coefficients derived from the Thomson-Haskell layer matrices) after which only the compressional reflection from the multiples and interconversions of the lower reflecting zone is considered. Then the reflected compressional wave is transmitted back to the surface and the vertical and horizontal displacement components of F are computed by using the first order term in the expansion of the free-surface reflection coefficients. The second significant approximation is related to the quadrature scheme used to evaluate the integrals over wavenumber in Eq. (1.1). Fuchs and Müller numerically integrate only over wavenumbers corresponding to the body waves (low k values corresponding to phase velocities higher than the fundamental surface-wave phase velocity). Moreover, they employ trapezoidal rule of integration which requires an exhaustive number of evaluations of the integrands whenever the Bessel functions become too oscillatory.

1.2.2 Ray-Theoretical Methods

In the ray-theoretical approach, the total time-dependent wave field in a layered medium is decomposed into contributions attributed to

an infinite set of rays from the source to the point of observation as in Spencer (1960). Each ray contribution is evaluated by a numerical solution of the impulse response as in Bortfield (1967), Müller (1968, 1970), or by the Cagniard-deHoop technique (1939, 1960) as in Pekeris, et al. (1965), Helmberger (1968), Červený and Ravindra (1971), Gilbert and Helmberger (1972), and Wiggins and Helmberger (1974). The solution for each ray can be obtained exactly (Helmberger, 1968). However, the number of rays selected is invariably limited by the computational difficulties for each ray calculation. Yet, as is pointed out by Hron, Kanesavich and Alpaslan (1974), if the selection of rays is poor, the synthetic seismograms are misleading since rays with significant amplitudes may have been omitted.

Hron and Kanasevich (1971) systematized the selection of a set of rays for a given observation point based on the kinematic and dynamic characteristics of particular types of rays (e.g., the rays with the largest amplitudes are generally those with the least number of reflections and hence the most transmissions). However, in cases where multiples and interconversions are important (see Kennett, 1974), the number of rays increases strongly as shown in Table 1 of Müller (1970). For example, to consider rays up to order seven in a ten layer model, it would require 760804 separate ray calculations for every source-receiver pair even when conversions from P to S and S to P are neglected. Furthermore, as pointed out by Chapman (1974), no matter how many rays are selected from the infinite ray expansion, the response is necessarily band limited in frequency since the theoretical seismograms consist of a series of pulses that must be low-pass filtered to a frequency corresponding to the

transition time for the layers. Yet, when layers sufficiently thin to obtain the desired high frequency signal are considered, it become inefficient to include higher order rays. On the other hand, Müller (1970) and Chapman (1974) have shown the importance of multiple reflections in long period seismograms so that convergence in a homogeneous layered medium using the ray-theoretical method is at most justified for short period studies, where the higher order rays are less important in general.

Acknowledging that the ray-theoretical method is at best a high frequency method, Wiggins and Helmberger (1974) present several approximations that increase the efficiency of the individual ray calculations. Chapman (1974) lessens the long-period limitations by considering the reflections from velocity and density gradients rather than from impedance mismatches at the layer interfaces. Thereby, the summation of impulses due to multiple reflections may be replaced by an iterative scheme involving multiple depth integrals at long periods.

In summary, the drawbacks in the ray-theoretical approach include the following: 1) selection of appropriate set of rays is difficult; 2) separate Cagniard paths must be found numerically by Newton's method for every point on the contour and for each kinematic group (rays with same travel time) and for each source-receiver pair before the amplitude response functions can be sampled at the time points; 3) ray expansion is convergent only at sufficiently high frequencies; and 4) attenuation for P and S waves is difficult to include since the response is obtained directly in the time domain (would have to use Carpenter's empirical approach (1966) as discussed previously).

To accomodate the objectives stated in section 1.1, the ray-theoretical approach is clearly inadequate, while the wavenumber integration approach shows considerable promise.

1.3 DESCRIPTION OF PRESENT METHOD

In compliance with the objectives stated in section 1.1, the problem of three-dimensional wave propagation in layered viscoelastic media is formulated and solved in the frequency domain by a wavenumber integration approach. If desired, the response in the time domain may be obtained through Fourier synthesis. The azimuthal dependence is represented by a Fourier series expansion so that the response at a particular frequency reduces to the evaluation of a semi-infinite integral over wavenumber, as typified by Eq. (1.1) of the previous section. The integrands of these Hankel transform-type integral representations over wavenumber correspond to complete solutions of the equations of motion in the frequency-wavenumber domain.

The kernels of the Hankel transform-type integrals (i.e., the functions F) contain all the depth dependence, which includes receiver depth, source depth and viscoelastic layer properties. In the present wavenumber integration method, the F integrands are evaluated at a particular frequency and wavenumber without approximation, in contrast to the reflectivity method of Fuchs and Müller (1971). The F integrands are given in terms of highly efficient factorizations of the upgoing and downgoing wave amplitudes in each layer. The factorizations are based on the generalized reflection and transmission coefficient matrices, which are formed recursively, from one layer boundary to the next, so as

to include all the reflection/conversion/transmission properties of the layered medium.

The appearance of common factors in the factorizations is taken advantage of when computing the displacement and stress components for multiple source-receiver depth pairs. Another desirable feature is that the present approach lends itself to a physical ray interpretation, analogously to discussions by Cisternas, et al. (1973) and Kennett (1974).

Introduction of realistic attenuation for shear and compressional waves in each layer shifts the singularities of the F integrands off the real wavenumber axis, thus permitting the Hankel transform-type integrals to be numerically evaluated along the real wavenumber axis without recourse to principal values or contour integration. A numerical integration method is implemented to economize the integration procedure while at the same time eliminating the oscillation hazard of the Bessel functions at large arguments.

The F integrands are sequentially sampled at discrete k points satisfying the requirement that quartic polynomials accurately interpolate the amplitudes of the F integrands over each 5-point integration interval. Thereby, the numerical integration with the Bessel functions can be performed analytically over each integration interval, thus avoiding the oscillation hazards of the Bessel functions. The tail ends of the semi-infinite integrals are either handled analytically or else the decay of the F integrands as a function of wavenumber determines the upper integration limit. Since the radial dependence appears only in the Bessel functions, it is expedient to calculate the integrals for multiple epicentral distances simultaneously.

Even though the F integrands become more involved at higher frequencies, there are no instabilities and hence no frequency limitations. Within the realm of the physical model considered (e.g., horizontally parallel viscoelastic layers), there are no limitations on the source-receiver geometry or the layer properties. Since the method is formulated in the frequency domain, any or all of the layer parameters may include a specified frequency dependence. The procedure is relatively cost-efficient and is highly flexible, allowing its usage in all the applications suggested in section 1.1.

Integral representations of the displacement and stress fields are presented in Chapter 2 for use in Chapter 3 as general solutions to the equations of motion in cylindrical coordinates. Expressions for source terms such as concentrated point loads and ring loads are also given. The response of a layered viscoelastic half-space to a buried source is formulated in Chapter 3, where the wave propagation problem is decoupled into vertically and horizontally polarized waves. Preceeded by a summary of all the integral representations from Chapter 3, the method of numerical integration over wavenumber is described in Chapter 4. Chapter 5 includes validation tests, comparisons and results to verify the accuracy of the method in addition to exhibiting the flexibility of the method. Chapter 6 presents a summary of the method and the results from Chapter 5.

Expressions for the reflection and transmission coefficients are given in Appendix I and modifications for propagation of vertically polarized waves at large wavenumbers is presented in Appendix II. Static integral representations of the displacement and stress fields are listed

in Appendix III, and the implementation procedure for point double couple sources is derived in Appendix IV.

CHAPTER 2

INTEGRAL REPRESENTATION OF THE DISPLACEMENT AND STRESS FIELDS

2.1 GENERAL SOLUTION OF THE EQUATIONS OF MOTION IN CYLINDRICAL COORDINATES

General solutions of the inhomogeneous equations of motion for a uniform isotropic viscoelastic medium are derived in this section. The equations of motion in cylindrical coordinates (r, θ, z) for forced steady-state vibrations with time dependence $\exp(i\omega t)$ are

$$\mu\left[\nabla^2 u_r - \frac{1}{r}\left(2\,\frac{\partial u_\theta}{r\partial\theta} + \frac{u_r}{r}\right)\right] + (\lambda + \mu)\,\frac{\partial \Delta}{\partial r} + \omega^2 \rho u_r + F_r = 0$$

$$\mu\left[\nabla^2 u_\theta - \frac{1}{r}\left(\frac{u_\theta}{r} - 2\,\frac{\partial u_r}{r\partial\theta}\right)\right] + (\lambda + \mu)\,\frac{\partial \Delta}{r\partial\theta} + \omega^2 \rho u_\theta + F_\theta = 0$$

$$\mu\nabla^2 u_z + (\lambda + \mu)\,\frac{\partial \Delta}{\partial z} + \omega^2 \rho u_z + F_z = 0 \tag{2.1}$$

in which u_r, u_θ, u_z and F_r, F_θ, F_z correspond to the components of the displacement and body force per unit volume in the r, θ and z directions respectively. The Lamé constants (which may be complex) are denoted by λ and μ, while the density and the frequency are represented by ρ and ω, respectively. In the equations above,

$$\nabla^2 = \frac{\partial^2}{\partial r^2} + \frac{1}{r}\,\frac{\partial}{\partial r} + \frac{1}{r^2}\,\frac{\partial^2}{\partial \theta^2} + \frac{\partial^2}{\partial z^2} \tag{2.2}$$

represents the Laplacian operator, while

$$\Delta = \frac{\partial u_r}{\partial r} + \frac{u_r}{r} + \frac{\partial u_\theta}{r\partial\theta} + \frac{\partial u_z}{\partial z} \tag{2.3}$$

denotes the dilatation.

Expanding the displacements and body forces in a Fourier series with respect to the azimuth θ, it is possible to write

$$u_r(r, \theta, z; \omega) = \frac{r_o}{4\pi\bar{\mu}r}\sum_{n=0} Q_n U_{rn}(r_o, z_o)\cos n(\theta - \theta_o)$$

$$u_\theta(r, \theta, z; \omega) = \frac{r_o}{4\pi\bar{\mu}r}\sum_{n=0} Q_n U_{\theta n}(r_o, z_o)\sin n(\theta - \theta_o) \tag{2.4}$$

$$u_z(r, \theta, z; \omega) = \frac{r_o}{4\pi\bar{\mu}r}\sum_{n=0} Q_n U_{zn}(r_o, z_o)\cos n(\theta - \theta_o)$$

$$F_r(r, \theta, z; \omega) = \frac{\omega^3}{4\pi\bar{\beta}^3}\sum_{n=0} Q_n F_{rn}(r_o, z_o)\cos n(\theta - \theta_o)$$

$$F_\theta(r, \theta, z; \omega) = \frac{\omega^3}{4\pi\bar{\beta}^3}\sum_{n=0} Q_n F_{\theta n}(r_o, z_o)\sin n(\theta - \theta_o) \tag{2.5}$$

$$F_z(r, \theta, z; \omega) = \frac{\omega^3}{4\pi\bar{\beta}^3}\sum_{n=0} Q_n F_{zn}(r_o, z_o)\cos n(\theta - \theta_o)$$

in which θ_o is an arbitrary angle and Q_n are constants with dimensions of force to be defined later. The constants $\bar{\mu}$, $\bar{\rho}$ and $\bar{\beta} = (\bar{\mu}/\bar{\rho})^{\frac{1}{2}}$ correspond to a shear modulus, density and shear wave velocity of reference. The dimensionless variables r_o, z_o are defined by

$$r_o = \omega r/\bar{\beta} \ , \quad z_o = \omega z/\bar{\beta} \ . \tag{2.6}$$

Substitution from Eqs. (2.4) and (2.5) into Eqs. (2.1) leads after some rearrangement to the following equations

$$\mu_o \nabla^2_{n\pm1} \ (U_{rn} \pm U_{\theta n}) + (\lambda_o + \mu_o)\left(\frac{\partial \Delta_n}{\partial r_o} \mp \frac{n}{r_o} \Delta_n\right)$$

$$+ \rho_o(U_{rn} \pm U_{\theta n}) + (F_{rn} \pm F_{\theta n}) = 0 \tag{2.7}$$

$$\mu_o \nabla^2_n U_{zn} + (\lambda_o + \mu_o) \frac{\partial \Delta_n}{\partial z_o} + \rho_o U_{zn} + F_{zn} = 0$$

where $\lambda_o = \lambda/\bar{\mu}$, $\mu_o = \mu/\bar{\mu}$, $\rho_o = \rho/\bar{\rho}$,

$$\nabla^2_n = \frac{\partial^2}{\partial r_o^2} + \frac{1}{r_o}\frac{\partial}{\partial r_o} - \frac{n^2}{r_o^2} + \frac{\partial^2}{\partial z_o^2} \tag{2.8}$$

and

$$\Delta_n = \frac{\partial U_{rn}}{\partial r_o} + \frac{U_{rn}}{r_o} + \frac{n}{r_o} U_{\theta n} + \frac{\partial U_{zn}}{\partial z_o} \ . \tag{2.9}$$

At this point it is convenient to define

$$\pm u_{1n}(z_o, k) + u_{3n}(z_o, k) = \int_0^\infty r_o(U_{rn} \pm U_{\theta n}) J_{n\pm1}(kr_o) dr_o$$

$$u_{2n}(z_o, k) = \int_0^\infty r_o U_{zn} J_n(kr_o) dr_o \tag{2.10}$$

and

$$\pm F_{1n}(z_o, k) + F_{3n}(z_o, k) = \int_o^\infty r_o(F_{rn} \pm F_{\theta n})J_{n\pm1}(kr_o)dr_o$$

$$F_{2n}(z_o, k) = \int_o^\infty r_o F_{zn} J_n(kr_o)dr_o \quad . \tag{2.11}$$

By taking appropriate Hankel transforms with respect to r_o of Eqs. (2.7) and recalling the well-known formulae

$$\int_o^\infty r_o \nabla_n^2 \phi J_n(kr_o)dr_o = \left(\frac{d^2}{dz_o^2} - k^2\right)\int_o^\infty r_o \phi J_n(kr_o)dr_o \tag{2.12}$$

$$\int_o^\infty r_o \left(\frac{d\phi}{dr_o} \pm \frac{n}{r_o}\phi\right) J_{n\pm1}(kr_o)dr_o = \mp k \int_o^\infty r_o \phi J_n(kr_o)dr_o \quad , \tag{2.13}$$

it is possible to show that Eqs. (2.7) reduce to

$$\begin{aligned} &\mu_o\left(\frac{d^2}{dz_o^2} - k^2 + \frac{\rho_o}{\mu_o}\right)(\pm u_{1n} + u_{3n}) \mp (\lambda_o + \mu_o)k\bar{\Delta}_n \\ &\qquad + (\pm F_{1n} + F_{3n}) = 0 \\ &\mu_o\left(\frac{d^2}{dz_o^2} - k^2 + \frac{\rho_o}{\mu_o}\right) u_{2n} + (\lambda_o + \mu_o)\frac{d}{dz_o}\bar{\Delta}_n + F_{2n} = 0 \end{aligned} \tag{2.14}$$

where

$$\bar{\Delta}_n = \int_o^\infty r_o \Delta_n J_n(kr_o)dr_o \quad . \tag{2.15}$$

Substitution from Eq. (2.9) into Eq. (2.15), and use of Eqs. (2.13) and (2.10) leads to

$$\overline{\Delta}_n = ku_{1n} + \frac{du_{2n}}{dz_o} . \tag{2.16}$$

Recombining Eqs. (2.14) and making use of Eq. (2.16), the following ordinary second-order differential equations for u_{1n}, u_{2n} and u_{3n} are obtained

$$\left[\mu_o \frac{d^2}{dz_o^2} - (\lambda_o + 2\mu_o)k^2 + \rho_o\right]u_{1n} - (\lambda_o + \mu_o)k \frac{du_{2n}}{dz_o} + F_{1n} = 0 \tag{2.17}$$

$$-(\lambda_o + \mu_o)k \frac{du_{1n}}{dz_o} - \left[(\lambda_o + 2\mu_o) \frac{d^2}{dz_o^2} - \mu_o k^2 + \rho_o\right]u_{2n} - F_{2n} = 0 \tag{2.18}$$

and

$$\mu_o\left(\frac{d^2}{dz_o^2} - k^2 + \frac{\rho_o}{\mu_o}\right)u_{3n} + F_{3n} = 0 . \tag{2.19}$$

The terms $u_{1n}(z_o, k)$ and $u_{2n}(z_o, k)$ are coupled through Eqs. (2.17) and (2.18) and are independent of $u_{3n}(z_o, k)$ which must satisfy Eq. (2.19). The terms u_{1n} and u_{2n} are associated with waves whose particle motion is polarized in vertical planes (P and SV waves), while the term u_{3n} is associated with waves whose particle motion is polarized in horizontal planes (SH waves).

A general solution of Eqs. (2.17) and (2.18) may be obtained by the method of variation of parameters. In this case, u_{1n} and u_{2n}

are written in the form

$$\begin{Bmatrix} u_{1n}(z_o, k) \\ u_{2n}(z_o, k) \end{Bmatrix} = \begin{bmatrix} -k & \nu' & -k & \nu' \\ -\nu & k & \nu & -k \end{bmatrix} \begin{Bmatrix} \eta_{1n}(z_o, k)\exp\left[-\nu(z_o - z_o^u)\right] \\ \eta_{2n}(z_o, k)\exp\left[-\nu'(z_o - z_o^u)\right] \\ \eta_{3n}(z_o, k)\exp\left[\nu(z_o - z_o^d)\right] \\ \eta_{4n}(z_o, k)\exp\left[-\nu'(z_o - z_o^d)\right] \end{Bmatrix} \tag{2.20}$$

where the unknown functions $\eta_{in}(z_o, k)$ $(i = 1, 4)$ are to be determined, while z_o^u and z_o^d are arbitrary constants introduced here for later use, and

$$\nu = \left[k^2 - \left(\frac{\rho_o}{\lambda_o + 2\mu_o}\right)\right]^{\frac{1}{2}}, \quad \nu' = \left[k^2 - \left(\frac{\rho_o}{\mu_o}\right)\right]^{\frac{1}{2}} . \tag{2.21}$$

Requiring that the functions $\eta_i(z_o, k)$ $(i = 1, 4)$ satisfy the conditions

$$\begin{bmatrix} -k & \nu' & -k & \nu' \\ -\nu & k & \nu & -k \end{bmatrix} \begin{Bmatrix} \eta_{1n}'\exp\left[-\nu(z_o - z_o^u)\right] \\ \eta_{2n}'\exp\left[-\nu'(z_o - z_o^u)\right] \\ \eta_{3n}'\exp\left[\nu(z_o - z_o^d)\right] \\ \eta_{4n}'\exp\left[\nu'(z_o - z_o)\right] \end{Bmatrix} = \begin{Bmatrix} 0 \\ 0 \end{Bmatrix} \tag{2.22}$$

in which the prime denotes derivative with respect to z_o, leads, after substitution from Eqs. (2.20) and (2.22) into Eqs. (2.17) and (2.18), to the following system of first order differential equations

$$\begin{bmatrix} -k & \nu' & -k & \nu' \\ -\nu & k & \nu & -k \\ -\nu k & (\nu')^2 & \nu k & -(\nu')^2 \\ -\nu^2 & \nu' k & -\nu^2 & \nu' k \end{bmatrix} \begin{Bmatrix} \eta'_{1n} \exp\left[-\nu(z_o - z_o^u)\right] \\ \eta'_{2n} \exp\left[-\nu'(z_o - z_o^u)\right] \\ \eta'_{3n} \exp\left[\nu(z_o - z_o^d)\right] \\ \eta'_{4n} \exp\left[\nu'(z_o - z_o^d)\right] \end{Bmatrix} = \begin{Bmatrix} 0 \\ 0 \\ F_{1n}/\mu_o \\ F_{2n}/(\lambda_o + 2\mu_o) \end{Bmatrix} . \tag{2.23}$$

Inverting the square matrix appearing on the left-hand side of Eq. (2.23) and integrating with respect to z_o results in

$$\eta_{in}(z_o, k) = A_{in}(k) + S_{in}(z_o, k) \quad (i = 1, 4) \tag{2.24}$$

where $A_{in}(k)$ $(i = 1, 4)$ are coefficients independent of z_o to be determined by boundary or other conditions, and $S_{in}(z_o, k)$ $(i = 1, 4)$ correspond to the source terms given by

$$\begin{Bmatrix} S_{1n}(z_o, k) \\ S_{2n}(z_o, k) \end{Bmatrix} = \frac{1}{2\rho_o} \int_{z_o^u}^{z_o} \begin{bmatrix} \frac{-k}{\nu} \exp\left[\nu(z'_o - z_o^u)\right] & \exp\left[\nu(z'_o - z_o^u)\right] \\ -\exp\left[\nu'(z'_o - z_o^u)\right] & \frac{k}{\nu'} \exp\left[\nu'(z'_o - z_o^u)\right] \end{bmatrix} \times \begin{Bmatrix} F_{1n}(z'_o, k) \\ F_{2n}(z'_o, k) \end{Bmatrix} dz'_o \tag{2.25}$$

$$\begin{Bmatrix} S_{3n}(z_o, k) \\ S_{4n}(z_o, k) \end{Bmatrix} = \frac{-1}{2\rho_o} \int_{z_o}^{z_o^d} \begin{bmatrix} \frac{k}{\nu} \exp\left[-\nu(z'_o - z_o^d)\right] & \exp\left[-\nu(z'_o - z_o^d)\right] \\ \exp\left[-\nu'(z'_o - z_o^d)\right] & \frac{k}{\nu'} \exp\left[-\nu'(z'_o - z_o^d)\right] \end{bmatrix} \times \begin{Bmatrix} F_{1n}(z'_o, k) \\ F_{2n}(z'_o, k) \end{Bmatrix} dz'_o \ . \tag{2.26}$$

The terms associated with η_{1n} and η_{2n} correspond respectively to downwardly propagating compressional and shear waves, while those associated with η_{3n} and η_{4n} correspond respectively to upwardly propagating compressional and shear waves. Particular forms for the source terms $S_{in}(z_o, k)$ are presented later for the case of concentrated point and ring loads.

Proceeding in a similar fashion it may be found that the general solution of Eq. (2.19) is given by

$$u_{3n}(z_o, k) = k \left\{ \eta_{5n}(z_o, k) \exp\left[-\nu'(z_o - z_o^u)\right] + \eta_{6n}(z_o, k) \exp\left[\nu'(z_o - z_o^d)\right] \right\} \tag{2.27}$$

where

$$\eta_{in}(z_o, k) = A_{in}(k) + S_{in}(z_o, k) \qquad (i = 5, 6) \tag{2.28}$$

and

$$S_{5n}(z_o, k) = \frac{1}{2\mu_o} \frac{1}{k\nu'} \int_{z_o^u}^{z_o} \exp\left[\nu'(z_o' - z_o^u)\right] F_{3n}(z_o', k) dz_o' \tag{2.29}$$

$$S_{6n}(z_o, k) = \frac{1}{2\mu_o} \frac{1}{k\nu'} \int_{z_o}^{z_o^d} \exp\left[-\nu'(z_o' - z_o^d)\right] F_{3n}(z_o', k) dz_o' \; . \tag{2.30}$$

In Eq. (2.27) the terms associated with η_{5n} and η_{6n} correspond to down- and upwardly propagating SH waves, respectively. In writing Eqs. (2.25), (2.26), (2.29) and (2.30), it has been assumed that the body forces vanish outside the depth range $\left[z_o^u, z_o^d\right]$.

Having obtained general solutions for u_{1n}, u_{2n} and u_{3n}, it only remains to invert the Hankel transforms appearing in Eqs. (2.10) to obtain

$$U_{rn}(r_o, z_o) \pm U_{\theta n}(r_o, z_o) = \int_0^\infty k\left[\pm u_{1n}(z_o, k) + u_{3n}(z_o, k)\right]J_{n\pm1}(kr_o)dk$$

$$U_{zn}(r_o, z_o) = \int_0^\infty k u_{2n}(z_o, k)J_n(kr_o)dk \ . \tag{2.31}$$

Substitution from Eqs. (2.31) into Eqs. (2.4) leads to the desired integral representation of the general solution of the equations of motion in cylindrical coordinates.

2.2 INTEGRAL REPRESENTATION FOR THE STRESS COMPONENTS

An integral representation for the stress field corresponding to the displacement field described in the previous section is obtained here. The stress-displacement relations in cylindrical coordinates are given by

$$\sigma_{rz} = \mu\left(\frac{\partial u_z}{\partial r} + \frac{\partial u_r}{\partial z}\right)$$

$$\sigma_{\theta z} = \mu\left(\frac{\partial u_\theta}{\partial z} + \frac{\partial u_z}{r\partial \theta}\right)$$

$$\sigma_{zz} = 2\mu\frac{\partial u_z}{\partial z} + \lambda\Delta$$

$$\sigma_{rr} = 2\mu\frac{\partial u_r}{\partial z} + \lambda\Delta \tag{2.32}$$

$$\sigma_{\theta\theta} = 2\mu\left(\frac{\partial u_\theta}{r\partial\theta} + \frac{u_r}{r}\right) + \lambda\Delta$$

$$\sigma_{\theta r} = \mu\left(\frac{\partial u_r}{r\partial\theta} + \frac{\partial u_\theta}{\partial r} - \frac{u_\theta}{r}\right)$$

in which Δ is defined by Eq. (2.3). Expanding the stress components in a Fourier series with respect to the azimuth θ leads to

$$\begin{aligned}
\sigma_{rz}(r, \theta, z; \omega) &= \frac{r_o^2}{4\pi r^2}\sum_{n=0} Q_n \Sigma_{rzn}(r_o, z_o)\cos n(\theta - \theta_o) \\
\sigma_{\theta z}(r, \theta, z; \omega) &= \frac{r_o^2}{4\pi r^2}\sum_{n=0} Q_n \Sigma_{\theta zn}(r_o, z_o)\sin n(\theta - \theta_o) \\
\sigma_{zz}(r, \theta, z; \omega) &= \frac{r_o^2}{4\pi r^2}\sum_{n=0} Q_n \Sigma_{zzn}(r_o, z_o)\cos n(\theta - \theta_o) \\
\sigma_{rr}(r, \theta, z; \omega) &= \frac{r_o^2}{4\pi r^2}\sum_{n=0} Q_n \Sigma_{rrn}(r_o, z_o)\cos n(\theta - \theta_o) \\
\sigma_{\theta\theta}(r, \theta, z; \omega) &= \frac{r_o^2}{4\pi r^2}\sum_{n=0} Q_n \Sigma_{\theta\theta n}(r_o, z_o)\cos n(\theta - \theta_o) \\
\sigma_{\theta r}(r, \theta, z; \omega) &= \frac{r_o^2}{4\pi r^2}\sum_{n=0} Q_n \Sigma_{\theta rn}(r_o, z_o)\sin n(\theta - \theta_o) \ .
\end{aligned} \tag{2.33}$$

By use of Eqs. (2.4), (2.32) and (2.33), it can be shown that

$$\Sigma_{rzn} \pm \Sigma_{\theta zn} = \mu_o \frac{\partial U_{zn}}{\partial r_o} \mp \frac{n}{r_o} U_{zn} + \frac{\partial}{\partial z_o}(U_{rn} \pm U_{\theta n})$$

$$\Sigma_{zzn} = 2\mu_o \frac{\partial U_{zn}}{\partial z_o} + \lambda_o \Delta_n$$

$$\Sigma_{rrn} + \Sigma_{\theta\theta n} = 2\left[(\lambda_o + \mu_o)\Delta_n - \mu_o \frac{\partial U_{zn}}{\partial z_o}\right] \tag{2.34}$$

$$\Sigma_{rrn} + \frac{2\mu_o}{r_o}(U_{rn} + nU_{\theta n}) = (\lambda_o + 2\mu_o)\Delta_n - 2\mu_o \frac{\partial U_{zn}}{\partial z_o}$$

$$\Sigma_{\theta rn} + \frac{2\mu_o}{r_o}(nU_{rn} + U_{\theta n}) = \frac{\mu_o}{2}\left[\left(\frac{\partial}{\partial r_o}\frac{n+1}{r_o}\right)(U_{\theta n} + \theta_{\theta n}) - \left(\frac{\partial}{\partial r_o} - \frac{n-1}{r_o}\right)(U_{rn} - U_{\theta n})\right]$$

where Δ_n is given by Eq. (2.9). Substitution from Eqs. (2.31) and recalling from Eqs. (2.15) and (2.16) that

$$\Delta_h = \int_0^\infty k\left[ku_{1n} + \frac{du_{2n}}{dz_o}\right] J_n(kr_o)dk \tag{2.35}$$

leads to

$$\Sigma_{rzn} \pm \Sigma_{\theta zn} = \int_0^\infty k\left[\pm \sigma_{21n}(z_o, k) + \sigma_{23n}(z_o, k)\right] J_{n\pm1}(kr_o)dk$$

$$\Sigma_{zzn} = \int_0^\infty k\sigma_{22n}(z_o, k)J_n(kr_o)dk$$

$$\Sigma_{rrn} + \Sigma_{\theta\theta n} + \int_0^\infty k\sigma_{33n}(z_o, k)J_n(kr_o)dk \tag{2.36}$$

$$\Sigma_{rrn} + \frac{2\mu_o}{r_o}(U_{rn} + nU_{\theta n}) = \int_0^\infty k\sigma_{11n}(z_o, k)J_n(kr_o)dk$$

$$\Sigma_{\theta rn} + \frac{2\mu_o}{r_o}(nU_{rn} + U_{\theta n}) = \int_0^\infty k\sigma_{13n}(z_o, k)J_n(kr_o)dk$$

in which

$$\sigma_{21n}(z_o, k) = \mu_o\left(\frac{du_{1n}}{dz_o} - ku_{2n}\right)$$

$$\sigma_{22n}(z_o, k) = (\lambda_o + 2\mu_o)\left(ku_{1n} + \frac{du_{2n}}{dz_o}\right) - 2\mu_o ku_{1n}$$

$$\sigma_{23n}(z_o, k) = \mu_o \frac{du_{3n}}{dz_o} \tag{2.37}$$

$$\sigma_{33n}(z_o, k) = 2\left[(\lambda_o + 2\mu_o)\left(ku_{1n} + \frac{du_{2n}}{dz_o}\right) - \mu_o\left(ku_{1n} + 2\frac{du_{2n}}{dz_o}\right)\right]$$

$$\sigma_{11n}(z_o, k) = (\lambda_o + 2\mu_o)\left(ku_{1n} + \frac{du_{2n}}{dz_o}\right) - 2\mu_o \frac{du_{2n}}{dz_o}$$

$$\sigma_{13n}(z_o, k) = \mu_o ku_{3n}.$$

Finally, substitution from Eqs. (2.20) and (2.27) into Eqs. (2.37) results in

$$\begin{Bmatrix} \sigma_{21n} \\ \sigma_{22n} \\ \sigma_{33n} \\ \sigma_{11n} \end{Bmatrix} = \mu_o \begin{bmatrix} 2\nu k & -(2k^2 - \beta_o^{-2}) & -2k\nu & (2k^2 - \beta_o^{-2} \\ (2k^2 - \beta_o^{-2}) & -2k\nu' & (2k^2 - \beta_o^{-2}) & -2k\nu' \\ 2\beta_o^{-2}(2\gamma^2 - 1) - 2k^2 & 2k\nu' & 2\beta_o^{-2}(2\gamma^2 - 1) - 2k^2 & 2k\nu' \\ \beta_o^{-2}(2\gamma^2 - 1) - 2k^2 & 2k\nu' & \beta_o^{-2}(2\gamma^2 - 1) - 2k^2 & 2k\nu' \end{bmatrix}$$

$$\times \begin{Bmatrix} \eta_{1n}(z_o,k)\exp\left[-\nu(z_o - z_o^u)\right] \\ \eta_{2n}(z_o,k)\exp\left[-\nu'(z_o - z_o^u)\right] \\ \eta_{3n}(z_o,k)\exp\left[\nu(z_o - z_o^d)\right] \\ \eta_{4n}(z_o,k)\exp\left[\nu'(z_o - z_o^d)\right] \end{Bmatrix} \tag{2.38}$$

and

$$\begin{Bmatrix} \sigma_{23n} \\ \sigma_{13n} \end{Bmatrix} = \mu_o \begin{bmatrix} -k\nu' & k\nu' \\ k^2 & k^2 \end{bmatrix} \begin{Bmatrix} \eta_{5n}(z_o, k)\exp\left[-\nu'(z_o - z_o^u)\right] \\ \eta_{6n}(z_o, k)\exp\left[\nu'(z_o - z_o^d)\right] \end{Bmatrix} \tag{2.39}$$

where β_o is the normalized (complex) shear wave velocity

$$\beta_o = \sqrt{\frac{\mu_o}{\rho_o}} = \frac{1}{\bar{\beta}} \sqrt{\frac{\mu}{\rho}} \tag{2.40}$$

and γ is the (complex) ratio of the shear wave velocity to the compressional wave velocity

$$\gamma^2 = \frac{\mu_o}{\lambda_o + 2\mu_o} = \frac{\mu}{\lambda + 2\mu} \, . \tag{2.41}$$

Eqs. (2.33), (2.36), (2.38) and (2.39) provide the desired integral representation for the stress components in cylindrical coordinates.

2.3 SOURCE TERMS FOR CONCENTRATED POINT LOADS

The source terms described in Section 2.1 are obtained here for the particular case of a point load acting at the point of coordinates $(0, 0, z^s)$ as illustrated in Figure 2.1. The body forces per unit volume in Cartesian coordinates are given in this case by

$$\begin{aligned} F_x(x, y, z; \omega) &= Q_1 \cos\theta_o \delta(x)\delta(y)\delta(z - z^s) \\ F_y(x, y, z; \omega) &= Q_1 \sin\theta_o \delta(x)\delta(y)\delta(z - z^s) \\ F_z(x, y, z; \omega) &= Q_0 \delta(x)\delta(y)\delta(z - z^s) \end{aligned} \tag{2.42}$$

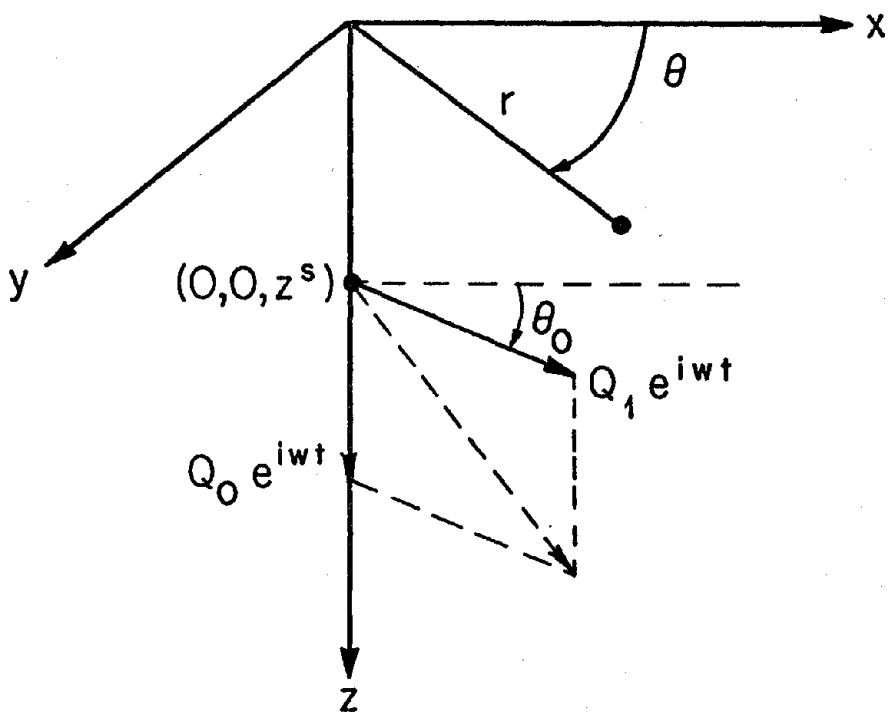

Figure 2.1. Source-receiver geometry for concentrated harmonic force acting at point of coordinates $(0, 0, z^s)$.

where Q_0 represents the vertical component of the concentrated force while Q_1 represents the horizontal component of the body force which acts on a line forming the angle θ_0 with the x-axis. In cylindrical coordinates, the components of the body forces per unit volume are

$$F_r = \left(\frac{\omega}{\bar{\beta}}\right)^3 Q_1 \cos(\theta - \theta_0) \frac{\delta(r_0)}{2\pi r_0} \delta(z_0 - z_0^s)$$

$$F_\theta = -\left(\frac{\omega}{\bar{\beta}}\right)^3 Q_1 \sin(\theta - \theta_0) \frac{\delta(r_0)}{2\pi r_0} \delta(z_0 - z_0^s) \qquad (2.43)$$

$$F_z = \left(\frac{\omega}{\bar{\beta}}\right)^3 Q_0 \frac{\delta(r_0)}{2\pi r_0} \delta(z_0 - z_0^s)$$

where the dimensionless coordinates r_0, z_0 and $z_0^s = \omega z^s / \bar{\beta}$ have been used. Comparison of Eq. (2.43) with Eq. (2.5) leads to

$$F_{r0}(r_0, z_0) = 0 , \quad F_{\theta 0}(r_0, z_0) = 0 ,$$

$$F_{z0}(r_0, z_0) = \frac{2}{r_0} \delta(r_0)\delta(z_0 - z_0^s)$$

$$F_{r1}(r_0, z_0) = -F_{\theta 1}(r_0, z_0) = \frac{2}{r_0} \delta(r_0)\delta(z_0 - z_0^s) , \qquad (2.44)$$

$$F_{z1}(r_0, z_0) = 0 .$$

Equations (2.5) and (2.44) indicate that the vertical component Q_0 of the concentrated force leads to source terms that are independent of the azimuth θ ($n = 0$) while the horizontal component Q_1 leads to source terms that depend on $\cos(\theta - \theta_0)$ and $\sin(\theta - \theta_0)$ ($n = 1$).

Substitution from Eqs. (2.44) into Eqs. (2.11) results in

$$F_{10}(z_o, k) = 0 \ , \quad F_{20}(z_o, k) = 2\delta(z_o - z_o^s) \ , \quad F_{30}(z_o, k) = 0$$

$$F_{11}(z_o, k) = -F_{31}(z_o, k) = -2\delta(z_o - z_o^s) \ , \quad F_{21}(z_o, k) = 0 \ . \tag{2.45}$$

Finally, Eqs. (2.45) together with Eqs. (2.25), (2.26), (2.29) and (2.30) lead to

$$\begin{Bmatrix} S_{10}(z_o, k) \\ S_{20}(z_o, k) \\ S_{30}(z_o, k) \\ S_{40}(z_o, k) \end{Bmatrix} = \frac{1}{\rho_o} \begin{Bmatrix} \exp\left[\nu(z_o^s - z_o^u)\right] H(z_o - z_o^s) \\ \frac{k}{\nu'} \exp\left[\nu'(z_o^s - z_o^u)\right] H(z_o - z_o^s) \\ -\exp\left[-\nu(z_o^s - z_o^d)\right] H(z_o^s - z_o) \\ -\frac{k}{\nu'} \exp\left[-\nu'(z_o^s - z_o^d)\right] H(z_o^s - z_o) \end{Bmatrix} \tag{2.46}$$

$$\begin{Bmatrix} S_{50}(z_o, k) \\ S_{60}(z_o, k) \end{Bmatrix} = \begin{Bmatrix} 0 \\ 0 \end{Bmatrix} \tag{2.47}$$

and

$$\begin{Bmatrix} S_{11}(z_o, k) \\ S_{21}(z_o, k) \\ S_{31}(z_o, k) \\ S_{41}(z_o, k) \end{Bmatrix} = \frac{1}{\rho_o} \begin{Bmatrix} \frac{k}{\nu} \exp\left[\nu(z_o^s - z_o^u)\right] H(z_o - z_o^s) \\ \exp\left[\nu'(z_o^s - z_o^u)\right] H(z_o - z_o^s) \\ \frac{k}{\nu} \exp\left[-\nu(z_o^s - z_o^d)\right] H(z_o^s - z_o) \\ \exp\left[-\nu'(z_o^s - z_o^d)\right] H(z_o^s - z_o) \end{Bmatrix} \tag{2.48}$$

$$\begin{Bmatrix} S_{51}(z_o, k) \\ S_{61}(z_o, k) \end{Bmatrix} = \frac{1}{\mu_o k \nu'} \begin{Bmatrix} \exp\left[\nu'(z_o^s - z_o^u)\right] H(z_o - z_o^s) \\ \exp\left[-\nu'(z_o^s - z_o^d)\right] H(z_o^s - z_o) \end{Bmatrix} \tag{2.49}$$

In the above equations $H(x)$ denotes the Heaviside step function. The source terms for the vertical component of the concentrated force are given by Eqs. (2.46) and (2.47), while the source terms for the horizontal component of the force are given by Eqs. (2.48) and (2.49). Equation (2.47) indicates that a concentrated vertical force will not excite SH waves. It should be mentioned that the source terms corresponding to downwardly propagating waves (S_1, S_2 and S_5) are zero above the source ($z_o < z_o^S$) while the source terms associated with upwardly propagating waves (S_3, S_4 and S_6) are zero below the source ($z_o > z_o^S$).

2.4 SOURCE TERMS FOR RING LOADS

The solution of a variety of axisymmetric problems in elasticity may be simplified by considering the response of a viscoelastic medium to loads distributed on a ring. In this section, the source terms and some rearrangements of the integral representations described in previous sections are derived for the case of ring loads.

In the first place a vertical load distributed on a horizontal ring of radius $\underline{a}$ as illustrated in Figure 2.2a is considered. Assuming that the vertical load per unit arc is $(Q_n/2\pi a)\cos n(\theta - \theta_o)$, then the distribution of body forces in the medium is

$$F_r(r, \theta, z; \omega) = F_\theta(r, \theta, z; \omega) = 0 \ ;$$
$$F_z(r, \theta, z; \omega) = \frac{Q_n}{2\pi a} \cos n(\theta - \theta_o)\delta(r - a)\delta(z - z^S) \ . \tag{2.50}$$

Introducing the dimensionless variables r_o, z_o, $a_o = \omega a/\bar{\beta}$ and $z_o^S = \omega z^S/\bar{\beta}$, it is possible to rewrite Eq. (2.50) in the form

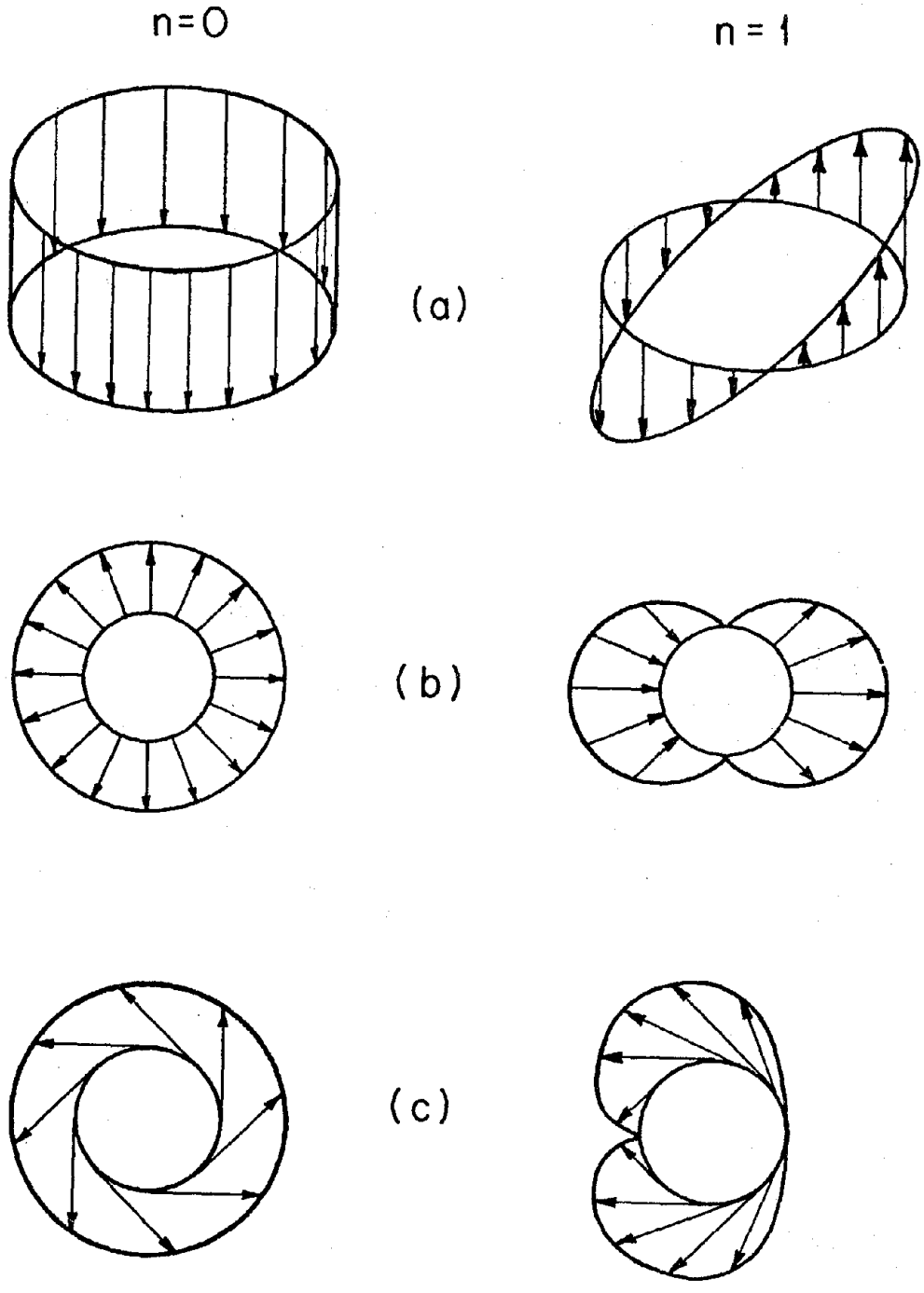

Figure 2.2. Azimuthal dependence of concentrated loads distributed on a horizontal ring of radius a. Vertical, radial and tangential ring loads are shown in Figures a, b and c, respectively, for ring orders n = 0 and n = 1. Figure c for n = 0 cooresponds to $n\theta_o = \pi/2$ (all other figures are for $n\theta_o = 0$).

$$F_r = F_\theta = 0 \; ; \quad F_z(r, \theta, z; \omega) = \left(\frac{\omega}{\beta}\right)^3 \frac{Q_n}{2\pi a_o} \cos n(\theta - \theta_o)$$

$$\times \delta(r_o - a_o)\delta(z_o - z_o^s) \; . \quad (2.51)$$

Comparison with Eq. (2.5) leads to

$$F_{rn} = F_{\theta n} = 0 \; ; \quad F_{zn} = 2 \frac{\delta(r_o - a_o)}{a_o} \delta(z_o - z_o^s) \; . \quad (2.52)$$

Substitution from Eq. (2.52) into Eq. (2.11) results in

$$F_{1n}(z_o, k) = F_{3n}(z_o, k) = 0 \; ;$$

$$F_{2n}(z_o, k) = 2J_n(ka_o)\delta(z_o - z_o^s) \; . \quad (2.53)$$

Comparison with the corresponding terms for a concentrated point load indicates that the source terms $S_{in}^V(z_o, k)$ $(i = 1, 6)$ for the vertical ring load can be expressed as

$$S_{in}^V(z_o, k) = S_{i0}(z_o, k)J_n(ka_o) \; , \quad (i = 1, 4)$$

$$S_{5n}^V(z_o, k) = S_{6n}^V(z_o, k) = 0 \quad (2.54)$$

where $S_{i0}(z_o, k)$ $(i = 1, 4)$ represent the source terms for a concentrated vertical point load as given by Eq. (2.46).

Taking advantage of the particular form of Eqs. (2.54), it is possible to obtain the following integral representation for the Fourier components (with respect to the azimuth θ) of the displacement and stress components for a vertical ring load:

$$U^V_{rn} \pm U^V_{\theta n} = \pm \int_0^\infty ku_{10}(z_o, k)J_n(ka_o)J_{n\pm1}(kr_o)dk$$

$$U^V_{zn} = \int_0^\infty ku_{20}(z_o, k)J_n(ka_o)J_n(kr_o)dk$$

$$\Sigma^V_{rzn} \pm \Sigma^V_{\theta zn} = \pm \int_0^\infty k\sigma_{210}(z_o, k)J_n(ka_o)J_{n\pm1}(kr_o)dk$$

$$\Sigma^V_{zzn} = \int_0^\infty k\sigma_{220}(z_o, k)J_n(ka_o)J_n(kr_o)dk \qquad (2.55)$$

$$\Sigma^V_{rrn} + \Sigma^V_{\theta\theta n} = \int_0^\infty k\sigma_{330}(z_o, k)J_n(ka_o)J_n(kr_o)dk$$

$$\Sigma^V_{rrn} + \frac{2\mu_o}{r_o}(U^V_{rn} + nU^V_{\theta n}) = \int_0^\infty k\sigma_{110}(z_o, k)J_n(ka_o)J_n(kr_o)dk$$

$$\Sigma^V_{\theta rn} + \frac{2\mu_o}{r_o}(nU^V_{rn} + U^V_{\theta n}) = 0 \ .$$

In these equations, the terms $u_{i0}(z_o, k)$ and $\sigma_{ij0}(z_o, k)$ correspond to those defined by Eqs. (2.20) and (2.38) for the case of a concentrated vertical point load. Eqs. (2.55) indicate that to obtain the response for a vertical ring load it is only necessary to introduce the factor $J_n(ka_o)$ in the integral representation for a concentrated vertical point load. Another interesting point is that a vertical ring load does not generate SH waves as shown by the fact that the source terms S^V_{5n} and S^V_{6n} are zero.

Next, a radial load distributed on a horizontal ring of radius a as illustrated in Fig. 2.2b is considered. Assuming that the radial load per unit arc is $(Q_n/2\pi a)\cos n(\theta - \theta_o)$, the distribution of body forces in the medium is

$$F_r(r, \theta, z; \omega) = \frac{Q_n}{2\pi a} \cos n(\theta - \theta_o)\delta(r - a)\delta(z - z^s) ,$$
$$F_\theta(r, \theta, z; \omega) = F_z(r, \theta, z; \omega) = 0 . \tag{2.56}$$

Proceeding in the same fashion as described for a vertical ring load it is found that

$$F_{1n}(z_o, k) = \left[J_{n+1}(ka_o) - J_{n-1}(ka_o)\right]\delta(z_o - z_o^s)$$
$$F_{2n}(z_o, k) = 0 \tag{2.57}$$
$$F_{3n}(z_o, k) = \left[J_{n+1}(ka_o) - J_{n-1}(ka_o)\right]\delta(z_o - z_o^s)$$

from which the source terms $S_{in}^R(z_o, k)$ $(i = 1, 6)$ for a radial ring load are obtained:

$$S_{in}^R(z_o, k) = S_{i1}(z_o, k)\left[J_{n-1}(ka_o) - J_{n+1}(ka_o)\right]/2 \quad (i=1,4)$$
$$S_{in}^R(z_o, k) = S_{i1}(z_o, k)\left[J_{n-1}(ka_o) + J_{n+1}(ka_o)\right]/2 \quad (i=5,6) \tag{2.58}$$

where $S_{i1}(z_o, k)$ $(i = 1, 6)$ represent the source terms for a concentrated horizontal point load as given by Eqs. (2.48) and (2.49).

Finally, for a tangential ring load $(Q_n/2\pi a)\sin n(\theta - \theta_o)$ per unit arc as illustrated in Fig. 2.2c the distribution of body forces is

$$F_\theta(r, \theta, z; \omega) = \frac{Q_n}{2\pi a} \sin n(\theta - \theta_o)\delta(r - a)\delta(z - z^s) \; ;$$

$$F_r(r, \theta, z; \omega) = F_z(r, \theta, z; \omega) = 0 \tag{2.59}$$

and the source terms $S^T_{in}(z_o, k)$ $(i = 1, 6)$ are

$$S^T_{in}(z_o, k) = -S_{i1}(z_o, k)\left[J_{n-1}(ka_o) + J_{n+1}(ka_o)\right]/2 \quad (i = 1, 4)$$

$$S^T_{in}(z_o, k) = -S_{i1}(z_o, k)\left[J_{n-1}(ka_o) - J_{n+1}(ka_o)\right]/2 \quad (i = 5, 6) \; . \tag{2.60}$$

Given the particular form of the source terms for radial and tangential ring loads, the following integral representation for the Fourier components of the displacement and stress components may be obtained:

$$\left(U^R_{rn} + U^T_{rn}\right) \pm \left(U^R_{\theta n} + U^T_{\theta n}\right) = \int_0^\infty k\left[\mp u_{11} + u_{31}\right]J_{n+1}(ka_o)\; J_{n\pm1}(kr_o)dk$$

$$\left(U^R_{rn} - U^T_{rn}\right) \pm \left(U^R_{\theta n} - U^T_{\theta n}\right) = \int_0^\infty k\left[\pm u_{11} + u_{31}\right]J_{n-1}(ka_o)\; J_{n\pm1}(kr_o)dk$$

$$U^R_{zn} \pm U^T_{zn} = \mp\int_0^\infty k u_{21} J_{n\pm1}(ka_o)J_n(kr_o)dk$$

$$\left(\Sigma^R_{rzn} + \Sigma^T_{rzn}\right) \pm \left(\Sigma^R_{\theta zn} + \Sigma^T_{\theta zn}\right) = \int_0^\infty k\left[\mp\sigma_{211} + \sigma_{231}\right]\; J_{n+1}(ka_o)J_{n\pm1}(kr_o)dk$$

$$\left(\Sigma^R_{rzn} - \Sigma^T_{rzn}\right) \pm \left(\Sigma^R_{\theta zn} - \Sigma^T_{\theta zn}\right) = \int_0^\infty k\left[\pm\sigma_{211} + \sigma_{231}\right]J_{n-1}(ka_o)J_{n\pm1}(kr_o)dk$$

$$\Sigma^R_{zzn} \pm \Sigma^T_{zzn} = \mp \int_0^\infty k\sigma_{221} J_{n\pm1}(ka_o) J_n(kr_o)\,dk$$

$$\left(\Sigma^R_{rrn} \pm \Sigma^T_{rrn}\right) + \left(\Sigma^R_{\theta\theta n} \pm \Sigma^T_{\theta\theta}\right) = \mp \int_0^\infty k\sigma_{331} J_{n\pm1}(ka_o) J_n(kr_o)\,dk$$

$$\left(\Sigma^R_{rrn} \pm \Sigma^T_{rrn}\right) + 2\,\frac{\mu_o}{r_o}\left[\left(U^R_{rn} \pm U^T_{rn}\right) + n\left(U^r_{\theta n} \pm U^T_{\theta n}\right)\right]$$

$$= \mp \int_0^\infty k\sigma_{111} J_{n\pm1}(ka_o) J_n(kr_o)\,dk$$

$$\left(\Sigma^R_{\theta rn} \pm \Sigma^T_{\theta rn}\right) + 2\,\frac{\mu_o}{r_o}\left[n\left(U^R_{rn} \pm U^T_{rn}\right) + \left(U^R_{\theta n} \pm U^T_{\theta n}\right)\right]$$

$$= \int_0^\infty k\sigma_{131} J_{n\pm1}(ka_o) J_n(kr_o)\,dk \quad . \tag{2.61}$$

In these equations the terms $u_{ij1}(z_o, k)$ and $\sigma_{ijl}(z_o, k)$ correspond to those defined by Eqs. (2.20) and (2.38) for the case of a concentrated horizontal point load.

2.5 ATTENUATION

It is well known that dissipation of energy accompanies transmission of stress waves in solids, even when the waves have small amplitudes. In general, this conversion of elastic energy into heat produces attenuation and dispersion of the stress waves, although the dispersion is typically small for earthquake waves.

The dissipative properties of solids are commonly measured by analyzing the decay rate of standing wave amplitudes in free vibration experiments in the laboratory or the actual decay of waves propagating in the field, where the amplitude decay will include the effects of heterogeneities in the Earth.

Analogously to the familiar expression in electrical circuit theory, the following dimensionless measure of dissipation, $1/Q$, is commonly accepted in seismology (for instance, see Knopoff, 1964):

$$2\pi/Q = \Delta E/E \ . \tag{2.62}$$

In Eq. (2.62), ΔE is the amount of energy dissipated per cycle of a harmonic excitation in a certain volume and E is the elastic energy stored in the same volume when the strain is a maximum. There is considerable evidence from measurements of homogeneous materials in the laboratory and in the field that the specific attenuation factor, Q, is substantially independent of frequency.

Various modifications to Hooke's law have been attempted in order to account for the deviations in behavior between real materials and perfectly elastic materials. One classical modification is the Kelvin-Voigt solid in which dissipation is attributed to an added stress proportional

to the rate of strain. Ignoring the tensorial relations involved, the stress-strain relation for a Kelvin-Voigt solid is

$$\sigma = \mu\varepsilon + \mu' \frac{d\varepsilon}{dt} \tag{2.63}$$

so that the effective shear modulus is complex:

$$\mu^* = \mu\left(1 + i\,\frac{\omega\mu'}{\mu}\right) . \tag{2.64}$$

The phase velocity for a damped harmonic wave in the Kelvin-Voigt solid is given by

$$c = \left[\frac{2\mu}{\rho}\,\frac{1 + (\omega\mu'/\mu)^2}{\sqrt{1 + (\omega\mu'/\mu)^2} + 1}\right]^{1/2} , \tag{2.65}$$

which assumes a value $(\mu/\rho)^{1/2}$, appropriate for an elastic body when $\omega = 0$ and increases with frequency, becoming infinite as $\omega \to \infty$ (completely attenuated wave). The specific attenuation factor for the damped harmonic wave is given by

$$2\pi Q^{-1}(\omega) = 1 - \exp\left[-4\pi\left(\frac{\sqrt{1 + (\omega\mu'/\mu)^2} - 1}{\sqrt{1 + (\omega\mu'/\mu)^2} + 1}\right)^{1/2}\right] . \tag{2.66}$$

Assuming that $\mu' << \mu$ or $Q >> 1$ leads to

$$Q^{-1} \approx \omega\mu'/\mu \tag{2.67}$$

so that Q is inversely proportional to frequency for the Kelvin-Voigt solid.

Another classical modification to Hooke's law is the Maxwellian relation

$$\frac{d\varepsilon}{dt} = \frac{1}{\mu}\frac{d\sigma}{dt} + \frac{1}{\mu'}\sigma \tag{2.68}$$

so that the dissipation is attributed to the actual permanent deformation. The complex shear modulus for the Maxwell solid is

$$\mu^* = \mu\left(1 - i\,\frac{\mu}{\mu'\omega}\right)^{-1} , \tag{2.69}$$

and the phase velocity is given by

$$c = \left[\frac{2\mu}{\rho}\,\frac{1}{\sqrt{1 + \left(\frac{1}{\omega\mu'}\right)^2} + 1}\right]^{1/2} , \tag{2.70}$$

which assumes a value $(\mu/\rho)^{1/2}$ as $\omega\mu' \to \infty$ and a value $(2\mu\omega\mu'/\rho)^{1/2}$ as $\omega\mu' \to 0$. The corresponding specific attenuation for a damped harmonic wave is approximately

$$Q^{-1} \approx \frac{\mu}{\omega\mu'} \tag{2.71}$$

so that Q is proportional to frequency for the Maxwell solid. For both models, the complex shear modulus is approximately

$$\mu^* = \mu(1 + i/Q) . \tag{2.72}$$

The attenuation model considered in this dissertation for a layered viscoelastic half-space employs a complex shear modulus defined in the same way, except that

$$\mu^* = \mu(1 + i/Q_\beta) \tag{2.73}$$

where Q_β is assumed to be frequency independent. The shear wave

velocity is given by

$$\beta^* = (\mu^*/\rho)^{1/2} = \beta(1 + i/Q_\beta)^{1/2} ,$$

in which Q_β is termed the shear wave specific attenuation factor. Similarly, the compressional wave velocity is given by

$$\alpha^* = \left(\frac{\lambda^* + 2\mu^*}{\rho}\right)^{1/2} = \alpha(1 + i/Q_\alpha)^{1/2} , \qquad (2.74)$$

in which Q_α is termed the compressional wave specific attenuation factor.

Although Q_β and Q_α are assumed to be independent of frequency for this model, any frequency dependence may be incorporated since the Green's functions are formed directly in the frequency domain. Furthermore, Futterman (1962) points out that a frequency independent Q is inconsistent with causality. Since $Q^{-1} = 0$ at $\omega = 0$, then there would necessarily be a discontinuous slope at the origin and a phase velocity independent of frequency. Futterman and others have investigated models in which Q is independent of frequency only above a characteristic lower cutoff frequency. Allowing the phase velocity to be frequency dependent, reasonable models include the expression in Eq. (2.66) divided by ω or a logarithmic dependence in which the dispersion introduced by causality is of the order Q^{-1}, where Q is roughly constant over a rather broad frequency band.

All the results presented in this dissertation assume a frequency independent Q. The imaginary parts of the Green's functions as $\omega \to 0$ are roughly proportional to $1/2Q$. In engineering terminology,

$1/2Q$ corresponds approximately to the critical damping ratio in the material.

It is useful to point out that β, Q_β, α, Q_α may not all be measurable quantities for a given problem. For example, it is more common to know the real and imaginary parts of the wave velocities. Since the formulae in Eqs. (2.73), (2.74) result in increases of the velocities by factors of $(1 + 1/Q^2)^{1/4}$, then a more rational definition for the complex velocities would be

$$\frac{1}{\beta^*} = \frac{1}{\beta} - \frac{i}{2\beta Q_\beta}, \qquad \frac{1}{\alpha^*} = \frac{1}{\alpha} - \frac{i}{2\alpha Q_\alpha}. \tag{2.75}$$

Also, if it is assumed that no dissipation occurs in pure compression, then Q_α may be related to Q_β by the expression

$$Q_\alpha = \frac{3}{4}\left(\frac{\alpha}{\beta}\right)^2 Q_\beta . \tag{2.76}$$

As discussed in Chapter 4, the effect of introducing complex velocities into the multilayered half-space not only results in a more realistic model, but also allows the numerical integration procedure to be performed along the real wavenumber axis without recourse to principal values or contour integration.

CHAPTER 3

RESPONSE OF A LAYERED VISCOELASTIC HALF-SPACE TO BURIED SOURCES

3.1 MATHEMATICAL FORMULATION

In this Chapter a new procedure to obtain the three-dimensional response of a layered viscoelastic half-space to buried sources with time dependence of the type $\exp[i\omega t]$ is described.

The viscoelastic half-space $(z \geq 0)$ under consideration is assumed to be formed by N parallel horizontal layers overlying a uniform half-space as illustrated in Fig. 3.1. The jth layer $(j = 1, N)$ has a thickness $h_j = z_j - z_{j-1}$ and is bounded by upper and lower interfaces located at depths z_{j-1} and z_j, respectively $(z_0 = 0)$. Each of the $N + 1$ viscoelastic media forming the layered half-space is characterized by a complex compressional wave velocity α_j, complex shear wave velocity β_j and density ρ_j $(j = 1, N + 1)$. For the purpose of the discussion and without loss of generality it will be assumed that the buried source corresponds to a concentrated point load within the ℓth medium at the point of coordinates $(0, 0, z^s)$.

In the jth medium, the displacement vector in cylindrical coordinates $(u_r^j, u_\theta^j, u_z^j)$ must satisfy the homogeneous $(j \neq \ell)$ or inhomogeneous $(j = \ell)$ equations of motion depending on whether or not the source is located within the jth medium. In addition, the displacement and stress fields must satisfy the traction-free boundary condition on the surface $z = 0$ of the half space, the conditions of continuity of displacements and tractions across each interface, and finally, the radiation condition in the underlying half-space. In cylindrical

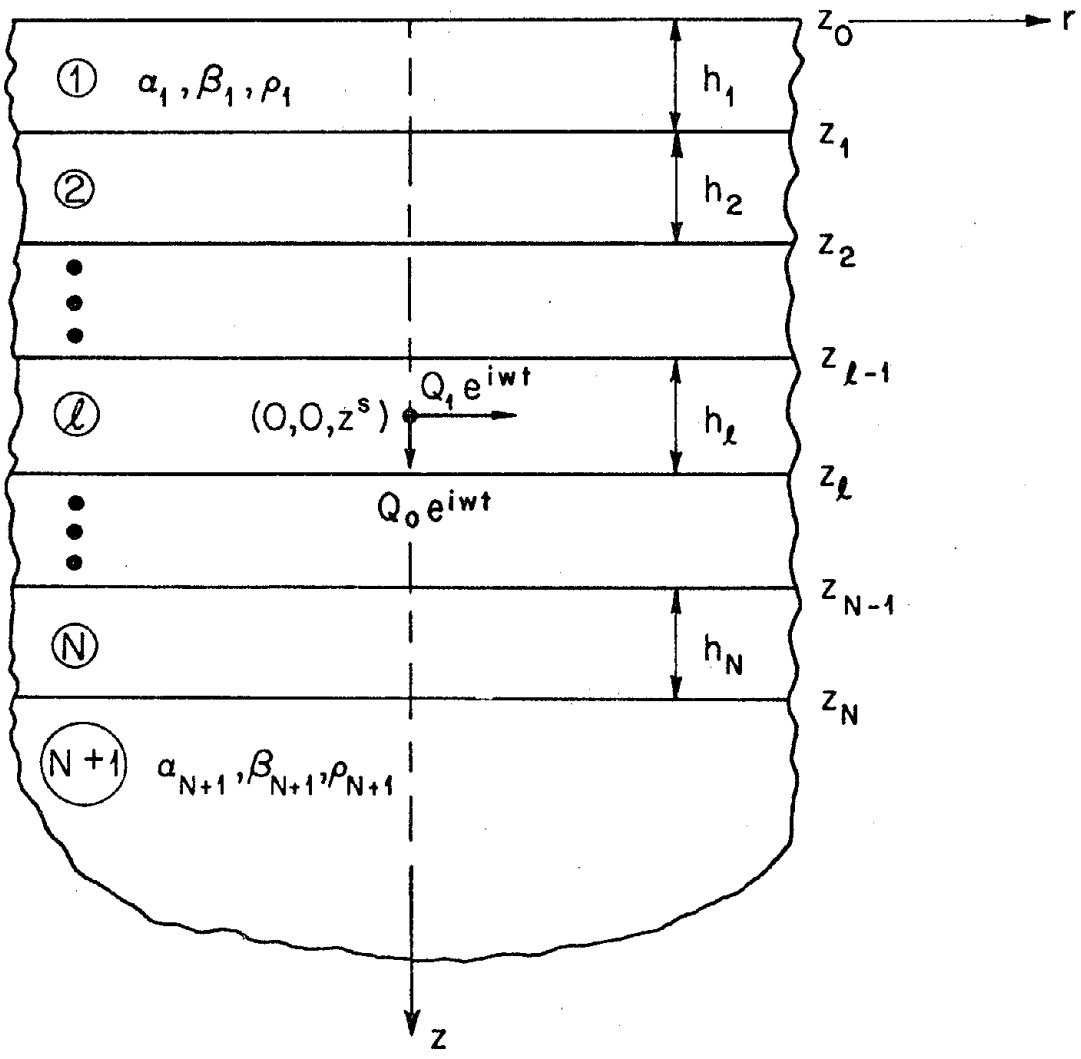

Figure 3.1. Model for layered viscoelastic half-space formed by N parallel horizontal layers overlying a uniform half-space.

coordinates, the traction-free boundary condition on the surface $z = 0$ of the layered half-space is

$$\sigma_{rz}^{1} = 0 \ , \quad \sigma_{\theta z}^{1} = 0 \ , \quad \sigma_{zz}^{1} = 0 \quad \text{on} \quad z = z_0 = 0 \tag{3.1}$$

while the continuity conditions across interfaces are

$$\begin{aligned} &u_r^j = u_r^{j+1} \ , \quad u_\theta^j = u_\theta^{j+1} \ , \quad u_z^j = u_z^{j+1} \\ &\sigma_{rz}^j = \sigma_{rz}^{j+1} \ , \quad \sigma_{\theta z}^j = \sigma_{\theta z}^{j+1} \ , \quad \sigma_{zz}^j = \sigma_{zz}^{j+1} \quad \text{on} \quad z = z_j \ (j = 1, N). \end{aligned} \tag{3.2}$$

In Eqs. (3.1) and (3.2), σ_{rz}^j, $\sigma_{\theta z}^j$, ... etc. correspond to the stress components in cylindrical coordinates in the jth medium. A detailed expression for the radiation condition will be given later. At this point it is sufficient to say that the radiation condition leads to three additional scalar equations in the underlying half-space ($j = N + 1$). In the previous Chapter it was shown that the general solution of the equations of motion in a viscoelastic medium involves six undetermined coefficients. The evaluation of the response of a layered half-space consisting of $N + 1$ viscoelastic media in contact reduces then, essentially, to the determination of $6(N + 1)$ undetermined coefficients by imposing the $6(N + 1)$ restrictions corresponding to the boundary, continuity and radiation conditions just described.

Recalling the integral representations obtained in Chapter 2, it is possible to express the displacement and stress components in the jth medium in the form

$$\begin{Bmatrix} u_r^j(r, \theta, z; \omega) \\ u_\theta^j(r, \theta, z; \omega) \\ u_z^j(r, \theta, z; \omega) \end{Bmatrix} = \frac{r_o}{4\pi\bar{\mu}r} \sum_n Q_n \begin{Bmatrix} U_{rn}^j(r_o, z_o)\cos n(\theta - \theta_o) \\ U_{\theta n}^j(r_o, z_o)\sin n(\theta - \theta_o) \\ U_{zn}^j(r_o, z_o)\cos n(\theta - \theta_o) \end{Bmatrix} \tag{3.3}$$

$$\begin{Bmatrix} \sigma_{rz}^j(r, \theta, z; \omega) \\ \sigma_{\theta z}^j(r, \theta, z; \omega) \\ \sigma_{zz}^j(r, \theta, z; \omega) \end{Bmatrix} = \frac{r_o^2}{4\pi r^2} \sum_n Q_n \begin{Bmatrix} \Sigma_{rzn}^j(r_o, z_o)\cos n(\theta - \theta_o) \\ \Sigma_{\theta zn}^j(r_o, z_o)\sin n(\theta - \theta_o) \\ \Sigma_{zzn}^j(r_o, z_o)\cos n(\theta - \theta_o) \end{Bmatrix} \tag{3.4}$$

$$\begin{Bmatrix} \sigma_{rr}^j(r, \theta, z; \omega) \\ \sigma_{\theta\theta}^j(r, \theta, z; \omega) \\ \sigma_{\theta r}^j(r, \theta, z; \omega) \end{Bmatrix} = \frac{r_o^2}{4\pi r^2} \sum_n Q_n \begin{Bmatrix} \Sigma_{rrn}^j(r_o, z_o)\cos n(\theta - \theta_o) \\ \Sigma_{\theta\theta n}^j(r_o, z_o)\cos n(\theta - \theta_o) \\ \Sigma_{\theta rn}^j(r_o, z_o)\sin n(\theta - \theta_o) \end{Bmatrix} \tag{3.5}$$

$$(z_{j-1} \le z \le z_j \ , \quad z_0 = 0 \ , \quad z_{N+1} = \infty \ , \quad j = 1, N + 1)$$

where $r_o = \omega r/\bar{\beta}$, $z_o = \omega z/\bar{\beta}$, $\bar{\beta}$ and $\bar{\mu}$ correspond to a shear wave velocity and a shear modulus of reference, and Q_0 denotes the vertical component of the point load while Q_1 represents the horizontal component along the $\theta = \theta_o$ azimuthal direction. The terms U_{rn}^j , ... , Σ_{rzn}^j , ... , are given by

$$U^j_{rn} \pm U^j_{\theta n} = \int_0^\infty k\left[\pm u^j_{1n}(z_o, k) + u^j_{3n}(z_o, k)\right] J_{n\pm1}(kr_o)dk$$

$$U^j_{zn} = \int_0^\infty k u^j_{2n}(z_o, k) J_n(kr_o)dk \tag{3.6}$$

$$\Sigma^j_{rzn} \pm \Sigma^j_{r\theta n} = \int_0^\infty k\left[\pm\sigma^j_{21n}(z_o, k) + \sigma^j_{23n}(z_o, k)\right] J_{n\pm1}(kr_o)dk$$

$$\Sigma^j_{zzn} = \int_0^\infty k\sigma^j_{22n}(z_o, k) J_n(kr_o)dk \tag{3.7}$$

$$\Sigma^j_{rrn} + \Sigma^j_{\theta\theta n} = \int_0^\infty k\sigma^j_{33n}(z_o, k) J_n(kr_o)dk$$

$$\Sigma^j_{rrn} + 2\frac{c_j}{d_j r_o}\left(U^j_{rn} + nU^j_{\theta n}\right) = \int_0^\infty k\sigma^j_{11n}(z_o, k) J_n(kr_o)dk \tag{3.8}$$

$$\Sigma^j_{\theta rn} + 2\frac{c_j}{d_j r_o}\left(nU^j_{rn} + U^j_{\theta n}\right) = \int_0^\infty k\sigma^j_{13n}(z_o, k) J_n(kr_o)dk$$

where

$$\begin{Bmatrix} u_{1n}^{j}(z_o, k) \\ u_{2n}^{j}(z_o, k) \\ \sigma_{21n}^{j}(z_o, k) \\ \sigma_{22n}^{j}(z_o, k) \\ \sigma_{33n}^{j}(z_o, k) \\ \sigma_{11n}^{j}(z_o, k) \end{Bmatrix} = \left[I_1^j(k)\right] \begin{Bmatrix} \eta_{1n}^{j}(z_o, k)\exp\left[-\nu_j(z_o - z_o^{j-1})\right] \\ \eta_{2n}^{j}(z_o, k)\exp\left[-\nu_j'(z_o - z_o^{j-1})\right] \\ \eta_{3n}^{j}(z_o, k)\exp\left[\nu_j(z_o - z_o^{j})\right] \\ \eta_{4n}^{j}(z_o, k)\exp\left[\nu_j'(z_o - z_o^{j})\right] \end{Bmatrix} \quad (3.9)$$

and

$$\begin{Bmatrix} u_{3n}^{j}(z_o, k) \\ \sigma_{23n}^{j}(z_o, k) \\ \sigma_{13n}^{j}(z_o, k) \end{Bmatrix} = \left[I_3^j(k)\right] \begin{Bmatrix} \eta_{5n}^{j}(z_o, k)\exp\left[-\nu_j'(z_o - z_o^{j-1})\right] \\ \eta_{6n}^{j}(z_o, k)\exp\left[\nu_j'(z_o - z_o^{j})\right] \end{Bmatrix} \quad (3.10)$$

In Eqs. (3.9) and (3.10), $z_o^j = \omega z_j/\bar{\beta}$ $(j = 0, N)$, $z_o^{N+1} = z_o^N$, the terms $I_1^j(k)$ and $I_3^j(k)$ denote the (6 x 4) and (3 x 2) matrices defined by

$$\left[I_1^j(k)\right] = \frac{1}{d_j}\begin{bmatrix} -kd_j & \nu_j'd_j & -kd_j & \nu_j'd_j \\ -\nu_j d_j & kd_j & \nu_j d_j & -kd_j \\ 2k\nu_j c_j & -(2k^2c_j-1) & -2k\nu_j c_j & (2k^2c_j-1) \\ (2k^2c_j - 1) & -2k\nu_j'c_j & (2k^2c_j-1) & -2k\nu_j'c_j \\ 2(2\gamma_j^2-1) - 2k^2c_j & 2k\nu_j'c_j & 2(2\gamma_j^2-1) - 2k^2c_j & 2k\nu_j'c_j \\ (2\gamma_j^2-1) - 2k^2c_j & 2k\nu_j'c_j & (2\gamma_j^2-1) - 2k^2c_j & 2k\nu_j'c_j \end{bmatrix} \quad (3.11)$$

and

$$\left[I_3^j(k)\right] = \frac{1}{d_j}\begin{bmatrix} kd_j & kd_j \\ -k\nu_j' c_j & k\nu_j' c_j \\ k^2 c_j & k^2 c_j \end{bmatrix} . \tag{3.12}$$

In the above equations the following notation has been used

$$\nu = \left[k^2 - (\bar{\beta}/\alpha_j)^2\right]^{1/2} , \quad \nu' = \left[k^2 - (\bar{\beta}/\beta_j)^2\right]^{1/2}$$
$$d_j = \bar{\rho}/\rho_j , \quad c_j = (\beta_j/\bar{\beta})^2 , \quad \gamma_j = (\beta_j/\alpha_j) \tag{3.13}$$

where $\bar{\rho}$ is again a density of reference ($\bar{\mu} = \bar{\beta}^2 \bar{\rho}$). In Eqs. (3.9) and (3.10), the terms η_{1n}^j, η_{2n}^j and η_{5n}^j ($j = 1, N + 1$) are associated with downwardly propagating P, SV and SH waves, respectively, while the terms η_{3n}^j, η_{4n}^j and η_{6n}^j ($j = 1, N + 1$) represent the corresponding upwardly propagating waves. The terms $\eta_{in}^j(z_o, k)$ ($i = 1, 6$; $j = 1, n + 1$) may be written in the form

$$\eta_{in}^j(z_o, k) = A_{in}^j(k) + \delta_{j\ell} S_{in}^{\ell}(z_o, k) , \quad (i = 1, 6; j = 1, N + 1) \tag{3.14}$$

in which, $A_{in}^j(k)$ are undetermined functions of the dimensionless wave number k to be determined by the boundary, continuity and radiation conditions, $\delta_{j\ell}$ is the Krönecker delta function and $S_{in}^{\ell}(z_o, k)$ are the source terms given by

$$\begin{Bmatrix} S_{10}^{\ell}(z_o, k) \\ S_{20}^{\ell}(z_o, k) \\ S_{30}^{\ell}(z_o, k) \\ S_{40}^{\ell}(z_o, k) \end{Bmatrix} = d_{\ell} \begin{Bmatrix} \exp\left[\nu_{\ell}(z_o^S - z_o^{\ell-1})\right] H(z_o - z_o^S) \\ (k/\nu_{\ell}')\exp\left[\nu_{\ell}'(z_o^S - z_o^{\ell-1})\right] H(z_o - z_o^S) \\ -\exp\left[-\nu_{\ell}(z_o^S - z_o^{\ell})\right] H(z_o^S - z_o) \\ -(k/\nu_{\ell}')\exp\left[-\nu_{\ell}'(z_o^S - z_o)\right] H(z_o^S - z_o) \end{Bmatrix} \tag{3.15}$$

$$\begin{Bmatrix} S_{50}^{\ell}(z_o, k) \\ S_{60}^{\ell}(z_o, k) \end{Bmatrix} = \begin{Bmatrix} 0 \\ 0 \end{Bmatrix} \tag{3.16}$$

$$\begin{Bmatrix} S_{11}^{\ell}(z_o, k) \\ S_{21}^{\ell}(z_o, k) \\ S_{31}^{\ell}(z_o, k) \\ S_{41}^{\ell}(z_o, k) \end{Bmatrix} = d_{\ell} \begin{Bmatrix} (k/\nu_{\ell})\exp\left[\nu_{\ell}(z_o^S - z_o^{\ell-1})\right] H(z_o - z_o^S) \\ \exp\left[\nu_{\ell}'(z_o^S - z_o^{\ell-1})\right] H(z_o - z_o^S) \\ (k/\nu_{\ell})\exp\left[-\nu_{\ell}(z_o^S - z_o^{\ell})\right] H(z_o^S - z_o) \\ \exp\left[-\nu_{\ell}'(z_o^S - z_o^{\ell})\right] H(z_o^S - z_o) \end{Bmatrix} \tag{3.17}$$

$$\begin{Bmatrix} S_{51}^{\ell}(z_o, k) \\ S_{61}^{\ell}(z_o, k) \end{Bmatrix} = \frac{d_{\ell}}{k\nu_{\ell}'c_{\ell}} \begin{Bmatrix} \exp\left[\nu_{\ell}'(z_o^S - z_o^{\ell-1})\right] H(z_o - z_o^S) \\ \exp\left[-\nu_{\ell}'(z_o^S - z_o^{\ell})\right] H(z_o^S - z_o) \end{Bmatrix} \tag{3.18}$$

where $z_o^S = \omega z^S/\bar{\beta}$ and $H(x)$ denotes the Heaviside step function.

Having presented the integral representation for the displacement and stress field, it becomes clear that the radiation condition in the bottom half-space ($j = N+1$) can be expressed by

$$A_{3n}^{N+1}(k) = 0 \ , \quad A_{4n}^{N+1}(k) = 0 \ , \quad A_{6n}^{N+1}(k) = 0 \tag{3.19}$$

corresponding to the condition that only downwardly propagating waves are considered as $z \to \infty$.

Given the particular form of the integral representation provided by Eqs. (3.3) through (3.7), it is possible to separate the boundary condition given by Eq. (3.1), the continuity conditions given by Eq. (3.2) and the radiation condition given by Eq. (3.19) into two groups of conditions. The first group of equations corresponds to the boundary, continuity and radiation conditions for waves with particle motion polarized in vertical planes (P, SV and Rayleigh waves), and it is given by

$$\sigma_{21n}^{1}(0, k) = 0 , \quad \sigma_{22n}^{1}(0, k) = 0 \tag{3.20}$$

$$u_{1n}^{j}(z_o^j, k) = u_{1n}^{j+1}(z_o^j, k) , \quad u_{2n}^{j}(z_o^j, k) = u_{2n}^{j+1}(z_o^j, k) , \quad (j = 1, N)$$

$$\sigma_{21n}^{j}(z_o^j, k) = \sigma_{21n}^{j+1}(z_o^j, k) , \quad \sigma_{22n}^{j}(z_o^j, k) = \sigma_{22}^{j+1}(z_o^j, k) , \quad (j = 1, N) \tag{3.21}$$

$$A_3^{N+1}(k) = 0 , \quad A_4^{N+1}(k) = 0 \tag{3.22}$$

These $4(N + 1)$ equations will be used in Section 3.2 to determine the $4(N + 1)$ undetermined coefficients $A_{in}^{j}(k)$ $(i = 1, 4; j = N + 1)$ on which u_{1n}^{j}, u_{2n}^{j}, σ_{21n}^{j} and σ_{22}^{j} depend.

The second group of equations representing the boundary, continuity and radiation conditions for waves with particle motion polarized in horizontal planes (SH, Love waves) is

$$\sigma_{23n}^{1}(0, k) = 0 \tag{3.23}$$

$$u_{3n}^{j}(z_o^j, k) = u_{3n}^{j+1}(z_o^j, k) \ , \quad (j = 1, N)$$

$$\sigma_{23n}^{j}(z_o^j, k) = \sigma_{23n}^{j+1}(z_o^j, k) \ , \quad (j = 1, N) \tag{3.24}$$

$$A_6^{N+1}(k) = 0 \tag{3.25}$$

These $2(N + 1)$ equations will be used in Section 3.3, to determine the $2(N + 1)$ undetermined coefficients $A_{in}^{j}(k)$ $(i = 5, 6; j = 1, N + 1)$ on which u_{3n}^{j} and σ_{23n}^{j} depend.

Once the coefficients $A_{in}^{j}(k)$ have been found, the displacement and stress components given by Eqs. (3.3), (3.4) and (3.5) may be obtained by performing the integrations indicated in Eqs. (3.6), (3.7) and (3.8).

3.2 PROPAGATION OF VERTICALLY POLARIZED WAVES

In this section the $4(N + 1)$ undetermined coefficients $A_{in}^{j}(k)$ $(i = 1, 4; j = 1, N + 1)$, or, equivalently, the $4(N + 1)$ unknown functions $n_{in}^{j}(z_o, k)$ $(i = 1, 4; j = 1, N + 1)$ appearing in the terms associated with waves whose particle motion is polarized in vertical planes (P, SV and Rayleigh waves) are determined by imposing the boundary, continuity and radiation conditions given by Eqs. (3.20), (3.21) and (3.22). As discussed in Chapter 1, a variety of procedures have been proposed by different authors to solve the $4(N + 1)$ linear algebraic equations representing the conditions just mentioned. Most of these methods are numerically unstable at extremely low and high frequencies. The new procedure proposed here closely parallels the physics of the problem and eliminates the frequency limitations.

Considering Eqs. (3.9) and (3.11), it is possible to write the boundary and continuity conditions given by Eqs. (3.20) and (3.21) in the form

$$\begin{bmatrix} 2k\nu_1 c_1 & -(2k^2 c_1 - 1) \\ (2k^2 c_1 - 1) & -2k\acute{\nu}_1 c_1 \end{bmatrix} \begin{Bmatrix} \eta^1_{1n}(0, k) \\ \eta^1_{2n}(0, k) \end{Bmatrix}$$

$$= \begin{bmatrix} 2k\nu_1 c_1 & -(2k^2 c_1 - 1) \\ -2k^2 c_1 - 1 & 2k\acute{\nu}_1 c_1 \end{bmatrix} \begin{Bmatrix} \eta^1_{3n}(0, k)\exp(-\nu_1 h^1_0) \\ \eta^1_{4n}(0, k)\exp(-\acute{\nu}_1 h^1_0) \end{Bmatrix} \tag{3.26}$$

$$[I_{j+1,j}(k)] \begin{Bmatrix} \eta^{j+1}_{1n}(z^j_o, k) \\ \eta^{j+1}_{2n}(z^j_o, k) \\ \eta^j_{3n}(z_o, k) \\ \eta^j_{4n}(z^j_o, k) \end{Bmatrix} = [I_{j,j+1}(k)] \begin{Bmatrix} \eta^j_{1n}(z^j_o, k)\exp(-\nu_j h^j_o) \\ \eta^j_{2n}(z^j_o, k)\exp(-\acute{\nu}_j h^j_o) \\ \eta^{j+1}_{3n}(z^j_o, k)\exp(-\nu_{j+1} h^{j+1}_o) \\ \eta^{j+1}_{4n}(z^j_o, k)\exp(-\acute{\nu}_{j+1} h^{j+1}_o) \end{Bmatrix} \tag{3.27}$$

where $h^j_o = z^j_o - z^{j-1}_o$ $(j = 1, N)$, $h^{N+1}_o = 0$, and

$$[I_{p,q}(k)] = \begin{bmatrix} k & -\acute{\nu}_p & -k & \acute{\nu}_q \\ \nu_p & -k & \nu_q & -k \\ -2k\nu_p c_p d_p^{-1} & (2k^2 c_p - 1)d_p^{-1} & -2k\nu_q c_q d_q^{-1} & (2k^2 c_q - 1)d_q^{-1} \\ -(2k^2 c_p - 1)d_p^{-1} & 2k\nu_p c_p d_p^{-1} & (2k^2 c_q - 1)d_q^{-1} & -2k\acute{\nu}_q c_q d_q^{-1} \end{bmatrix} \tag{3.28}$$

Inverting the matrices appearing on the left hand side of Eqs. (3.26) and (3.27) leads to

$$\begin{Bmatrix} \eta_{1n}^{1}(0,\ k) \\ \eta_{2n}^{1}(0,\ k) \end{Bmatrix} = \left[R_o^u\right] \begin{Bmatrix} \eta_{3n}^{1}(0,\ k) \\ \eta_{4n}^{1}(0,\ k) \end{Bmatrix} \tag{3.29}$$

and

$$\begin{Bmatrix} \eta_{1n}^{j+1}(z_o^j,\ k) \\ \eta_{2n}^{j+1}(z_o^j,\ k) \\ \eta_{3n}^{j}(z_o^j,\ k) \\ \eta_{4n}^{j}(z_o^j,\ k) \end{Bmatrix} = \left[\begin{array}{c|c} T_j^d & R_j^u \\ \hline R_j^d & T_j^u \end{array}\right] \begin{Bmatrix} \eta_{1n}^{j}(z_o^j,\ k) \\ \eta_{2n}^{j}(z_o^j,\ k) \\ \eta_{3n}^{j+1}(z_o^j,\ k) \\ \eta_{4n}^{j+1}(z_o^j,\ k) \end{Bmatrix} \quad (j = 1,\ N) \tag{3.30}$$

in which R_j^u and R_j^d are the 2 x 2 matrices of reflection coefficients for plane waves impinging on the j^{th} interface from below and above, respectively, modified to account for transmission path. T_j^u and T_j^d are the corresponding 2 x 2 matrices of modified transmission coefficients. The modified reflection and transmission matrices are given by

$$\left[R_o^u\right] = \begin{bmatrix} 2k\nu_1 c_1 & -(2k^2 c_1 - 1) \\ (2k^2 c_1 - 1) & -2k\nu_1' c_1 \end{bmatrix}^{-1} \begin{bmatrix} 2k\nu_1 c_1 & -(2k^2 c_1 - 1) \\ -(2k^2 c_1 - 1) & 2k\nu_1' c_1 \end{bmatrix}$$

$$\times \begin{bmatrix} e^{-\nu_1 h_1^1} & 0 \\ 0 & e^{-\nu_1' h_0^1} \end{bmatrix} \tag{3.31}$$

$$\left[\begin{array}{c|c} T_j^d & R_j^u \\ \hline R_j^d & T_j^u \end{array}\right] = [I_{j+1,j}(k)]^{-1}[I_{j,j+1}(k)]$$

$$\times \operatorname{diag}\left(e^{-\nu_j h_o^j},\ e^{-\nu_j' h_o^j},\ e^{-\nu_{j+1} h_o^{j+1}},\ e^{-\nu_{j+1}' h_o^{j+1}}\right) \quad (j = 1,\ N) \tag{3.32}$$

Explicit expressions for the reflection and transmission coefficients are presented in Appendix I.

The boundary and continuity conditions given by Eqs. (3.29) and (3.30) may be expressed as

$$\eta_{dn}^{1}(0) = R_o^u \eta_{un}^{1}(0) \tag{3.33}$$

$$\eta_{dn}^{j+1}(z_o^j) = T_j^d \eta_{dn}^{j}(z_o^j) + R_j^u \eta_{un}^{j+1}(z_o^j) \qquad (j = 1, N) \tag{3.34}$$

$$\eta_{un}^{j}(z_o^j) = R_j^d \eta_{dn}^{j}(z_o^j) + T_j^u \eta_{un}^{j+1}(z_o^j) \qquad (j = 1, N) \tag{3.35}$$

where

$$\eta_{dn}^{j}(z_o) = \begin{Bmatrix} \eta_{1n}^{j}(z_o, k) \\ \eta_{2n}^{j}(z_o, k) \end{Bmatrix} \tag{3.36}$$

$$\eta_{un}^{j}(z_o) = \begin{Bmatrix} \eta_{3n}^{j}(z_o, k) \\ \eta_{4n}^{j}(z_o, k) \end{Bmatrix} . \tag{3.37}$$

The 2×1 vector η_{dn}^{j} represents the downwardly propagating P and SV waves in the jth medium, while the 2×1 vector η_{un}^{j} represents the corresponding upwardly propagating waves. The physical interpretation of Eqs. (3.33) to 3.35) is quite simple as illustrated in Fig. 3.2. It must be pointed out that the vectors η_{dn}^{j} and η_{un}^{j} are independent of z_o if $j \neq \ell$; i.e.,

$$\eta_{dn}^{j}(z_o) = \begin{Bmatrix} A_{1n}^{j}(k) \\ A_{2n}^{j}(k) \end{Bmatrix} , \quad \eta_{un}^{j}(z_o) = \begin{Bmatrix} A_{3n}^{j}(k) \\ A_{4n}^{j}(k) \end{Bmatrix} \tag{3.38}$$

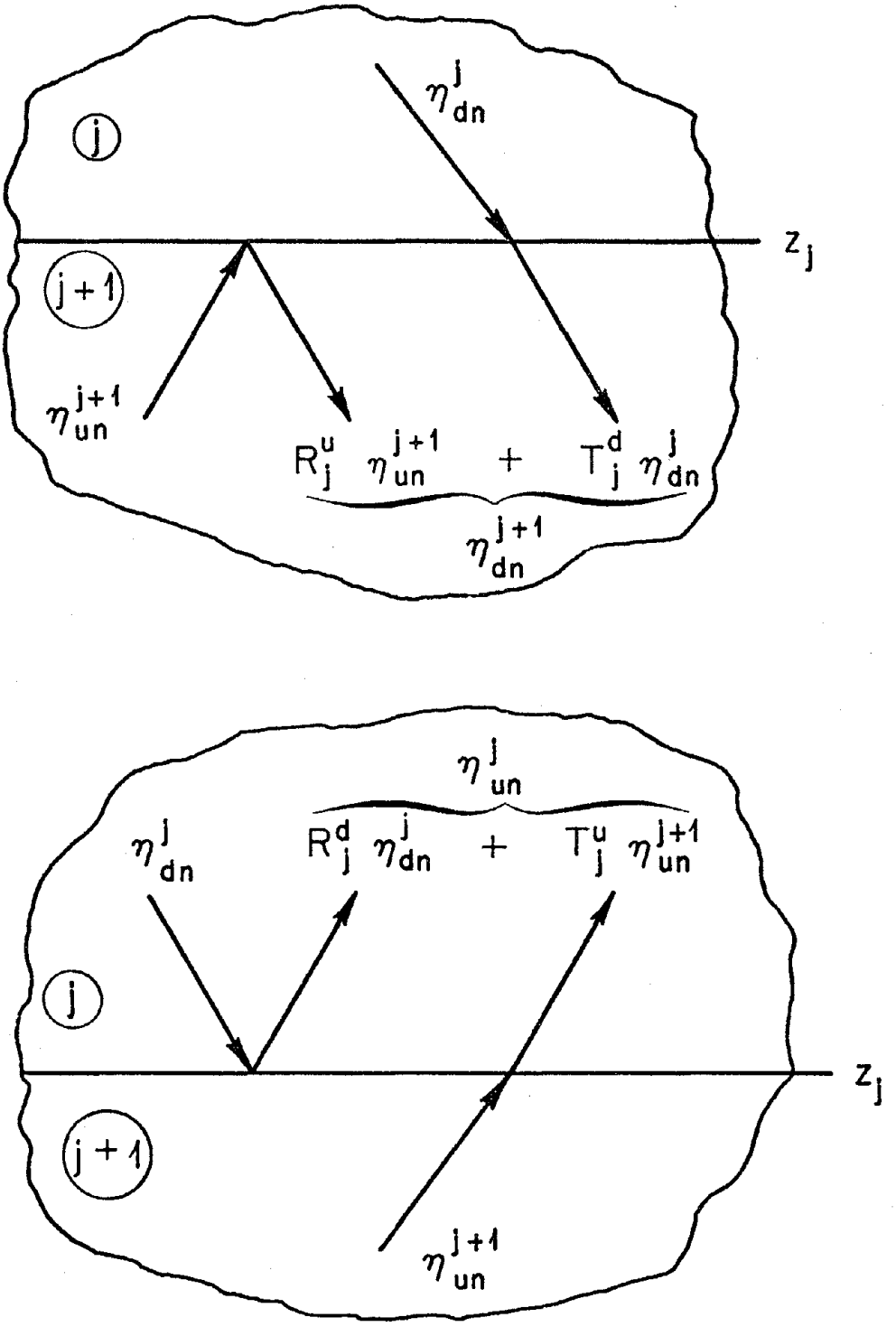

Figure 3.2. Schematic representation of modified reflection/transmission coefficients for downwardly and upwardly propagating waves in the j^{th} medium of the N-layered half-space.

$$\left(z_o^{j-1} \leq z_o \leq z_o^j \ , \quad j \neq \ell\right) .$$

In the medium containing the source ($j = \ell$) ,

$$\eta_{dn}^{\ell}(z_o) = \begin{Bmatrix} A_{1n}^{\ell}(k) \\ A_{2n}^{\ell}(k) \end{Bmatrix} + S_{dn}^{\ell}(k)H(z_o - z_o^s) \tag{3.39}$$

$$\eta_{un}^{\ell}(z_o) = \begin{Bmatrix} A_{3n}^{\ell}(k) \\ A_{4n}^{\ell}(k) \end{Bmatrix} + S_{un}^{\ell}(k)H(z_o^s - z_o) \ , \tag{3.40}$$

$$\left(z_o^{\ell-1} \leq z_o \leq z_o^{\ell}\right)$$

where

$$S_{dn}^{\ell}(k) = \begin{Bmatrix} S_{1n}^{\ell}(z_o^{\ell}, k) \\ S_{2n}^{\ell}(z_o^{\ell}, k) \end{Bmatrix}, \quad S_{un}^{\ell}(k) = \begin{Bmatrix} S_{3n}^{\ell}(z_o^{\ell-1}, k) \\ S_{4n}^{\ell}(z_o^{\ell-1}, k) \end{Bmatrix} \tag{3.41}$$

the 2 x 1 vectors S_{dn}^{ℓ} and S_{un}^{ℓ} correspond respectively to the direct contributions of the source to the downwardly and upwardly propagating waves in the ℓth medium.

At this point it is convenient to introduce the following factorization

$$\eta_{un}^{j}(z_o) = \hat{T}_j^u \hat{T}_{j+1}^u \ \cdots \ \hat{T}_{\ell-1}^u \eta_{un}^{\ell}(z_o^{\ell-1}) \ , \quad (j = 1, \ell - 1) \tag{3.42}$$

$$\eta_{dn}^{j}(z_o) = \hat{R}_{j-1}^u \hat{T}_j^u \hat{T}_{j+1}^u \ \cdots \ \hat{T}_{\ell-1}^u \eta_{un}^{\ell}(z_o^{\ell-1}) \ , \quad (j = 1, \ell - 1) \tag{3.43}$$

for the layers above the source, and

$$\eta^{j}_{dn}(z_o) = \hat{T}^{d}_{j-1}\hat{T}^{d}_{j-2} \cdots \hat{T}^{d}_{\ell}\eta^{\ell}_{dn}(z_o^{\ell}) , \quad (j = \ell + 1, N + 1) \tag{3.44}$$

$$\eta^{j}_{un}(z_o) = \hat{R}^{d}_{j}\hat{T}^{d}_{j-1}\hat{T}^{d}_{j-2} \cdots \hat{T}^{d}_{\ell}\eta^{\ell}_{dn}(z_o^{\ell}) , \quad (j = \ell + 1, N + 1) \tag{3.45}$$

for the layers below the source. The 2×2 matrices $\hat{T}^{u}_{j}$, $\hat{T}^{d}_{j}$ and $\hat{R}^{u}_{j}$, $\hat{R}^{d}_{j}$ are designated here as generalized transmission and reflection matrices at the jth interface for reasons to be described shortly. These matrices are independent of z_o.

Substitution from Eqs. (3.42) and (3.43) into Eqs. (3.33), (3.34) and (3.35) shows that the free-boundary condition at $z_o = 0$ and the continuity conditions at the interfaces above the source $(1 \leq j \leq \ell - 1)$ are satisfied if the generalized transmission and reflection matrices $\hat{T}^{u}_{j}$, $\hat{R}^{u}_{j}$ obey the recurrence relations

$$\hat{R}^{u}_{o} = R^{u}_{o} \tag{3.46}$$

$$\hat{T}^{u}_{j} = \left(I - R^{d}_{j}\hat{R}^{u}_{j-1}\right)^{-1} T^{u}_{j} , \quad (j \geq 1) \tag{3.47}$$

$$\hat{R}^{u}_{j} = R^{u}_{j} + T^{d}_{j}\hat{R}^{u}_{j-1}\hat{T}^{u}_{j} , \quad (j \geq 1) \tag{3.48}$$

and,

$$\eta^{\ell}_{dn}\left(z_o^{\ell-1}\right) = \hat{R}^{u}_{\ell-1}\eta^{\ell}_{un}\left(z_o^{\ell-1}\right) . \tag{3.49}$$

Similarly, from Eqs. (3.44), (3.45) it can be shown that the radiation condition at infinity $\left(A_3^{N+1} = 0, A_4^{N+1} = 0\right)$ and the continuity conditions at the interfaces below the source $(\ell \leq j \leq N)$ given by Eqs. (3.34) and (3.35) are satisfied if the generalized transmission

and reflection matrices $\hat{T}_j^d$, $\hat{R}_j^d$ obey the recurrence relations

$$\hat{R}_{N+1}^d = 0 \tag{3.50}$$

$$\hat{T}_j^d = \left(I - R_j^u \hat{R}_{j+1}^d\right)^{-1} T_j^d \ , \quad (j \leq N) \tag{3.51}$$

$$\hat{R}_j^d = R_j^d + T_j^u \hat{R}_{j+1}^d \hat{T}_j^d \ , \quad (j \leq N) \tag{3.52}$$

and

$$\eta_{un}^{\ell}\left(z_o^{\ell}\right) = \hat{R}_{\ell}^d \eta_{dn}^{\ell}\left(z_o^{\ell}\right) \ . \tag{3.53}$$

In Eqs. (3.47) and (3.51), $\underline{I}$ denotes the 2 x 2 identity matrix. The recurrence relations given by Eqs. (3.47), (3.48), (3.51) and (3.52) provide a simple procedure to determine the generalized transmission and reflection matrices once the modified transmission and reflection matrices are known.

The factorization given by Eqs. (3.42) to (3.45) provides the means to determine the field within each layer above or below the source once the field in the medium containing the source is known. The field in the medium containing the source ($j = \ell$) can be easily obtained by use of Eqs. (3.39), (3.40), (3.49), (3.53) and (3.54), and by noting that

$$\eta_{dn}^{\ell}\left(z_o^{\ell-1}\right) = \begin{Bmatrix} A_{1n}^{\ell}(k) \\ A_{2n}^{\ell}(k) \end{Bmatrix} \ , \quad \eta_{un}^{\ell}\left(z_o^{\ell}\right) = \begin{Bmatrix} A_{3n}^{\ell}(k) \\ A_{4n}^{\ell}(k) \end{Bmatrix} \ . \tag{3.54}$$

The result is

$$\eta^{\ell}_{un}(z_o) = \left(I - \hat{R}^{d}_{\ell}\hat{R}^{u}_{\ell-1}\right)^{-1}\left(S^{\ell}_{un} + \hat{R}^{d}_{\ell}S^{\ell}_{dn}\right)$$

$$\eta^{\ell}_{dn}(z_o) = \hat{R}^{u}_{\ell-1}\,\eta^{\ell}_{un}(z_o^{\ell-1}) \quad , \quad \left(z_o^{\ell-1} \le z_o \le z_o^{s}\right), \tag{3.55}$$

$$\eta^{\ell}_{dn}(z_o) = \left(I - \hat{R}^{u}_{\ell-1}\hat{R}^{d}_{\ell}\right)^{-1}\left(S^{\ell}_{dn} + \hat{R}^{u}_{\ell-1}\,S^{\ell}_{un}\right)$$

$$\eta^{\ell}_{un}(z_o) = \hat{R}^{d}_{\ell}\,\eta^{\ell}_{dn}(z_o) \quad , \quad \left(z_o^{s} \le z_o \le z_o^{\ell}\right), \tag{3.56}$$

In particular, if the source is located in the underlying half-space $(\ell = N + 1)$,

$$\eta^{\ell}_{un}(z_o) = \begin{cases} S^{N+1}_{un} \quad , \quad \left(z_o^{N} \le z_o \le z_o^{s}\right) \\ 0 \quad , \quad \left(z_o^{s} \le z_o < \infty\right) \quad , \quad (\ell = N + 1) \end{cases} \tag{3.57}$$

$$\eta^{\ell}_{dn}(z_o) = \begin{cases} \hat{R}^{u}_{N}S^{N+1}_{un} \quad , \quad \left(z_o^{N} \le z_o \le z_o^{s}\right) \\ S^{N+1}_{dn} + \hat{R}^{u}_{N}S^{N+1}_{un}, \quad \left(z_o^{s} \le z_o < \infty\right) \quad , \quad (\ell = N + 1) \ . \end{cases} \tag{3.58}$$

Equations (3.55) and (3.56) together with Eqs. (3.42) to (3.45) provide a complete description of the field associated with waves polarized in vertical planes. The particular form of these equations makes possible the simultaneous evaluation of the response at a number of observation locations for a number of different source locations.

The physical interpretation of the generalized reflection and transmission coefficients is illustrated in Fig. 3.3. In particular, $\hat{R}^{u}_{j}$ corresponds to the waves reflected into the j+1 th medium when upwardly propagating waves impinge on the jth interface. These generalized reflection coefficients include the multiple reflections, conversions and transmissions on the layers above the jth interface as shown in Fig. 3.3.

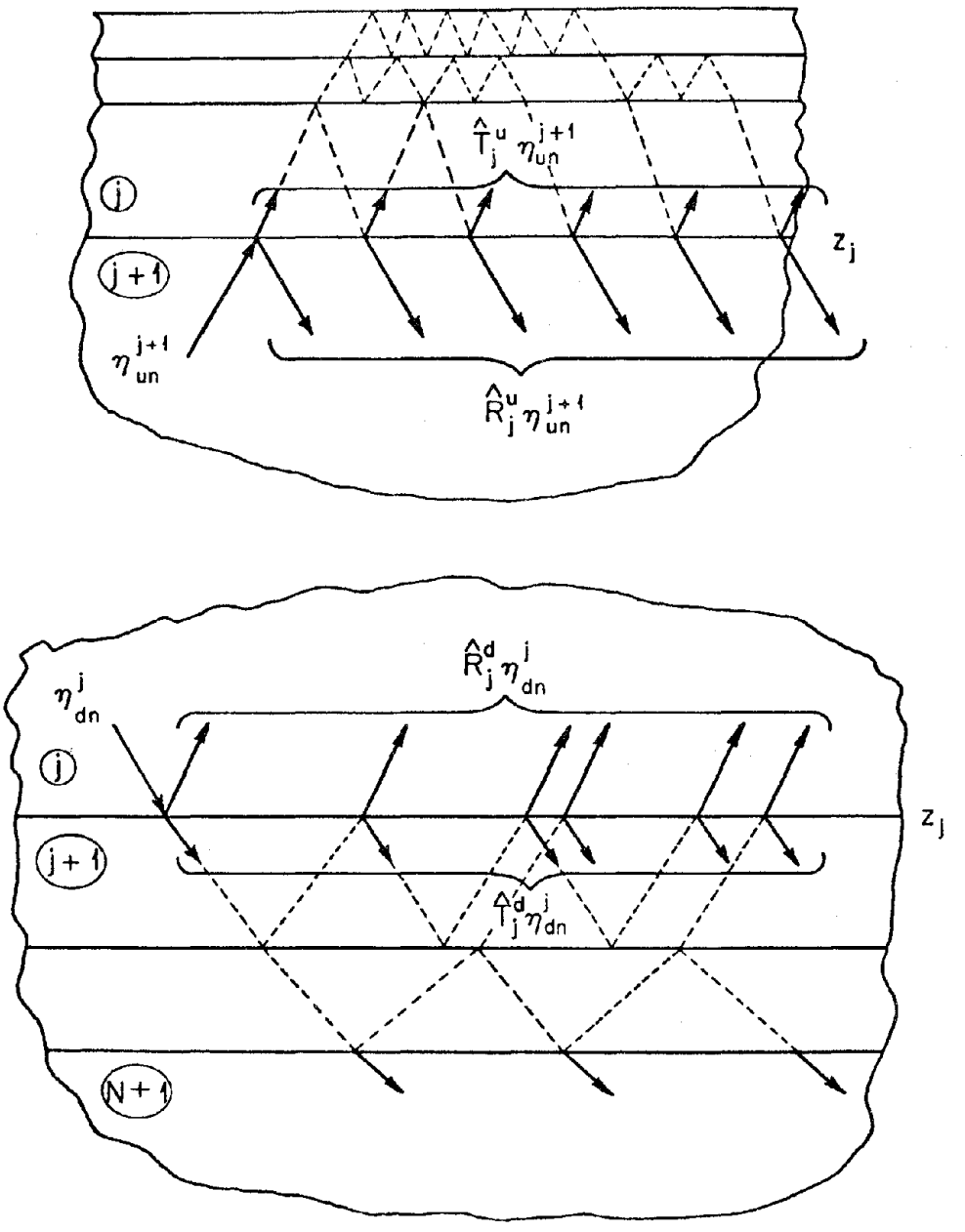

Figure 3.3. Schematic representation of generalized reflection and transmission coefficients. For example, $\hat{T}_j^d$ corresponds to the waves transmitted into the $j+1^{st}$ medium (including all multiple reflections, conversions and transmissions in the layers below the j^{th} interface) when downwardly propagating waves impinge on the j^{th} interface.

The physical interpretation of the recurrence relations given by Eqs. (3.47) and (3.48) is illustrated in Fig. 3.4.

The factorization introduced by Eqs. (3.42) to (3.45) can be easily interpreted in terms of generalized rays. In particular, expansion in series of the matrix $(I - R_j^d \hat{R}_{j-1}^u)^{-1}$ appearing in Eq. (3.47) leads to

$$\hat{T}_j^u = T_j^u + R_j^d \hat{R}_{j-1}^u T_j^u + R_j^d \hat{R}_{j-1}^u R_j^d \hat{R}_{j-1}^u T_j^u + \ldots . \tag{3.59}$$

in which the contributions of the multiple reflections become apparent. By similar expansion of the inverse of the matrices appearing in Eqs. (3.47), (3.51), (3.55) and (3.56) and by use of the recurrence relations, it is possible to obtain an expansion of the response on any layer in terms of multiply reflected and transmitted rays.

Finally, it should be mentioned that the dispersion relations for the layered medium can be easily obtained by determining the zeroes of the determinant of $(I - R_N^d \hat{R}_{N-1}^u)$.

3.3 PROPAGATION OF VERTICALLY POLARIZED WAVES FOR LARGE VALUES OF THE WAVENUMBER

For high values of the dimensionless wavenumber k or for very low frequencies, the procedure described in the previous section needs to be modified to account for the fact that the differences between terms associated with P and SV waves become small and may be altered by numerical roundoff. The integral representation will be modified in such a way that the dominant terms approach the corresponding static values as k tends to infinity.

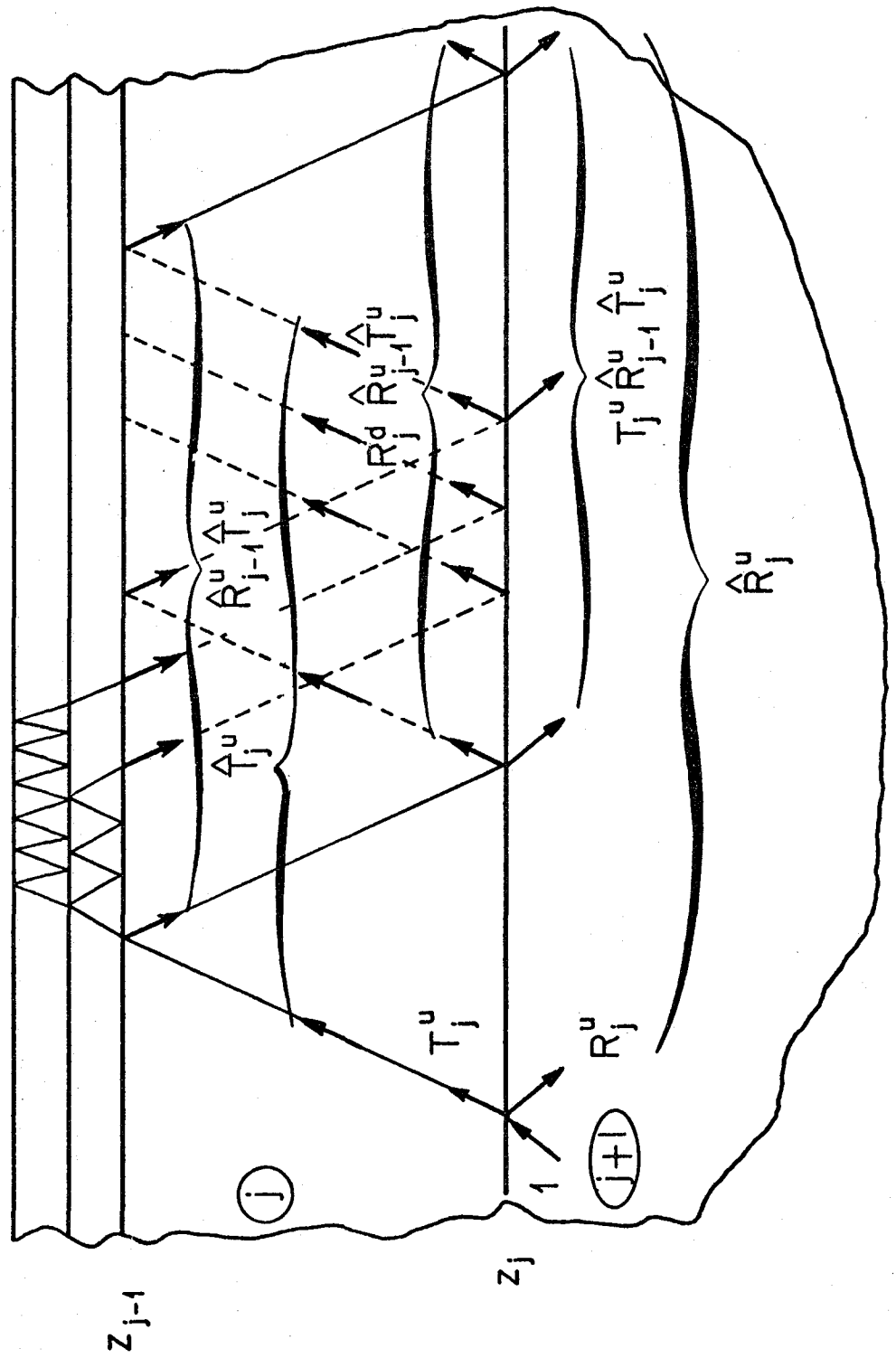

Figure 3.4. Schematic representation of the recurrence relations for the generalized reflection and transmission coefficients $\hat{T}^u_j$ and $\hat{R}^u_j$.

The integral representation used in the previous section may be written in the form

$$\left\{\begin{array}{c} u^j_{1n} \\ u^j_{2n} \\ \hline \sigma^j_{21n} \\ \sigma^j_{22n} \\ \hline \sigma^j_{33n} \\ \sigma^j_{11n} \end{array}\right\} = \left[\begin{array}{c|c} I^j_{11} & I^j_{12} \\ \hline I^j_{21} & I^j_{22} \\ \hline I^j_{31} & I^j_{32} \end{array}\right] \left[\begin{array}{c|c} E^j_d(z_o) & 0 \\ \hline 0 & E^j_u(z_o) \end{array}\right] \left\{\begin{array}{c} \eta^j_{dn}(z_o) \\ \hline \eta^j_{un}(z_o) \end{array}\right\} \tag{3.60}$$

where, the 2 x 2 matrices I^j_{pq} $(p = 1,2,3;\ q = 1,2)$ are obtained by partitioning the 6 x 6 matrix $[I^j_1(k)]$ defined by Eq. (3.11); the 2 x 1 vectors $\eta^j_{dn}(z_o)$ and $\eta^j_{un}(z_o)$ are defined by Eqs. (3.36) and (3.37); and the 2 x 2 matrices $E^j_d(z_o)$ and $E^j_u(z_o)$ are given by

$$\begin{aligned} E^j_d(z_o) &= \text{diag}\left(\exp\left[-\nu_j(z_o - z_o^{j-1})\right],\ \exp\left[-\nu'_j(z_o - z_o^{j-1})\right]\right) \\ E^j_u(z_o) &= \text{diag}\left(\exp\left[\nu_j(z_o - z_o^{j})\right],\ \exp\left[\nu'_j(z_o - z_o^{j})\right]\right) \quad . \end{aligned} \tag{3.61}$$

For high values of k it is necessary to recombine terms maintaining the form of the representation. In this case Eq. (3.60) is written as

$$\begin{Bmatrix} u_{1n}^j \\ u_{2n}^j \\ \sigma_{21n}^j \\ \sigma_{22n}^j \\ \sigma_{33n}^j \\ \sigma_{11n}^j \end{Bmatrix} = \left[\begin{array}{c|c} \bar{I}_{11}^j & \bar{I}_{12}^j \\ \hline \bar{I}_{21}^j & \bar{I}_{22}^j \\ \hline \bar{I}_{31}^j & \bar{I}_{32}^j \end{array}\right] \left[\begin{array}{c|c} \bar{E}_d^j(z_o) & 0 \\ \hline 0 & \bar{E}_u^j(z_o) \end{array}\right] \begin{Bmatrix} \bar{\eta}_{dn}^j(z_o) \\ \bar{\eta}_{un}^j(z_o) \end{Bmatrix} \tag{3.62}$$

in which

$$\bar{I}_{pq}^j = I_{pq}^j \, A_j^{-1} \qquad (p = 1,2,3;\ q = 1,2)$$

$$\bar{E}_d^j(z_o) = A_j \, E_d^j(z_o) \, A_j^{-1}$$

$$\bar{E}_u^j(z_o) = A_j \, E_u^j(z_o) \, A_j^{-1} \tag{3.63}$$

$$\bar{\eta}_{dn}^j(z_o) = A_j \, \eta_{dn}^j(z_o)$$

$$\bar{\eta}_{un}^j(z_o) = A_j \, \eta_{un}^j(z_o)$$

and A_j^{-1} is the inverse of the 2 x 2 matrix

$$A_j = -\frac{1}{\kappa_j} \begin{bmatrix} (k - \nu_j) & (k - \nu_j') \\ \nu_j + (\kappa_j - 1)k & -k - (\kappa_j - 1)\nu_j' \end{bmatrix} \tag{3.64}$$

in which $\kappa_j = (1 + \gamma_j^2)/(1 - \gamma_j^2)$. Detailed expressions for $\bar{I}_{pq}^j$, $\bar{E}_d^j$ and $\bar{E}_u^j$ are given in Appendix II.

The modifications introduced have the advantage that as k tends to infinity

$$\begin{bmatrix} \bar{I}^j_{11} & \bar{I}^j_{12} \\ \bar{I}^j_{21} & \bar{I}^j_{22} \\ \bar{I}^j_{31} & \bar{I}^j_{32} \end{bmatrix} \sim \left[\begin{array}{cc:cc} 1 & 1 & 1 & 1 \\ -(\kappa_j-1) & 1 & (\kappa_j-1) & -1 \\ \hdashline (\kappa_j-3)k\mu_{oj} & -2k\mu_{oj} & -(\kappa_j-3)k\mu_{oj} & 2k\mu_{oj} \\ (\kappa_j-1)k\mu_{oj} & -2k\mu_{oj} & (\kappa_j-1)k\mu_{oj} & -2k\mu_{oj} \\ \hdashline 2(4-\kappa_j)k\mu_{oj} & 2k\mu_{oj} & 2(4-\kappa_j)k\mu_{oj} & 2k\mu_{oj} \\ (5-\kappa_j)k\mu_{oj} & 2k\mu_{oj} & (5-\kappa_j)k\mu_{oj} & 2k\mu_{oj} \end{array}\right] \tag{3.65}$$

$$\bar{E}^j_d(z_o) \sim \begin{bmatrix} 1 & 0 \\ -k(z_o-z_o^{j-1}) & 1 \end{bmatrix} \exp\left[-k(z_o-z_o^{j-1})\right] \tag{3.66}$$

$$\bar{E}^j_u(z_o) \sim \begin{bmatrix} 1 & 0 \\ k(z_o-z_o^{j-1}) & 1 \end{bmatrix} \exp\left[k(z_o-z_o^{j})\right] \tag{3.67}$$

which correspond to the static representation obtained by Muki [1955]. In Eq. (3.65), $\mu_{oj} = \mu_j/\bar{\mu}$.

Since the modifications introduced for large values of k have not altered the form of the integral representation, it is possible to determine the functions $\bar{n}^j_{dn}(z_o)$ and $\bar{n}^j_{un}(z_o)$ $(j=1, N+1)$ using the same procedure described in Section 3.2. In particular, for layers above the source

$$\bar{\eta}^{j}_{un}(z_o) = \hat{\bar{T}}^{u}_{j}\ \hat{\bar{T}}^{u}_{j+1} \cdots \hat{\bar{T}}^{u}_{\ell-1}\ \bar{\eta}^{\ell}_{un}\ (z_o^{\ell-1}) \qquad (j=1,\ \ell-1)$$

$$\bar{\eta}^{j}_{dn}(z_o) = \hat{\bar{R}}^{u}_{j-1}\ \bar{\eta}^{j}_{un}\ (z_o^{j-1}) \qquad (j=1,\ \ell-1) \tag{3.68}$$

and

$$\bar{\eta}^{\ell}_{un}(z_o) = \left(\bar{I} - \hat{\bar{R}}^{d}_{\ell}\ \hat{\bar{R}}^{u}_{\ell-1}\right)^{-1} \left(\bar{S}_{un} + \hat{\bar{R}}^{d}_{\ell}\ \bar{S}^{\ell}_{dn}\right), \qquad (z_o^{\ell-1} \leq z_o < z_o^{s})$$

$$\eta^{\ell}_{dn}(z_o) = \hat{\bar{R}}^{u}_{\ell-1}\ \bar{\eta}^{\ell}_{un}(z_o^{\ell-1}), \qquad (z_o^{\ell-1} \leq z_o < z_o^{s}) \tag{3.69}$$

where

$$\bar{S}^{\ell}_{un} = A_{\ell}\ S^{\ell}_{un}, \qquad \bar{S}^{\ell}_{dn} = A_{\ell}\ S^{\ell}_{dn}. \tag{3.70}$$

Expressions similar to those given in Eqs. (3.44), (3.45) and (3.56) hold for layers below the source. The modified source terms $\bar{S}^{\ell}_{un}$ and $\bar{S}^{\ell}_{dn}$ defined by Eq. (3.70) are given in detail in Appendix II.

The new matrices of generalized transmission and reflection coefficients are obtained from the recurrence relations

$$\hat{\bar{R}}^{u}_{o} = \bar{R}^{u}_{o}$$

$$\hat{\bar{T}}^{u}_{j} = \left(I - \bar{R}^{d}_{j}\ \hat{\bar{R}}^{u}_{j-1}\right)^{-1} \bar{T}^{u}_{j} \qquad (j \geq 1)$$

$$\hat{\bar{R}}^{u}_{j} = \bar{R}^{u}_{j} + \bar{T}^{d}_{j}\ \hat{\bar{R}}^{u}_{j-1}\ \bar{T}^{u}_{j} \qquad (j \geq 1) \tag{3.71}$$

$$\hat{\bar{R}}^d_{N+1} = 0$$

$$\hat{\bar{T}}^d_j = \left(I - \bar{R}^u_j \hat{\bar{R}}^d_{j+1}\right)^{-1} \bar{T}^d_j \qquad (j \leq N)$$

$$\hat{\bar{R}}^d_j = \bar{R}^d_j + \bar{T}^u_j \hat{\bar{R}}^d_{j+1} \hat{\bar{T}}^d_j \qquad (j \leq N) \tag{3.72}$$

in which the new matrices of modified reflection and transmission coefficients are given by

$$\bar{R}^u_o = -\left(\bar{I}^1_{21}\right)^{-1} \bar{I}^1_{22}\, \bar{E}^1_u(0) \tag{3.73}$$

$$\left[\begin{array}{c|c} \bar{T}^d_j & \bar{R}^u_j \\ \hline \bar{R}^d_j & \bar{T}^u_j \end{array}\right] = \left[\begin{array}{c|c} -\bar{I}^{j+1}_{11} & \bar{I}^j_{12} \\ \hline -\bar{I}^{j+1}_{21} & \bar{I}^j_{22} \end{array}\right]^{-1} \left[\begin{array}{c|c} -\bar{I}^j_{11} & \bar{I}^{j+1}_{12} \\ \hline -\bar{I}^j_{21} & \bar{I}^{j+1}_{22} \end{array}\right] \left[\begin{array}{c|c} \bar{E}^j_d(z^j_o) & 0 \\ \hline 0 & \bar{E}^{j+1}_u(z^j_o) \end{array}\right] . \tag{3.74}$$

3.4 PROPAGATION OF HORIZONTALLY POLARIZED WAVES

In this section, the $2(N+1)$ undetermined coefficients $A^j_{in}(k)$ $(i=5,6;\ j=1,\ N+1)$, or equivalently, the $2(N+1)$ unknown functions $n^j_{in}(z_o,\ k)$ $(i=5,6;\ j=1,\ N+1)$ appearing in the terms associated with waves whose particle motion is polarized in horizontal plans (SH, Love waves) are determined by imposing the boundary, continuity and radiation conditions given by Eqs. (3.23), (3.24) and (3.25).

Considering Eqs. (3.10) and (3.12) it is possible to write the boundary and continuity conditions given by Eqs. (3.23) and (3.24) in the form

$$\eta_{5n}^{1}(0,\ k) = \eta_{6n}^{1}(0,\ k)\ \exp(-\nu_1' h_o^1) \tag{3.75}$$

$$[I_{j+1,j}'] \begin{Bmatrix} \eta_{5n}^{j+1}(z_o^j,\ k) \\ \eta_{6n}^{j}(z_o^j,\ k) \end{Bmatrix} = [I_{j,j+1}'] \begin{Bmatrix} \eta_{5n}^{j}(z_o^j,\ k)\ \exp(-\nu_j' h_o^j) \\ \eta_{6n}^{j+1}(z_o^j,\ k)\ \exp(-\nu_{j+1}' h_o^{j+1}) \end{Bmatrix}$$

$$(j = 1,\ N) \tag{3.76}$$

where $h_o^j = z_o^j - z_o^{j-1}$ $(j = 1,\ N)$, $h_o^{N+1} = 0$, and

$$[I_{p,q}'] = \begin{bmatrix} -1 & 1 \\ \nu_p' c_p d_p^{-1} & \nu_q' c_q d_q^{-1} \end{bmatrix} . \tag{3.77}$$

Eqs. (3.75) and (3.76) can be written as

$$\eta_{5n}^{1}(0,\ k) = R_o^u \eta_{6n}^{1}(0,\ k) \tag{3.78}$$

$$\begin{Bmatrix} \eta_{5n}^{j+1}(z_o^j,\ k) \\ \eta_{6n}^{j}(z_o^j,\ k) \end{Bmatrix} = \begin{bmatrix} T_j^d & R_j^u \\ R_j^d & T_j^u \end{bmatrix} \begin{Bmatrix} \eta_{5n}^{j}(z_o^j,\ k) \\ \eta_{6n}^{j+1}(z_o^j,\ k) \end{Bmatrix} \quad (j = 1,N) \tag{3.79}$$

where

$$R_o^u = \exp(\nu_1' h_o^1) \tag{3.80}$$

and,

$$T_j^d = 2\nu_j' c_j d_j^{-1}\ \exp(-\nu_j' h_o^j)/\Delta_j$$

$$R_j^d = \left(\nu_j' c_j d_j^{-1} - \nu_{j+1}' c_{j+1} d_{j+1}^{-1}\right)\ \exp(-\nu_j' h_o^j)/\Delta_j$$

$$R_j^u = -\left(\nu_j' c_j d_j^{-1} - \nu_{j+1}' c_{j+1} d_{j+1}^{-1}\right) \exp\left(-\nu_{j+1}' h_o^{j+1}\right)/\Delta_j$$

$$T_j^u = 2\nu_{j+1}' c_{j+1} d_{j+1}^{-1} \exp\left(-\nu_{j+1}' h_o^{j+1}\right)/\Delta_j \qquad (j = 1,N) \quad (3.81)$$

in which,

$$\Delta_j = \nu_j' c_j d_j^{-1} + \nu_{j+1}' c_{j+1} d_{j+1}^{-1} \; . \qquad (3.82)$$

The terms denoted here by R_j^u, R_j^d and T_j^u, T_j^d correspond to the reflection and transmission coefficients for plane SH waves impinging on the jth interface from below and above, respectively. These coefficients have been modified to account for the transmission path.

Introducing the change in notation

$$\eta_{dn}^j(z_o) = \eta_{5n}^j(z_o, k)$$

$$\eta_{un}^j(z_o) = \eta_{6n}^j(z_o, k) \; , \qquad (j = 1, N + 1) \; , \qquad (3.83)$$

it may be seen that Eqs. (3.78) and (3.79) take the same form as Eqs. (3.33), (3.34) and (3.35) with the exception of being scalar equations.

Following the same procedure described in Section 3.2, it is found that the functions η_{dn}^j and η_{un}^j which satisfy the boundary, continuity and radiation conditions are given by

$$\eta_{un}^j(z_o) = \hat{T}_j^u \, \hat{T}_{j+1}^u \cdots \hat{T}_{\ell-1}^u \, \eta_{un}^\ell(z_o^{\ell-1})$$

$$\eta_{dn}^j(z_o) = \hat{R}_{j-1}^u \, \hat{T}_j^u \, \hat{T}_{j+1}^u \cdots \hat{T}_{\ell-1}^u \, \eta_{un}^\ell(z_o^{\ell-1}) \; , \qquad (j=1, \ell-1) \quad (3.84)$$

for the layers above the source, and

$$\eta^{j}_{dn}(z_o) = \hat{T}^{d}_{j-1}\,\hat{T}^{d}_{j-2} \cdots \hat{T}^{d}_{\ell}\,\eta^{\ell}_{dn}(z^{\ell}_o)$$

$$\eta^{j}_{un}(z_o) = \hat{R}^{d}_{j}\,\hat{T}^{d}_{j-1}\,\hat{T}^{d}_{j-2} \cdots \hat{T}^{d}_{\ell}\,\eta^{\ell}_{dn}(z^{\ell}_o)\ , \quad (j=\ell-1,\ N+1) \tag{3.85}$$

for the layers below the source. In the medium containing the source

$$\eta^{\ell}_{un}(z_o) = \left(1 - \hat{R}^{d}_{\ell}\hat{R}^{u}_{\ell-1}\right)^{-1}\left(S^{\ell}_{un} + \hat{R}^{d}_{\ell}\,S^{\ell}_{dn}\right),$$

$$\eta^{\ell}_{dn}(z_o) = \hat{R}^{u}_{\ell-1}\,\eta^{\ell}_{un}\,(z^{\ell-1}_o)\ , \qquad (z^{\ell-1}_o \le z_o \le z^{s}_o) \tag{3.86}$$

$$\eta^{\ell}_{dn}(z_o) = \left(1 - \hat{R}^{u}_{\ell-1}\,\hat{R}^{d}_{\ell}\right)\left(S^{\ell}_{dn} + \hat{R}^{u}_{\ell-1}\,S^{\ell}_{un}\right)$$

$$\eta^{\ell}_{un}(z_o) = \hat{R}^{d}_{\ell}\,\eta^{\ell}_{dn}\,(z^{\ell}_o)\ , \qquad (z^{s}_o \le z_o \le z^{\ell}_o)\ . \tag{3.87}$$

The generalized scalar transmission and reflection coefficients $\hat{T}^{d}_{j}$, $\hat{T}^{u}_{j}$, $\hat{R}^{d}_{j}$ and $\hat{R}^{u}_{j}$ appearing in the above equations are obtained from the modified reflection and transmission coefficients given by Eqs. (3.80) and (3.81) by use of the recurrence relations

$$\hat{R}^{u}_{o} = R^{u}_{o} \tag{3.88}$$

$$\hat{T}^{u}_{j} = \left(1 - R^{d}_{j}\,\hat{R}^{u}_{j-1}\right)^{-1} T^{u}_{j}\ , \qquad (j \ge 1) \tag{3.89}$$

$$\hat{R}^{u}_{j} = R^{u}_{j} + T^{d}_{j}\,\hat{R}^{u}_{j-1}\,\hat{T}^{u}_{j}\ , \qquad (j \ge 1) \tag{3.90}$$

and

$$\hat{R}^d_{N+1} = 0 \tag{3.91}$$

$$\hat{T}^d_j = \left(1 - R^u_j \hat{R}^d_{j+1}\right)^{-1} T^d_j , \quad (j \leq N) \tag{3.92}$$

$$\hat{R}^d_j = R^d_j + T^u_j \hat{R}^d_{j+1} \hat{T}^d_j , \quad (j \leq N) . \tag{3.93}$$

In Eqs. (3.86) and (3.87) the source terms S^ℓ_{dn} and S^ℓ_{un} are given by

$$S^\ell_{dn} = S^\ell_{5n}(z^\ell_o, k) , \quad S^\ell_{un} = S^\ell_{6n}(z^{\ell-1}_o, k) . \tag{3.94}$$

The procedure just described is valid for all values of k and does not need to be modified for large values of k.

CHAPTER 4

NUMERICAL INTEGRATION

4.1 SUMMARY OF INTEGRAL REPRESENTATION

Before presenting the method of integration used to evaluate the Green's functions it is convenient to summarize the integral representation derived in Chapters 2 and 3.

The cylindrical components of the displacement and stress fields in the jth layer associated with a concentrated source located in the ℓth medium can be written as

$$4\pi\left(\bar{\mu}ru_r^j,\ r^2\sigma_{rz}^j,\ r^2\sigma_{rr}^j\right) = \sum_{n=0} Q_n\left(r_o U_{rn}^j,\ r_o^2\,\Sigma_{rzn}^j,\ r_o^2\,\Sigma_{rrn}^j\right)\cos[n(\theta-\theta_o)]$$

$$4\pi\left(\bar{\mu}ru_\theta^j,\ r_\theta^2\sigma_{\theta z}^j,\ r^2\sigma_{\theta r}^j\right) = \sum_{n=0} Q_n\left(r_o U_{\theta n}^j,\ r_o^2\,\Sigma_{\theta zn}^j,\ r_o^2\,\Sigma_{\theta rn}^j\right)\sin[n(\theta-\theta_o)]$$

$$4\pi\left(\bar{\mu}ru_z^j,\ r^2\sigma_{zz}^j,\ r^2\sigma_{\theta\theta}^j\right) = \sum_{n=0} Q_n\left(r_o U_{zn}^j,\ r_o^2\,\Sigma_{zzn}^j,\ r_o^2\,\Sigma_{\theta\theta n}^j\right)\cos[n(\theta-\theta_o)] \qquad (4.1)$$

where $r_o = \omega r/\bar{\beta}$, $\bar{\beta}$ and $\bar{\mu}$ correspond to a shear wave velocity and a shear modulus of reference, Q_o denotes the vertical component of the point load while Q_1 represents the horizontal component of the point load along the $\theta = \theta_o$ azimuthal direction. The terms U_{rn}^j, ... , Σ_{rzn}^j, ... , are functions of the dimensionless variables r_o and $z_o = \omega z/\bar{\beta}$, and are obtained from the following Hankel transform-type integrals

$$\begin{Bmatrix} U^j_{rn} \pm U^j_{\theta n} \\ \Sigma^j_{rzn} \pm \Sigma^j_{\theta zn} \end{Bmatrix} = \int_0^\infty \begin{Bmatrix} \pm u^j_{1n} + u^j_{3n} \\ \pm \sigma^j_{21n} + \sigma^j_{23n} \end{Bmatrix} k\, J_{n\pm1}(kr_o)dk$$

$$\begin{Bmatrix} U^j_{zn} \\ \Sigma^j_{zzn} \\ \Sigma^j_{rrn} + \Sigma^j_{\theta\theta n} \\ \Sigma^j_{rrn} + \frac{2c_j}{d_j r_o}\left(U^j_{rn} + nU^j_{\theta n}\right) \\ \Sigma^j_{\theta rn} + \frac{2c_j}{d_j r_o}\left(nU^j_{rn} + U^j_{\theta n}\right) \end{Bmatrix} = \int_0^\infty \begin{Bmatrix} u^j_{2n} \\ \sigma^j_{22n} \\ \sigma^j_{33n} \\ \sigma^j_{11n} \\ \sigma^j_{31n} \end{Bmatrix} k\, J_n(kr_o)dk$$

(4.2)

in which $c_j = (\beta_j/\bar{\beta})^2$, $d_j = \bar{\rho}/\rho_j$, β_j and ρ_j correspond, respectively, to the shear wave velocity and density in the jth layer, and $\bar{\beta}$ and $\bar{\rho}$ are a shear wave velocity and density of reference ($\bar{\mu} = \bar{\beta}^2\bar{\rho}$). The terms u_{1n}, u_{2n}, σ_{21n}, σ_{22n}, σ_{33n} and σ_{11n} are associated with waves polarized in vertical planes (P, SV, Rayleigh), while the terms u_{3n}, σ_{23n} and σ_{31n} are associated with waves polarized in horizontal planes (SH, Love). All of these terms are functions of k and of the dimensionless variable z_o. In the near field, the terms U_{rn}, Σ_{rzn}, Σ_{rrn}, $\Sigma_{\theta\theta n}$ include some particle motion polarized in horizontal planes while the terms $U_{\theta n}$, $\Sigma_{\theta zn}$, $\Sigma_{\theta rn}$ include some particle motion polarized in vertical planes. For example,

$$U^j_{\theta n} = \int_0^\infty \left\{ u^j_{1n}\left[\frac{nJ_n(kr_o)}{(kr_o)}\right] - u^j_{3n}\left[\frac{\partial J_n(kr_o)}{\partial(kr_o)}\right]\right\} k\, dk\ .$$

The terms associated with waves polarized in vertical planes are obtained from

$$\begin{Bmatrix} u^j_{1n} \\ u^j_{2n} \\ \hline \sigma^j_{21n} \\ \sigma^j_{22n} \\ \hline \sigma^j_{33n} \\ \sigma^j_{11n} \end{Bmatrix} = \left[\begin{array}{c|c} I^j_{11} & I^j_{12} \\ \hline I^j_{21} & I^j_{22} \\ \hline I^j_{31} & I^j_{32} \end{array}\right] \left[\begin{array}{c|c} E^j_d(z_o) & 0 \\ \hline 0 & E^j_u(z_o) \end{array}\right] \begin{Bmatrix} \eta^j_{dn}(z_o) \\ \hline \eta^j_{un}(z_o) \end{Bmatrix} \tag{4.3}$$

where the 2 x 2 matrices I^j_1, I^j_{12}, ... are defined by

$$\left[\begin{array}{c|c} I^j_{11} & I^j_{12} \\ \hline I^j_{21} & I^j_{22} \\ \hline I^j_{31} & I^j_{32} \end{array}\right] = d_j^{-1} \left[\begin{array}{cc|cc} -kd_j & \nu'_j d_j & -kd_j & \nu'_j d_j \\ -\nu_j d_j & kd_j & \nu_j d_j & -kd_j \\ \hline 2k\nu_j c_j & -(2k^2c_j-1) & -2k\nu_j c_j & (2k^2c_j-1) \\ (2k^2c_j-1) & -2k\nu'_j c_j & (2k^2c_j-1) & -2k\nu'_j c_j \\ \hline 2(2\gamma_j^2-1) - 2k^2c_j & 2k\nu'_j c_j & 2(2\gamma_j^2-1) - 2k^2c_j & 2k\nu'_j c_j \\ (2\gamma_j^2-1) - 2k^2c_j & 2k\nu'_j c_j & (2\gamma_j^2-1) - 2k^2c_j & 2k\nu'_j c_j \end{array}\right] \tag{4.4}$$

while the 2 x 2 matrices $E^j_d(z_o)$ and $E^j_u(z_o)$ are given by

$$E^j_d(z_o) = \text{diag}\left(\exp\left[-\nu_j(z_o - z_o^{j-1})\right], \exp\left[-\nu'_j(z_o - z_o^{j-1})\right]\right) \tag{4.5}$$

$$E^j_u(z_o) = \text{diag}\left(\exp\left[\nu_j(z_o - z_o^{j})\right], \exp\left[\nu'_j(z_o - z_o^{j})\right]\right) \tag{4.6}$$

In the above equations, $\nu_j = [k^2 - \bar{\beta}/\alpha_j)^2]^{1/2}$, $\nu'_j = [k^2 - (\bar{\beta}/\beta_j)^2]^{1/2}$, $\gamma_j = \beta_j/\alpha_j$, and $z_o^j = \omega z_j/\bar{\beta}$ $(Z_o^{N+1} = z_o^N)$ in which z_j defines the position of the lower interface of the jth layer $(z_o^0 = 0)$.

The 2 x 1 vectors $\eta_{dn}^j(z_o)$ and $\eta_{un}^j(z_o)$ correspond to the amplitudes of the downwardly and upwardly propagating P and SV waves in the jth layer. These amplitudes are independent of z_o in all layers with exception of the ℓth layer in which the source is located. The wave amplitudes η_{un}^j and η_{dn}^j in the jth layer are obtained from the following factorization

$$
\begin{cases}
\eta_{un}^j(z_o) = \hat{T}_j^u \, \hat{T}_{j+1}^u \, \cdots \, \hat{T}_{\ell-1}^u \, \eta_{un}^\ell(z_o^{\ell-1}) & (j = 1, \ell-1) \\
\eta_{dn}^j(z_o) = \hat{R}_{j-1}^u \, \eta_{un}^j(z_o^{j-1}) & (j = 1, \ell-1)
\end{cases}
$$

$$
\begin{cases}
\eta_{dn}^j(z_o) = \hat{T}_{j-1}^d \, \hat{T}_{j-2}^d \, \cdots \, \hat{T}_{\ell}^d \, \eta_{dn}^\ell(z_o^\ell) & (j = \ell+1, N+1) \\
\eta_{un}^j(z_o) = \hat{R}_j^d \, \eta_{dn}^j(z_o^j) & (j = \ell+1, N+1)
\end{cases}
$$

$$
\begin{cases}
\eta_{un}^\ell(z_o) = \left(I - \hat{R}_\ell^d \, \hat{R}_{\ell-1}^u\right)^{-1}\left(S_{un}^\ell + \hat{R}_\ell^d \, S_{dn}^\ell\right) & (z_o^{\ell-1} \leq z_o < z_o^s) \\
\eta_{dn}^\ell(z_o) = \hat{R}_{\ell-1}^u \, \eta_{un}^\ell(z_o^{\ell-1}) & (z_o^{\ell-1} \leq z_o < z_o^s)
\end{cases}
$$

$$
\begin{cases}
\eta_{dn}^\ell(z_o) = \left(I - \hat{R}_{\ell-1}^u \, \hat{R}_\ell^d\right)^{-1}\left(S_{dn}^\ell + \hat{R}_{\ell-1}^u \, S_{un}^\ell\right) & (z_o^s < z_o \leq z_o^\ell) \\
\eta_{un}^\ell(z_o) = \hat{R}_\ell^d \, \eta_{dn}^\ell(z_o^\ell) & (z_o^s < z_o \leq z_o^\ell)
\end{cases}
\qquad (4.7)
$$

in which I denotes the 2 x 2 identity matrix, $z_o^s = \omega z^s/\bar{\beta}$, z_s defines the location of the point source, and

$$S^{\ell}_{d0} = d_{\ell} \begin{Bmatrix} \exp\left[\nu_{\ell}(z_o^s - z_o^{\ell-1})\right] \\ \frac{k}{\nu'_{\ell}} \exp\left[\nu'_{\ell}(z_o^s - z_o^{\ell-1})\right] \end{Bmatrix}, \quad S^{\ell}_{u0} = -d_{\ell} \begin{Bmatrix} \exp\left[-\nu_{\ell}(z_o^s - z_o^{\ell})\right] \\ \frac{k}{\nu'_{\ell}} \exp\left[-\nu'_{\ell}(z_o^s - z_o^{\ell})\right] \end{Bmatrix}$$

$$S^{\ell}_{d1} = d_{\ell} \begin{Bmatrix} \frac{k}{\nu_{\ell}} \exp\left[\nu_{\ell}(z_o^s - z_o^{\ell-1})\right] \\ \exp\left[\nu'_{\ell}(z_o^s - z_o^{\ell-1})\right] \end{Bmatrix}, \quad S^{\ell}_{u1} = d_{\ell} \begin{Bmatrix} \frac{k}{\nu_{\ell}} \exp\left[-\nu_{\ell}(z_o^s - z_o^{\ell})\right] \\ \exp\left[-\nu'_{\ell}(z_o^s - z_o^{\ell})\right] \end{Bmatrix}$$

The 2 x 2 matrices of generalized reflection and transmission coefficients $\hat{R}^u_j$, $\hat{R}^d_j$, $\hat{T}^u_j$ and $\hat{T}^d_j$ are obtained from the recurrence relations

$$\begin{cases} \hat{R}^u_o = R^u_o \\ \hat{T}^u_j = \left(I - R^d_j \hat{R}^u_{j-1}\right)^{-1} T^u_j & (j \geq 1) \\ \hat{R}^u_j = R^u_j + T^d_j \hat{R}^u_{j-1} \hat{T}^u_j & (j \geq 1) \end{cases}$$

$$\begin{cases} \hat{R}^d_{N+1} = 0 \\ \hat{T}^d_j = \left(I - R^u_j \hat{R}^d_{j+1}\right)^{-1} T^d_j & (j \leq N) \\ \hat{R}^d_j = R^d_j + T^u_j \hat{R}^d_{j+1} \hat{T}^d_j & (j \leq N) \end{cases} \tag{4.9}$$

in which the 2 x 2 matrices of modified reflection and transmission coefficients are given by

$$R_o^u = -\left(I_{21}^1\right)^{-1} I_{22}^1 E_u^1(0)$$

$$\left[\begin{array}{c|c} T_j^d & R_j^u \\ \hline R_j^d & T_j^u \end{array}\right] = \left[\begin{array}{c|c} -I_{11}^{j+1} & I_{12}^j \\ \hline -I_{21}^{j+1} & I_{22}^j \end{array}\right]^{-1} \left[\begin{array}{c|c} -I_{11}^j & I_{12}^{j+1} \\ \hline -I_{21}^j & I_{22}^{j+1} \end{array}\right] \left[\begin{array}{c|c} E_d^j(z_o^j) & 0 \\ \hline 0 & E_u^{j+1}(z_o^j) \end{array}\right]$$

$$(1 \leq j \leq N) \qquad (4.10)$$

Explicit expression for the modified reflection and transmission coefficients are given in Appendix I.

To insure the numerical convergence of the integral representation for large values of the dimensionless wavenumber k, it is necessary to introduce some modifications to the procedure just described. The general formalism remains intact except for the following changes:

(i) The matrices I_{pq}^j $(p = 1,2,3;\ q = 1,2)$ appearing in Eqs. (4.3) and (4.10) are replaced by

$$\bar{I}_{pq}^j = I_{pq}^j A_j^{-1} \qquad (p = 1,2,3;\ q = 1,2) \qquad (4.11)$$

where A_j^{-1} is the inverse of the 2×2 matrix

$$A_j = -\frac{1}{\kappa_j}\begin{bmatrix} (k - \nu_j) & (k - \nu_j') \\ \nu_j + (\kappa_j - 1)k & -k - (\kappa_j - 1)\nu_j' \end{bmatrix} \qquad (4.12)$$

in which $\kappa_j = (1 + \gamma_j^2)/(1 - \gamma_j^2)$.

(ii) The diagonal matrices $E_d^j(z_o)$ and $E_u^j(z_o)$ appearing in Eqs. (4.3) and (4.10) are replaced by

$$\bar{E}_d^j(z_o) = A_j \, E_d^j(z_o) \, A_j^{-1}$$

$$\bar{E}_u^j(z_o) = A_j \, E_u^j(z_o) \, A_j^{-1} \qquad (4.13)$$

and,

(iii) The source terms S_{dn}^{ℓ} and S_{un}^{ℓ} appearing in Eqs. (4.7) are replaced by

$$\bar{S}_{dn}^{\ell} = A_{\ell} \, S_{dn}^{\ell}$$

$$\bar{S}_{un}^{\ell} = A_{\ell} \, S_{un}^{\ell} \; . \qquad (4.14)$$

Detailed expressions for $\bar{I}_{pq}^j$, $\bar{E}_d^j$, $\bar{E}_u^j$, $\bar{S}_{dn}^{\ell}$ and $\bar{S}_{un}^{\ell}$ as well as for the resulting modified reflection and transmission coefficients are presented in Appendix II.

The terms u_{3n}, σ_{23n} and σ_{31n} associated with waves polarized in horizontal planes are obtained from

$$\begin{Bmatrix} u_{3n}^j \\ \sigma_{23n}^j \\ \sigma_{13n}^j \end{Bmatrix} = \begin{bmatrix} I_{11}^j & I_{12}^j \\ I_{21}^j & I_{22}^j \\ I_{31}^j & I_{32}^j \end{bmatrix} \begin{bmatrix} E_d^j(z_o) & 0 \\ 0 & E_u^j(z_o) \end{bmatrix} \begin{Bmatrix} \eta_{dn}^j(z_o) \\ \eta_{un}^j(z_o) \end{Bmatrix} \qquad (4.15)$$

which has the same form as Eq. (4.3) except that in this case the quantities involved are scalars. The terms I_{11}^j, I_{12}^j, ... , are defined by

$$\begin{bmatrix} I_{11}^{j} & I_{12}^{j} \\ I_{21}^{j} & I_{22}^{j} \\ I_{31}^{j} & I_{32}^{j} \end{bmatrix} = \begin{bmatrix} k & k \\ -k\nu_j' c_j d_j^{-1} & k\nu_j' c_j d_j^{-1} \\ k^2 c_j d_j^{-1} & k^2 c_j d_j^{-1} \end{bmatrix} \tag{4.16}$$

while

$$E_d^j(z_o) = \exp\left[-\nu_j'(z_o - z_o^{j-1})\right] \tag{4.17}$$

$$E_u^j(z_o) = \exp\left[\nu_j'(z_o - z_o^{j})\right] \quad . \tag{4.18}$$

The terms $n_{dn}^{j}(z_o)$ and $n_{un}^{j}(z_o)$ correspond to the amplitudes of the downwardly and upwardly propagating SH waves in the jth layer. The wave amplitudes n_{dn}^{j} and n_{un}^{j} are also obtained from the factorization given in Eq. (4.7) except that the terms S_{dn}^{ℓ} and S_{un}^{ℓ} are now given by

$$S_{d0}^{\ell} = 0 \ , \qquad S_{u0}^{\ell} = 0 \ ,$$

$$S_{d1}^{\ell} = \left(k\nu_\ell' c_\ell d_\ell^{-1}\right)^{-1} \exp\left[\nu_\ell'(z_o^s - z_o^{\ell-1})\right] \ , \tag{4.19}$$

$$S_{u1}^{\ell} = \left(k\nu_\ell' c_\ell d_\ell^{-1}\right)^{-1} \exp\left[-\nu_\ell'(z_o^s - z_o^{\ell})\right] \quad .$$

The generalized reflection and transmission coefficients for the case of horizontally polarized waves follow the same recurrence relations presented in Eq. (4.9). The modified reflection and transmission coefficients are also given in this case by Eq. (4.10) with the terms appearing in that equation defined as in Eqs. (4.16), (4.17) and (4.18). In

particular, these coefficients are given by

$$R_o^u = \exp(-\nu_1' z_o^1)$$

$$\begin{bmatrix} T_j^d & R_j^u \\ R_j^d & T_j^u \end{bmatrix} = \frac{1}{\Delta} \begin{bmatrix} 2\nu_j' c_j d_j^{-1} & -\left(\nu_j' c_j d_j^{-1} - \nu_{j+1}' c_{j+1} d_{j+1}^{-1}\right) \\ \left(\nu_j' c_j d_j^{-1} - \nu_{j+1}' c_{j+1} d_{j+1}^{-1}\right) & 2\nu_{j+1}' c_{j+1} d_{j+1}^{-1} \end{bmatrix}$$

$$\times \begin{bmatrix} \exp\left[-\nu_j'(z_o^j - z_o^{j-1})\right] & 0 \\ 0 & \exp\left[\nu_{j+1}'(z_o^j - z_o^{j+1})\right] \end{bmatrix},$$

$$(1 \leq j \leq N) \qquad (4.20)$$

in which $\Delta = \nu_j' c_j d_j^{-1} + \nu_{j+1}' c_{j+1} d_{j+1}^{-1}$.

In the case of horizontally polarized waves the integral representation just described is valid for all values of the dimensionless wavenumber k and does not need to be modified for large values of k.

The response of a layered viscoelastic medium to loads distributed over a ring can be obtained by the same procedure just described except that Eq. (4.2) must be modified as in Eqs. (2.55) and (2.61) of Chapter 2.

4.2 METHOD OF INTEGRATION

4.2.1 Introduction

The Hankel transform-type integral representations of the displacement and stress components in the frequency domain are summarized in Eq. (4.2) and involve quantities of the form

$$I_n(r_o,z_o) = \int_0^\infty F(k,z_o)\, J_n(kr_o)\, dk \ , \qquad n = 0,1,2 \ . \qquad (4.21)$$

for the concentrated point loads. The kernel $F(k,z_o)$ depends upon wavenumber, frequency, receiver and source depth and layer properties; whereas, the Bessel functions $J_n(kr_o)$ depend only upon the product of wavenumber times normalized epicentral observation distance ($r_o = \omega r/\overline{\beta}$). An effective procedure to evaluate the F integrands has been presented in Chapter 3 based on highly efficient factorizations for the upgoing and downgoing wave amplitudes in each layer (refer to summary in Eqs. (4.3) through (4.7)). All that remains then is to develop an efficient numerical integration scheme capable of handling the oscillatory nature of the Bessel functions in addition to the vigorous behavior of the pervasive F integrands (as a function of wavenumber).

4.2.2 Description of Kernel

Before describing the method of integration, it is instructive to portray the dependence of the F integrands on frequency and wavenumber.

The real parts of two representative F integrands are pictured in Figure 4.1 for the simple soil models also shown in the figure. The three-dimensional plots in the left-hand column represent the F integrands for the vertical displacement at the free surface due to a concentrated vertical point force at the free surface (viz., U^1_{20}); the plots in the right-hand column represent the F integrands for the tangential displacement due to a concentrated horizontal point force (viz., U^1_{31}). The axes running from left to right correspond to the dimensionless wavenumber k which is inversely proportional to the phase velocity (the range from $k = 0$ to $k = 2$ is shown in the plots). High frequency is in the foreground and low frequency is in the background.

The poles of the F integrands are shifted off the real k axis by introducing attenuation for shear and compressional waves so that all the peaks have finite amplitudes. This not only facilitates implementation of an integration scheme over real k values, but at the same time models physically realizable attenuation in the Earth. The plots on the left involve P-SV-Rayleigh waves while those on the right involve SH-Love waves.

For a half-space with source and receiver at the surface, the function F is frequency independent as is apparent in the upper left plot of Figure 4.1. The large undispersed dipole shape corresponds to the Rayleigh wave for the half-space and the small inflection represents the compressional wave. For a layer overlying a half-space, higher surface wave modes appear as the frequency is increased as depicted in the center plots. All the surface waves are normally dispersed since on a given mode, the phase velocity decreases as the frequency is increased. In the lower

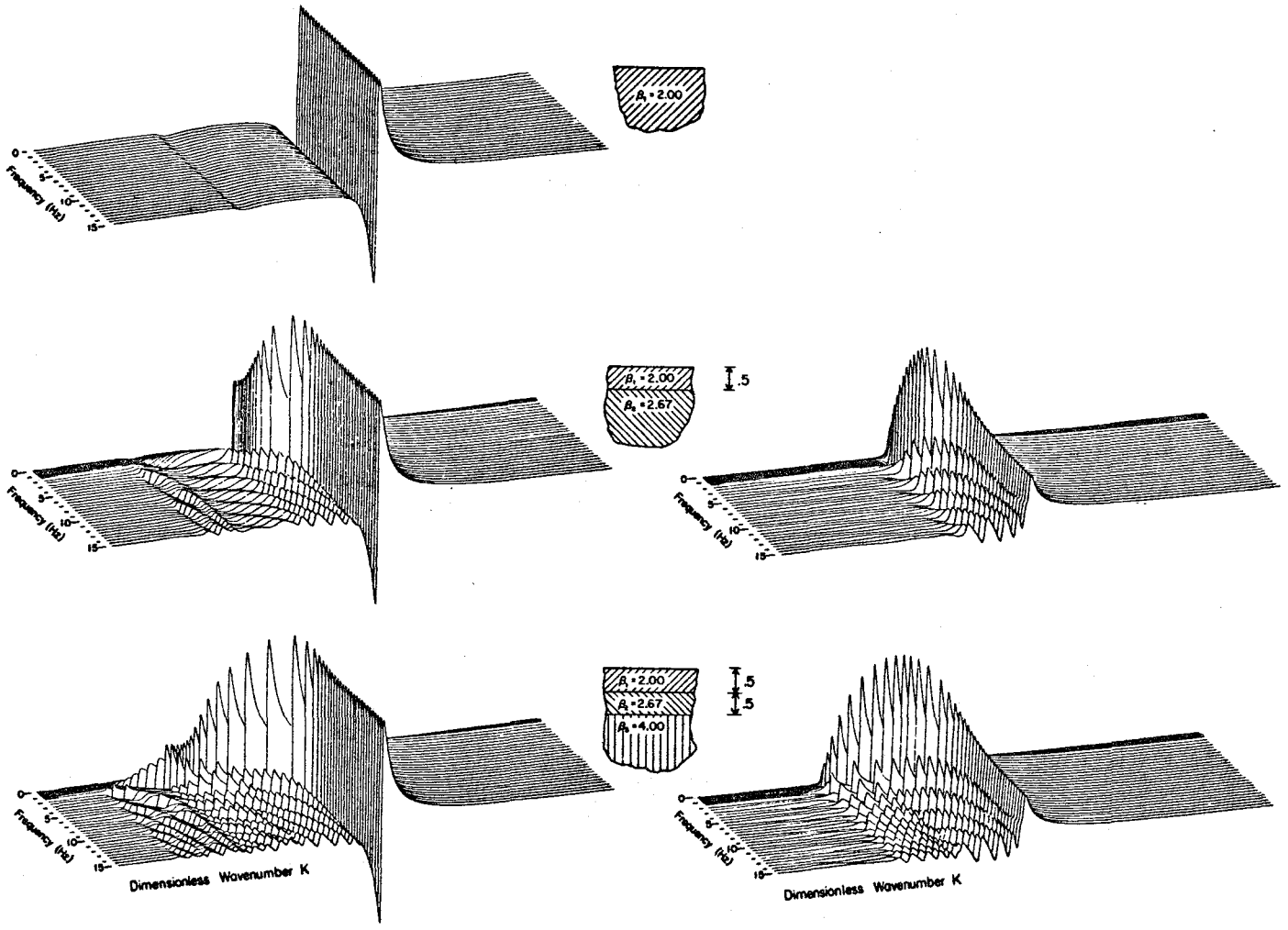

$U^1_{20}(z_o,k)$ $U^1_{31}(z_o,k)$

Figure 4.1. Real parts of the free-surface displacement components in the frequency-wavenumber domain due to a concentrated force at the free-surface of a uniform half-space. In each three-dimensional figure, dimensionless wavenumbers from 0 to 2 run from left to right; frequencies from 15 to 0 Hz run from front to back.

plots, the two layers which overlie a half-space have the same properties (velocities, density, attenuation factors and thickness) as used in the center model. Thereby, at sufficiently high frequencies, when the waves become insensitive to the underlying half-space, the most fundamental surface wave modes should match those for the center model. The plots shown also reveal that the F integrands are uninvolved at large wavenumbers indicating that the tail-ends of the wavenumber integrals can be evaluated without difficulty.

The plots in Figure 4.2 illustrate the behavior of the F integrands for a more realistic earth structure, which is defined in Table 5.2. The source is a vertical point force buried in the sixth of 15 layers. Also, the lesser amount of attenuation contributes to the more pronounced behavior. Each plot now represents a different frequency from one cycle/sec in the top curve to 10 cycles/sec in the bottom curve, and wavenumber is still displayed horizontally. The component shown corresponds to the real part of the F integrand for the vertical displacement evaluated at the surface of the layered half-space (viz., U^1_{20}). Clearly, a sophisticated scheme is needed to inner-product the F integrands with the Bessel functions at each frequency for all wavenumbers.

4.2.3 Upper Limit of Integration and Low Frequency Switchover

Independent of the type of quadrature implemented to evaluate the semi-infinite wavenumber integral in Eq. (4.21), two fundamental decisions must be made: 1) how to determine the upper limit of integration; and 2) how to determine the switchover k value at which the low frequency expansions are used to calculate the F integrands. So long as

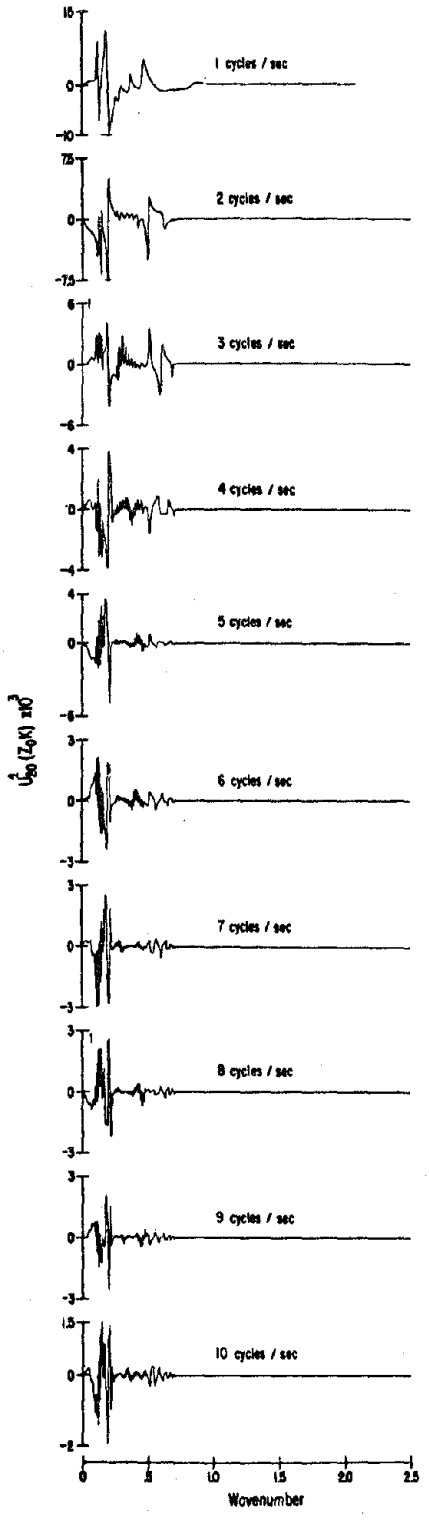

Figure 4.2. Real part of the vertical displacement component at the free surface in the frequency-wavenumber domain due to a concentrated force buried in the layered half-space model depicted in Table 5.2.

no receiver depth coincides with any source depth, the exponential decay of the F integrands may be relied upon to define the upper limit of integration, k_ℓ. This reduces the semi-infinite integral in Eq. (4.21) to the following finite integral:

$$I_n(\omega) = \int_0^{k_\ell} F(\omega)\, J_n\, dk \tag{4.22}$$

in which the arguments have been omitted for brevity and clarity.

An alternative procedure is obtained by considering that for high values of k the F integrands for any frequency tend to the value of the F integrands in the static case. Taking advantage of this property, the integral in Eq. (4.21) can be written in the form

$$I_n(\omega) = I_n(0) + \int_0^{k_\ell} [F(\omega) - F(0)]\, J_n\, dk \tag{4.23}$$

in which F(0) represents the static (ω=0) F integrands and I(0) represents the corresponding static (ω=0) integrals. The upper limit of integration, k_ℓ, is thereby defined in this case by the convergence of the dynamic integrands to the static integrands.

The procedure of Eq. (4.23) is particularly useful when source and receiver are at the same depth, in which case the decay of the F integrands as a function of k is slow. In Eq. (4.23), the static F integrands and integrals may correspond to those static integrands and integrals for a uniform half-space with properties of the layer containing the source-receiver pair. Although the dynamic F integrands may converge more slowly to the half-space static F integrands, the

advantage is that analytic expressions are available for the half-space static integrands and integrals (see Appendix III).

When using Eq. (4.23) for the proximate source-receiver depths, it becomes essential to implement the low frequency expansions of the F integrands at high k in order to insure that $[F(\omega) - F(0)]$ properly approaches zero as k is increased. The switchover k value at which the low frequency procedure is used to evaluate the $F(\omega)$ integrands in either Eq. (4.22) or (4.23) is determined by

$$k \geq \omega \, h_{min}/\overline{\beta} \tag{4.24}$$

where h_{min} is the minimum layer thickness. The minimum layer thickness appears in the inequality because the thinner the layer (or the lower the frequency), the smaller the value of k at which the differences between the compressional and shear waves can be accurately calculated. Although the low frequency formulation for the F integrands is valid all the way back to k equals zero, its use is unnecessary at low k values. Therefore, the inequality in Eq. (4.24) need only be tested when k is larger than, say, 0.5 divided by the slowest phase velocity of the problem.

4.2.4 Formulation for Method of Integration

The basic philosophy behind the method of integration is to sample the F integrands sufficiently fine to allow piecewise polynomials to interpolate the amplitudes of the F functions between the integration points. Thereby, the numerical integration over the Bessel functions can be performed analytically over each integration interval, thus avoiding the oscillation hazard of the Bessel functions.

For reasons that will become clearer later in the discussion, quartic polynomial interpolation is the most effective order scheme to employ in general. The five integration points on a given interval are defined as k_1, k_2, k_3, k_4, k_5 with the quartic polynomial determined by

$$F(k,z_o) = \sum_{m=1}^{5} A_m \left(\frac{k - k_2}{\Delta k} \right)^{m-1} , \qquad (4.25)$$

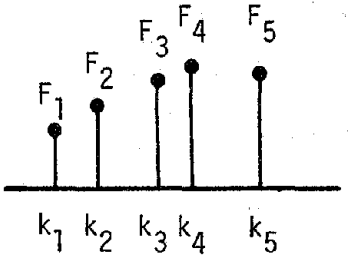

in which $\Delta k = k_4 - k_2$. The normalization inherent in Eq. (4.25) is chosen with the intention of integrating from k_2 to k_4 on each interval and overlapping k_1 and k_5 into the outer intervals in order to insure a smoother fit to $F(k,z_o)$ between k_2 and k_4.

Introducing matrix notation, the coefficients A_m ($m = 1, 5$) are uniquely determined by the five $F(k_m,z_o)$ according to

$$\begin{Bmatrix} A_1 \\ A_2 \\ A_3 \\ A_4 \\ A_5 \end{Bmatrix} = \begin{bmatrix} 1 & a & a^2 & a^3 & a^4 \\ 1 & 0 & 0 & 0 & 0 \\ 1 & b & b^2 & b^3 & b^4 \\ 1 & c & c^2 & c^3 & c^4 \\ 1 & d & d^2 & d^3 & d^4 \end{bmatrix}^{-1} \begin{Bmatrix} F_1 \\ F_2 \\ F_3 \\ F_4 \\ F_5 \end{Bmatrix}$$

$$= \underset{5x5}{[C]} \quad \underset{5x1}{\{F\}} \qquad (4.26)$$

in which $F_m = F(k_m, z_o)$ and

$$a = \frac{1}{\Delta k}(k_1 - k_2)$$

$$b = \frac{1}{\Delta k}(k_3 - k_2)$$

$$c = \frac{1}{\Delta k}(k_4 - k_2)$$

$$d = \frac{1}{\Delta k}(k_5 - k_2) \qquad (4.27)$$

The elements, C_{ij} $(i,j = 1,5)$ of the 5 x 5 matrix [C] appearing in Eq. (4.26) are

$$C_{11} = 0$$

$$C_{12} = 1$$

$$C_{13} = 0$$

$$C_{14} = 0$$

$$C_{15} = 0$$

$$C_{21} = \frac{-bcd}{a(a-b)(a-c)(a-d)}$$

$$C_{22} = \frac{-a(bc+bd+cd)-bcd}{abcd}$$

$$C_{23} = \frac{acd}{b(a-b)(b-c)(b-d)}$$

$$C_{24} = \frac{-abd}{c(a-c)(b-c)(c-d)}$$

$$C_{25} = \frac{abc}{d(a-d)(b-d)(c-d)}$$

$$C_{31} = \frac{b(c+d) + cd}{a(a-b)(a-c)(a-d)}$$

$$C_{32} = \frac{a(b+c+d) + b(c+d) + cd}{abcd}$$

$$C_{33} = \frac{-a(c+d) - cd}{b(a-b)(b-c)(b-d)}$$

$$C_{34} = \frac{a(b+d) + bd}{c(a-c)(b-c)(c-d)}$$

$$C_{35} = \frac{-a(b+c) - bc}{d(a-d)(b-d)(c-d)}$$

$$C_{41} = \frac{-(b+c+d)}{a(a-b)(a-c)(a-d)}$$

$$C_{42} = \frac{-(a+b+c+d)}{abcd}$$

$$C_{43} = \frac{(a+c+d)}{b(a-b)(b-c)(b-d)}$$

$$C_{44} = \frac{-(a+b+d)}{c(a-c)(b-c)(c-d)}$$

$$C_{45} = \frac{(a+b+c)}{d(a-d)(b-d)(c-d)}$$

$$C_{51} = \frac{1}{a(a-b)(a-c)(a-d)}$$

$$C_{52} = \frac{1}{abcd}$$

$$C_{53} = \frac{-1}{b(a-b)(b-c)(b-d)}$$

$$C_{54} = \frac{1}{c(a-c)(b-c)(c-d)}$$

$$C_{55} = \frac{-1}{d(a-d)(b-d)(c-d)} \qquad (4.28)$$

Rewriting the integral appearing in, say, Eq. (4.22) as a summation of integrals over each interval (k_2, k_4) with $F(k,z_o)$ replaced by the quartic polynomial defined in Eqs. (4.25) through (4.28) leads to the following expression for $I_n(r_o,z_o)$:

$$I_n = \sum_{\text{intervals}} \left[\underset{1x5}{(F_1,F_2,F_3,F_4,F_5)} \; \underset{5x5}{[C]^T} \int_{k_2}^{k_4} \left\{ \begin{matrix} 1 \\ \left(\frac{k-k_2}{\Delta k}\right) \\ \left(\frac{k-k_2}{\Delta k}\right)^2 \\ \left(\frac{k-k_2}{\Delta k}\right)^3 \\ \left(\frac{k-k_2}{\Delta k}\right)^4 \end{matrix} \right\}_{5x1} J_n(kr_o)\,dk \right] \qquad (4.29)$$

in which superscript T denotes the transpose matrix. The summation in Eq. (4.29) is carried out over all the intervals of integration from k_2 to k_4, except for the first interval on which the integration is performed from k_1 to k_4 since no overlapping is possible from a previous interval.

It is important to notice in Eq. (4.29) that the product of the 5x5 matrix [C] times the 5x3 matrix of integrals (n=0,1,2) is independent of source and receiver depth; hence needs to be formed only once for each epicentral range. Since the integrals in Eq. (4.29) can be evaluated analytically, the oscillation hazard of the Bessel functions is completely circumvented and the number of integration points is restricted to the tolerance desired in sampling the F integrands.

4.2.5 Sampling/Integration Criteria

After the calculation for a given frequency is initialized by evaluating the F integrands at five equally spaced k points, the calculation proceeds as follows until k_4 exceeds the upper limit of integration, k_ℓ. The error in passing a quartic polynomial through each of the F integrands at the five k points is estimated by forming the fourth difference of the amplitudes of the F integrands on the i^{th} interval. This fourth difference is then multiplied by Δk in order to estimate the relative error in performing the integral on the i^{th} interval from k_2 to k_4, since the integral is roughly proportional to Δk.

If the relative error is below a specified tolerance for all the F components, then the integrals are performed on the i^{th} interval with the results added to the respective integrals from the previous i-1 intervals. Otherwise, a new k point is inserted midway between the widest spacing of the k points on the i^{th} interval and the relative error is resampled, with the F amplitudes from the extra k point saved for later intervals. To proceed to the next interval after integrating from k_2 to k_4 the F integrands are evaluated at two new

k points beyond k_5 with the step in Δk determined by the maximum relative error from the previous interval. Of course, if new k points are already available from the resampling process, then new F integrands need not be evaluated until the previously stored F integrands are exhausted.

4.2.6 Integration Branch

What remains to be discussed is the technique used to evaluate integrals of the type appearing in Eq. (4.29). Although formulae are available for these definite Bessel integrals, the following branch on the integration procedure for a given interval proves to be the more efficient methodology. As depicted in Figure 4.3, the integration branch depends on the magnitude of the argument of the Bessel functions—namely, the product of dimensionless wavenumber k times dimensionless epicentral distance r_o.

In region 2 of Figure 4.3, the arguments of the Bessel functions are sufficiently large to allow Hankel's asymptotic expansions to replace the Bessel functions:

$$J_n(kr_o) = \sqrt{\frac{2}{\pi kr_o}}\left[P(n,kr_o)\cos(\chi) - Q(n,kr_o)\sin(\chi)\right] \qquad (4.30)$$

where $\chi = kr_o - \left(\frac{n}{2} + \frac{1}{4}\right)\pi$ and, with $\delta = 4n^2$

$$P(n,kr_o) \sim 1 - \frac{(\delta-1)(\delta-9)}{2!(8kr_o)^2} + \frac{(\delta-1)(\delta-9)(\delta-25)(\delta-49)}{4!(8kr_o)^4} - \ldots$$

$$Q(n,kr_o) \sim \frac{(\delta-1)}{(8kr_o)} - \frac{(\delta-1)(\delta-9)(\delta-25)}{3!(8kr_o)^3} + \ldots \quad . \qquad (4.31)$$

Using trigonometric identities, Eq. (4.30) can be rearranged into the more convenient form

$$J_n(kr_o) = \hat{P}(n,kr_o)\cos(kr_o) - \hat{Q}(n,kr_o)\sin(kr_o) \qquad (4.32)$$

in which

$$\hat{P}(n,kr_o) = \sqrt{\frac{2}{\pi kr_o}}\left[P(n,kr_o)\cos\left(\frac{n}{2}+\frac{1}{4}\right)\pi + Q(n,kr_o)\sin\left(\frac{n}{2}+\frac{1}{4}\right)\pi\right]$$

$$\hat{Q}(n,kr_o) = \sqrt{\frac{2}{\pi kr_o}}\left[Q(n,kr_o)\cos\left(\frac{n}{2}+\frac{1}{4}\right)\pi - P(n,kr_o)\sin\left(\frac{n}{2}+\frac{1}{4}\right)\pi\right] .$$

Now, for an interval contained within region 2 (i.e., $k_1 r_o > \hat{x}$), the Bessel functions are replaced by the expansions in Eq. (4.32), with the smoothly varying functions $\hat{P}(n,kr_o)$ and $\hat{Q}(n,kr_o)$ included in the polynomial interpolation of the F integrands. Therewith, the integral on the i^{th} interval may be written as follows if $k_1 r_o > \hat{x}$:

$$I_n^i(r_o,z_o) = \underset{1x5}{\{F\}^T}\ \underset{5x5}{\left[\hat{P}_n\right]}\ \underset{5x5}{[C]^T}\int_{k_2}^{k_4}\underset{5x1}{\{\kappa\}}\cos(kr_o)dk$$

$$- \underset{1x5}{\{F\}^T}\ \underset{5x5}{\left[\hat{Q}_n\right]}\ \underset{5x5}{[C]^T}\int_{k_2}^{k_4}\underset{5x1}{\{\kappa\}}\sin(kr_o)dk$$

in which

$$\text{diag}_m\left[\hat{P}_n\right] = \hat{P}(n,k_m r_o) \ , \quad \text{diag}_m\left[\hat{Q}_n\right] = \hat{Q}(n,k_m r_o)$$

and

$$\kappa_m = \left(\frac{k-k_2}{\Delta k}\right)^{m-1} \ , \quad m = 1,2,3,4,5 \ .$$

In region 1 of Figure 4.3, $\Delta k = k_4 - k_2$ is required to be small enough to insure that the Bessel functions oscillate slowly over the integration interval. Thereby, the entire Bessel function may be included in the polynomial interpolation of the F integrands, so that the integral on the i^{th} interval located in region 1 may be written as

$$I_n^i(r_o,z_o) = \underset{1x5}{\{F\}^T} \underset{5x5}{[J_n]} \underset{5x5}{[C]} \int_{k_2}^{k_4} \underset{5x1}{\{\kappa\}}\, dk \qquad (4.35)$$

in which

$$\text{diag}_m [J_n] = J_n(k_m r_o)$$

and

$$\int_{k_2}^{k_4} \kappa_m dk = \Delta k/m , \quad m = 1,2,3,4,5.$$

The degree of smoothness necessary in the Bessel functions for Eq. (4.35) to be valid in region 1 depends on the accuracy desired in the numerical integration at a given frequency. The smoothness provision in region 1 is exclusively a function of the product $\Delta x = \Delta k r_o$, since the magnitude of Δx determines the number of quadrature points used per Bessel function oscillation. Realizing that the Bessel function oscillations have wavelengths of order 2π, then in order to accomodate say ten quadrature points per oscillation, Δx must be restricted to values less than $\Delta\hat{x}$ (with $\Delta\hat{x} = 1$) in region 1.

The restriction on Δx in region 1 is virtually inconsequential in determining the value of Δk during an actual numerical integration. Since $k_1 r_o < \hat{x}$ in region 1, it is straightforward to show that $\Delta k r_o < \Delta\hat{x}$ if and only if

$$\Delta k < \left(\frac{\Delta\hat{x}}{\hat{x}}\right) k_1 \ , \tag{4.36}$$

independent of r_o. With $\Delta\hat{x} = 1$ and $\hat{x} = 5$, Δk is merely required to be less than one fifth of k_1 — a condition automatically satisfied in general by sampling the F integrands to within a specified error tolerance. Enforcing the inequality for Δk in Eq. (4.36) (in addition to the sampling criteria) insures that the so-called "fast" integration will be valid whenever $k_1 r_o < \hat{x}$ (which is necessary since the so-called "asymptotic" integration is never applicable in region 1). The "fast" integration, on the other hand, is often times valid (i.e., $\Delta k r_o < \hat{x}$) in region 2 and should be used instead of the "asymptotic" integration whenever applicable since it is more efficient.

One final point of interest regarding the restriction of Δk for the validity of the integration branch can be made by referring to Figure 4.3. For integration intervals having k_5 less than k^* or k_1 greater than k^S, the inequality in Eq. (4.36) is more stringent than necessary. In the latter case, $k_1 r_o$ always falls within region 2 indicating that the inequality may be disregarded (since the validity of the "fast" integration need not be insured with all the integration intervals situated interior to region 2). In the former case, the integration intervals lie entirely within region 1, so that the "fast" integration must be applicable (i.e., must have $\Delta k r_o < \Delta\hat{x}$). Since,

however, $\hat{x}/k_1$ is larger than r_o, it is less constraining to merely require that

$$\Delta k < \frac{\Delta \hat{x}}{(r_o)_{max}} \tag{4.37}$$

for $k_5 < k^*$.

To complete the description of the method of integration, expressions for the integrals appearing in Eq. (4.34) are presented:

$$\int_{k_2}^{k_4} \begin{matrix}\cos\\ \sin\end{matrix}(kr_o)dk = \Delta k \left\{ \begin{matrix}\cos\\ \sin\end{matrix}(\bar{x})S \right\}$$

$$\int_{k_2}^{k_4} \left(\frac{k-k_2}{\Delta k}\right) \begin{matrix}\cos\\ \sin\end{matrix}(kr_o)dk = \Delta k \left\{ \frac{1}{2} \begin{matrix}\cos\\ \sin\end{matrix}(\bar{x})\, S \mp \frac{1}{\Delta x} \begin{matrix}\sin\\ \cos\end{matrix}(\bar{x}) \left[S - \cos\left(\frac{\Delta x}{2}\right)\right] \right\}$$

$$\int_{k_2}^{k_4} \left(\frac{k-k_2}{\Delta k}\right)^2 \begin{matrix}\cos\\ \sin\end{matrix}(kr_o)dk = \Delta k \left\{ \frac{1}{2} \begin{matrix}\cos\\ \sin\end{matrix}(\bar{x}) \left[S - \frac{4}{(\Delta x)^2}\left(S - \cos\frac{\Delta x}{2}\right)\right] \right.$$

$$\left. \mp \frac{1}{\Delta x} \begin{matrix}\sin\\ \cos\end{matrix}(\bar{x}) \left[S - \cos\left(\frac{\Delta x}{2}\right)\right] \right\}$$

$$\int_{k_2}^{k_4} \left(\frac{k-k_2}{\Delta k}\right)^3 \begin{matrix}\cos\\ \sin\end{matrix}(kr_o)dk = \Delta k \left\{ \frac{1}{2} \begin{matrix}\cos\\ \sin\end{matrix}(\bar{x}) \left[S - \frac{6}{(\Delta x)^2}\left(S - \cos\frac{\Delta x}{2}\right)\right] \right.$$

$$\left. \mp \frac{1}{\Delta x} \begin{matrix}\sin\\ \cos\end{matrix}(\bar{x}) \left[\left(1.5\, S - \cos\frac{\Delta x}{2}\right) - \frac{6}{(\Delta x)^2}\left(S - \cos\frac{\Delta x}{2}\right)\right] \right\}$$

$$\int_{k_2}^{k_4} \left(\frac{k-k_2}{\Delta k}\right)^4 \begin{matrix}\cos \\ \sin\end{matrix}(kr_o)\,dk = \Delta k \left\{ \frac{1}{2} \begin{matrix}\cos \\ \sin\end{matrix}(\bar{x}) \left[S - \frac{8}{(\Delta x)^2}\left(1.5\,S - \cos\frac{\Delta x}{2}\right) \right.\right.$$

$$\left. + \frac{48}{(\Delta x)^4}\left(S - \cos\frac{\Delta x}{2}\right)\right] \mp \frac{1}{\Delta x} \begin{matrix}\sin \\ \cos\end{matrix}(\bar{x}) \left[\left(2.0\,S - \cos\frac{\Delta x}{2}\right)\right.$$

$$\left.\left. - \frac{12}{(\Delta x)^2}\left(S - \cos\frac{\Delta x}{2}\right)\right]\right\} \qquad (4.38)$$

in which

$$\bar{x} = \frac{1}{2}(k_2+k_4)r_o \;, \quad \Delta x = \Delta k r_o \;, \quad S = \frac{\sin(\Delta x/2)}{(\Delta x/2)} \;.$$

4.2.7 Modifications for Integral Representations Involving Concentrated Ring Loads

The integral representations of the displacement and stress components associated with concentrated ring loads are presented in Eqs. (2.55) and (2.61) are are of the form

$$I_{mn}(a_o,r_o,z_o) = \int_0^\infty F(k,z_o)J_m(ka_o)J_n(kr_o)\,dk \;,$$

$$n = m\text{-}1,\ m,\ m\text{+}1 \;. \qquad (4.39)$$

The distinction between Eqs. (4.39) and (4.21) is clearly the additional Bessel function $J_m(ka_o)$ which depends only upon the product of dimensionless wavenumber times normalized ring radius ($a_o = \omega a/\bar{\beta}$). Also, the order of the Bessel functions assumes the values ν-1, ν, ν+1 where ν is the azimuthal order of the ring source.

The method of integration previously described for concentrated point loads is still applicable; however, four branches must be considered instead of two, since each Bessel function conforms to the partitioning portrayed in Figure 4.3. The first branch corresponds to the case in which both $\Delta k r_o < \Delta\hat{x}$ and $k a_o < \Delta\hat{x}$, such that the product of the two Bessel functions may be included in the polynomial interpolation of the F integrands, similar to the "fast" integration described by Eq. (4.35). The second and third branches correspond to the cases in which the "fast" integration would be applicable for only one of the Bessel functions, while the "asymptotic" integration would be necessary for the other Bessel function. In either of these cases, the products of the slowly varying Bessel function times the Hankel coefficients, $\hat{P}$ and $\hat{Q}$, of the other Bessel function are included in the polynomial interpolation of the F integrands leading to a form similar to that of Eq. (4.34). The fourth branch corresponds to the case in which both Bessel functions are oscillating too rapidly to use the "fast" integration. For such a case, both Bessel functions are replaced by their respective Hankel expansions from Eq. (4.32). Then the products of the respective $\hat{P}$ and $\hat{Q}$ coefficients are included in the polynomial interpolation of the F integrands leaving integrals of $\{\kappa\}$ with products of cosines and sines to be evaluated analytically. It should be pointed out that in all four branches for the ring load integrations, the operational definition of $\Delta\hat{x}$ must be approximately half the value used for the point force integrations. This is due to the effective wavelength of the oscillations in the Bessel function product being potentially half that of each individual Bessel function.

4.2.8 Alternative Sampling/Integration Procedures

In certain instances, the method of sampling described above has the disadvantage of weighting all the integration intervals the same, irregardless of the relative contribution to the summation representing the total integral. One alternative is to take advantage of knowing the physics of the problem so as to require a denser spacing of quadrature points only near the surface wave, body wave and leaky mode poles of the F integrands. Numerically, this may be achieved by sampling changes in slope in the determinants for each layer such as the real part of the following quantities (refer to Chapter 3 for notation):

$$\frac{1}{\det\left[I - \hat{R}^u_{j-1}\,\hat{R}^d_j\right]}\,, \quad j = 1, 2, \ldots, N \tag{4.40}$$

which is easily shown to be related to the total determinant for P, SV, Rayleigh wave propagation. In addition, it is advisable to sample the product of the vertical wavenumbers $\nu_{\alpha j}$ and $\nu_{\beta j}$:

$$\frac{k^{2N+2}}{\nu_{\alpha 1}\,\nu_{\beta 1}\,\nu_{\alpha 2}\,\nu_{\beta 2}\cdots\nu_{\alpha N}\,\nu_{\beta N}} \tag{4.41}$$

even though the layer determinants in Eq. (4.40) contain information about every body wave arrival. The extra k^2 appearing in the numerator insures a sufficient number of quadrature points near the leaky wave modes; viz., at phase velocities between infinite (k=0) and the body wave arrivals ($k \sim \overline{\beta}/\alpha_{max}$).

Another nuance to the method of integration is the possibility of considering a substitute interpolation scheme. A quadratic scheme is

perhaps the most practical alternative since the piecewise integrations would still be executed over every other k point. However, experience has shown that not only is the fit to the F integrands superior with the quartic scheme (over the center three points of each five point interval), but the quadrature points are located more strategically by virtue of sampling the F integrands at five adjacent k points rather than at three. Therefore, the quartic scheme is the most efficient procedure, since the savings of implementing a three point scheme in lieu of the five point scheme is relatively insignificant for most problems.

The final alternative to be discussed is a discrete Fourier-Bessel representation. Although it is possible to conceive of fewer k points being used in low k regions, the savings are more than compensated elsewhere. Also, intuitively, it makes more sense to densely sample at low k (where most of the variations in the F integrands occur) and allow the spacing to increase at large k.

4.2.9 Time Domain Synthesis

To conclude the discussion on the method of integration, it should be briefly stated that the displacement and stress components are calculated in the time domain through Fourier synthesis of the frequency domain components:

$$I_n(r,z;\, t) = \frac{1}{2\pi} \int_{-\infty}^{\infty} I_n(r,z;\, \omega) e^{i\omega t}\, d\omega \ . \qquad (4.42)$$

A discrete Fast Fourier Transform algorithm is used to numerically evaluate the integral in Eq. (4.42). Various levels of sophistication

are possible to synthesize the time domain results: from equal spacing the frequency points when generating the discrete set of $I_n(r, z; \omega)$, to unequal spacing with the equally spaced set generated through spline interpolation. The advantage of unequally spacing the frequency points is to allow the frequency spacing to widen according to the length of time signal expected from a particular frequency band.

4.2.10 Summary

An efficient integration scheme has been developed that effectively deals with the hazards encountered in evaluating integrals of the type in Eq. (4.21) for concentrated point loads and of the type in Eq. (4.39) for concentrated ring loads. Since the radial dependence appears only in the Bessel integrals, it is highly efficient to consider multiple epicentral ranges simultaneously. Demonstrational plots of the F integrands were presented along with the strategy used to sequentially sample the same during the integration procedure. Finally, the Fourier synthesis procedure used to transform the frequency domain displacement and stress components into the time domain was briefly discussed.

CHAPTER 5

VALIDATION, COMPARISONS AND RESULTS

5.1 VALIDATION

The complexity of the numerical procedure used to evaluate the Green's functions suggests the need for an exhaustive set of validation calculations prior to employing the method in actual applications. A suite of five external checks is presented for such a purpose in the form of comparisons with known solutions. The first three tests validate the reliability of the numerical procedure when considering a uniform half-space, whereas the final two tests include a finite number of layers.

The first test confirms the accuracy of the displacements at the surface of a half-space caused by a point force also at the surface, while the second test allows the point force to be buried in the half-space. The third validation exercise proceeds to certify the stresses at depth for a surface point force as well as the free surface displacements for a double couple source at depth. Studies 4 and 5 extend the third validation to the case of a layered half-space.

In all five validation studies of this section, the complete solution obtained by the present method is compared to the complete solution obtained by totally unrelated methods. However, an exact match can only be expected in the first three tests, since the alternate methods employed in the final two tests do not provide exact solutions. The results presented in the comparison section 5.2 serve to further

validate the present method despite the fact that various assumptions and approximations are inherent in the other methods. In section 5.3, a small sample of results is presented to illustrate the flexibility and applicability of the method.

Perhaps the most demanding validation test conceivable is evidenced in Part II of the present work. To obtain accurate solutions of the integral equations in Part II, it is prerequisite that all the displacement and stress components be of near-perfect precision at a mesh of receiver points for ring loads at the mesh of source points.

5.1.1 Comparison with Contour Integration Approach (Wong, 1975)

In this first of five external validation exercises, the complex displacement components at the surface of a uniform half-space (dimensionless receiver depth $z_o = 0$) are evaluated as a function of dimensionless receiver distance $r_o = \omega r/\bar{\beta}$. The source is a harmonic point force acting at the free surface so that only four components are independent ($U^1_{z1}(r_o,0) = U^1_{r0}(r_o,0)$ using the notation of Eq. (3.3)). The half-space is defined by a reference shear wave velocity of $\bar{\beta}$ and a Poisson's ratio of 0.33.

The four complex displacement components for a perfectly elastic half-space (0% damping) using contour integration (Wong, 1975) are tabulated in Table 5.1 for values of r_o from 0 to 5.5. The displacements in the first two columns are for a vertical point force while those in the last two columns are for a horizontal point force, applied at the surface of the half-space in both cases.

$r_o = \omega r/\bar{\beta}$	$\frac{r_o}{4\pi} U^1_{r0}(r_o,0)$	$\frac{r_o}{4\pi} U^1_{z0}(r_o,0)$	$\frac{r_o}{4\pi} U^1_{r1}(r_o,0)$	$\frac{r_o}{4\pi} U^1_{\theta 1}(r_o,0)$
	Wong's (1975) Results with 0% Damping			
0.0	-.027, .000	.106, .000	.159, .000	-.106, .000
0.5	-.032, .007	.087, -.062	.146, -.058	-.089, .058
1.0	-.033, .025	.037, -.102	.112, -.105	-.045, .099
1.5	-.020, .047	-.029, -.108	.063, -.133	.015, .112
2.0	.006, .060	-.087, -.077	.011, -.137	.075, .093
2.5	.041, .058	-.120, -.017	-.034, -.120	.118, .045
3.0	.074, .035	-.114, .053	-.064, -.090	.132, -.020
3.5	.092, -.005	-.070, .110	-.076, -.054	.111, -.084
4.0	.087, -.054	-.001, .134	-.075, -.024	.059, -.132
4.5	.056, -.096	.072, .118	-.065, -.004	-.014, -.144
5.0	.005, -.120	.127, .064	-.054, .004	-.088, -.129
5.5	-.054, -.116	.144, -.013	-.048, .003	-.145, -.077
	Present Results with 0.01% Damping ($Q_\alpha = Q_\beta = 5000$)			
0.0	-.027, .000	.106, .000	.159, .000	-.106, .000
0.5	-.032, .007	.088, -.061	.146, -.058	-.090, .058
1.0	-.033, .025	.037, -.102	.112, -.105	-.046, .099
1.5	-.021, .046	-.028, -.108	.062, -.133	.013, .112
2.0	.006, .060	-.087, -.077	.009, -.137	.073, .093
2.5	.041, .057	-.120, -.017	-.037, -.120	.115, .045
3.0	.073, .035	-.114, .053	-.068, -.090	.128, -.020
3.5	.092, -.006	-.071, .109	-.081, -.055	.107, -.084
4.0	.087, -.054	-.002, .134	-.078, -.024	.056, -.131
4.5	.057, -.096	.072, .117	-.066, -.004	-.015, -.149
5.0	.006, -.120	.127, .063	-.052, .004	-.087, -.129
5.5	-.054, -.115	.145, -.013	-.044, .003	-.142, -.077

Table 5.1

Comparison of the present solution with the contour integration solution for the response of a uniform half-space to a concentrated point force acting at the free surface.

The corresponding results for a nearly elastic half-space (0.01 % damping or material attenuation coefficients $Q_\alpha = Q_\beta = 5000$) using the present approach are also compiled in Table 5.1 and match Wong's results to near-perfect precision. This is an extremely convincing argument that the method of integration is highly reliable since the branch points are only shifted infinitesimally off the real wavenumber axis by the large material attenuation factors.

5.1.2 Comparison with Cagniard Approach (Pekeris and Lifson, 1957)

The comparison with Pekeris and Lifson (1957) extends the validation to the case of a concentrated vertical force applied at a depth z_s in the uniform half-space. The time-dependence of the applied force is represented by the Heaviside unit function and Poisson's ratio is taken to be 0.25. Pekeris obtains the exact motion of the surface of the elastic half-space in the time domain through use of Cagniard's method (1937). Therefore, the validation test is performed in the time domain with the present results generated through Fourier synthesis as described in section 4.2.9.

Figure 5.1 displays Pekeris and Lifson's results for the vertical component of displacement at various epicentral ranges, r, as a function of dimensionless time $\tau = \bar{\beta}t/\sqrt{r^2 + z_s^2}$. The arrivals marked P, S, and R correspond to the compressional, shear, and Rayleigh waves, respectively; the arrivals marked SP correspond to the diffracted wave which starts as S and upon reaching the surface is converted into P (for epicentral distances beyond the critical distance of $z_s/\sqrt{2}$).

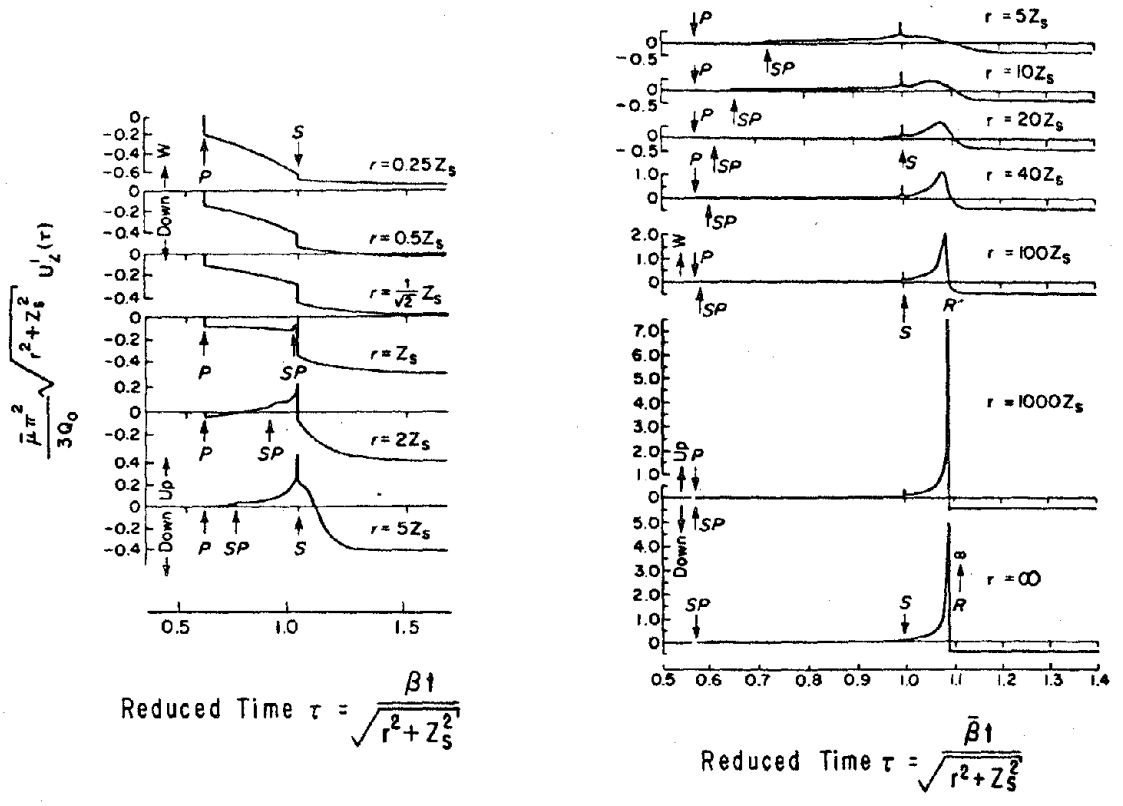

Figure 5.1. Pekeris-Cagniard solution for the vertical displacement components at the free surface due to a concentrated vertical force buried in a uniform half-space (Pekeris, 1957). Results are displayed as a function of dimensionless time and should be compared to present solution in Figure 5.2.

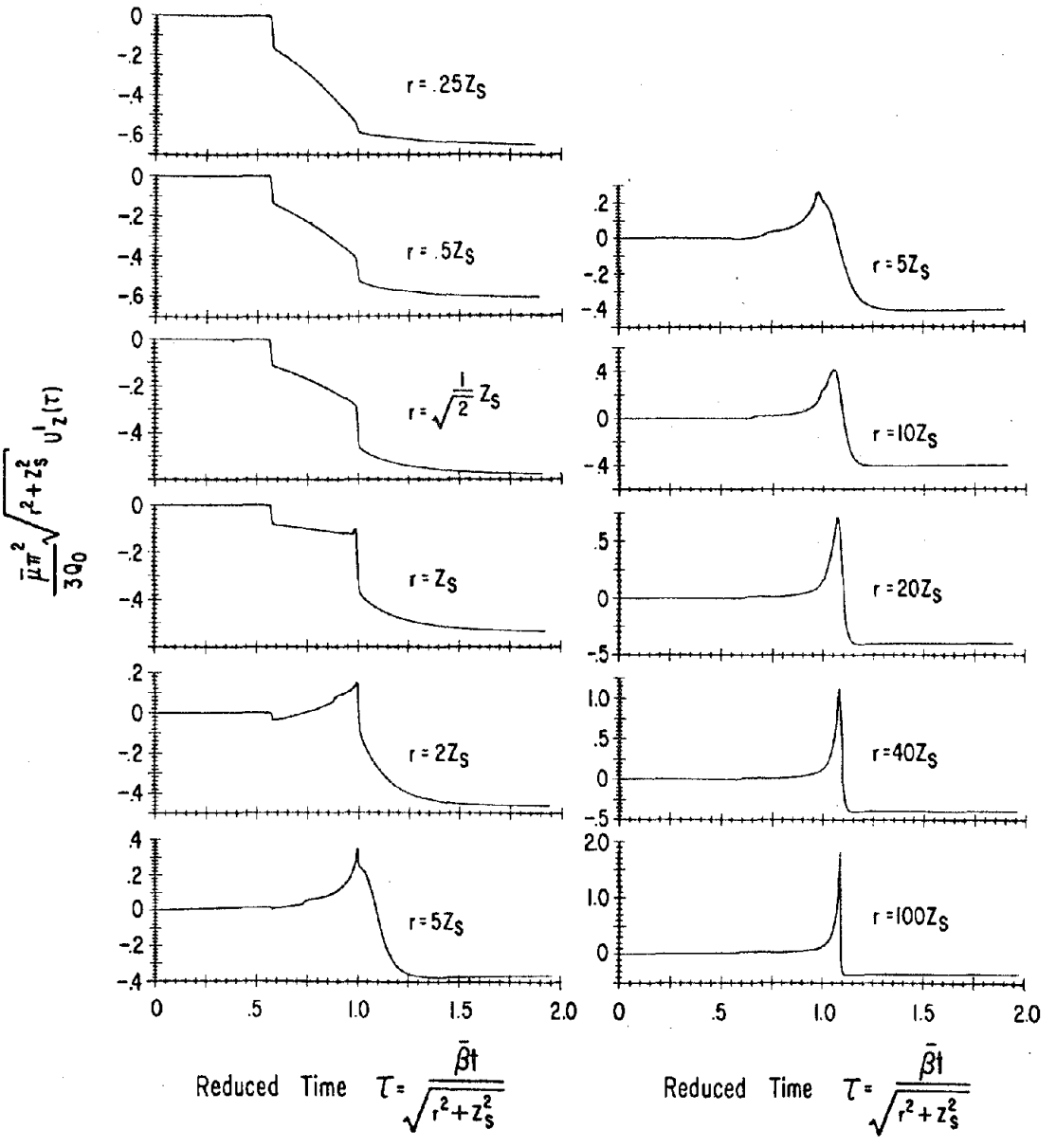

Figure 5.2. Present solution for the vertical displacement components at the free surface due to a concentrated vertical force buried in a uniform half-space. Results are displayed as a function of dimensionless time and should be compared to the Pekeris-Cagniard solution in Figure 5.1.

The high-frequency prominence of the Rayleigh wave for large values of r/z_s is deceptively exaggerated by the reduced time scale.

The analogous results obtained with the present method for a nearly elastic half-space ($Q_\alpha = 1000$, $Q_\beta = 500$) are shown in Figure 5.2. Owing to the difficulties associated with obtaining the original figures of Pekeris and Lifson, the plots are not to the identical scale and hence are displayed separately. Also, due to the reduced time parameter, it was necessary to continue the calculations out to extremely high frequencies to match the resolution for epicentral ranges less than $5z_s$ (left-hand column). Therewith, it may be stated that the match with Pekeris and Lifson's exact solution is once again of near-perfect precision. The only deficiency prevalent is the lack of acuity of the S-wave arrival at $\tau = 1$ in the right-hand column where the ultra-high frequency resolution was not pursued.

5.1.3 Comparison with Cagniard-deHoop Approach (Johnson, 1974)

In this subsection, the free surface displacements due to a buried double couple in a uniform half-space obtained by the present method are checked against the complete solution obtained by the Cagniard-deHoop method (Johnson, 1974). As described in Appendix IV, the Knopoff-deHoop (1958) representation theorem is used in conjunction with the present method to reciprocally generate the surface motion due to a buried dislocation by suitably combining the stress tensor solution evaluated at the depth of the source for a point force acting at the free surface.

The source time dependence is represented by an eight second ramp function and Poisson's ratio is taken to be 0.25. The attenuation factors used in the present solution are the same as in the previous validation study. The depth of the point dislocation is 5 km and the epicentral distance is 20 km. The surface displacements are evaluated at an observation azimuth of 22.5 degrees from the strike of the fault, and are normalized by the shear modulus $\bar{\mu}$ times 10^{10} cm^2 divided by the source moment M_o.

Six different fundamental orientations of the buried point dislocation are considered in Figures 5.3 through 5.8, respectively. A side view of the idealized fault dislocation appears adjacent to the comparative results in each figure. The vector $\vec{\nu}$ defines the normal to the fault and the vector $\vec{a}$ is the product of the slip vector times the fault area. If $\vec{\nu}$ points from the negative to the positive side of the fault, then $\vec{a}$ represents the displacement of the positive side relative to the negative side.

The upper, center, and lower curves in each figure correspond, respectively, to the horizontal displacement component along the direction of the nodal plane, the vertical displacement component, and the horizontal displacement component recorded 90 degrees from the nodal plane. The three displacement components are plotted to the scale appearing on the left and are displayed as a function of real time. The results obtained by the Cagniard-deHoop method are distinguished from the present results by the dots. Once again, as in the previous two validation studies, the comparisons are of near-perfect precision for

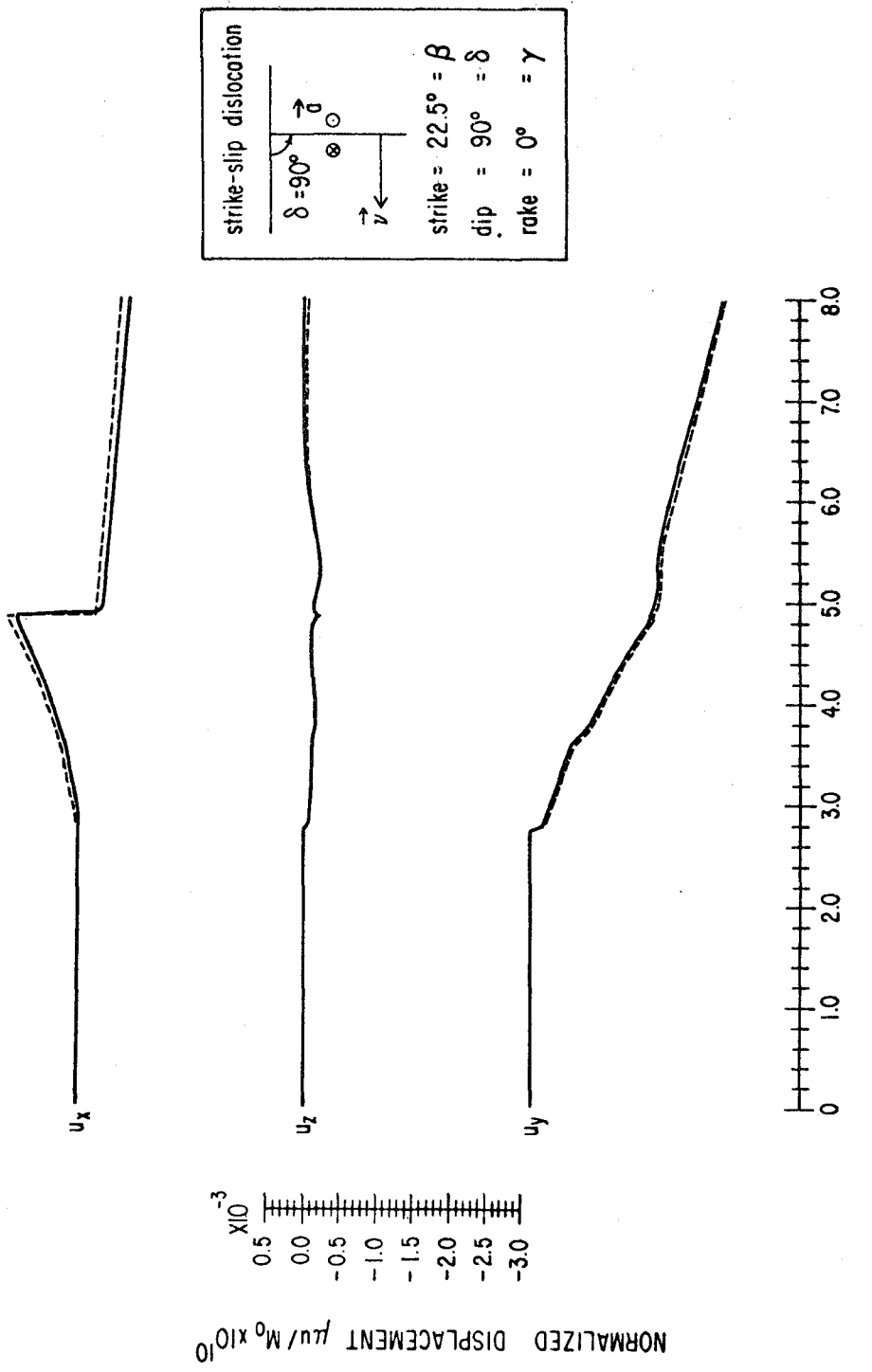

Figure 5.3. Comparison of the present solution with the Cagniard-deHoop solution for the response of a uniform half-space to a buried strike-slip dislocation with 90° dip (Johnson, 1974).

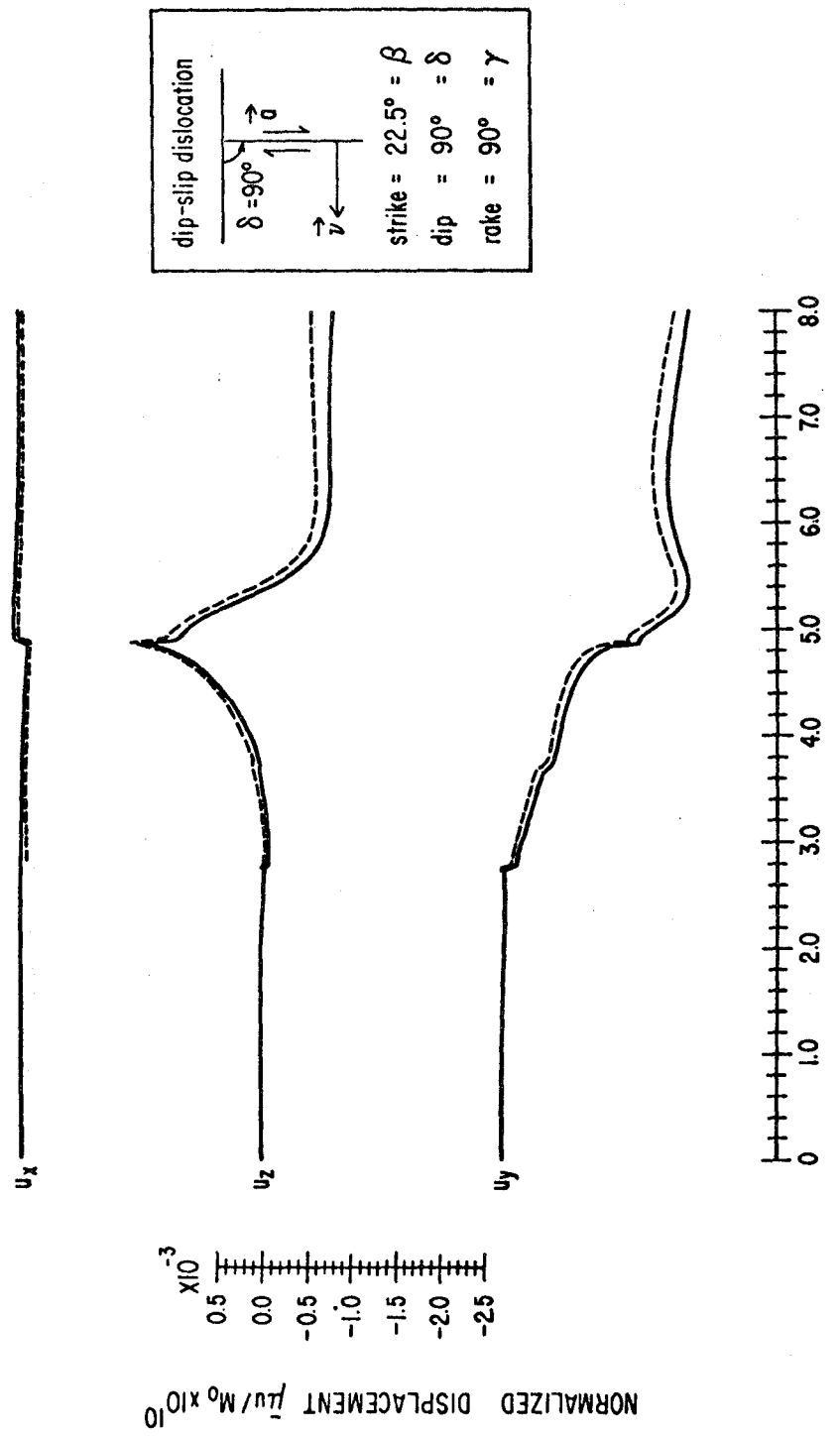

Figure 5.4. Comparison of the present solution with the Cagniard-deHoop solution for the response of a uniform half-space to a buried dip-slip dislocation with 90° dip (Johnson, 1974).

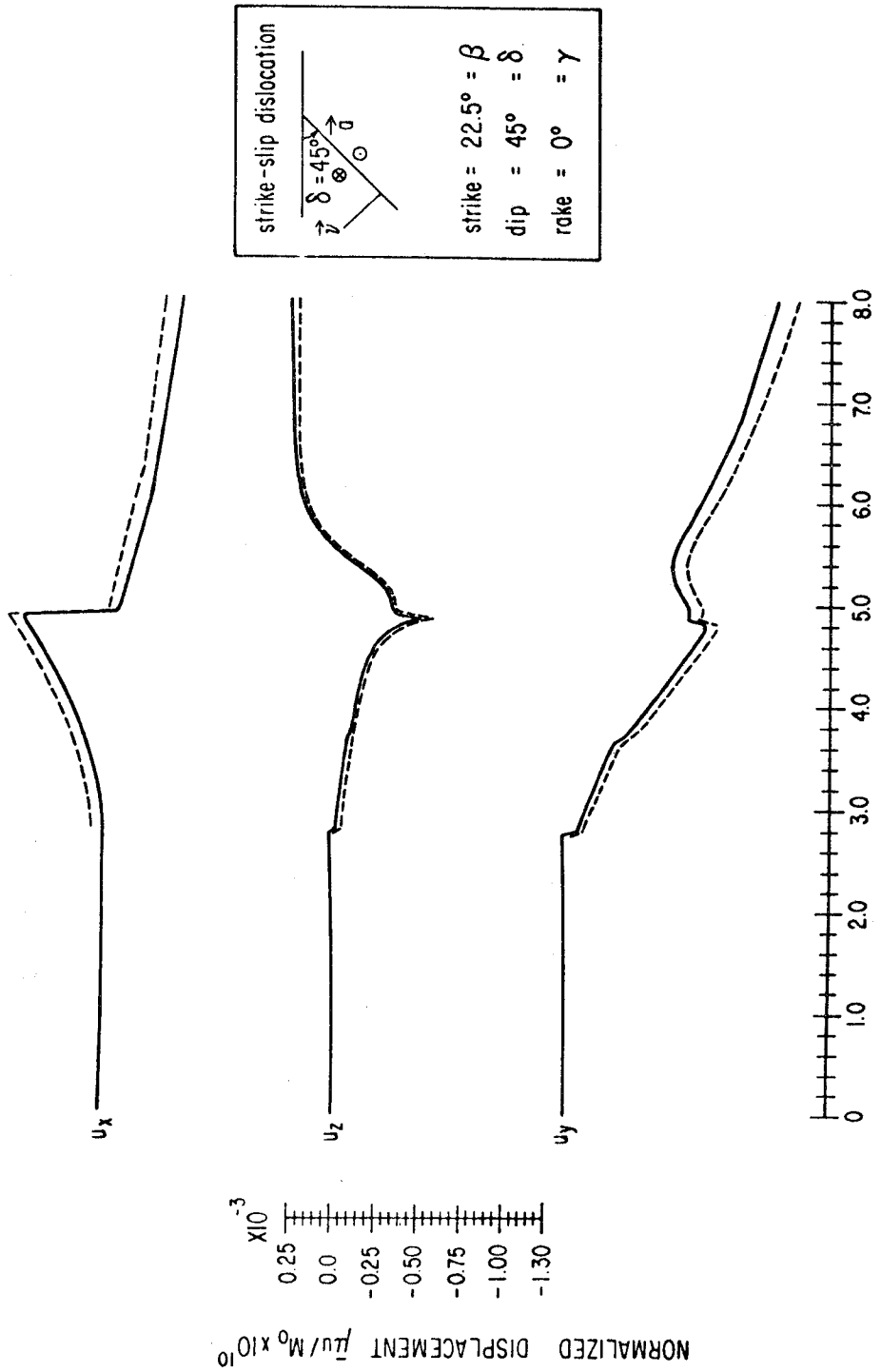

Figure 5.5. Comparison of the present solution with the Cagniard-deHoop solution for the response of a uniform half-space to a buried strike-slip dislocation with 45° dip (Johnson, 1974).

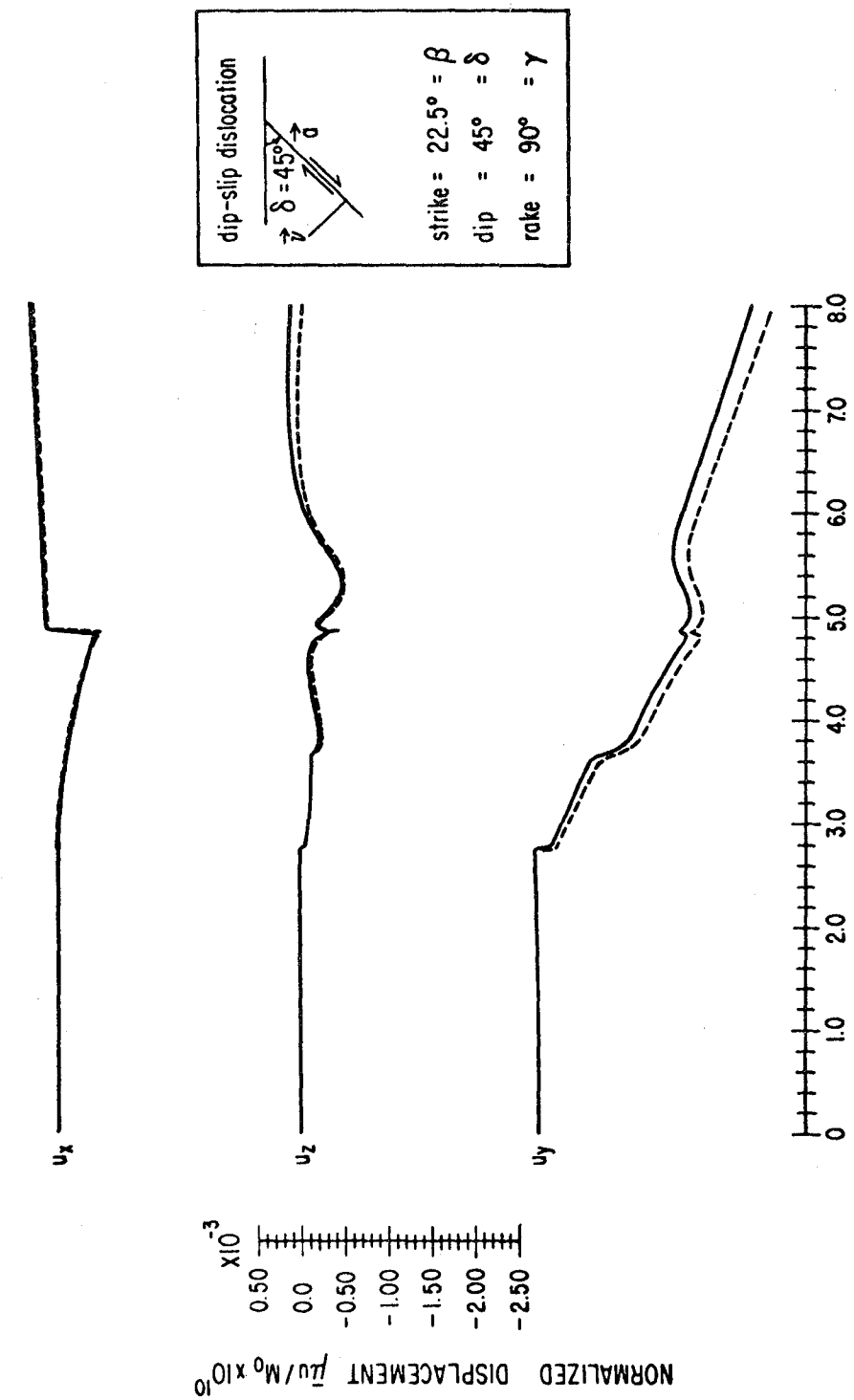

Figure 5.6. Comparison of the present solution with the Cagniard-deHoop solution for the response of a uniform half-space to a buried dip-slip dislocation with 45° dip (Johnson, 1974).

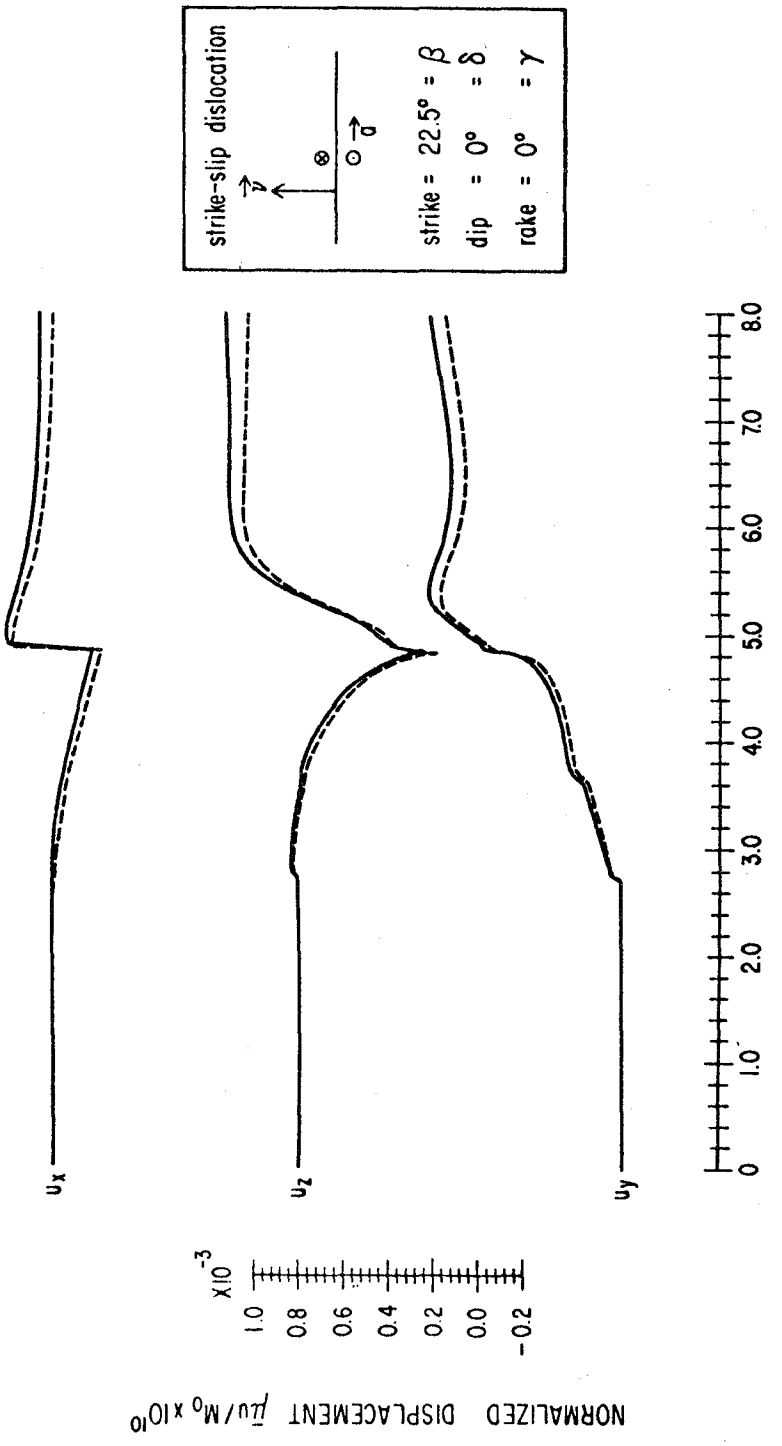

Figure 5.7. Comparison of the present solution with the Cagniard-deHoop solution for the response of a uniform half-space to a buried strike-slip dislocation with 0° dip (Johnson, 1974).

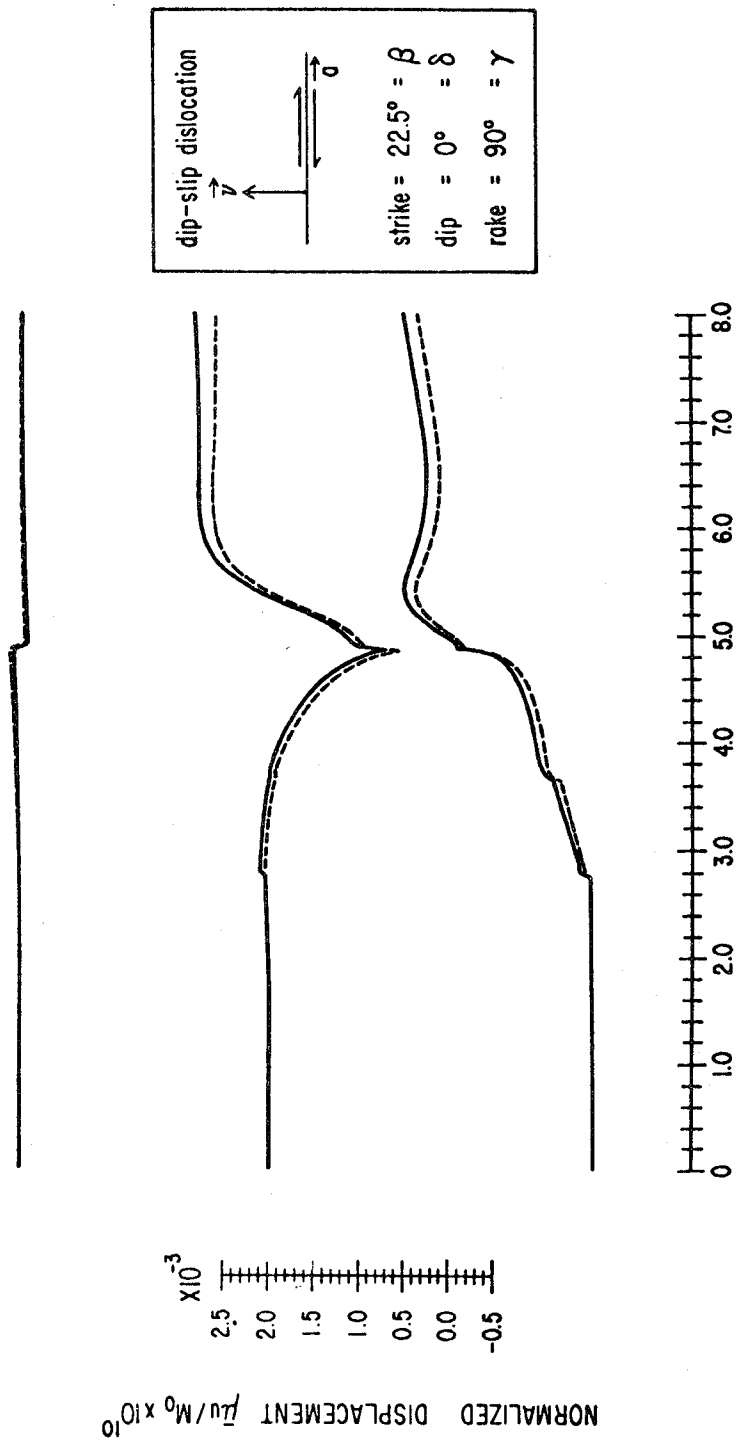

Figure 5.8. Comparison of the present solution with the Cagniard-deHoop solution for the response of a uniform half-space to a buried dip-slip dislocation with 0° dip (Johnson, 1974).

all components and all fault slip prescriptions. The slight differences at long time are probably related to having to doubly integrate the present results (i.e., to convolve with the ramp source function), whereas Johnson's results are obtained directly for the ramp time dependence.

In summary thus far, the comparisons with Wong (1975) and Pekeris and Lifson (1957) verify the accuracy of the displacements in a uniform half-space and the comparison with Johnson (1974) verifies the accuracy of the stresses in a uniform half-space. The following two subsections serve to substantiate the accuracy of the present solution for horizontally layered media.

5.1.4 Comparison with Finite Element Approach (Day, 1977)

The free surface displacements resulting from the action of a buried double couple source are tested once again, but now for the case of a horizontally layered Earth model. The model consists of two layers overlying a semi-infinite half-space as shown in Figure 5.9, where the individual parameters characterizing the layers are defined. The attenuation factors apply only to the present solution since the finite element solution (Day, 1977) contains no material attenuation.

Source depths of 5 km and 1 km are considered and the source time-dependence is represented by a ramp of one second duration in both cases. The source is equivalent to the vertical strike-slip dislocation depicted in Figure 5.3 with the receivers located at epicentral distances of 5, 15, 25 and 35 km at an azimuth of 22.5 degrees from the strike of the fault (in a dilatational quadrant). The ground motion is normalized by the ratio of the shear modulus in the source layer, μ, times 10^{10} cm^2

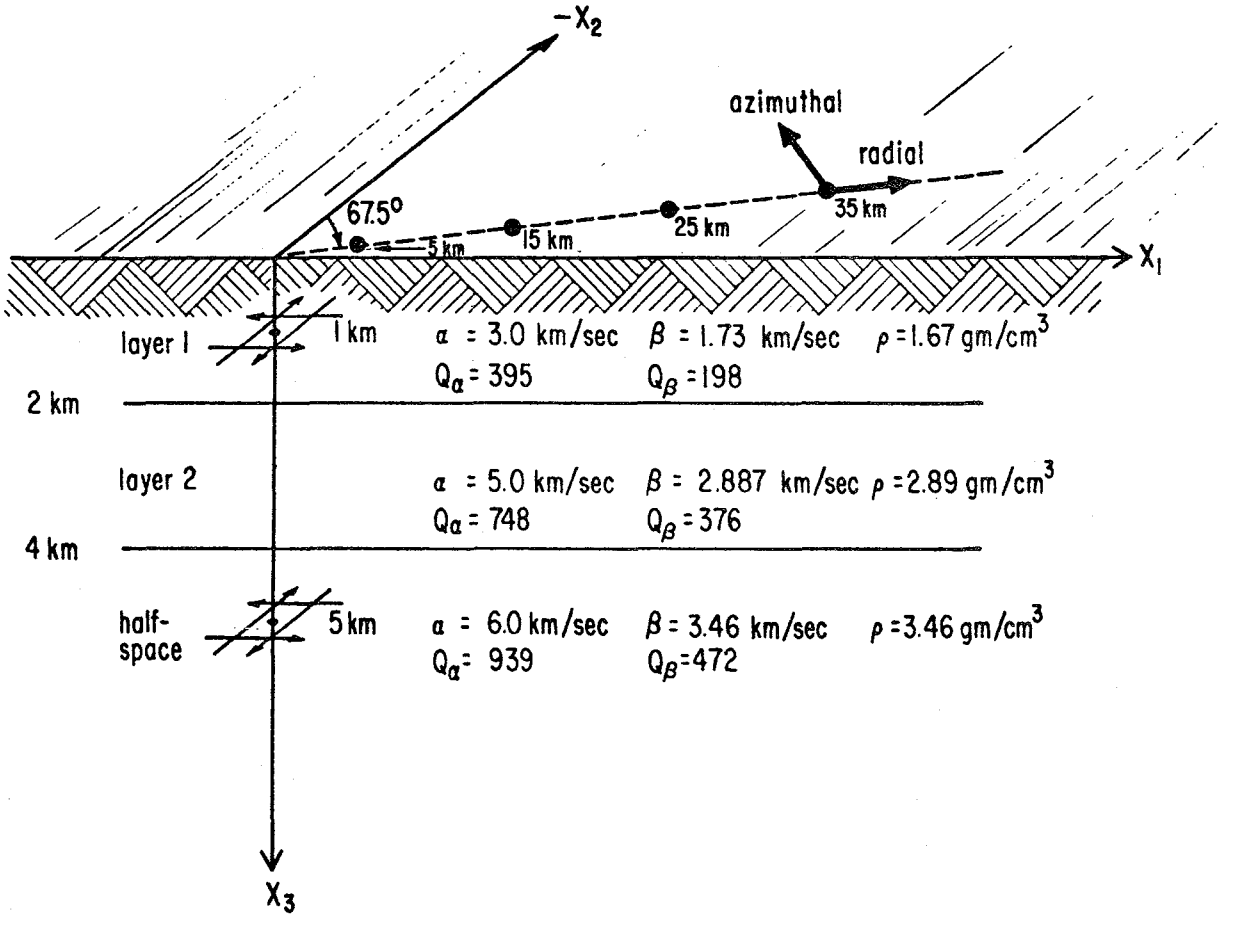

Figure 5.9. Source-receiver geometry and earth model, consisting of 2 layers overlying a half-space for use in comparison with the finite element solution.

to the source moment, M_o. The finite element results have been low-pass filtered down to 0.5 Hz to remove spurious numerical ringing; the present results are computed up to 5 Hz and passed through the same filter in order to maintain consistency in the comparisons.

The comparison to Day's (1977) finite element results for the deeper source is shown in Figure 5.10 at all four epicentral distances for the radial component of ground motion. The agreement is remarkable, especially in light of the vast differences between the two solution techniques. The slight deviations in phase have periods much lower than the expected resolution of two seconds (0.5 Hz). The comparison for the corresponding azimuthal component of motion is shown in Figure 5.11.

The results for the shallow source are displayed in Figures 5.12 and 5.13 for the radial and azimuthal components of motion, respectively. Once again, the match lends tremendous confidence in both methods of solution. It is interesting to notice that the peak amplitudes for the shallow source are approximately 50% larger than those for the deeper source.

What appears to be a late time phase lag in the finite element results is attributable to the numerical dispersion of the finite element grid. The origin of this trend in the finite element solution is further verified in the subsequent validation test with the discrete wavenumber/ finite element method (Olson, 1978).

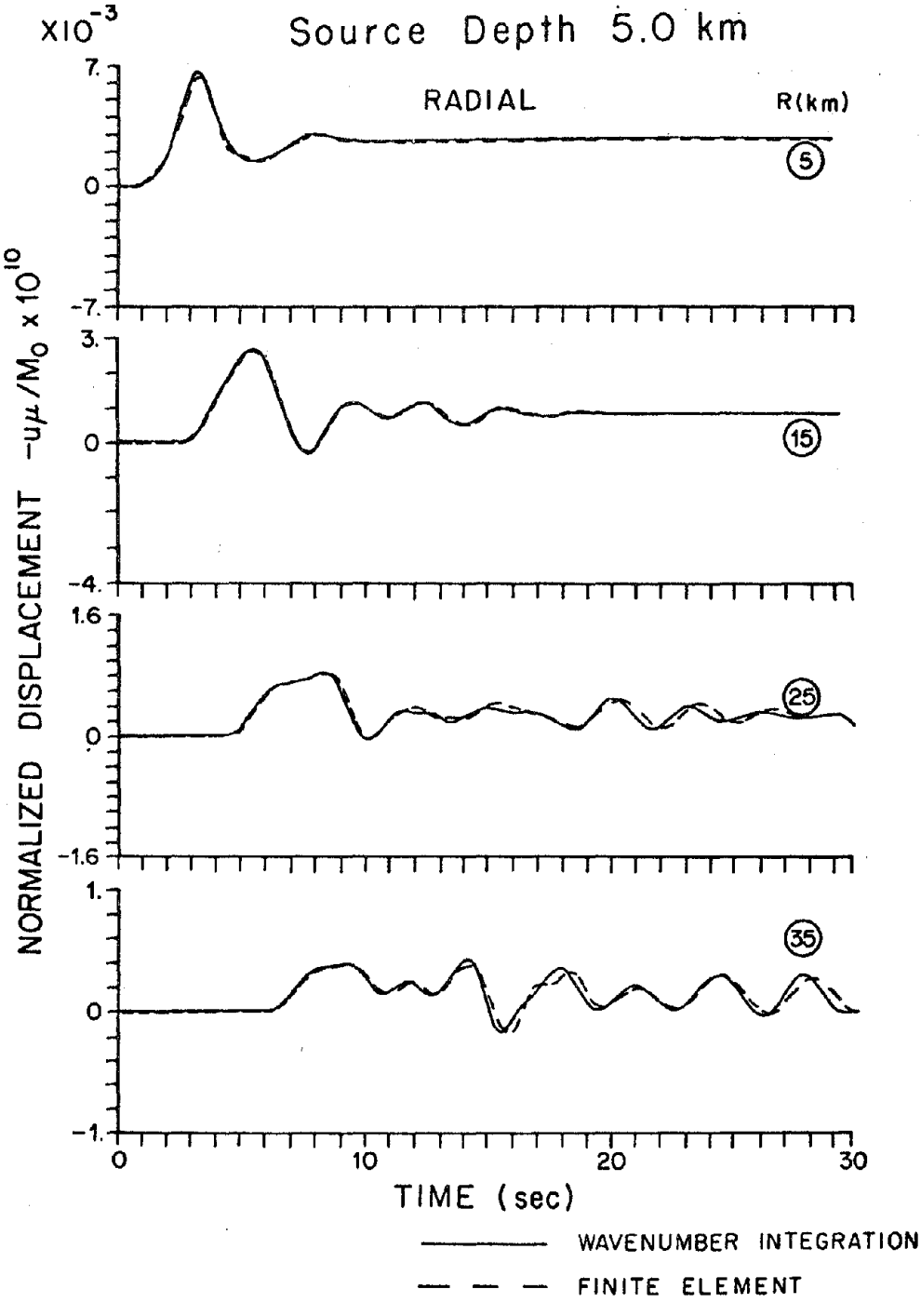

Figure 5.10. Comparison of the present solution with the finite element solution (Day, 1977) for the radial displacement component at the free surface due to a vertical strike-slip dislocation buried at a depth of 5 km in the earth model depicted in Figure 5.9.

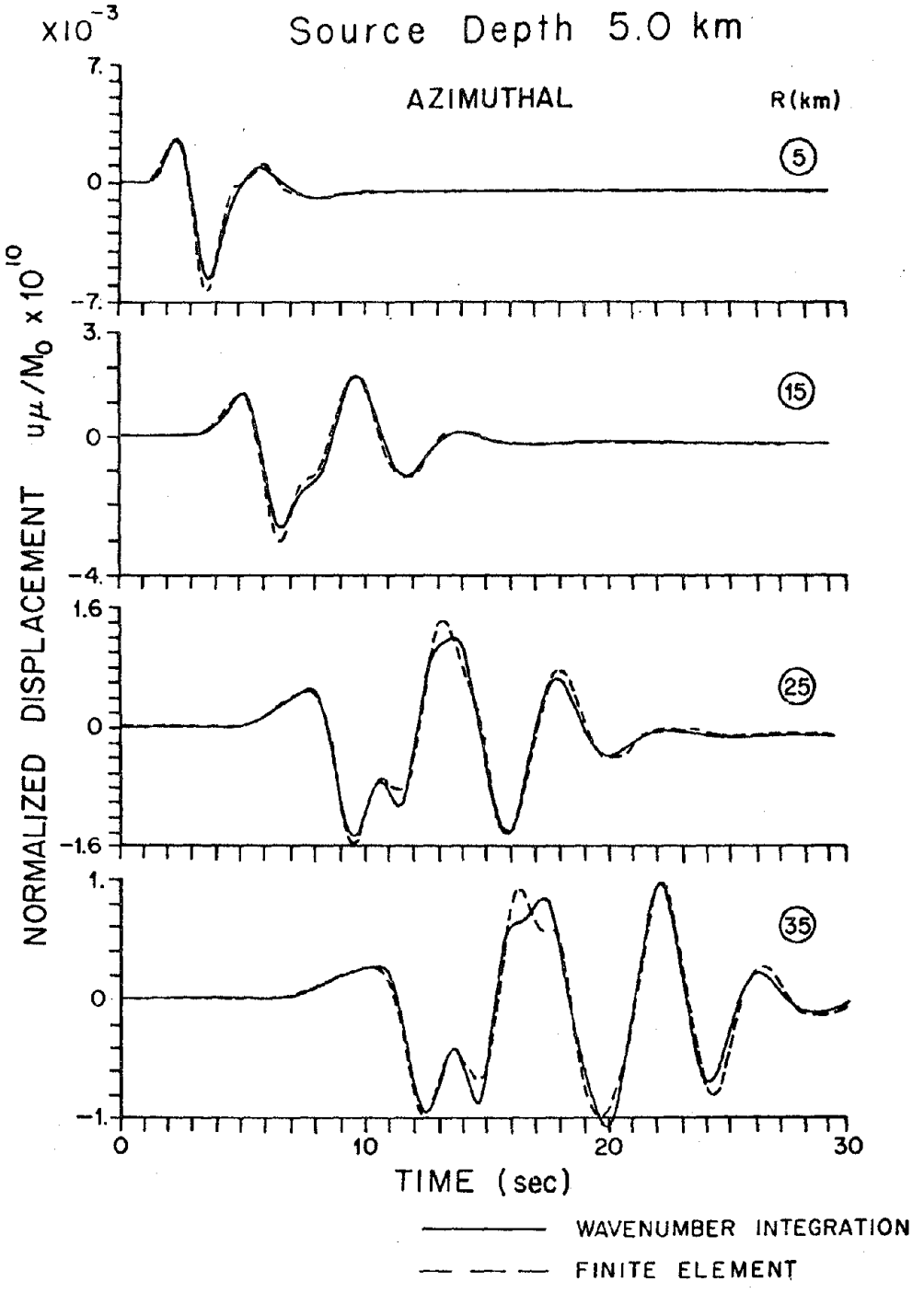

Figure 5.11. Corresponding comparison to Figure 5.10 for the azimuthal displacement component with the source buried at 5 km.

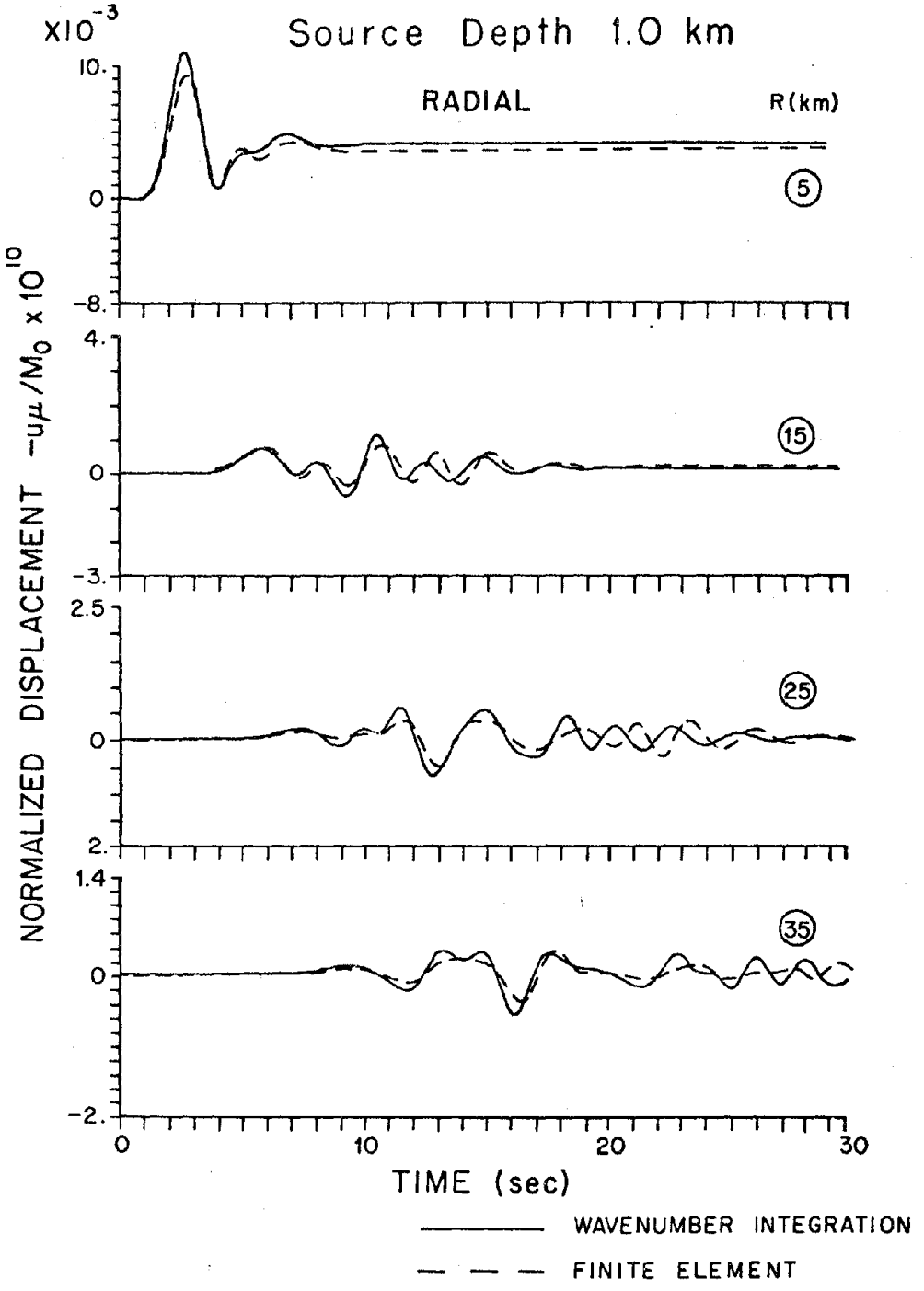

Figure 5.12. Corresponding comparison to Figure 5.10 for the radial displacement component with the source buried at 1 km.

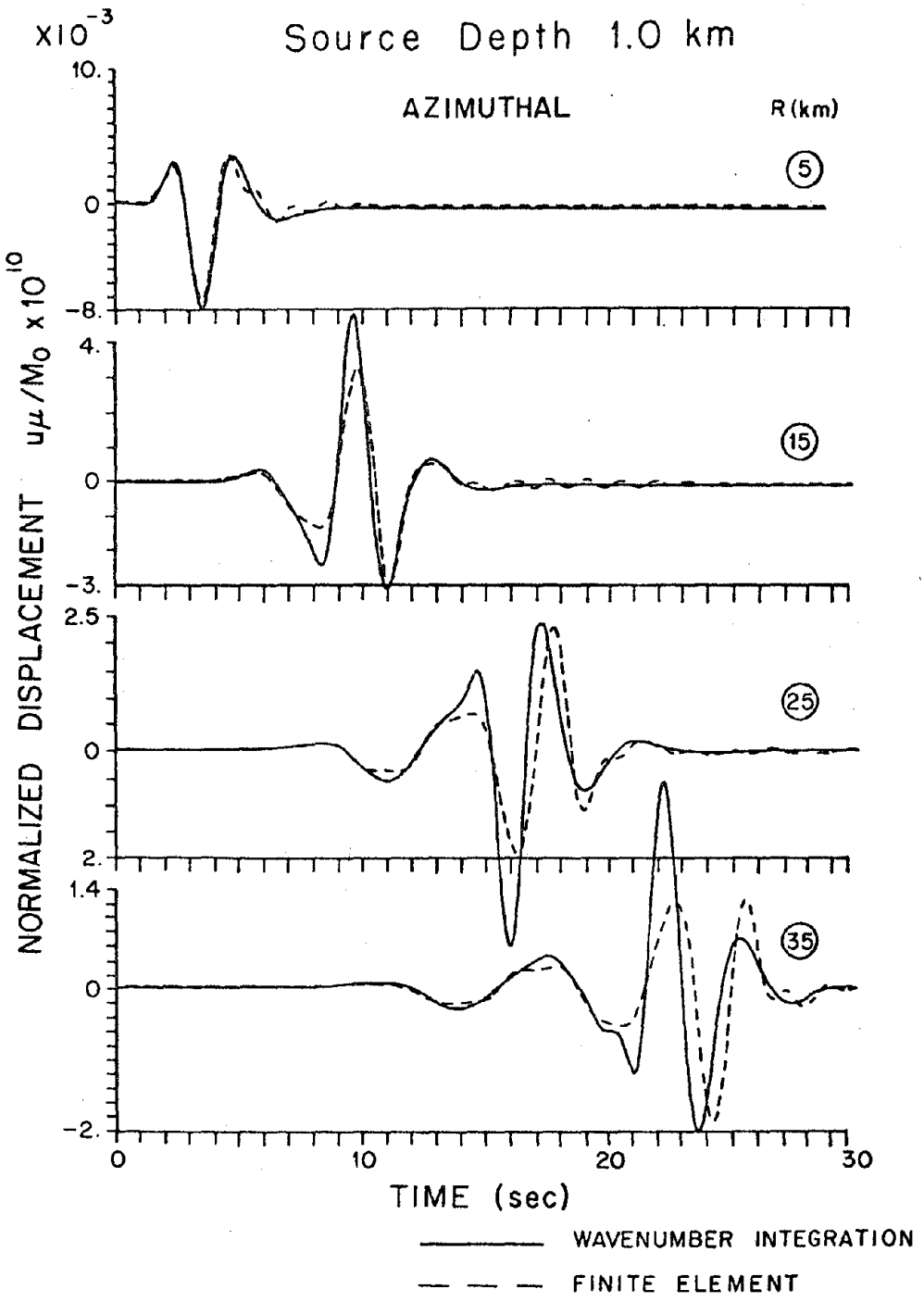

Figure 5.13. Corresponding comparison to Figure 5.10 for the azimuthal displacement component with the source buried at 1 km.

5.1.5 Comparison with Discrete Wavenumber/Finite Element Approach (Olson, 1978)

In this final validation study, the comparison of the previous subsection is repeated with the discrete wavenumber/finite element method (Olson, 1978). Only the 5 km source depth is considered and the comparisons for all three components of ground motion at epicentral distances of 5, 15, 25, and 35 km appear in Figures 5.14, 5.15, 5.16, and 5.17, respectively. Day's (1977) finite element results for the radial and azimuthal components of motion are also included in the figures. Once again, the agreement is superb and the phase coherence is nearly perfect.

Olson's discrete wavenumber/finite element method more closely resembles the present method than Day's finite element method in that the radial dependence is handled analytically through separation of variables. The major differences are: 1) the dependence with depth is calculated using a one-dimensional finite element treatment instead of the closed form facterization of the present method; 2) the response is transformed out of the wavenumber domain through Bessel series rather than direct integration; and 3) the procedure is performed explicitly in the time domain with no provision for material attenuation. When the wavelengths of interest are shorter than the changes in the geology as a function of depth, then Olson's method becomes less efficient than the direct integration method.

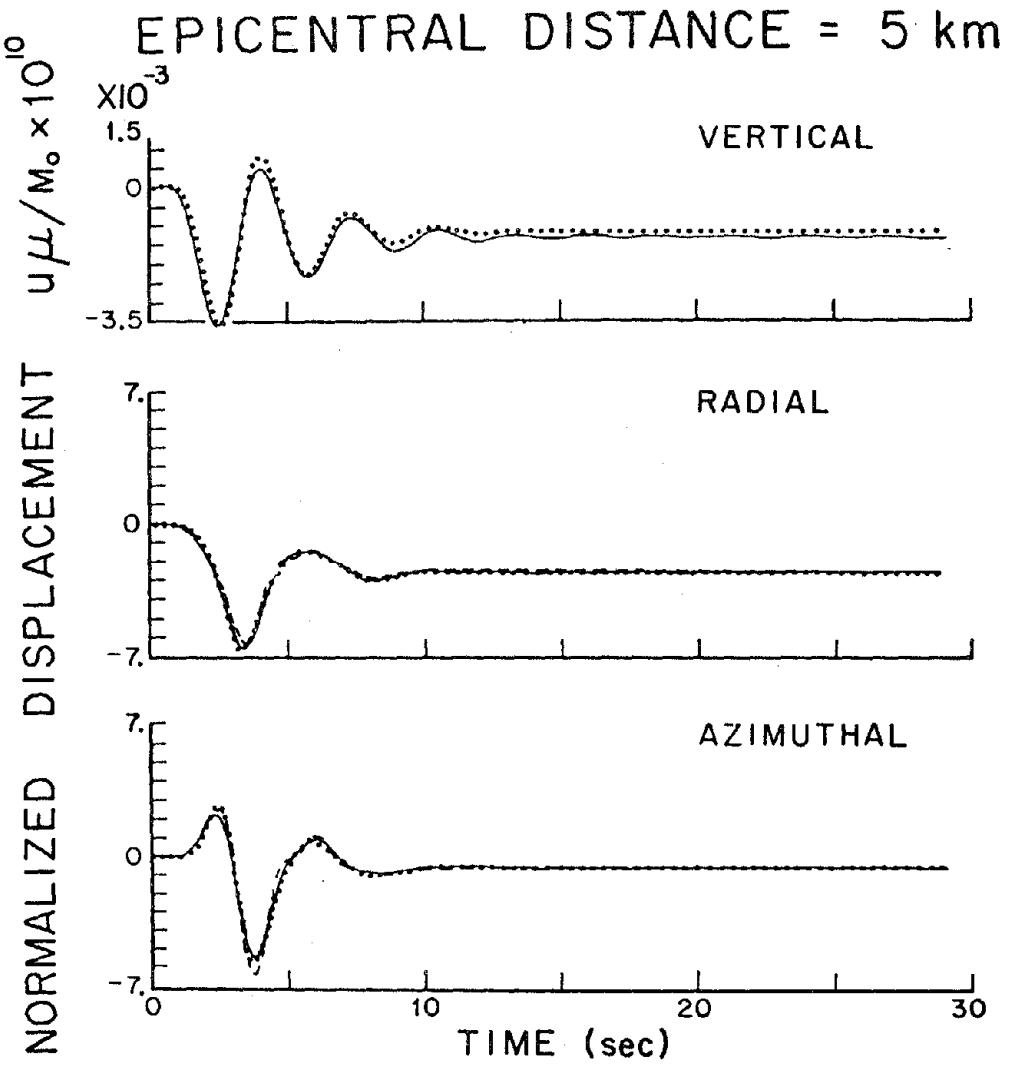

Figure 5.14. Comparison of the present solution with the discrete wavenumber/finite element solution (Olson, 1978) for the free surface displacement components at an epicentral distance of 5 km due to a vertical strike-slip dislocation buried at a depth of 5 km in the earth model depicted in Figure 5.9.

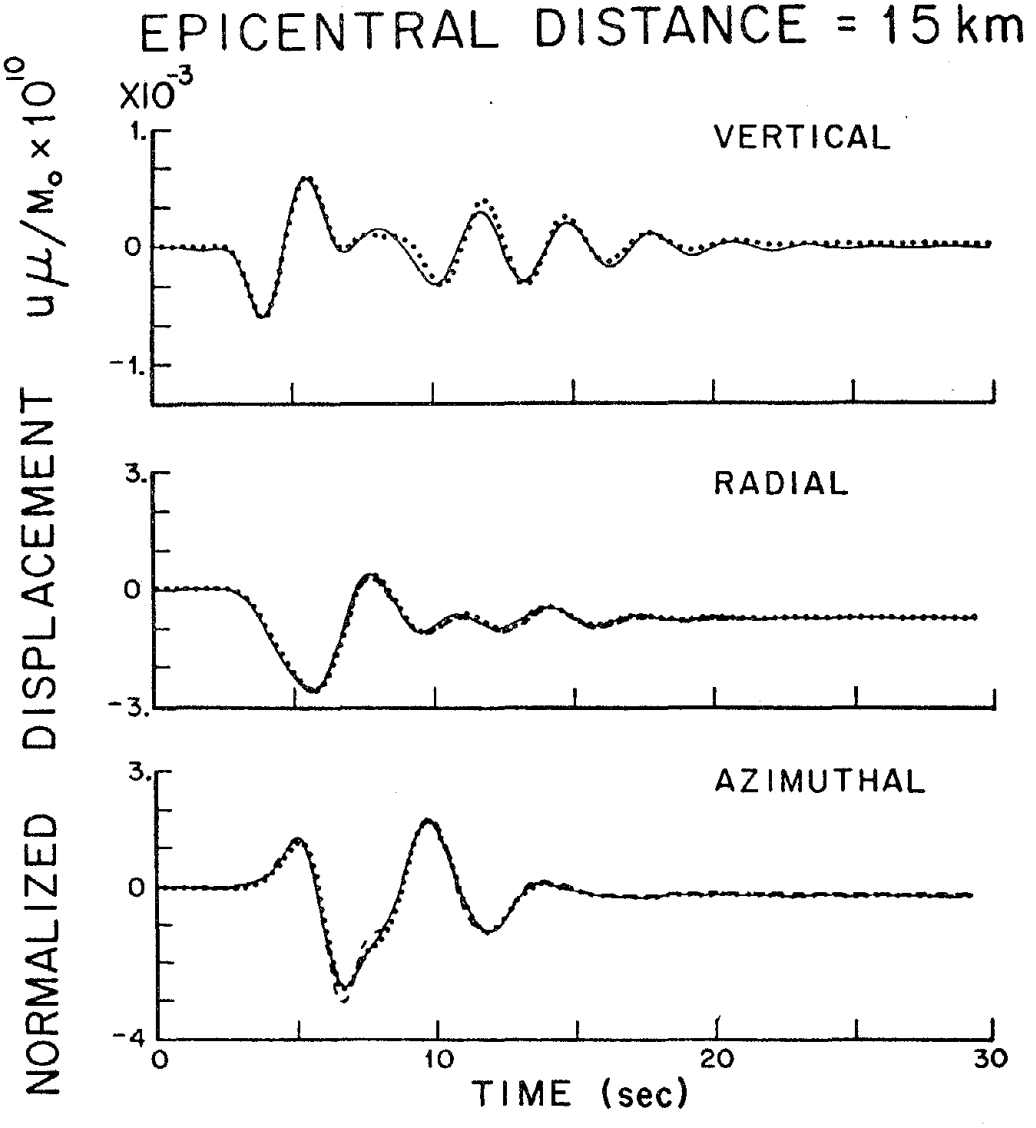

——— DISCRETE WAVENUMBER / FINITE ELEMENT (Olson)

····· WAVENUMBER INTEGRATION (Apsel)

- - - - - 3-D FINITE ELEMENT (Day, 1977)

Figure 5.15. Corresponding comparison to Figure 5.14 for the free surface displacement components at an epicentral distance of 15 km.

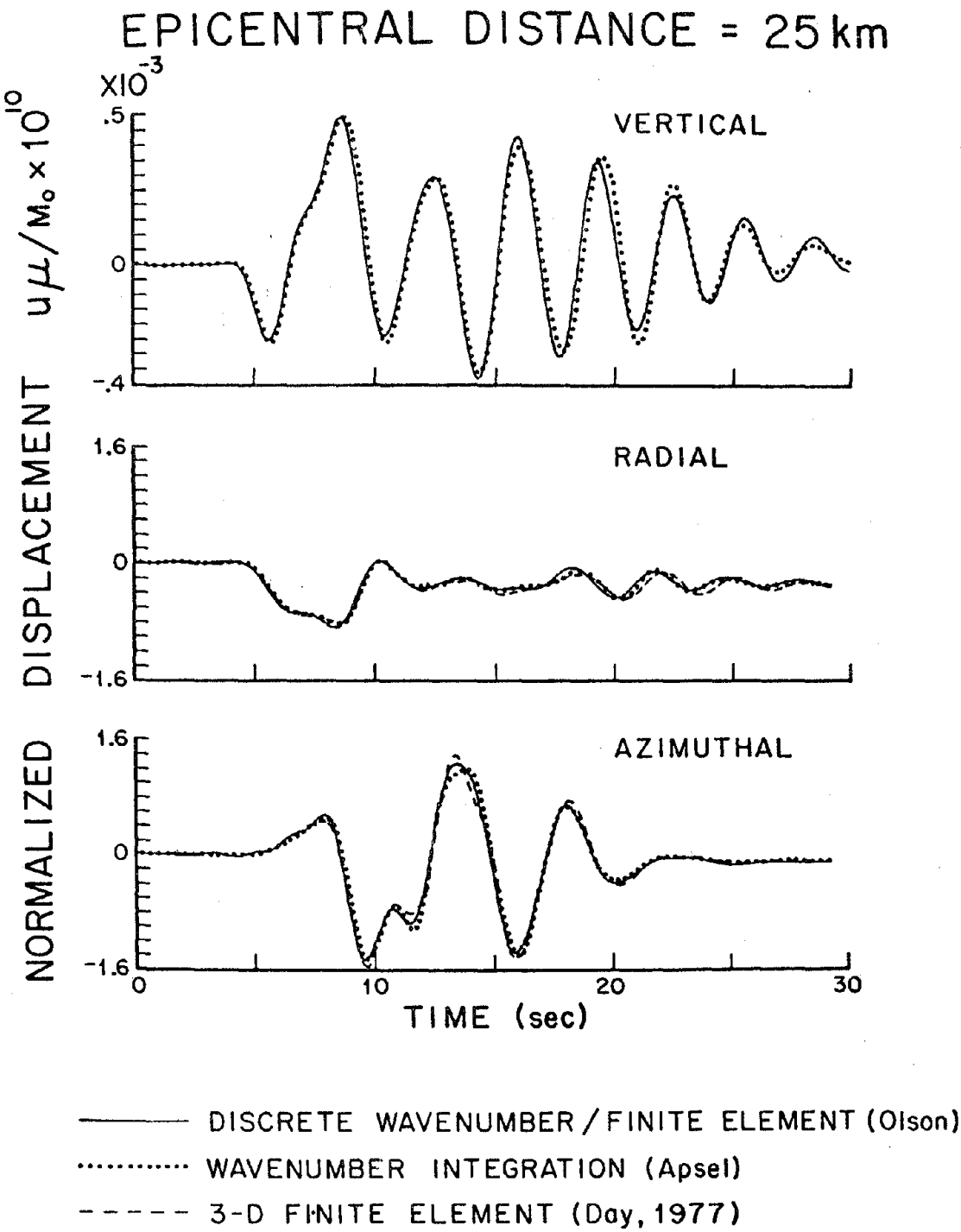

Figure 5.16. Corresponding comparison to Figure 5.14 for the free surface displacement components at an epicentral distance of 25 km.

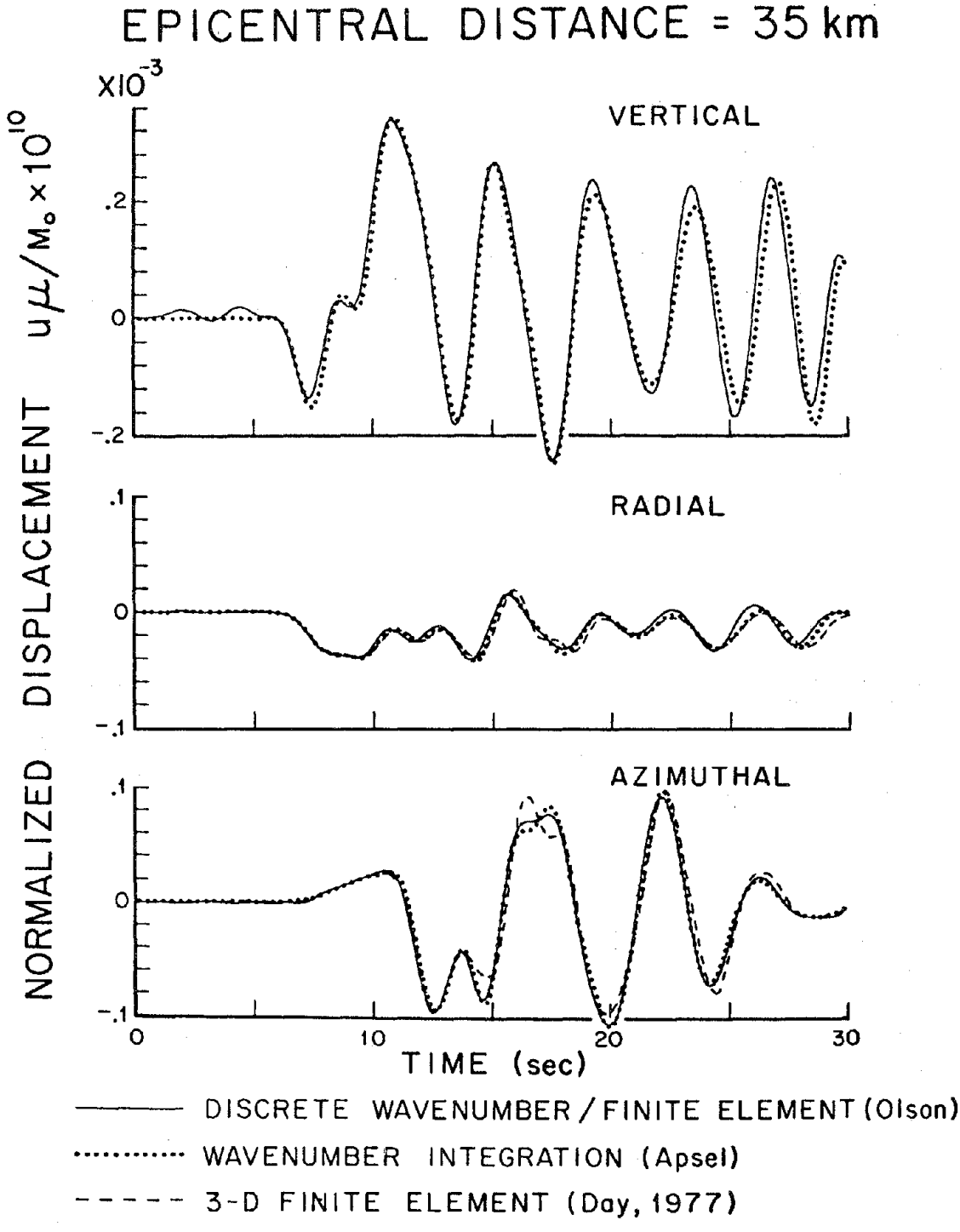

Figure 5.17. Corresponding comparison to Figure 5.14 for the free surface displacement components at an epicentral distance of 35 km.

5.2 COMPARISONS

The validation studies of the previous section (i.e., comparisons with known complete solutions) are complemented in this section by two comparative studies with known partial solutions (i.e., comparisons with solutions which include assumptions and/or approximations). Comparisons to results obtained using a generalized ray technique and to results obtained using a surface wave approach are undertaken in the two studies.

5.2.1 Comparison to Generalized Ray Techniques

In the generalized ray technique (Helmberger, 1974), the time-dependent wave field for a layered medium is decomposed into contributions attributed to an infinite set of rays travelling from the source to an individual receiver. Each ray contribution can be evaluated exactly by the Cagniard-deHoop technique (1939, 1960). However, the number of rays selected is invariably limited by the computational difficulties associated with finding the separate Cagniard paths for every point on the contour and for each kinematic group (rays with same travel time), for all source-receiver pairs. To reduce the cost for the comparisons, certain approximations are used in connection with the Bessel functions causing the generalized ray results to be least reliable at short distances and long periods. Also, differences can be expected in the decay of certain waves with distance since the generalized ray results include no material attenuation.

The soil model employed for the comparison consists of a single layer overlying a semi-infinite half-space as shown in Figure 5.18, where

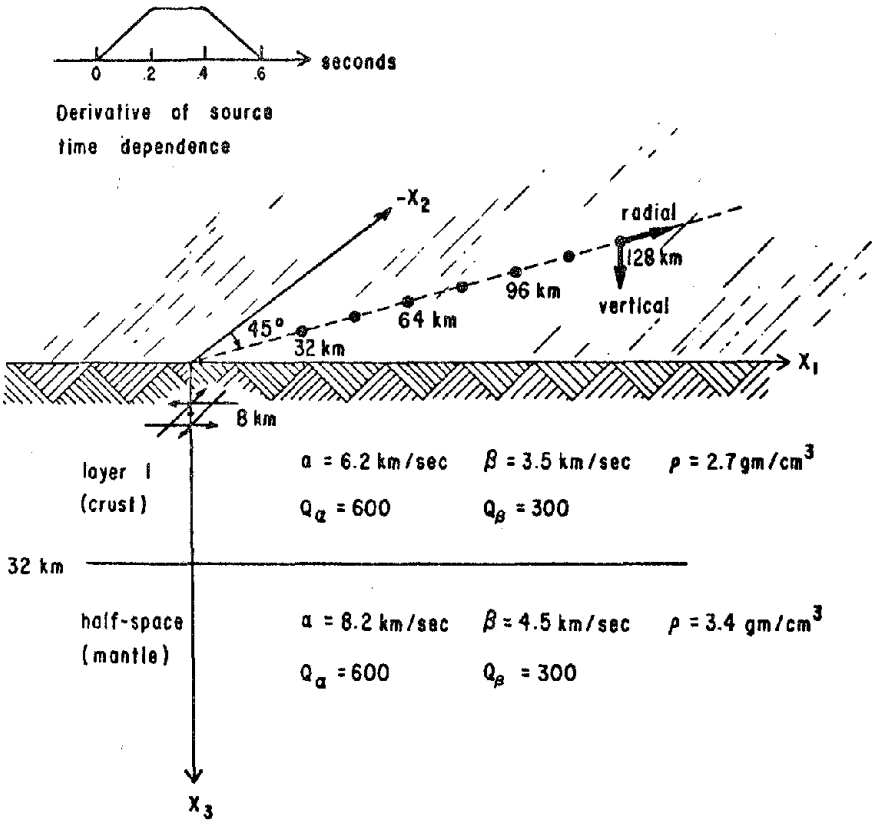

Figure 5.18. Source-receiver geometry and earth model, consisting of a 32 km thick crust overlying a half-space for use in comparison with the generalized ray solution.

the individual parameters characterizing the layers are defined (the specific attenuation factors apply only to the present solution). It is hoped that by representing the 32 km thick crust by a single layer, the generalized ray technique will be able to include a sufficient number of multiple reflections and interconversions to converge to the complete solution generated by the present approach.

The source depth is 8 km and the source time-dependence is a quadratic ramp defined by the time integral of the function appearing at the top of Figure 5.18. The source is equivalent to a vertical strike-slip dislocation; receivers are located at epicentral distances of 32, 48, 64, 80, 96, 112 and 128 km at an azimuth of 45 degrees from the strike (SH node) for the vertical and radial displacements and at an azimuth of 0 degrees from the strike (P-SV node) for the transverse displacements.

The generalized ray results (provided by Don Helmberger) are compared to the present results in Figures 5.19, 5.20 and 5.21 for the vertical, radial and transverse displacement components, respectively. The ground displacements are normalized by the ratio of the shear modulus in the source layer times 10^{10} cm^2 divided by the scalar moment of the source. The maximum amplitudes obtained by the respective techniques are self-scaled to fit within the same height on each figure and are shown above and below each seismogram. The time scales are shifted by a time correponding to the direct compressional arrival at each epicentral distance.

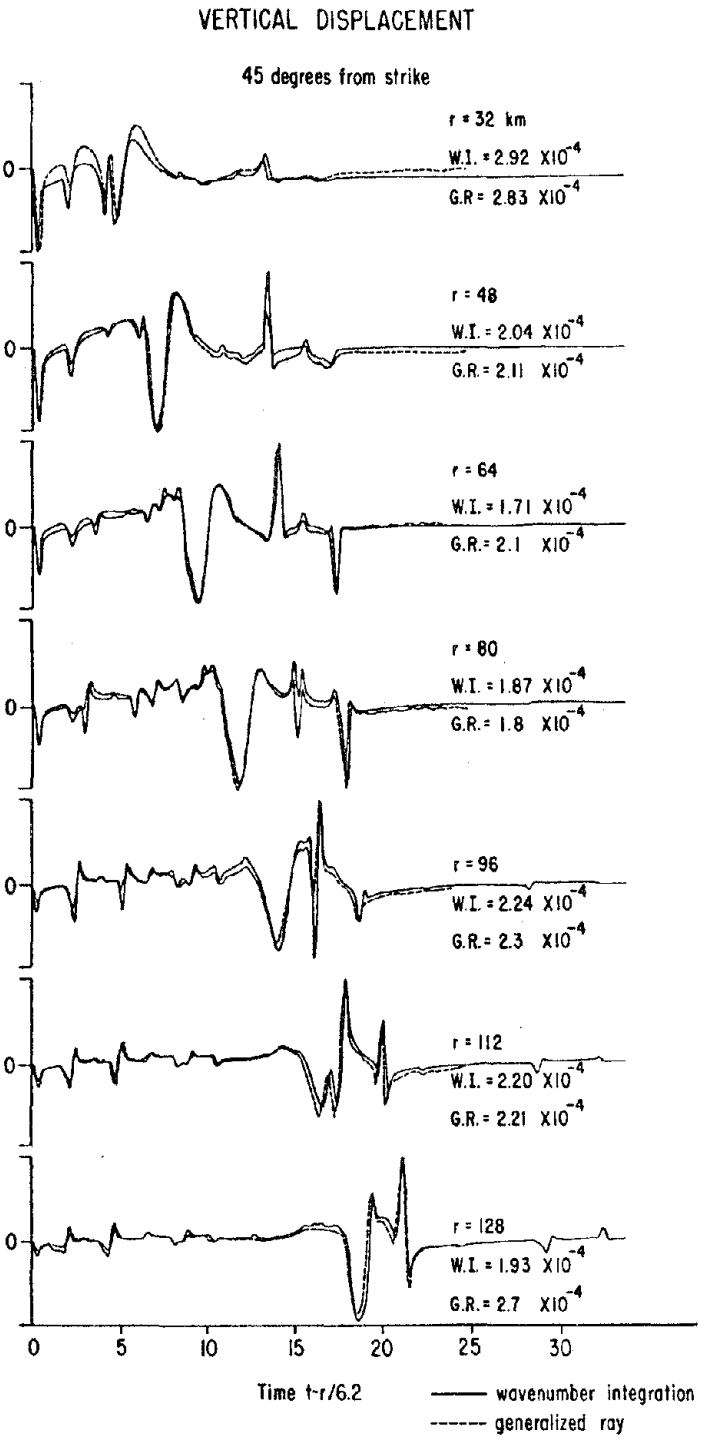

Figure 5.19. Comparison of the present solution with the generalized ray solution (Helmberger, 1974) for the vertical displacement component at the free surface due to a vertical strike-slip dislocation buried at a depth of 8 km in the earth model depicted in Figure 5.18.

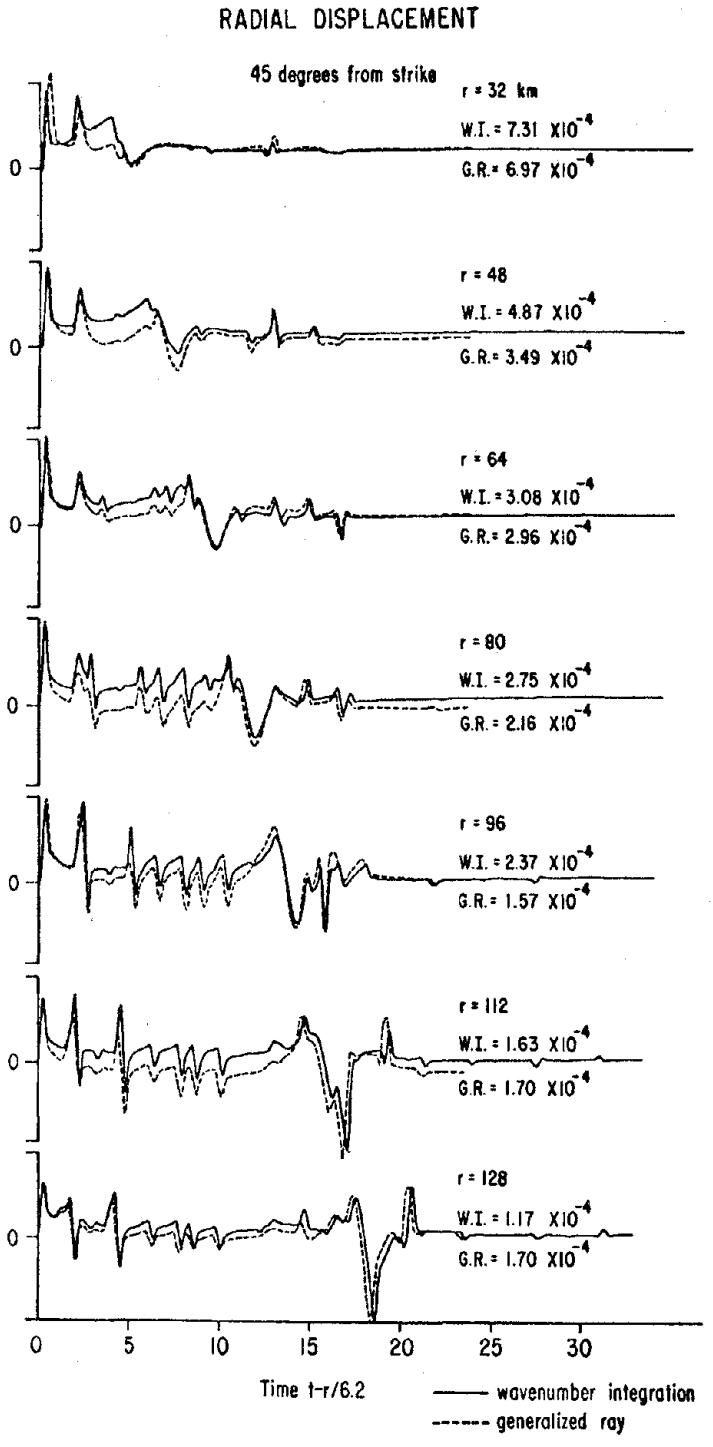

Figure 5.20. Corresponding comparison to Figure 5.19 for the radial displacement component.

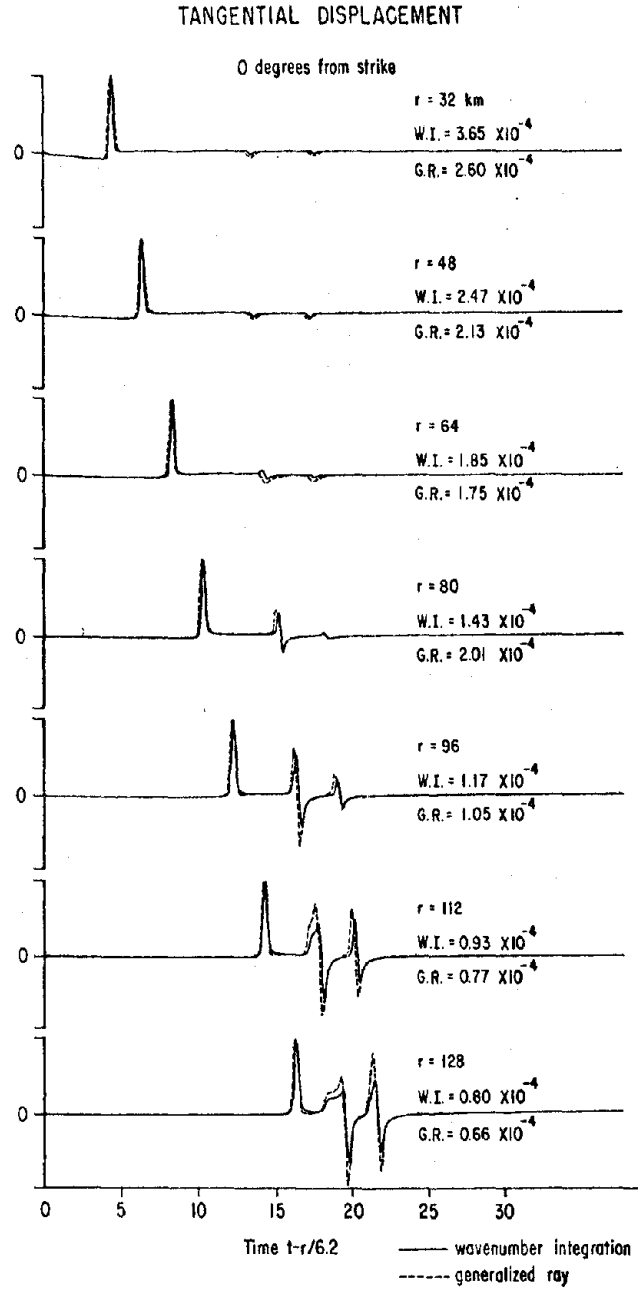

Figure 5.21. Corresponding comparison to Figure 5.19 for the azimuthal displacement component.

The phase coherence is nearly perfect at all epicentral distances considered for all three displacement components in Figures 5.19 through 5.21. Combined with the excellent overall agreement in amplitude, these results lend confidence in the generalized ray technique and further validate the present method. The deficiencies in amplitude at short distances in the generalized ray results are due to the approximations used in connection with the Bessel functions. The discrepancies in amplitude at the larger distances are probably related to the differences between using an elastic model versus a nearly elastic model (material attenuation factor of $Q_\beta = 300$ included in the present solution). Also, the convergence of the generalized ray expansion is impaired by the increased number of contributing rays at the larger epicentral distances. Finally, the discrepancies at long periods in the generalized ray technique are enhanced by the approximations made for the Bessel functions in the generalized ray calculation (especially in the radial displacements).

Several interesting features in the results merit discussion. In Figure 5.21, the contributions of the reflections beyond the critical angle are well illustrated. Beyond the distances at which the SmS and sSmS waves are critically reflected (69 and 89 km, respectively), the amplitudes of these critically reflected waves increase markedly. These waves eventually combine with other multiple reflections to form a dispersive Love wave. The direct SH wave decreases uniformly with distance according to a dependence of approximately r^{-1}. In Figures 5.19 and 5.20, the vertical and radial displacement records are more complicated since at an azimuth of 45 degrees from the strike they are excited by

P and SV waves emitted directly by the source as well as by the accompanying interconverted and multiply reflected waves.

In the next subsection, the present solution will be compared with both the generalized ray solution and a normal mode solution for epicentral distances between 100 and 1000 km for the same earth structure. The effect of using a Q_β of 10,000 versus a Q_β of 300 is also investigated at these epicentral distances.

5.2.2 Comparison to Normal Mode Technique (Harkrider, 1964, 1970)

The comparisons of the previous subsection are extended to the case of epicentral distances between 100 and 1000 km. The layered earth structure is the same as that depicted in Figure 5.18 except that attenuation factors of $Q_\beta = 10{,}000$ and $Q_\alpha = 20{,}000$ are used in the present solution so as to eliminate the predominant effects of damping for comparative purposes. The source is also the same as shown in Figure 5.18 except that the duration is 1.5 seconds instead of 0.6 second.

In addition to comparing with the generalized ray solution (Helmberger, 1974) at these larger distances, the present solution is matched against a solution constructed by superposition of surface-wave modes (Harkrider, 1964, 1970). Similar to the present method, the normal mode technique operates first in the frequency domain so that the number of layers offers no limitations. However, the increase in number of contributing modes with frequency restricts the practicability of the normal mode technique to frequencies lower than about 1 or 2 Hz. Also, the inadequacies of the normal mode solution for epicentral distances less than a few source depths (or for any problem in which the ground

motion is dominated by waves with relatively high horizontal phase velocities) are difficult to predict in general. For this problem, however, the normal mode solution is expected to provide a closer match to the complete wavenumber integration solution that the generalized ray solution since the surface waves will tend to dominate the ground motion at periods greater than 1 or 2 seconds.

The transverse displacements (SH-Love waves) are shown in Figure 5.22 for epicentral distances between 100 and 500 km and in Figure 5.23 for epicentral distances between 600 and 1000 km. The ground displacements for all three methods are normalized by the ratio of the shear modulus in the source layer times 10^{10} cm^2 divided by the scalar moment of the source. The maximum amplitudes obtained by the respective techniques are self-scaled to fit within the same height on each figure and are shown above each seismogram. The time scales are reduced by a time corresponding to the epicentral distance divided by the shear-wave velocity of the mantle, so as to align zero time with the first possible critically reflected arrival. The generalized ray and normal mode results are courtesy of Don Helmberger and David Harkrider, respectively.

As in the match to the generalized ray results at closer epicentral distances (see Figure 5.21), the phase coherence and amplitude agreement is superb. The somewhat larger time step in the normal mode calculations and the inadequate number of rays in the generalized ray calculation accounts for some of the amplitude discrepancies. Also, the modal superposition only includes the first five surface wave modes. The results in Figure 5.24 portray the transverse displacements (SH-Love

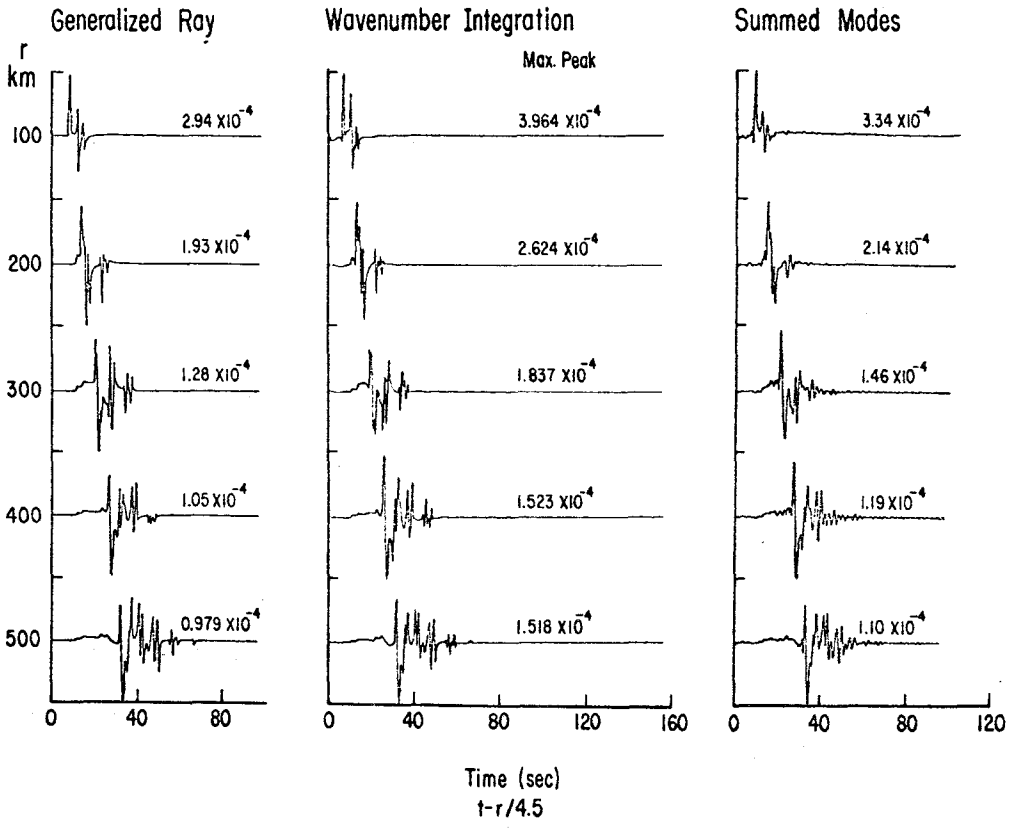

Figure 5.22. Comparison of the present solution with the summed normal mode solution (Harkrider, 1964) and the generalized ray solution (Helmberger, 1974) for the azimuthal displacement component at epicentral distances between 100 and 500 km due to a vertical strike-slip dislocation buried at a depth of 8 km in the earth model depicted in Figure 5.18.

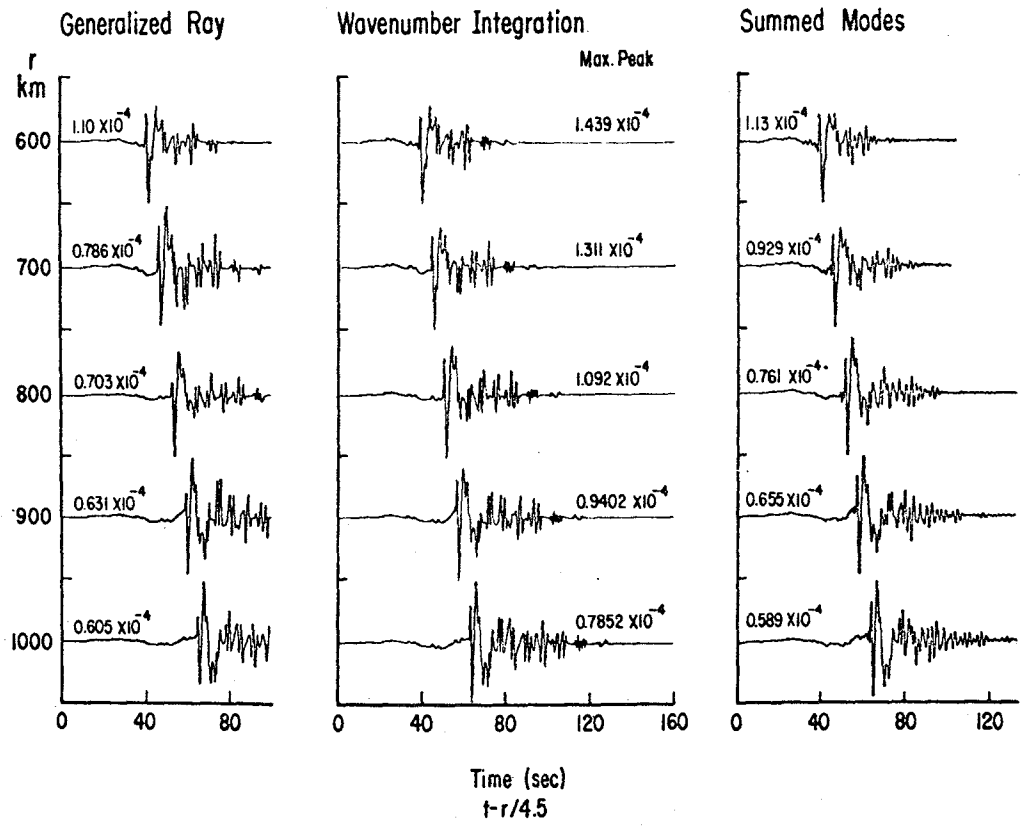

Figure 5.23. Corresponding comparison to Figure 5.22 for epicentral distances between 600 and 1000 km.

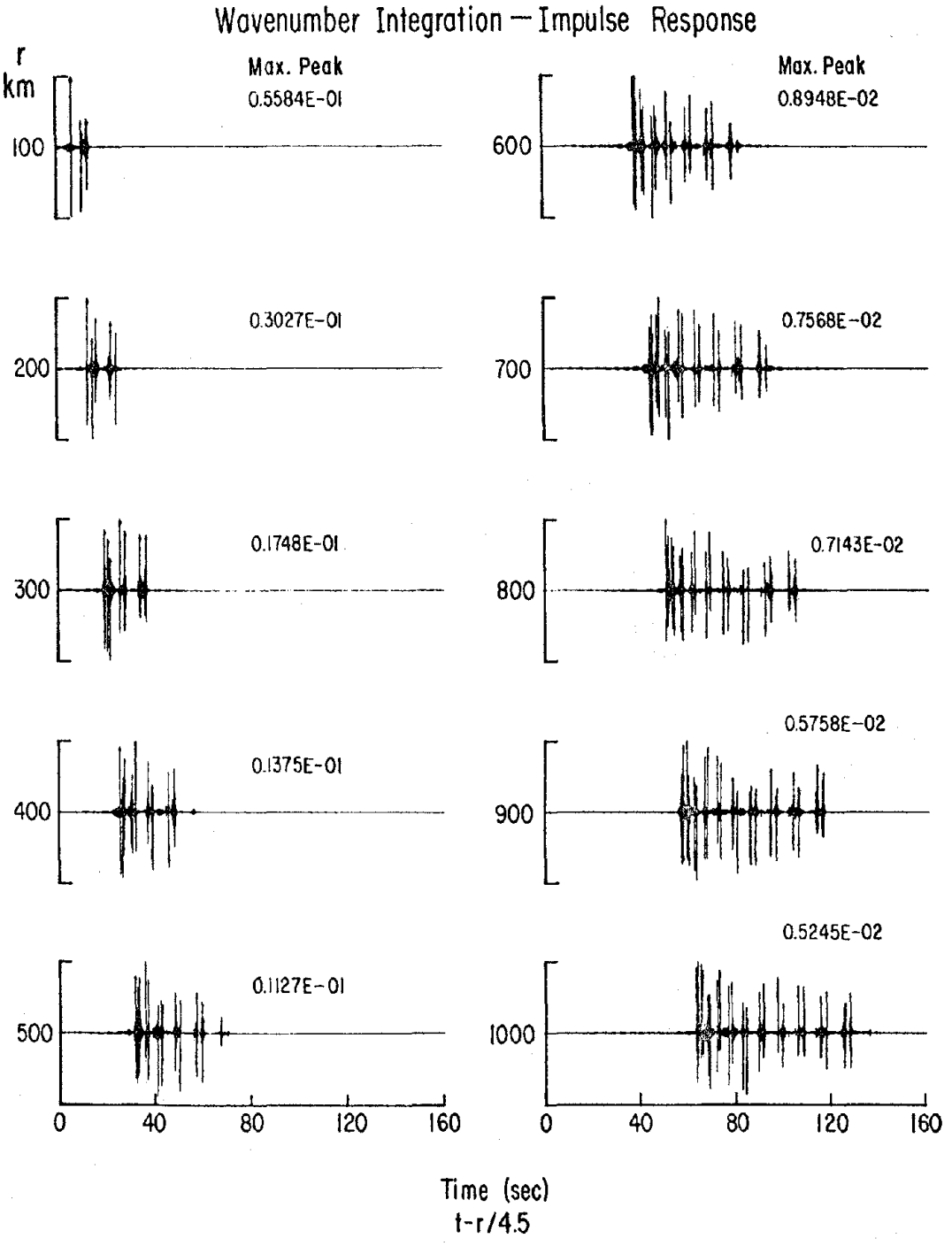

Figure 5.24. Present solution in response to same source used in Figures 5.22 and 5.23 but with delta-function time dependence.

waves) in response to the same source but with delta-function time dependence using the present method. The most important feature is the distinct set of pulses comprising the complete "elastic" (Q_β = 10,000) solution, so that the excellent match with the generalized ray results is not surprising for this simple problem.

Finally, the effects of using a nearly elastic (Q_β = 300) earth model versus an "elastic" (Q_β = 10,000) earth model in the present wavenumber integration approach are investigated in Figure 5.25. Even withstanding the low-pass filtering effect of the source, much more high frequency energy is able to reach the receivers in the "elastic" model. The maximum peaks for the "elastic" model correspond to the surface waves which decay with distance according to a dependence of approximately $r^{-1/2}$. The nearly elastic model experiences an additional decay of $r^{-1/2}$ due to the small amount of damping. Otherwise, the wave forms are quite similar.

This completes the validation/comparison studies with known solutions. The next section presents new results using the present wavenumber integration method for applications in theoretical seismology.

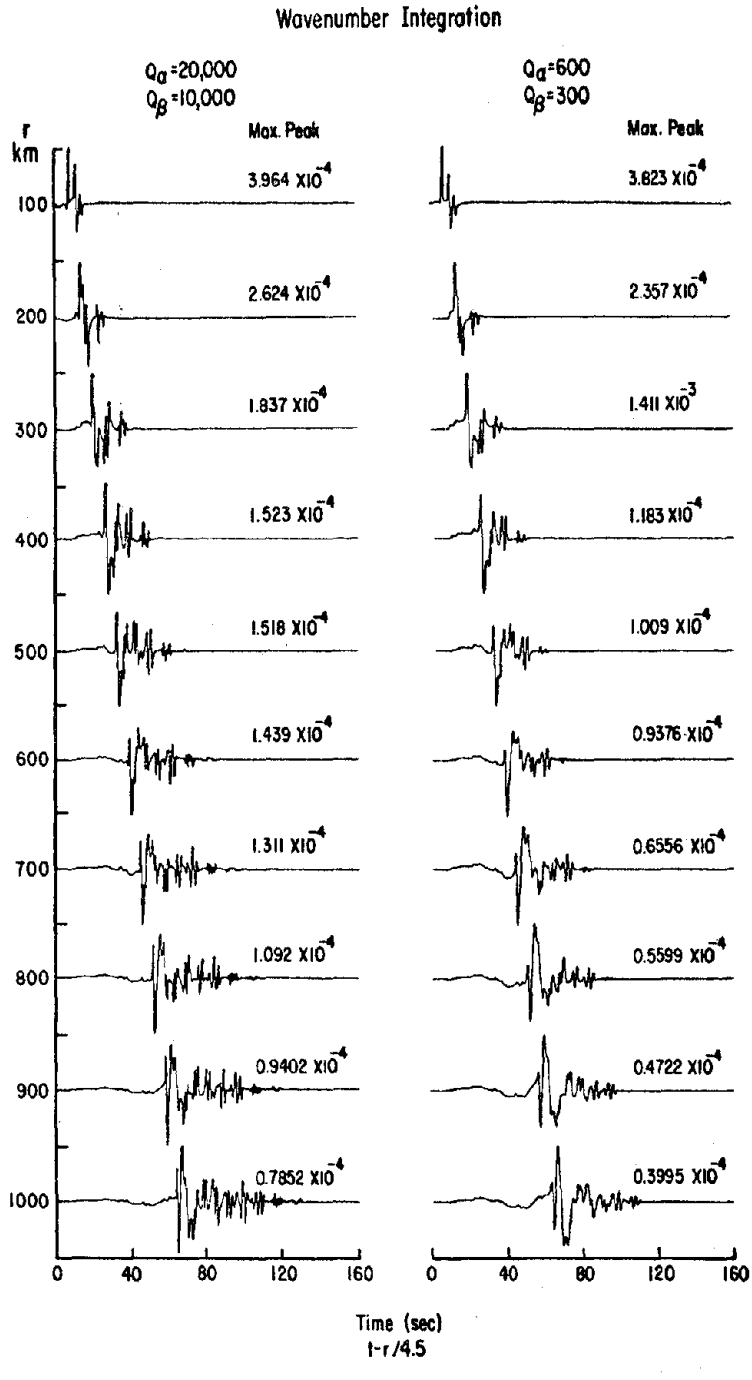

Figure 5.25. Effect on present solution of using a nearly elastic (Q_β = 300) earth model versus an "elastic" (Q_β = 10,000) earth model.

5.3 RESULTS

In this section, results are presented that further demonstrate the flexibility of the present method for seismological applications. Five typical applications are considered: 1) teleseismic ground motion from a simple source; 2) earthquake modeling; 3) ocean bottom seismology; 4) sensitivity to layer thickness; 5) sensitivity to material attenuation. Additional engineering applications are presented in Part II of this dissertation.

5.3.1 Teleseismic Ground Motion

Teleseismic ground motion due to a point dislocation is calculated with the present method. This is in contrast to the relatively close-in receivers studied elsewhere in this chapter. The idealized earth model must, however, be kept in mind when interpreting the results. For instance, the curvature of the layers is neglected so that certain reflections off the curved interfaces are neglected (although an earth-flattening approximation could have been incorporated into the reflection/transmission coefficients). Also, the shallow depth of the layering relative to the teleseismic distances considered prevents the synthesized waves from penetrating as deeply as teleseismic waves in the real Earth.

The earth structure is approximated by a stack of 11 parallel layers overlying a semi-infinite half-space. The wave velocities and attenuation factors for each layer are displayed graphically as a function of depth in Figure 5.26. Of interest is the low velocity, low attenuation crustal lid for this particular geologic site. The layers extend to a

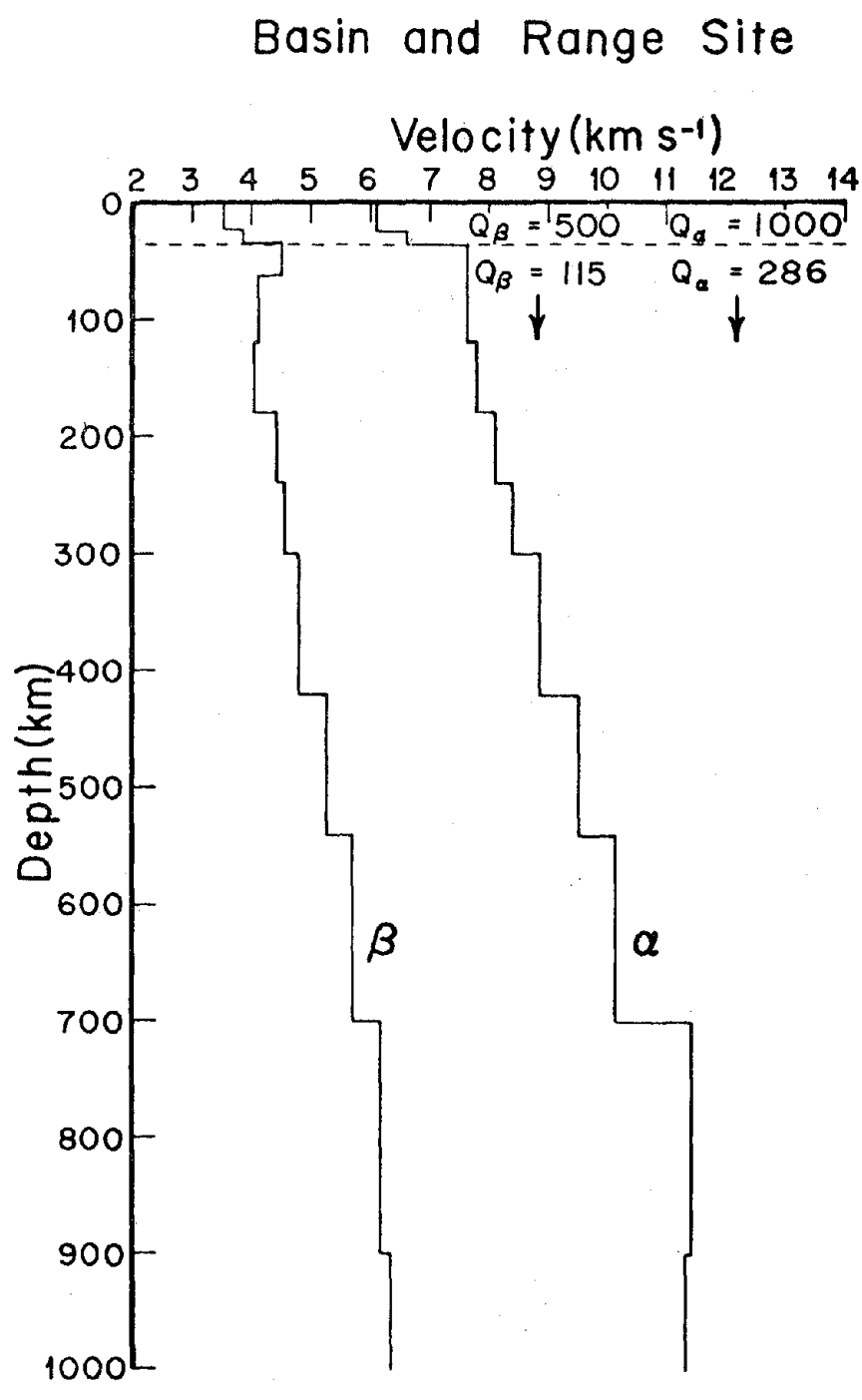

Figure 5.26. Velocity and material attenuation profiles as a function of depth for the 12-layer model of the Basin and Range geologic site.

depth of 900 km, whereas the epicentral distances considered range up to 25 degrees of the Earth's arclength (2555 km).

The source corresponds to a vertical strike-slip point dislocation at the free surface with a time dependence represented by the Heaviside unit function. Receivers are located at epicentral distances of 444.48, 888.96, 1444.56, 2000.16 and 2555.76 km along an azimuth of 22.5 degrees from the strike (to eliminate bias due to radiation pattern). The time response is calculated down to periods of 4 seconds (frequency content of 0 - 0.25 Hz).

The three components of the calculated teleseismic ground motion are displayed in Figures 5.27 through 5.31 for the five epicentral distances, respectively. The radial, vertical and azimuthal displacement components are shown vertically in each figure and are plotted as a function of time from 0 to 1000 seconds. The displacements are normalized by the ratio of the shear modulus of the first layer times 10^{10} cm^2 divided by the source moment and are scaled at each epicentral distance by the maximum peak found in the three components. This scaling factor appears at the top of each figure.

In Figure 5.27, the near-field P-SV contribution to the azimuthal displacement, which, referring to Eq. 4.2, has the form $\int_0^\infty k\, U_{1n}\, J_1(kr)/(kr)dk$, is still noticeable at 444 km, whereas it is completely attenuated at the larger epicentral distances. The calculated teleseismic ground displacements are dominated by normally dispersed surface waves followed by an Airy phase with an exponential tail in all five figures. The scaling factors therefore reflect the maximum surface

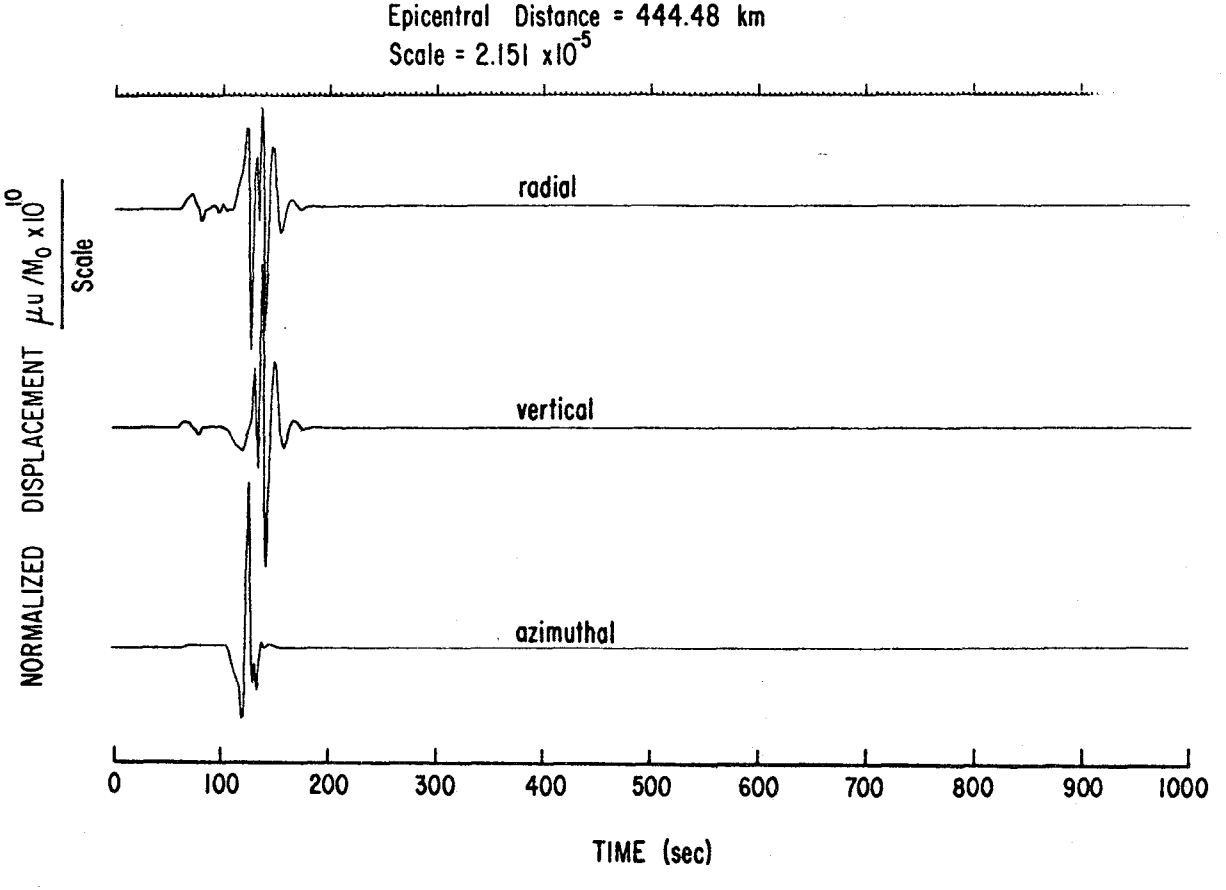

Figure 5.27. Calculated ground displacements at an epicentral distance of 444.48 km along an azimuth of 22.5 degrees from the strike of a vertical strike-slip point dislocation for the earth model shown in Figure 5.25. The source is a step function in time acting at the free surface.

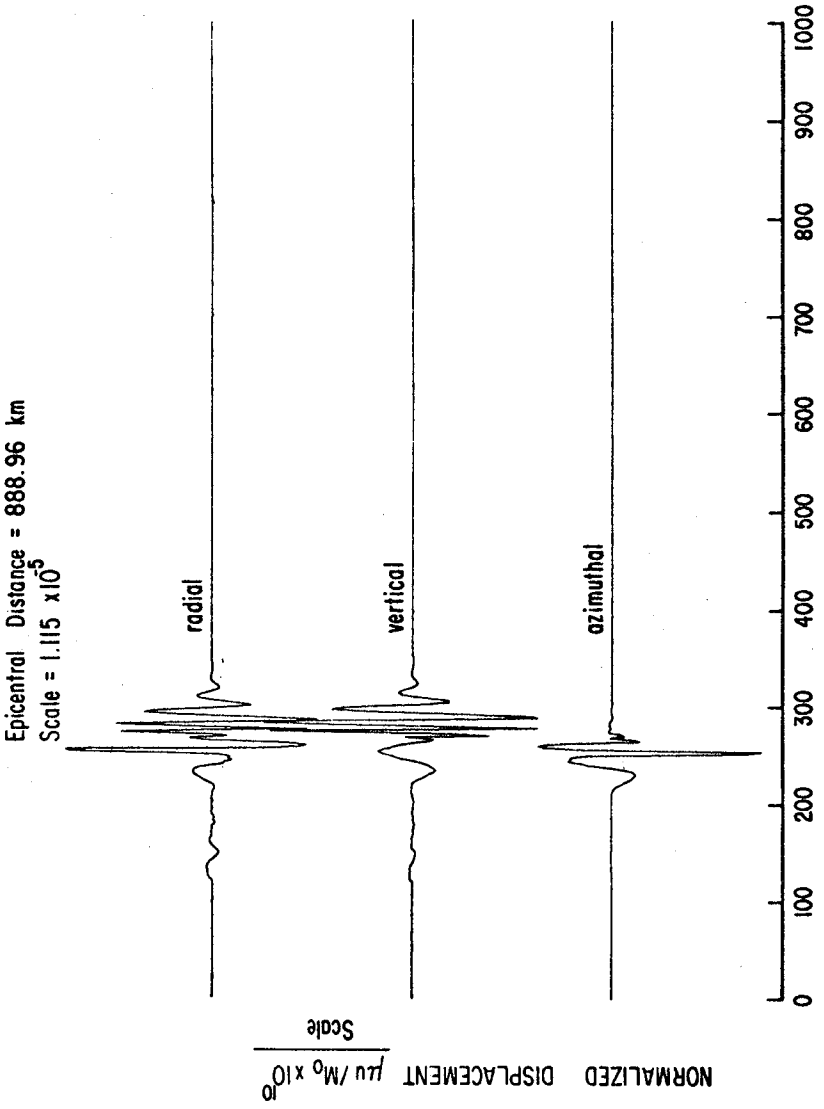

Figure 5.28. Corresponding results to Figure 5.26 for an epicentral distance of 888.96 km.

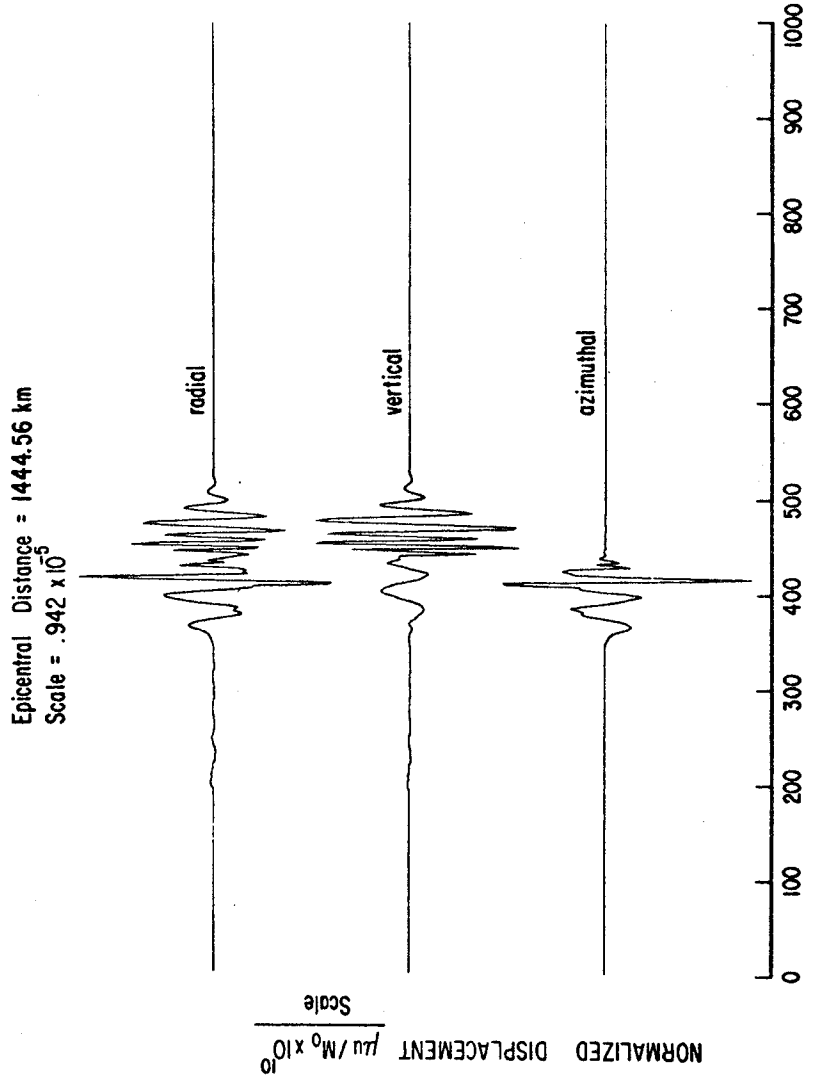

Figure 5.29. Corresponding results to Figure 5.26 for an epicentral distance of 1444.56 km.

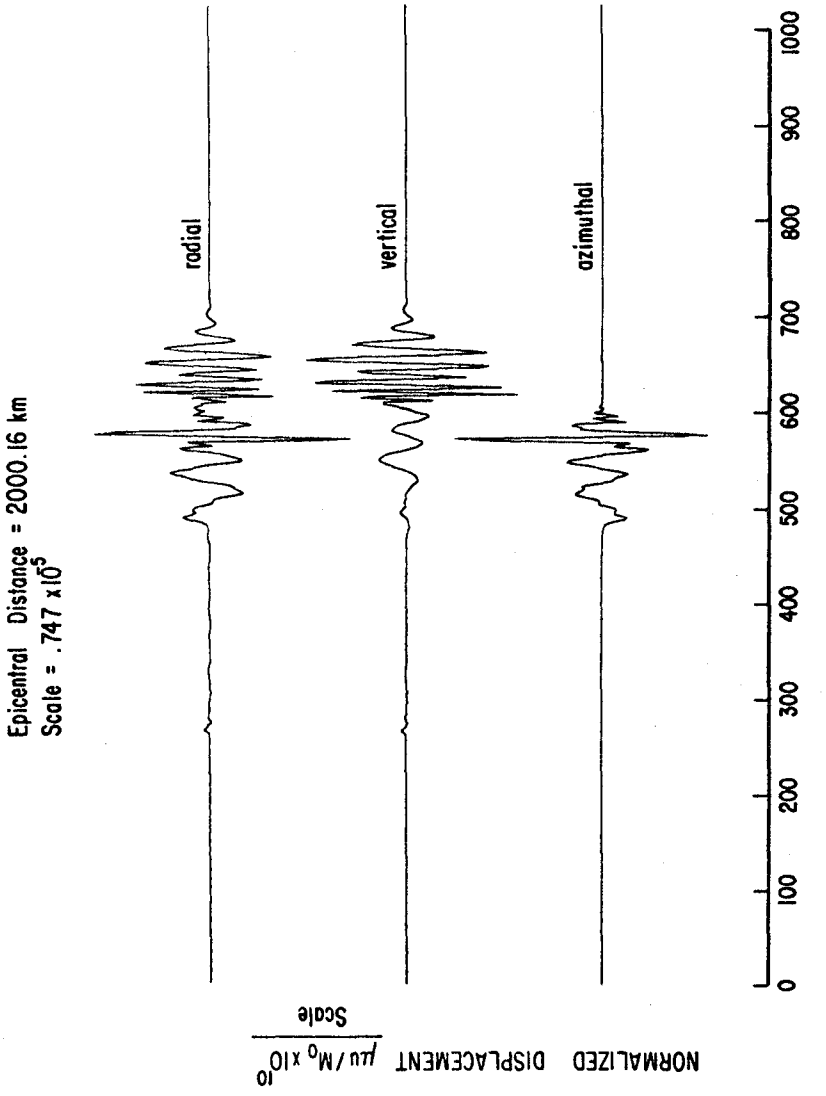

Figure 5.30. Corresponding results to Figure 5.26 for an epicentral distance of 2000.16 km.

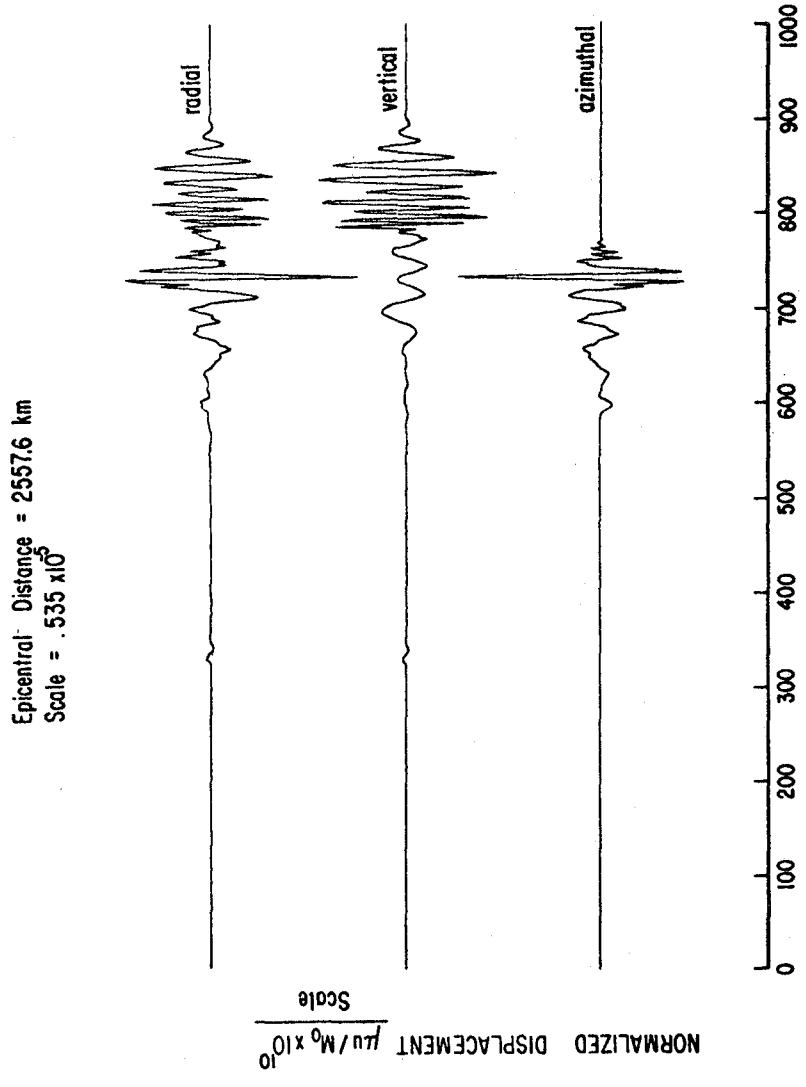

Figure 5.31. Corresponding results to Figure 5.26 for an epicentral distance of 2555.76 km.

wave amplitudes, leading to the conclusion that the amplitudes decrease with distance according to a dependence between $R^{-1/2}$ and R^{-1}, where R is the epicentral distance. The factor of $R^{-1/2}$ is attributable to the geometric radiation of energy, while the additional amplitude decay can be accounted for in terms of material attenuation. The static displacements resulting from the step-function source-time history decay with distance between R^{-2} and R^{-3} at these teleseismic distances. It is possible to identify the small static displacements only at the closest epicentral distance.

Again, these results demonstrate the ability of the present method to generate theoretical ground displacements at teleseismic distances although the idealized earth model may be limited at representing the realistic Earth.

5.3.2 Earthquake Modeling

The present method has been used by Hartzell (1978) to substantiate a hypothesized source depth for the October 6, 1974 Acapulco earthquake. The recorded displacements (i.e., the doubly integrated accelerograms) appear to consist primarily of normally dispersed surface waves, suggesting that the source was shallow. However, the recorded depth (based solely on P-wave arrival times) was 51 km with an epicentral distance of 25 km.

The predominant energy in the displacement records includes frequencies between 1 Hz and 10 Hz. The phase velocities vary smoothly from 3.1 km/sec at 10 Hz to 3.5 km/sec at 1 Hz. Considering the relatively simple surface geology of the Acapulco area, the earth structure is approximated by a single layer overlying a semi-infinite half-space.

three components of recorded ground motion for the Acapulco earthquake

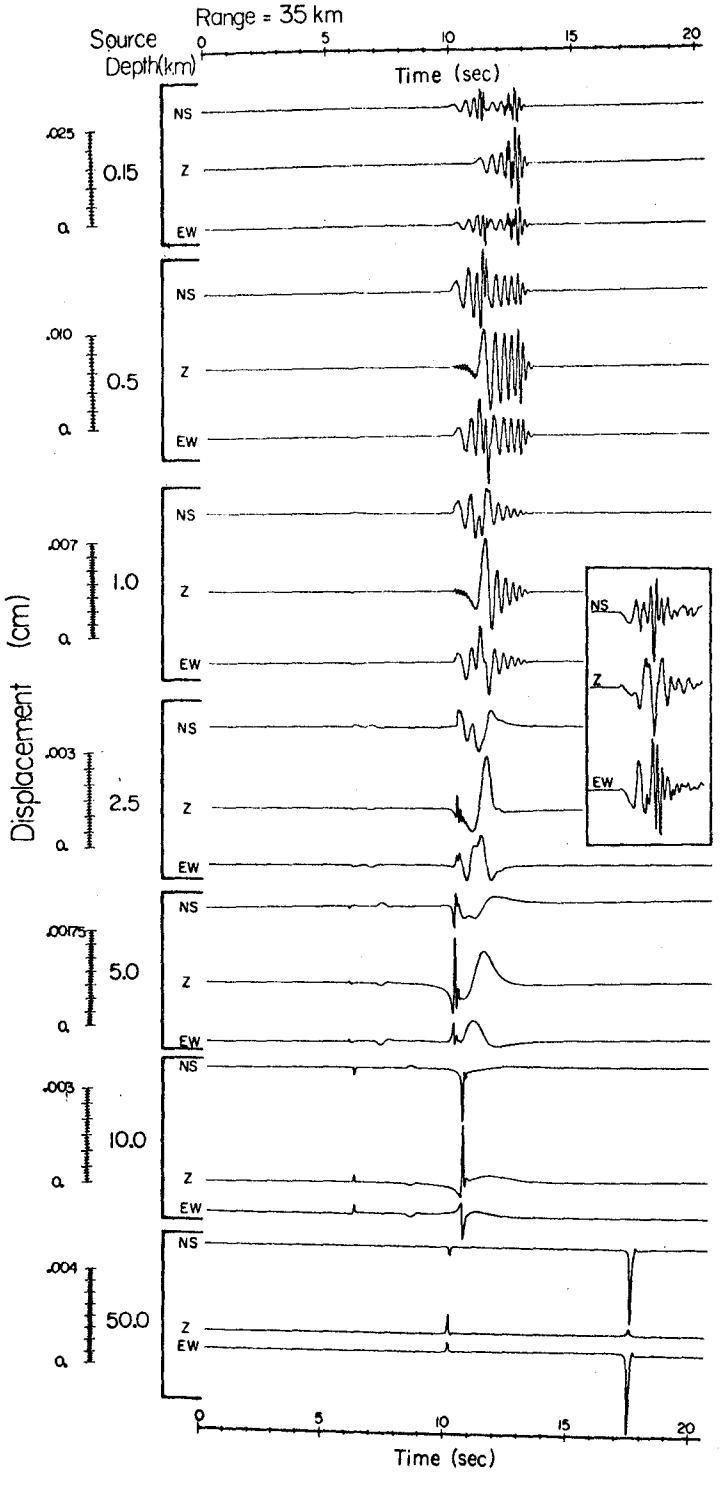

Figure 5.32. Synthetic seismograms illustrating the trade-off between surface wave and body wave energy with source depth for a point dislocation in the geology of the Acapulco area. The three components of displacement recorded for the October 6, 1974 Acapulco earthquake are shown at the same time scale in the box at the right center of the figure. Positive ground motion is down in the data and up in the synthetics. The figure is courtesy of Hartzell (1978).

are enclosed in the box at the right center of the figure. The time scales are identical for the synthetic and recorded ground motion.

The synthetics resulting from point dislocations of 2.5 km and deeper are quite dissimilar to the data in comparison to the match obtained for the shallower source depths. The observed surface wave excitation is best reproduced by a point dislocation of approximately 1.0 km depth, whereas the synthetic at the recorded depth of 50 km is completely dominated by body waves.

Other workers have used the present method for earthquake modeling involving finite sources (spatial integrals over the fault plane of a discrete mesh of propagating point dislocations).

5.3.3 Ocean Bottom Seismology

Apsel and Orcutt (1977) modified the present method to accomodate a fluid layer overlying a solid layered half-space. The modifications entailed replacing the free-surface reflection coefficients by their fluid counterparts and replacing the downgoing and upgoing reflection/transmission coefficients for the first layer interface by their fluid-solid and solid-fluid counterparts, respectively. This fully couples an oceanic overburden into the sea floor with all types of body and surface/interface waves represented in the complete solution.

Synthetic seismograms are generated for earthquakes on the Rivera Fracture Zone and Gorda Rise. The normal oceanic crustal model consists of 7 layers with the individual layer properties given in Figure 5.33. In order to realistically model the amplitude ratio of body and surface waves it was necessary to use velocity models with

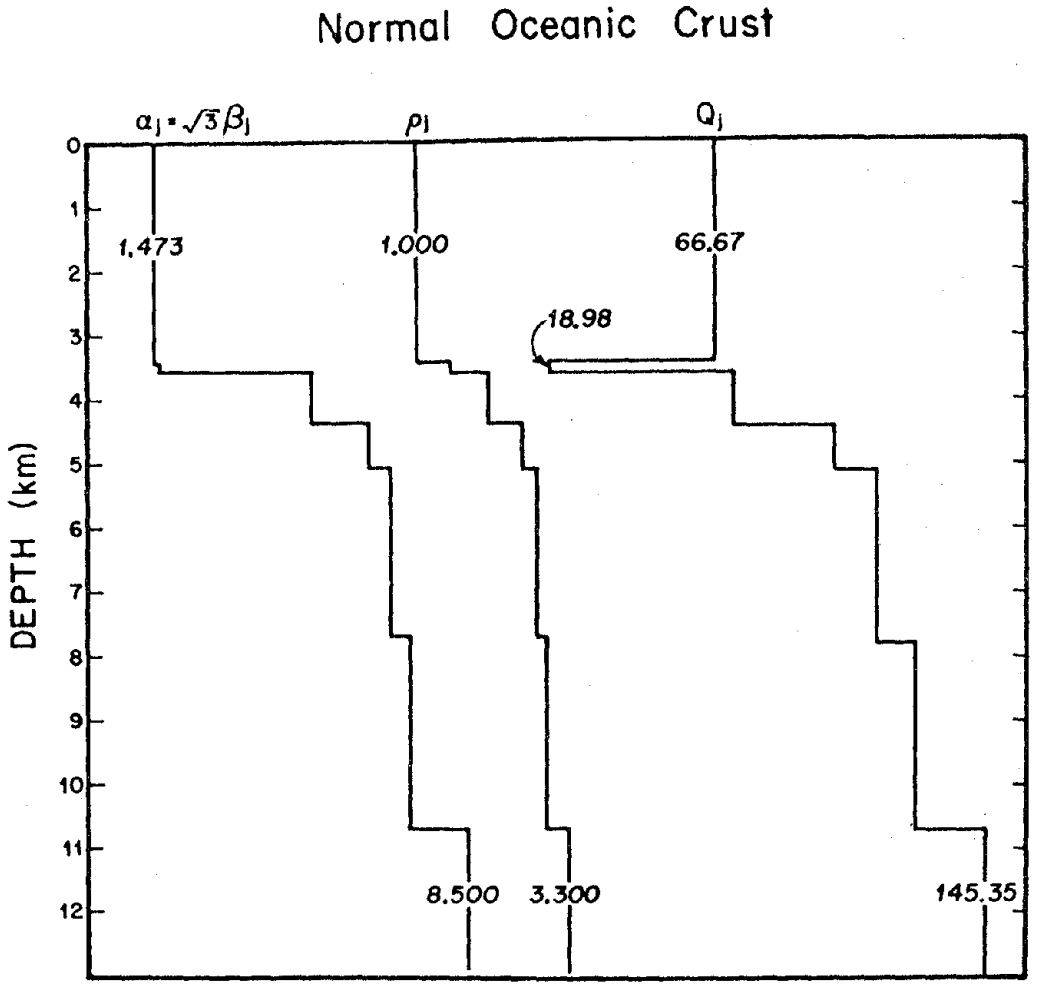

j	β_j	α_j	ρ_j	$Q_{\beta_j}=Q_{\alpha_j}$	h_j
1	———	1.473	1.00	66.67	3.399
2	.894893	1.550	1.50	18.98	0.170
3	2.886751	5.000	2.07	71.94	0.800
4	3.637307	6.300	2.60	101.63	0.700
5	3.925982	6.800	2.80	113.89	2.600
6	4.156922	7.200	2.96	125.00	3.000
7	4.618802	8.500	3.30	145.35	∞

Figure 5.33. Material properties as a function of depth for 7-layer model of Normal Oceanic Crust.

crustal gradients similar to those found in recent work in oceanic explosion seismology. The ocean layer extends to a depth of 3.399 km but unfortunately has an unrealistically large amount of material damping due to the choice of Q_α in the liquid layer.

Typical results are shown in Figures 5.34 and 5.35 for a receiver buried at the fluid/solid interface. The source is a concentrated point force buried in the oceanic basement, 1.0 km beneath the sea floor. The vertical displacement at the sea floor is displayed in Figure 5.34 as a function of time from 0 to 50 seconds for epicentral ranges from 2 km to 40 km at an increment of 2 km. The synthetics include energy from 0 to 8 Hz. The two columns of figures correspond to vertical and horizontal point forces, respectively. The displacements are normalized by the shear modulus of the first solid layer times the epicentral distance and the plots are scaled relative to the seismograms appearing at the top of each column.

The first thing to notice is that much, if not all, the S-wave "coda" can be realistically modeled as a superposition of higher mode interface waves without resorting to scattering mechanisms. The dispersion of the surface/interface waves becomes more prevalent as the epicentral distance is increased. It is interesting to observe the periodic arrivals corresponding to reflections off the surface of the ocean. The corresponding results for the normal component of stress at the sea floor are shown in Figure 5.35. Again, it is interesting to follow the various arrivals as a function of epicentral distance.

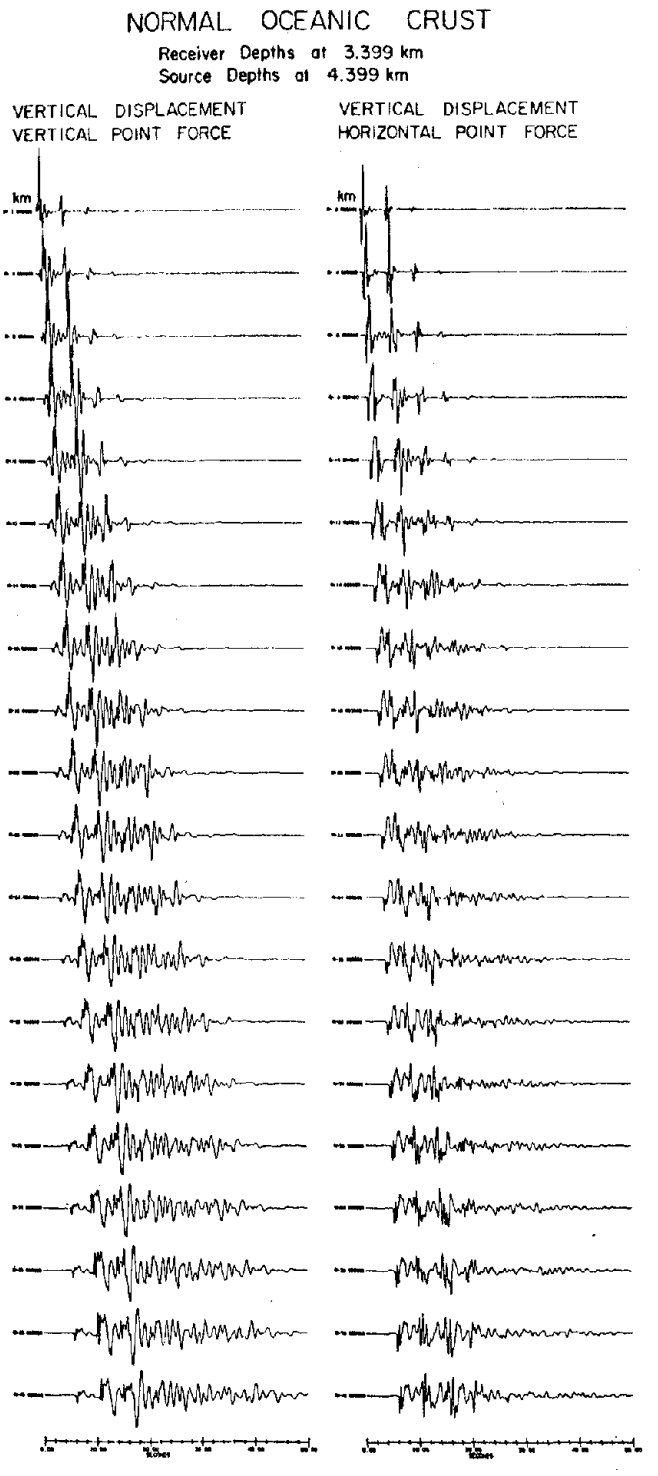

Figure 5.34. Calculated displacements at the sea floor for a concentrated point force buried at 1 km beneath the sea floor for normal oceanic crustal model delineated in Figure 5.33.

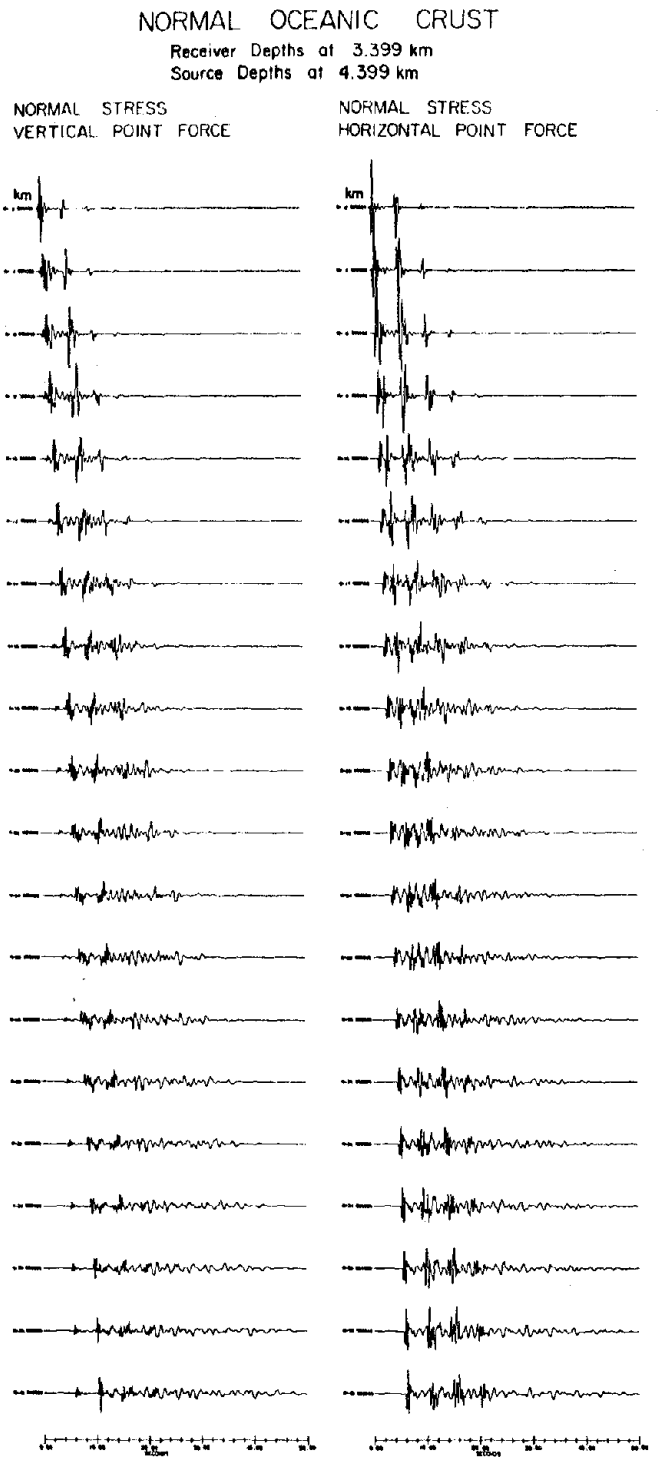

Figure 5.35. Corresponding results to Figure 5.34 for the normal stress at the sea floor.

5.3.4 Sensitivity to Layer Thickness

The issue of modeling continuously varying earth structures with a set of parallel horizontal layers is examined. Numerous questions can be asked in such an undertaking. For instance, can thick layers transmit the predominant high frequency energy similar to layers whose thickness is on the order of the wavelengths of interest? Also, what are the effects of allowing the waves to be reflected and refracted by the layer interfaces compared to the turning and bending associated with a more continuous profile?

An attempt to answer some of these questions is presented by studying the sensitivity to layer thickness for the geology near the 1940 Imperial Valley earthquake. Four plausible representations of the depth dependence for the shear wave velocity are shown in Figure 5.36. The model appearing to the left is the so-called continuous model with a linear gradient overlying a true layer followed by another linear gradient overlying a semi-infinite half-space. The three layered profiles are all equivalent to the continuous model in the sense that the layer properties are chosen to preserve the vertical travel time from the half-space to the free surface as well as the effective material attenuation in the vertical direction. The true layer and the underlying half-space are identical in the four models.

The vertical travel time is preserved through each gradient by independently insuring that both

$$\sum_i \frac{h_i}{\alpha_i} \quad \text{and} \quad \sum_i \frac{h_i}{\beta_i}$$

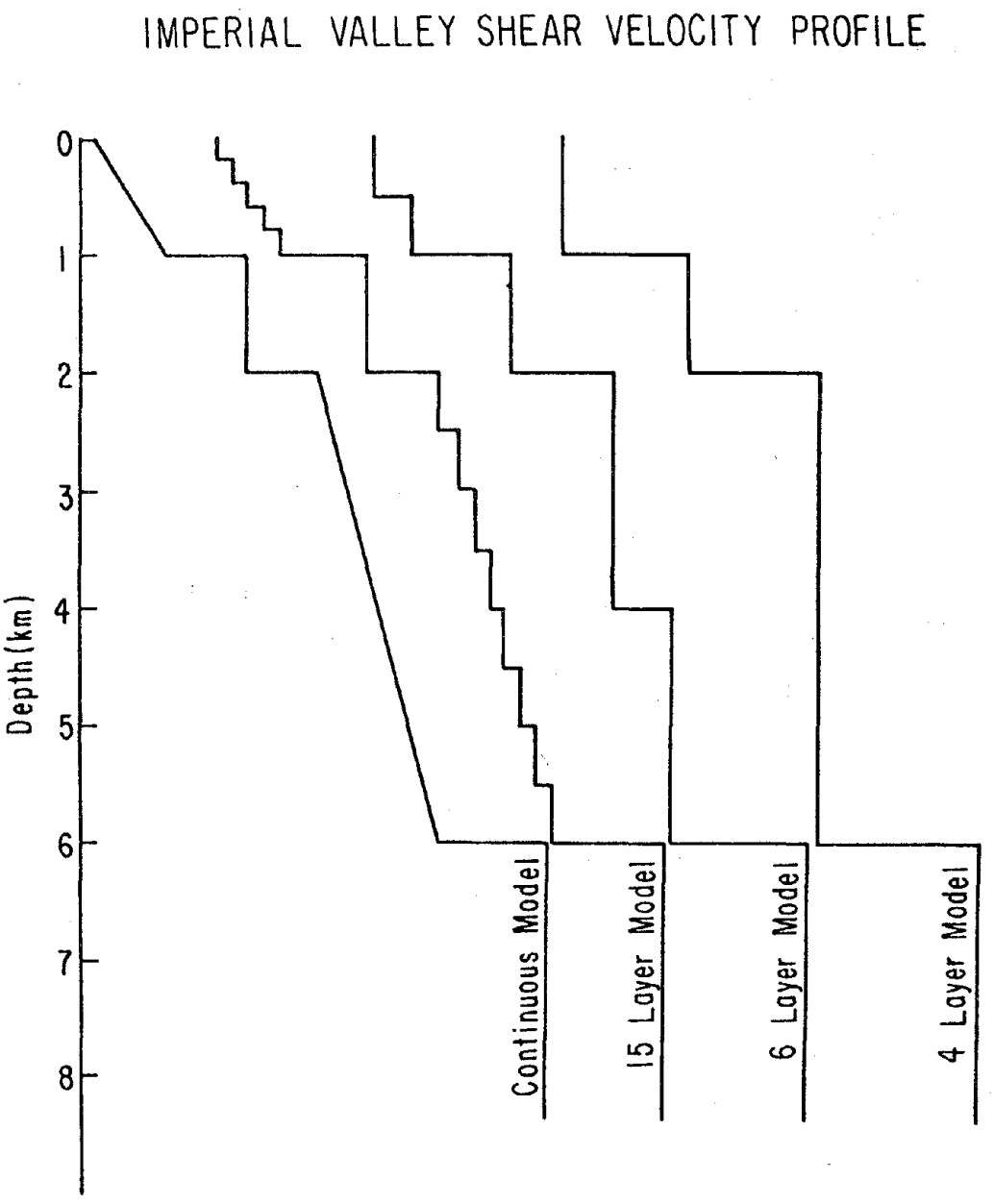

Figure 5.36. Imperial Valley shear-wave velocity profile as a function of depth for four "equivalent" earth structures.

are consistent between the models, where the summation extends over the layers composing the gradient. The material attenuation is preserved for vertically emerging waves in an approximate sense by independently insuring that both

$$\sum_i \frac{h_i}{\alpha_i Q_{\alpha_i}} \quad \text{and} \quad \sum_i \frac{h_i}{\beta_i Q_{\beta_i}}$$

are consistent between the models. This is the effective material attenuation as theorized in Section 2.5 and as demonstrated in the following subsection. The actual parameters defining the four models are presented in Tables 5.2 through 5.5.

The vertical displacements due to a vertical point force acting at a depth of 2 km are shown right to left in Figure 5.37 for the three layered models depicted in Figure 5.36. The three results are normalized by the shear modulus in the first layer of the 15-layer model times the epicentral distance. The first 50 seconds of 100 seconds of time signal are plotted for each epicentral distance (5-50 km at an increment of 5 km), and frequencies up to 10 Hz are included in the calculations.

It is important to realize that the lower frequency surface waves are virtually unaltered going from 4 to 6 to 15 layers, since the long period waves are influenced by an average value of the soil properties. Also, there exists no prevalent trend in the body waves as a function of layer thickness. However, it is difficult to interpret the significance of these results in terms of transmission of high frequency energy. First of all, the source is located just below the upper gradient zone and the reflections off the large impedance mismatch could

Layer	β km/sec	α km/sec	ρ gm/cm^3	Q_β	Q_α	Thickness km
1	.16	.47	1.56	15	95	.2
2	.28	.81	1.68	30	180	.2
3	.40	1.15	1.80	45	270	.2
4	.52	1.49	1.92	60	350	.2
5	.64	1.83	2.04	75	440	.2
6	1.40	2.70	2.20	200	560	1.0
7	2.03	3.86	2.420	290	770	.5
8	2.16	4.00	2.445	315	795	.5
9	2.29	4.14	2.470	340	820	.5
10	2.42	4.28	2.495	365	845	.5
11	2.55	4.42	2.520	390	870	.5
12	2.68	4.56	2.545	415	895	.5
13	2.81	4.70	2.570	440	920	.5
14	2.94	4.84	2.595	465	945	.5
15	3.90	6.40	2.800	640	1280	∞

Table 5.2

Material properties for the 15-layer model of the Imperial Valley geologic site.

Layer	β km/sec	α km/sec	ρ gm/cm^3	Q_β	Q_α	Thickness km
1	.217	.633	1.65	19.75	123.46	.5
2	.583	1.667	1.95	70.25	411.54	.5
3	1.400	2.700	2.20	200.00	560.00	1.0
4	2.185	4.029	2.45	319.24	799.97	2.0
5	2.785	4.671	2.55	435.76	915.03	2.0
6	3.900	6.400	2.80	640.00	1280.00	∞

Table 5.3

Material properties for the 6-layer model of the Imperial Valley geologic site.

Layer	β km/sec	α km/sec	ρ gm/cm^3	Q_β	Q_α	Thickness cm
1	.316	.918	1.80	24.24	152.92	1.0
2	1.400	2.700	2.20	200.00	560.00	1.0
3	2.449	4.326	2.50	361.78	849.43	4.0
4	3.900	6.400	2.80	640.00	1280.00	∞

Table 5.4

Material properties for the 4-layer model of the Imperial Valley geologic site.

Zone or Layer	β km/sec	α km/sec	gm/cm^3	Q_β	Q_α	Thickness km
1	.1-.7	.3-2.0	1.5-2.1	8-80	52-480	1.0
2	1.4	2.7	2.2	200	560	1.0
3	2.0-3.0	3.8-4.9	2.4-2.6	280-480	760-960	4.0
4	3.9	6.4	2.8	640	1280	∞

Table 5.5

Material properties for the continuous model of the Imperial Valley geologic site.

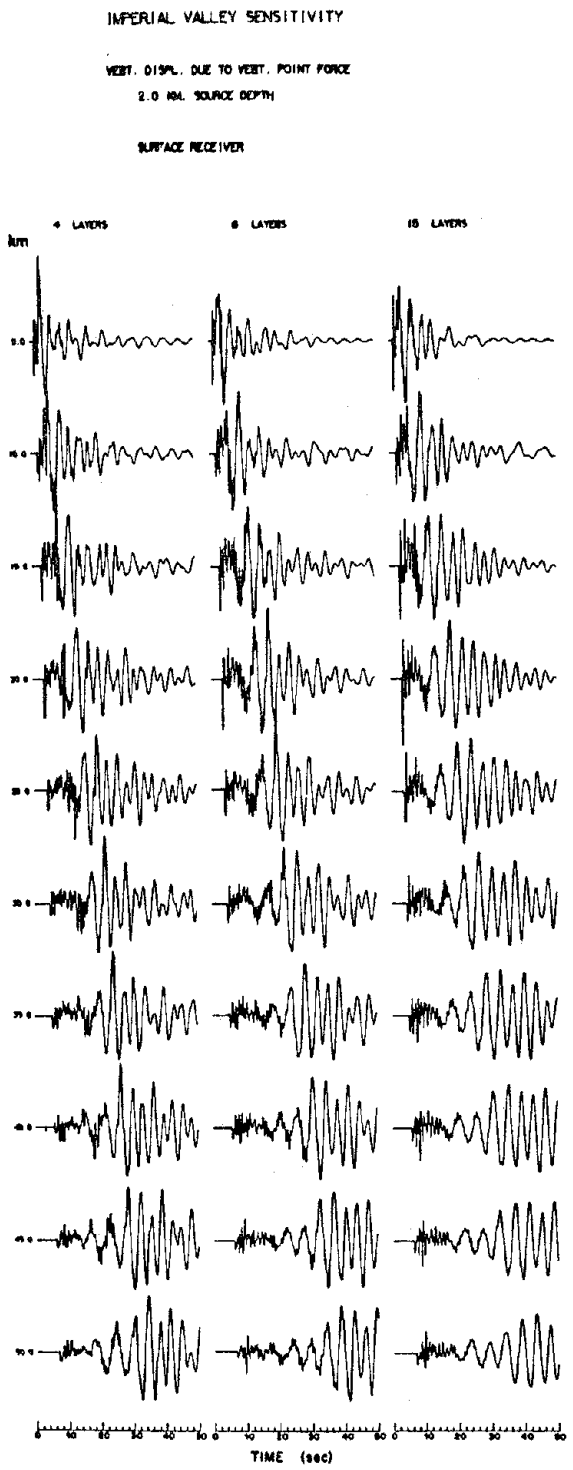

Figure 5.37. Sensitivity to layer thickness of the vertical displacement at the free surface due to a vertical point force at 2 km depth for the three layered models representing the geology at Imperial Valley as defined in Tables 5.3, 5.4, 5.5 and as shown graphically in Figure 5.36.

account for the high frequency content of the body and higher mode surface waves in the 4-layer model. Also, the transmission and reflections from the underlying material could obscure the comparisons at high frequency. Furthermore, to reduce the computing effort for the three calculations, the lowest phase velocities were not included at high frequency (where they are not expected to contribute information). It is possible to conclude, however, that the extra reflections and refractions in the 15-layer model have only a second order effect since the body wave region is no more complicated than in the 4- and 6-layer models.

It is interesting to notice how the surface waves dominate the signal for epicentral ranges larger than 30 km with the source buried at a depth of 2 km. The next three figures show the corresponding results for source depths of 5, 8, and 11 km, respectively. For these deeper source depths, the long period surface waves remain subordinate in amplitude to the body waves and higher mode surface waves, even at an epicentral distance of 50 km. Again, the seismograms look quite similar as a function of layer thickness, but the significance of such a result is beyond the scope of this work.

The analogous results for the tangential displacement due to horizontal point forces at depths of 2, 5, 8 and 11 km are shown in Figures 5.41 through 5.44. The same conclusions may be drawn here as in the previous four figures.

A direct comparison between a continuous model and a finely layered model for Imperial Valley is currently underway using the discrete wavenumber/finite element method (Olson, 1978 -- see Section 5.1.5) and the present method. Preliminary results indicate an excellent match for all frequencies considered.

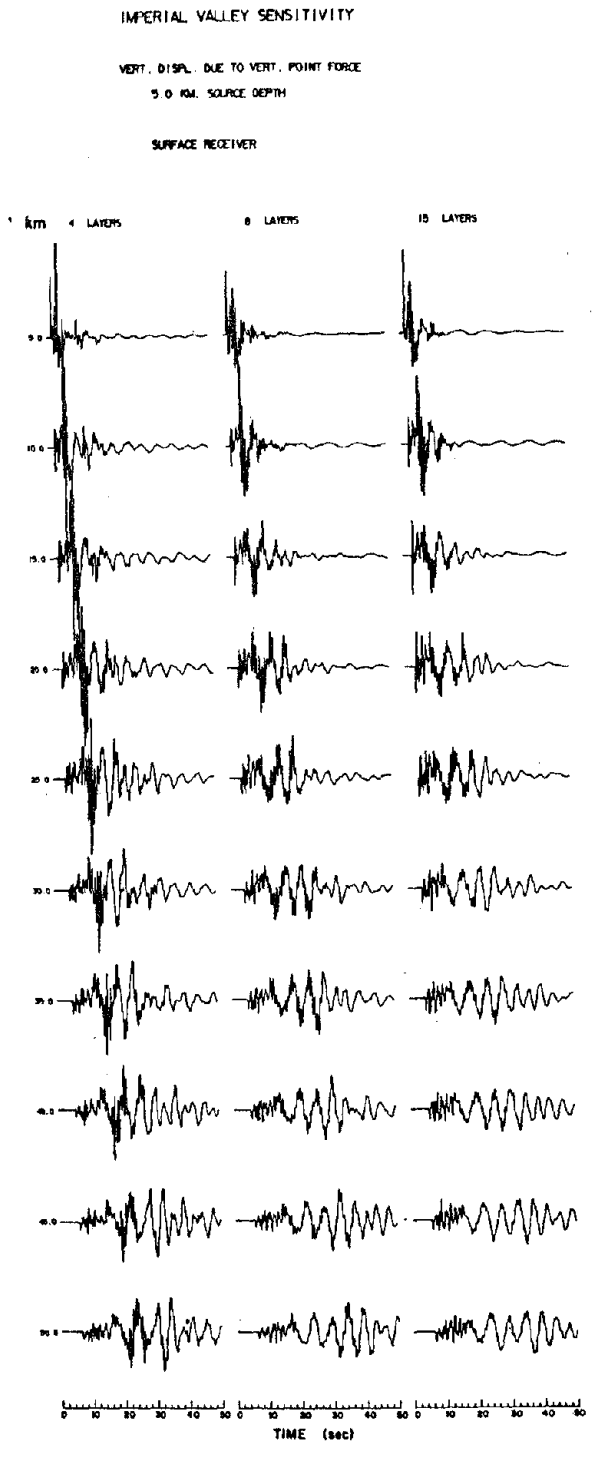

Figure 5.38. Corresponding sensitivity results to Figure 5.37 for a source depth of 5 km.

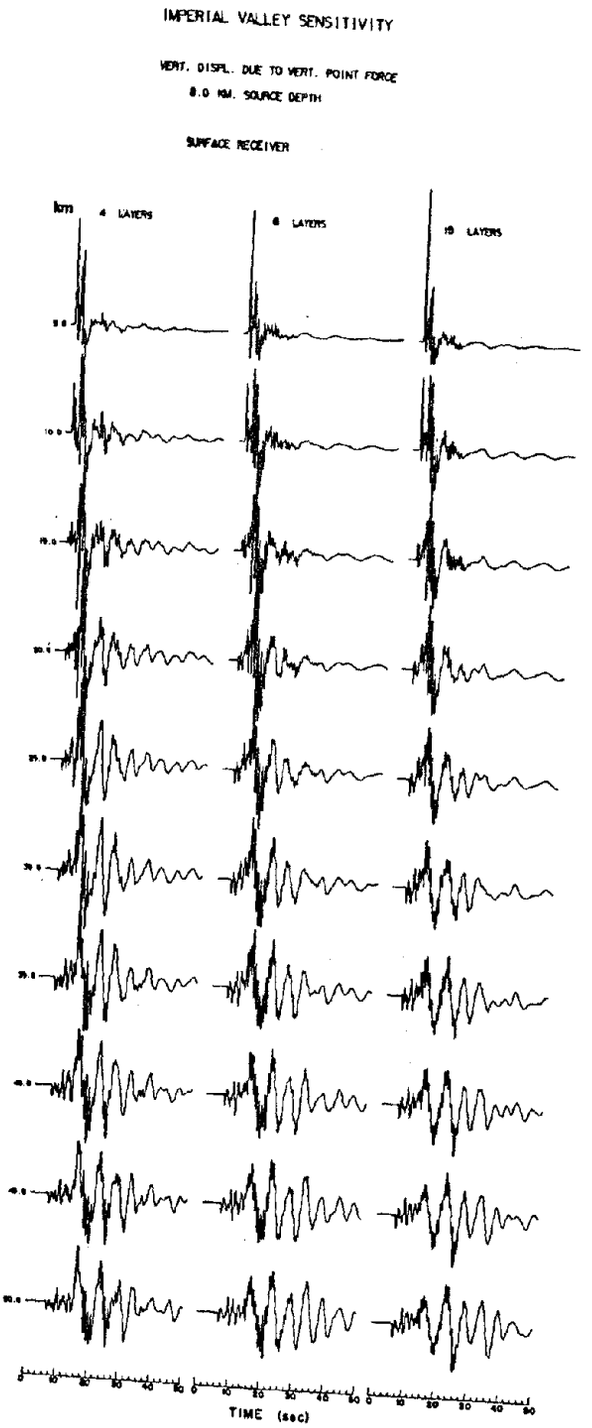

Figure 5.39. Corresponding sensitivity results to Figure 5.37 for a source depth of 8 km.

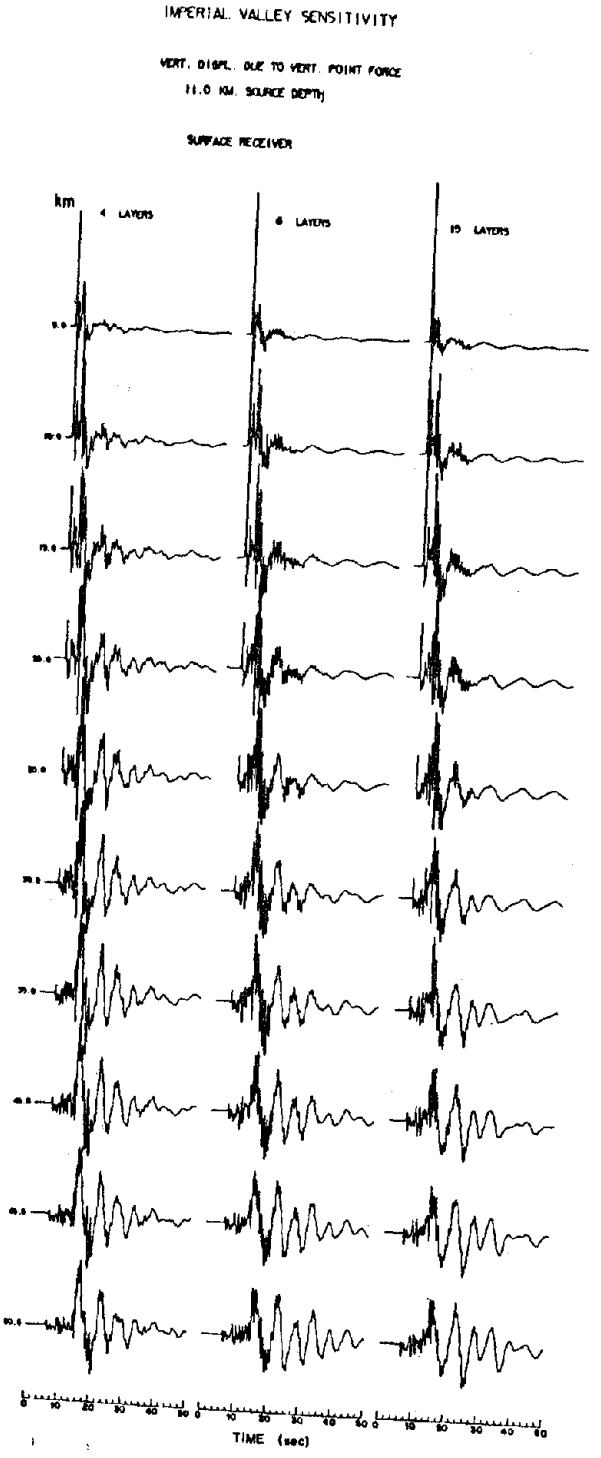

Figure 5.40. Corresponding sensitivity results to Figure 5.37 for a source depth of 11 km.

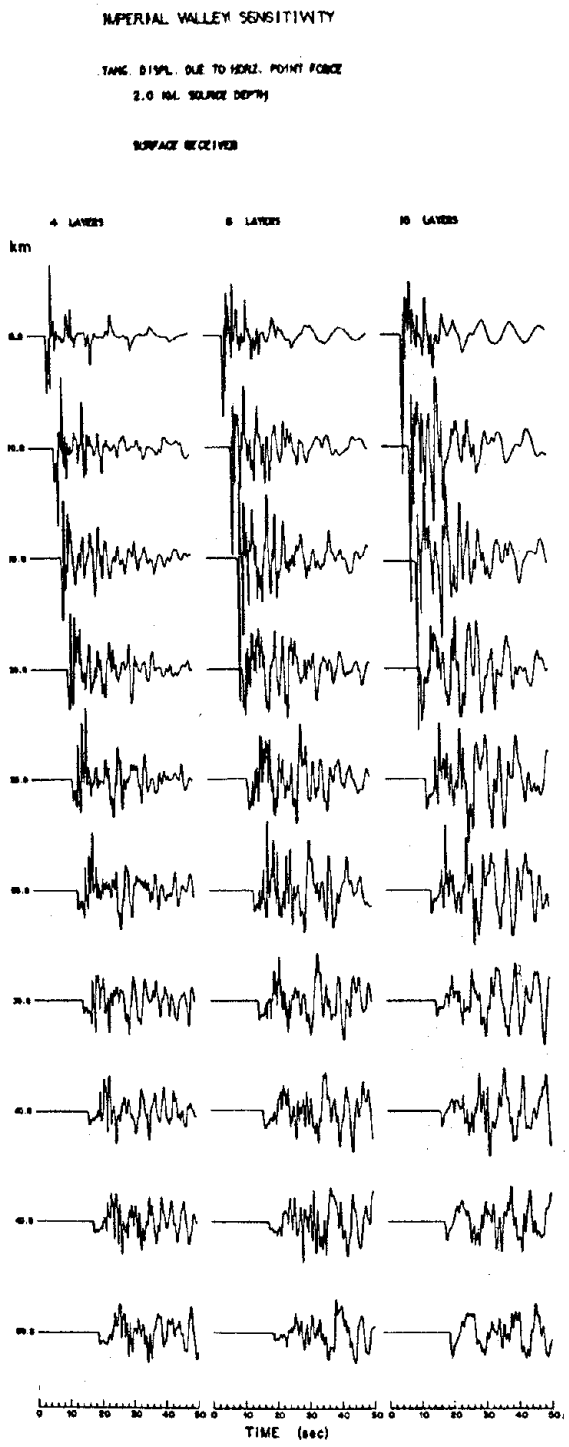

Figure 5.41. Corresponding sensitivity results to Figure 5.37 for the tangential displacement at the free surface due to a horizontal point force at 2 km depth.

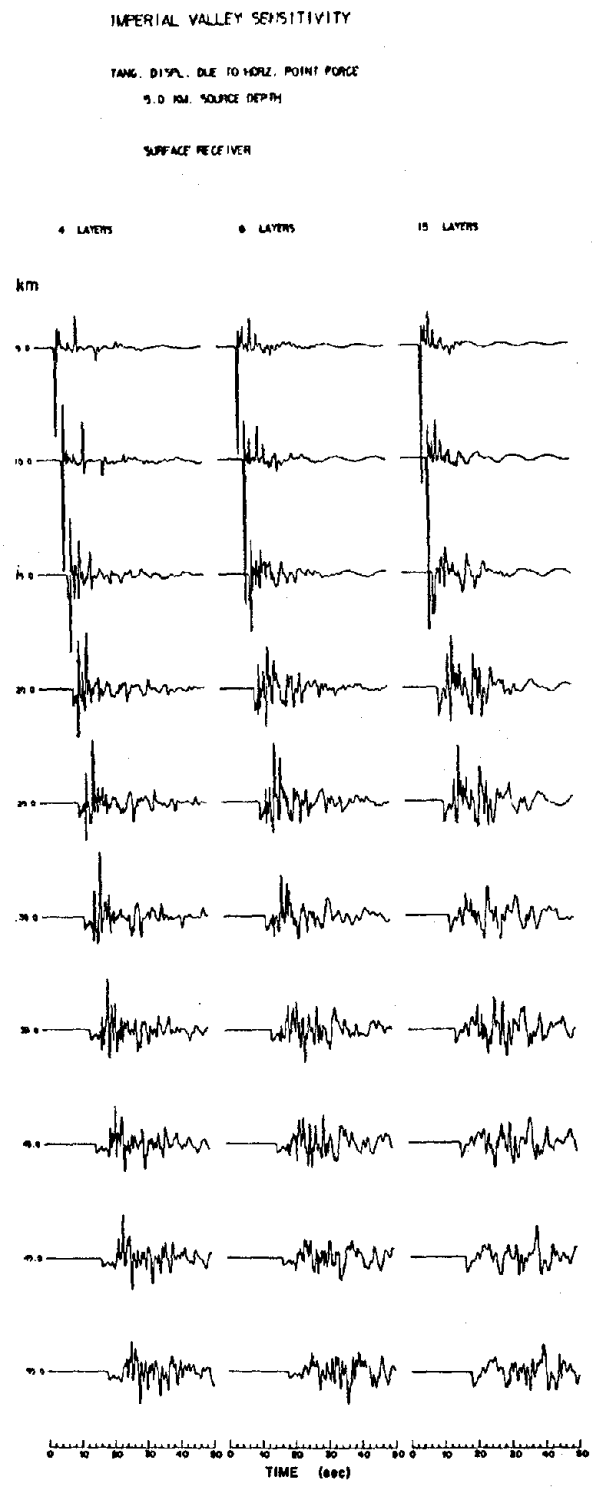

Figure 5.42. Corresponding sensitivity results to Figure 5.41 for a source depth of 5 km.

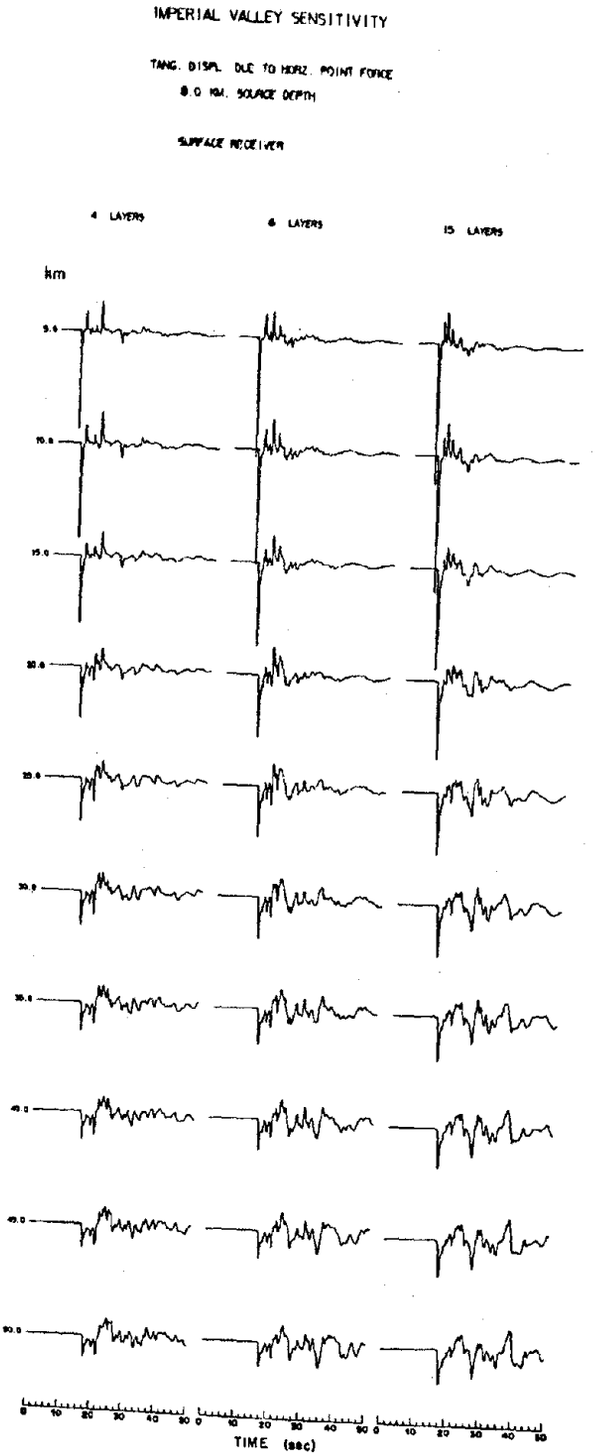

Figure 5.43. Corresponding sensitivity results to Figure 5.41 for a source depth of 8 km.

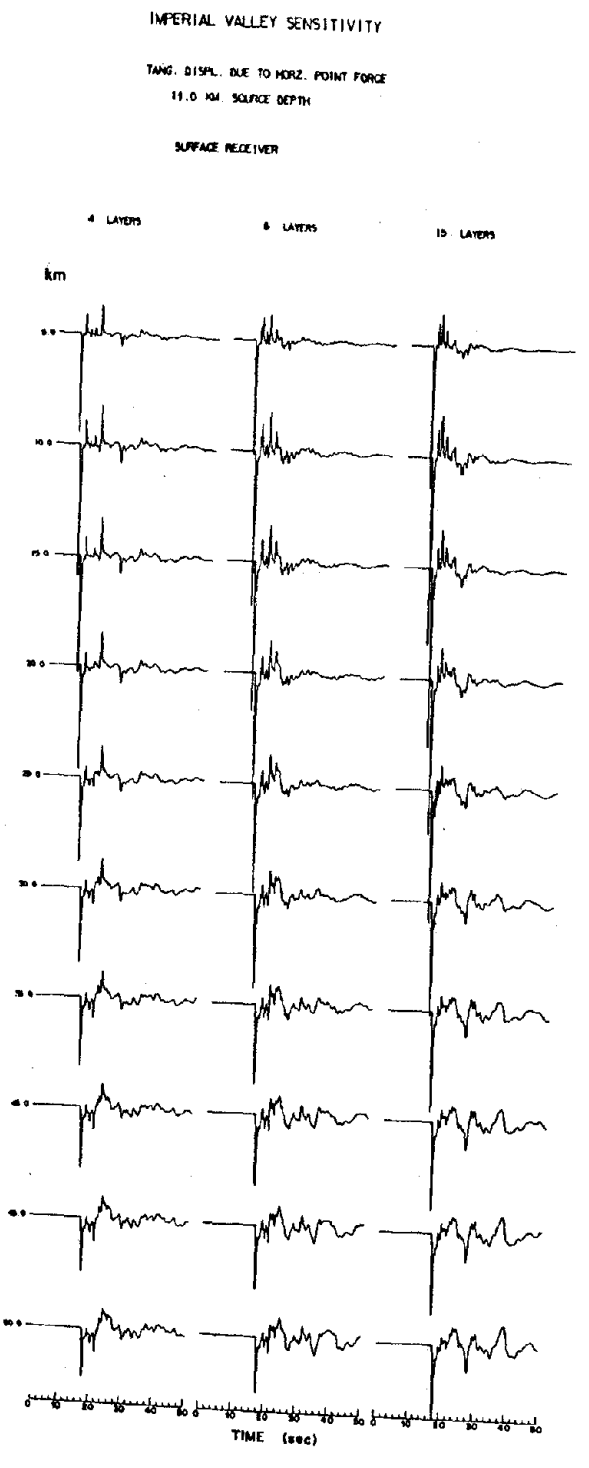

Figure 5.44. Corresponding sensitivity results to Figure 5.41 for a source depth of 11 km.

5.3.5 Sensitivity to Material Attenuation

The sensitivity of the Green's functions to material attenuation is investigated as a function of frequency and source-receiver geometry. The sensitivity is expected to show certain trends which can be partially explained in terms of simple geometric ray theory. The results presented in this subsection are courtesy of recent work done with Gerald Frazier and Jeff Fried of Del Mar Technical Associates.

The measure of sensitivity to be used is given in terms of the function $G(Q_j)$, which represents the spectral amplitude of one Green's function component for a particular parameter set Q_j of material attenuation factors, Q_{β_j} and Q_{α_j} ($j = 1, 2, \ldots,$ number of layers). The sensitivity measure, S, of $G(Q_j)$ with respect to Q_j is defined as

$$S(G, Q_j) = \frac{G(Q_j+\eta Q_j) - G(Q_j-\eta Q_j)}{2\eta G(Q_j)} \tag{5.1}$$

in which

$$G(Q_j+\eta Q_j) = G\Big(Q_{\beta_1} + \eta Q_{\beta_1}, Q_{\beta_2} + \eta Q_{\beta_2}, \ldots, Q_{\alpha_1} + \eta Q_{\alpha_1}, Q_{\alpha_2} + \eta Q_{\alpha_2}, \ldots\Big) \tag{5.2}$$

$$\eta = 0.1 \ . \tag{5.3}$$

In what follows, the function $G(Q_j)$ corresponds to the spectral amplitude of the azimuthal component of the displacement field at the free surface resulting from a buried vertical strike-slip point dislocation with delta function time dependence. The receivers are located at

Layer	β km/sec	α km/sec	ρ gm/cm^3	Q_β	Q_α	Thickness km
1	0.62	1.88	2.16	17	114	0.021
2	0.64	1.95	2.16	17	120	0.044
3	0.66	2.03	2.16	18	126	0.032
4	0.79	2.13	2.10	22	122	0.113
5	0.93	2.28	2.10	27	123	0.11
6	1.16	2.48	2.10	36	124	0.33
7	1.39	2.75	2.24	45	133	0.27
8	1.47	2.85	2.24	49	137	0.27
9	1.66	3.10	2.47	57	148	0.10
10	1.71	3.20	2.47	59	154	0.10
11	2.94	4.80	2.60	115	231	2.12
12	3.49	5.70	2.76	143	286	6.97
13	3.73	6.10	2.76	156	312	∞

Table 5.6

Material properties for the earth structure of reference used in sensitivity studies on material attenuation.

Source Depth (km)	GREEN'S FUNCTION SENSITIVITY Epicentral Distance (km) 1	10	30	70
		f = 1 Hz		
.484	.16	1.1	2.1	1.4
2.4	.15	.36	1.3	1.9
6.9	.20	.21	.44	.68
15.0	.25	.26	.33	.45
		f = 2 Hz		
.484	.28	2.8	1.2	1.4
2.4	.27	.27	1.2	2.7
6.9	.32	.46	.82	1.5
15.0	.41	.51	.70	.98
		f = 5 Hz		
.484	.71	.92	3.1	3.4
2.4	.62	.95	2.2	3.5
6.9	.67	1.0	1.6	3.2
15.0	.89	1.1	1.6	2.6
		f = 10 Hz		
.484	1.4	2.6	6.5	11.0
2.4	1.3	2.0	4.4	5.0
6.9	1.5	2.0	3.5	3.1
15.0	2.1	2.2	3.3	2.4
		f = 20 Hz		
.484	2.7	5.3	-.90	3.6
2.4	2.6	4.4	2.7	1.9
6.9	3.0	4.1	6.1	6.5
15.0	3.1	4.5	6.9	4.8

Table 5.7

Sensivity values of azimuthal displacement for changes in material attenuation factor Q_β in all layers of earth structure defined in Table 5.6.

η is approximately given by

$$S_{direct} \sim \frac{1}{\eta} \sinh\left[\eta \sum_j \frac{\omega R_j}{2\beta_j Q_{\beta_j}}\right] \tag{5.4}$$

in which the summation over j extends over the layers traced by the direct SH-wave. The variable R_j in Eq. (5.4) represents the distance traveled by the direct shear wave in the j^{th} layer according to Snell's law. For small values of $\eta \sum_j \frac{\omega R_j}{2\beta_j Q_{\beta_j}}$, the sensitivity of the direct rays in Eq. (5.4) can be reduced to

$$S_{direct} \sim \sum_j \frac{\omega R_j}{2\beta_j Q_{\beta_j}} \quad . \tag{5.5}$$

Referring to the sensitivity values in Table 5.7, the dependence of the sensitivity on frequency does in fact tend to be proportional to frequency for epicentral distances less than about 10 km, as predicted by Eq. (5.5) for the direct rays. Since the direct paths are not the most efficient paths for the more distant receivers, the more complex frequency dependence is not surprising for the epicentral distances greater than 10 km.

CHAPTER 6

SUMMARY AND CONCLUSIONS

An accurate and effective method for studying wave propagation in a layered viscoelastic half-space has been presented. The three-dimensional wave propagation problem is formulated and solved in the frequency domain with the azimuthal dependence represented by a Fourier series expansion. The complete response at a particular frequency for any source-receiver geometry is given in terms of semi-infinite integrals over wavenumber so as to automatically include all types of waves.

The integrands of these semi-infinite integrals consist of the product of a kernel that depends upon wavenumber, frequency, source-receiver geometry and earth structure times a Bessel function that depends upon wavenumber times epicentral distance. Based on the generalized reflection and transmission coefficient matrices, the kernels are evaluated in terms of highly efficient factorizations for the upgoing and downgoing wave amplitudes in each layer. The appearance of common factors is taken advantage of when computing the displacement and stress components for multiple source-receiver depth pairs.

The semi-infinite integrals are evaluated by direct integration along the real wavenumber axis. Basically, the kernels are sequentially sampled fine enough to allow piecewise polynomials to interpolate the amplitudes of the kernels between the integration points. Thereby, the numerical integration over each wavenumber interval is performed analytically, thus avoiding the oscillation hazard of the Bessel functions.

Also, since the radial dependence appears only in the Bessel functions, it is efficient to consider multiple epicentral distances simultaneously.

Introduction of realistic attenuation for shear and compressional waves shifts the singularities of the kernels off the real wavenumber axis. This facilitates the direct numerical integration along the real wavenumber axis without having to resort to principal values or contour integration. Since the response is obtained as a function of frequency, it is possible to allow any or all the earth parameters to vary with frequency. In particular, frequency dependent material attenuation can be implemented.

Source functions characterized by concentrated point forces, ring loads and point dislocations are considered in the formulation as well as in the numerical results. A set of five validation studies is presented to verify the accuracy and stability of the numerical integration scheme. The results of all the validation comparisons with other known complete solutions serve to lend considerable confidence in the method for uniform as well as layered semi-infinite media (the internal validations in Part II serve to further substantiate the reliability of the method).

The particular studies found in the validation section include comparisons to the following methods: exact contour integration approach for a uniform half-space (Wong, 1975); exact Cagniard approach for a uniform half-space (Pekeris and Lifson, 1957); exact Cagniard-deHoop approach for a uniform half-space (Johnson, 1974); complete finite element approach for a layered half-space (Day, 1977); complete discrete wavenumber/finite element approach for a layered half-space (Olson, 1978).

Studies appearing in the comparison section complement the validation exercises in that matches are obtained where the assumptions and/or approximations inherent in the partial solutions do not limit the results. The particular studies include comparisons to the generalized ray technique (Helmberger, 1968) and comparisons to the surface wave approach (Harkrider, 1964, 1970).

Studies found in the results section further demonstrate the utilizable flexibility of the method for seismological applications. In the first study, teleseismic ground motion due to a point dislocation is calculated at epicentral distances between 4 and 25 degrees of the earth's arclength. Next, the method is used to substantiate a hypothesized source depth for the October 6, 1974 Acapulco earthquake. In the third study, wave propagation in an oceanic crustal configuration is analyzed. The oceanic overburden is fully coupled into the sea floor by replacing the free-surface reflection coefficients and the first interface reflection and transmission coefficients by their fluid counterparts. The sensitivity to layer thickness is examined in the fourth study. Results for three "equivalent" layered profiles (coarse, intermediate and fine) are compared as a function of time and source-receiver geometry. The sensitivity to material attenuation as a function of frequency and source-receiver geometry is examined in the final study.

It is expected that the method and associated computer program will prove increasingly useful in various areas of theoretical seismology and earthquake engineering. Several earthquake engineering applications are presented in Part II of this dissertation.

REFERENCES

Ben-Menahem, A. and Vered, M., 1973. Extension and interpretation of the Cagniard-Pekeris method for dislocation sources, Bull. Seism. Soc. Am., 63, 1611-1636.

Bortfeld, R., 1967. Elastic waves in layered media, Geophys. Prospect., 15, 644.

Burridge, R., 1968. A new look at Lamb's problem, J. Physics Earth, 16, 169-171.

Cagniard, L., 1939. Reflexion et refraction des ondes seismigues progressives, Gauthier-Villars, Paris.

Cagniard, L., 1962. Reflection and refraction of progressive seismic waves, translated and revised by E. A. Flinn and C. H. Dix, McGraw Hill, New York.

Carpenter, E. W., 1966. A quantitative evaluation of teleseismic explosion records, Proc. Roy. Soc. (London) Ser. A, 290, 396-407.

Červený, V. and Ravindra, R., 1971. Theory of seismic head waves, University of Toronto Press.

Chapman, C. H., 1974. Generalized ray theory for an inhomogeneous medium, Geophys. J. R. astr. Soc., 36, 673-704.

Cisternas, A., Betancourt, O. and Leiva, A., 1973. Body waves in a "real earth". Part I, Bull. Seism. Soc. Am., 63, 145-156.

Day, S. M., 1977. Finite element analysis of seismic scattering problems, Ph.D. Thesis, University of California at San Diego, La Jolla, California.

deHoop, A. T., 1958. Representation theorems for the displacement in an elastic solid and their application to elastodynamic diffraction theory, D.Sc. Thesis, Technische Hogeschool, Delft.

deHoop, A. T., 1960. A modification of Cagniard's method for solving seismic pulse problems, Appl. Sci. Res., B8, 349-356.

Dickson, L. E., 1914. Elementary theory of equations, John Wiley and Sons, New York.

Dunkin, J. W., 1965. Computation of modal solutions in layered elastic media at high frequencies, Bull. Seism. Soc. Am., 55, 335-358.

Ewing, W. M., Jardetzky, W. S. and Press, F., 1957. Elastic waves in layered media, McGraw Hill, New York.

Fuchs, K. and Müller, G., 1971. Computation of synthetic seismograms with the reflectivity method and comparison with observations, Geophys. J. R. astr. Soc., 23, 417-433.

Futterman, W. I., 1962. Dispersive body waves, J. Geophys. Res., 67, 5279-5291.

Gilbert, F. and Backus, G. E., 1966. Propagator matrices in elastic wave and vibration problems, Geophysics, 31, 326-332.

Gilbert, F. and Helmberger, D. V., 1972. Generalized ray theory for a layered sphere, Geophys. J. R. astr. Soc., 27, 57-80.

Hannon, W. J., 1964. An application of the Haskell-Thomson matrix method to the synthesis of the surface motion due to dilatational waves, Bull. Seism. Soc. Am., 54, 2067-2079.

Harkrider, D. G., 1964. Surface waves in multilayered elastic media, Part I. Rayleigh and Love waves from buried sources in a multilayered elastic half-space, Bull. Seism. Soc. Am., 54, 627-680.

Harkrider, D. G., 1970. Surface waves in multilayered elastic media, Part II. Higher mode spectra and spectral ratios from point sources in plane layered earth models, Bull. Seism. Soc. Am., 60, 1937-1987.

Hartzell, S. H., 1978. Interpretation of earthquake strong ground motion and implications for earthquake mechanism, Ph.D. Thesis, University of California at San Diego, La Jolla, California.

Haskell, N. A., 1953. The dispersion of surface waves in multilayered media, Bull. Seism. Soc. Am., 43, 17-34.

Haskell, N. A., 1960. Crustal reflection of plane SH waves, J. Geophys. Res., 65, 4147-4150.

Haskell, N. A., 1962. Crustal reflection of plane P and SV waves, J. Geophys. Res., 67, 4751-4767.

Haskell, N. A., 1964. Radiation pattern of surface waves from point sources in a multilayered medium, Bull. Seism. Soc. Am., 54, 377-393.

Helmberger, D. V., 1968. The crust-mantle transition in the Bering Sea, Bull. Seism. Soc. Am., 58, 179-214.

Helmberger, D. V., 1974. Generalized ray theory for shear dislocations, Bull. Seism. Soc. Am., 64, 45-64.

Herrmann, R. B., 1977. Research study of earthquake generated SH waves in the near-field and near-regional field. Final report under contract DACW39-76-C-0058, Waterways Experiment Station, Vicksburg.

Pekeris, C. L., 1955, The seismic surface pulse, Proc. Nat. Acad. Sci., 41, 469-480.

Pekeris, C. L., 1955. The seismic buried pulse, Proc. Nat. Acad. Sci., 41, 629-639.

Pekeris, C. L. and Lifson, H., 1957. Motion of the surface of a uniform elastic half-space produced by a buried pulse, J. Acoust. Sci. Am., 29, 1233-1238.

Pekeris, C. L., Alterman, Z., Abramovici, F. and Jaroisch, H., 1965. Propagation of a compressional pulse in a layered solid, Rev. Geophys., 3, 25-47.

Pestel, E. C. and Leckie, F. A., 1963. Matrix methods in elastomechanics, McGraw Hill, New York.

Randall, M. J., 1967. Fast programs for layered half-space problems, Bull. Seism. Soc. Am., 57, 1299-1315.

Richards, P. G., 1971. Elastic wave solutions in stratified media, Geophysics, 36, 798-809.

Schwab, F., 1970. Surface-wave dispersion computations: Knopoff's Method, Bull. Seism. Soc. Am., 60, 1491-1520.

Spencer, T. W., 1960. The method of generalized reflection and transmission coefficients, Geophysics, 25, 625-641.

Thomson, W. T., 1950. Transmission of elastic waves through a stratified solid medium, J. Appl. Phys. 21, 89-93.

Thrower, E. N., 1965. The computation of the dispersion of elastic waves in layered media, J. Sound Vib., 2, 210-226.

Vered, M. and Ben-Menahem, A., 1973. Application of synthetic seismograms to the study of low-magnitude earthquakes and crustal structure in the Northern Red Sea Region, Bull. Seism. Soc. Am., 64, 1221-1237.

Watson, T. H., 1970. A note on fast computation of Rayleigh wave dispersion in the multilayered elastic half-space, Bull. Seism. Soc. Am., 60, 161-166.

Wiggins, R. A. and Helmberger, D. V., 1974. Synthetic seismogram computation by expansion in generalized rays, Geophys. J. R. astr. Soc., 37, 73-90.

Wong, H. L., 1975. Dynamic soil-structure interaction, Report EERL 75-01, Earthquake Engineering Research Laboratory, California Institute of Technology, Pasadena, California.

$$r^u_{spo} = -4k\nu_1\left(2k^2 - c_1^{-1}\right)/\Delta_R$$

$$r^u_{sso} = \left[\left(2k^2 - c_1^{-1}\right)^2 + 4k^2\nu_1\nu_1'\right]/\Delta_R \qquad \text{(A1.3)}$$

where

$$\Delta_R = \left(2k^2 - c_1^{-1}\right)^2 - 4k^2\nu_1\nu_1' \qquad \text{(A1.4)}$$

is the Rayleigh determinant for a half-space with the properties of the surface layer.

The reflection and transmission coefficients for waves impinging on the jth interface from below are

$$r^u_{ppj} = -\Big\{4k^2D^2(j,j+1)(k^2 - \nu_j\nu_j')(k^2 + \nu_{j+1}\nu_{j+1}')$$
$$- 4k^2D(j,j+1)\left[d_j(k^2 - \nu_j\nu_j') - d_{j+1}(k^2 + \nu_{j+1}\nu_{j+1}')\right]$$
$$+ \left[(d_{j+1} - d_j)^2 k^2 + (d_{j+1}\nu_{j+1}' + d_j\nu_j')(d_{j+1}\nu_{j+1} - d_j\nu_j)\right]\Big\}/\Delta(j,j+1)$$

$$r^u_{psj} = 2k\nu_{j+1}'\Big\{4k^2D^2(j,j+1)(k^2 - \nu_j\nu_j') + 2D(j,j+1)\left[2d_{j+1}k^2 - d_j(k^2 - \nu_j\nu_j')\right]$$
$$+ d_{j+1}(d_{j+1} - d_j)\Big\}/\Delta(j,j+1)$$

$$r^u_{spj} = -2k\nu_{j+1}\Big\{4k^2D^2(j,j+1)(k^2 - \nu_j\nu_j') + 2D(j,j+1)\left[2d_{j+1}k^2 - d_j(k^2 - \nu_j\nu_j')\right]$$
$$+ d_{j+1}(d_{j+1} - d_j)\Big\}/\Delta(j,j+1)$$

$$r^u_{ssj} = \Big\{4k^2D^2(j,j+1)(k^2 - \nu_j\nu_j')(k^2 + \nu_{j+1}\nu_{j+1}')$$
$$- 4k^2D(j,j+1)\left[d_j(k^2 - \nu_j\nu_j') - d_{j+1}(k^2 + \nu_{j+1}\nu_{j+1}')\right]$$
$$+ \left[(d_{j+1} - d_j)^2k^2 + (d_{j+1}\nu_{j+1}' - d_j\nu_j')(d_{j+1}\nu_{j+1} + d_j\nu_j)\right]\Big\}/\Delta(j,j+1)$$

(A1.5)

APPENDIX II.

MODIFICATIONS FOR LARGE WAVENUMBERS

The matrices $\bar{I}^j_{pq}$ (p = 1,2,3; q = 1,2) appearing in the integral representation described in Section 3 are given by

$$\bar{I}^j_{11} = \begin{bmatrix} 1 & 1 \\ -(\kappa_j-1) & 1 \end{bmatrix}, \quad \bar{I}^j_{12} = \begin{bmatrix} 1 & 1 \\ (\kappa_j-1) & -1 \end{bmatrix}$$

$$\bar{I}^j_{21} = d_j^{-1} \begin{bmatrix} (\kappa_j-3)kc_j - r_j & -2kc_j - \bar{\nu}_j \\ (\kappa_j-1)kc_j - r'_j & -2kc_j - \bar{\nu}'_j \end{bmatrix}$$

$$\bar{I}^j_{22} = d_j^{-1} \begin{bmatrix} -(\kappa_j-3)kc_j + r_j & +2kc_j + \bar{\nu}_1 \\ (\kappa_j-1)kc_j - r'_j & -2kc_j - \bar{\nu}'_j \end{bmatrix}$$

$$\bar{I}^j_{31} = \bar{I}^j_{32} = d_j^{-1} \begin{bmatrix} (4-\kappa_j)2kc_j - 2\left(\frac{\kappa_j-3}{\kappa_j+1}\right)r'_j & 2kc_j + 2\left(\frac{\kappa_j-3}{\kappa_j+1}\right)\bar{\nu}'_j \\ (5-\kappa_j)kc_j - \left(\frac{\kappa_j-3}{\kappa_j+1}\right)r'_j & 2kc_j + \left(\frac{\kappa_j-3}{\kappa_j+1}\right)\bar{\nu}'_j \end{bmatrix} \tag{A2.1}$$

in which, $\kappa_j = (1+\gamma_j^2)/(1-\gamma_j^2)$, and

$$\bar{\nu}_j = (\nu_j-k)/(k^2 - \nu_j\nu'_j) \ , \quad \bar{\nu}'_j = (\nu'_j-k)/(k^2 - \nu_j\nu'_j)$$

$$r_j = a_j + \bar{\nu}_j \ , \quad r'_j = a_j + (\kappa_j-1)\bar{\nu}'_j$$

$$a_j = \left[\frac{\kappa_j}{k^2-\nu_j\nu'_j} - (1+\kappa_j)c_j\right]k \ . \tag{A2.2}$$

The terms r_j, r_j', $\bar{\nu}_j$ and $\bar{\nu}_j'$ are order $1/k$ as $k \to \infty$. The asymptotic values of these matrices as $k \to \infty$ are

$$\begin{bmatrix} \bar{I}_{12}^j & \bar{I}_{21}^j \\ \bar{I}_{21}^j & \bar{I}_{22}^j \\ \bar{I}_{31}^j & \bar{I}_{32}^j \end{bmatrix} \sim \left[\begin{array}{cc:cc} 1 & 1 & 1 & 1 \\ -(\kappa_j-1) & 1 & (\kappa_j-1) & -1 \\ \hdashline (\kappa_j-3)k\mu_{oj} & -2k\mu_{oj} & -(\kappa_j-3)k\mu_{oj} & 2k\mu_{oj} \\ (\kappa_j-1)k\mu_{oj} & -2k\mu_{oj} & (\kappa_j-1)k\mu_{oj} & -k\mu_{oj} \\ \hdashline 2(4-\kappa_j)k\mu_{oj} & 2k\mu_{oj} & 2(4-\kappa_j)k\mu_{oj} & 2k\mu_{oj} \\ (5-\kappa_j)k\mu_{oj} & 2k\mu oj & (5-\kappa_j)k\mu_{oj} & 2k\mu_{oj} \end{array}\right] \tag{A2.3}$$

where $\mu_{oj} = \mu_j/\bar{\mu}$.

The matrix $\bar{E}_d^j(z_o)$ defined by Eq. (3.63) may be written in the form

$$\bar{E}_d^j(z_o) = e^{-\nu_j(z_o - z_o^{j-1})} \times \begin{bmatrix} 1 - \bar{\nu}_j'\left(k + \frac{\nu_j - k}{\kappa_j}\right) E_j(z_o - z_o^{j-1}) & -\bar{\nu}_j'\left(\frac{\nu_j - k}{\kappa_j}\right) E_j(z_o - z_o^{j-1}) \\ -\left(k + \frac{\nu_j - k}{\kappa_j}\right)\left[(1+\kappa_j)c_j k + r_j'\right] E_j(z_o - z_o^{j-1}) & 1 - \bar{\nu}_j\left[k + \left(\frac{\kappa_j - 1}{\kappa_j}\right)(\nu_j' - k)\right] E_j(z_o - z_o^{j-1}) \end{bmatrix} \tag{A2.4}$$

where

$$E_j(z_o) = \exp\left[(\nu_j - \nu_j')(z_o)\right] - 1 \tag{A2.5}$$

It is important to notice that

$$\bar{E}_d^j(z_o) \sim \exp\left[-k(z_o - z_o^{j-1})\right] \begin{bmatrix} 1 & 0 \\ -k(z_o - z_o^{j-1}) & 1 \end{bmatrix} \text{ as } k \to \infty \ . \tag{A2.6}$$

The matrix $\bar{E}_u^j(z_o)$ defined by Eq. (3.63) may be obtained from $\bar{E}_d^j(z_o)$ by

$$\bar{E}_u^j(z_o) = \bar{E}_d^j(z_o^{j-1} + z_o^j - z_o) \tag{A2.7}$$

In particular, as $k \to \infty$

$$\bar{E}_u^j(z_o) \sim \exp\left[k(z_o - z_o^j)\right] \begin{bmatrix} 1 & 0 \\ k(z_o - z_o^j) & 1 \end{bmatrix} \ . \tag{A2.8}$$

The source terms $\bar{S}_{dn}^{\ell}$ and $\bar{S}_{un}^{\ell}$ defined by Eqs. (3.70) may also be written in the form

$$\bar{S}_{d0}^{\ell} = \frac{(k/\nu_\ell')e^{\nu_\ell(z_o^s - z_o^{\ell-1})}}{(1+\kappa_\ell)c_\ell d_\ell^{-1}k + a_\ell d_\ell^{-1}} \begin{Bmatrix} -1 + \bar{\nu}_\ell k E_\ell(z_o^s - z_o^{\ell-1}) \\ 1 + \left[(1+\kappa_\ell)c_\ell k + r_\ell'\right] k E_\ell(z_o^s - z^{\ell-1}) \end{Bmatrix}$$

$$\bar{S}_{u0}^{\ell} = \frac{-(k/\nu_\ell')e^{\nu_\ell(z_o^\ell - z_o^s)}}{(1+\kappa_\ell)c_\ell d_\ell^{-1}k + a_\ell d_\ell^{-1}} \begin{Bmatrix} -1 + \bar{\nu}_\ell' k E_\ell(z_o^\ell - z_o^s) \\ 1 + \left[(1+\kappa_\ell)c_\ell k + r_\ell'\right] k E_\ell(z_o^\ell - z_o^s) \end{Bmatrix}$$

$$\bar{S}^{\ell}_{d1} = \frac{(k/\nu_\ell)e^{\nu_\ell(z_o^s - z_o^{\ell-1})}}{(1+\kappa_\ell)c_\ell d_\ell^{-1}k + a_\ell d_\ell^{-1}} \begin{Bmatrix} -1 + \bar{\nu}'_\ell \nu_\ell E_\ell (z_o^s - z_o^{\ell-1}) \\ -(\kappa_\ell - 1) + \left[(1+\kappa_\ell)c_\ell k + r'_\ell\right]\nu_\ell E_\ell (z_o^s - z_o^{\ell-1}) \end{Bmatrix}$$

$$\bar{S}^{\ell}_{u1} = \frac{(k/\nu_\ell)e^{\nu_\ell(z_o^\ell - z_o^s)}}{(1+\kappa_\ell)c_\ell d_\ell^{-1}k + a_\ell d_\ell^{-1}} \begin{Bmatrix} -1 + \bar{\nu}'_\ell \nu_\ell E_\ell (z_o^\ell - z_o^s) \\ -(\kappa_\ell - 1) + \left[(1+\kappa_\ell)c_\ell k + r'_\ell\right]\nu_\ell E_\ell (z_o^\ell - z_o^s) \end{Bmatrix} . \tag{A2.9}$$

The asymptotic values of the source terms are given by

$$\bar{S}^{\ell}_{d0} \sim \frac{e^{k(z_o^s - z_o^{\ell-1})}}{(1+\kappa_\ell)\mu_{o\ell}\, k} \begin{Bmatrix} -1 \\ 1 - k(z_o^s - z_o^{\ell-1}) \end{Bmatrix}$$

$$\bar{S}^{\ell}_{u0} \sim \frac{e^{k(z_o^\ell - z_o^s)}}{(1+\kappa_\ell)\mu_{o\ell}\, k} \begin{Bmatrix} 1 \\ -1 + k(z_o^\ell - z_o^s) \end{Bmatrix}$$

$$\bar{S}^{\ell}_{d1} \sim \frac{e^{k(z_o^s - z_o^{\ell-1})}}{(1+\kappa_\ell)\mu_{o\ell}\, k} \begin{Bmatrix} -1 \\ -(\kappa_\ell - 1) - k(z_o^s - z_o^{\ell-1}) \end{Bmatrix}$$

$$\bar{S}^{\ell}_{u1} \sim \frac{e^{k(z_o^\ell - z_o^s)}}{(1+\kappa_\ell)\mu_{o\ell}\, k} \begin{Bmatrix} -1 \\ -(\kappa_\ell - 1) - k(z_o^\ell - z_o^s) \end{Bmatrix} \quad \text{as} \quad k \to \infty . \tag{A2.10}$$

The asymptotic values presented in Eqs. (A2.3), (A2.6), (A2.8) and (A2.10) correspond to the static integral representation obtained by Muki [1955]. (In the static case the parameter $\bar{\beta}/\omega$ must be interpreted as a length of reference.)

APPENDIX III.

STATIC INTEGRAL REPRESENTATION OF THE DISPLACEMENT AND STRESS FIELDS

As discussed in Section 4.2, closed form expressions for the static displacement and stress fields are necessary in the method of integration over wavenumber when the receiver depth z_o coincides with the source depth z_o^s. To evaluate the Hankel transform-type integrals depicted in Eq. (4.21) for proximate source-receiver depths, the static integral representations are introduced as demonstrated in Eq. (4.23).

The static integrands (symbolized by F(0) in Eq. (4.23)) for a semi-infinite viscoelastic half-space having properties of the j^{th} layer (which contains both the source and the receiver) follow immediately for all the displacement and stress components. Utilizing the notation and normalization of Eq. (4.2), the closed form expressions for the n=0 components are given as:

$$U_{10}^j = \frac{-1}{2Kc_j}\left\{\left[K\left(\gamma_j^2-1\right)\left(z_o-z_o^s\right)\right]e_1 + \left[2K^2\left(\gamma_j^2-1\right)z_o z_o^s - K\left(\gamma_j^2+1\right)\left(z_o-z_o^s\right) - \left(\frac{2\gamma_j^2}{\gamma_j^2-1}\right)\right]e_2\right\}$$

$$U_{20}^j = \frac{-1}{2Kc_j}\left\{\left[K\left(\gamma_j^2-1\right)\left|z_o-z_o^s\right| - \left(\gamma_j^2+1\right)\right]e_1 + \left[2K^2\left(\gamma_j^2-1\right)z_o z_o^s - K\left(\gamma_j^2+1\right)\left(z_o+z_o^s\right) + \left(\frac{\gamma_j^4+1}{\gamma_j^2-1}\right)\right]e_2\right\}$$

γ_j^{-1} /J)

$$U_{21}^{j} = \frac{-1}{2Kc_j}\left\{\left[K\left(\gamma_j^2-1\right)\left(z_o-z_o^s\right)\right]e_1 - \left[2K^2\left(\gamma_j^2-1\right)z_o z_o^s + K\left(\gamma_j^2+1\right)\left(z_o-z_o^s\right) - \left(\frac{2\gamma_j^2}{\gamma_j^2-1}\right)\right]e_2\right\}$$

$$\sigma_{210}^{j} + \sigma_{230}^{j} = -\left\{\left[-K\left(\gamma_j^2-1\right)\left(z_o-z_o^s\right)\right]e_1 + \left[2K^2\left(\gamma_j^2-1\right)z_o z_o^s + K\left(\gamma_j^2+1\right)z_o - K\left(\gamma_j^2-1\right)z_o^s\right]e_2\right\}$$

$$-\sigma_{210}^{j} + \sigma_{230}^{j} = -\left\{\left[-K\left(\gamma_j^2-1\right)\left(z_o-z_o^s\right) - 2S\right]e_1 + \left[2K^2\left(\gamma_j^2-1\right)z_o z_o^s + K\left(\gamma_j^2+1\right)z_o - K\left(\gamma_j^2-1\right)z_o^s - 2\right]e_2\right\}$$

$$\sigma_{220}^{j} = -\left\{\left[-K\left(\gamma_j^2-1\right)\left|z_o-z_o^s\right| - \gamma_j^2\right]e_1 + \left[2K^2\left(\gamma_j^2-1\right)z_o z_o^s + K\left(\gamma_j^2+1\right)z_o + K\left(\gamma_j^2-1\right)z_o^s + \gamma_j^2\right]e_2\right\}$$

$$\sigma_{331}^{j} = -\left\{\left[K\left(\gamma_j^2-1\right)\left|z_o-z_o^s\right| - 3\left(\gamma_j^2-1\right)\right]e_1 + \left[-2K^2\left(\gamma_j^2-1\right)z_o z_o^s - K\left(\gamma_j^2+1\right)z_o + K\left(7\gamma_j^2-5\right)z_o^s + \left(\frac{3\gamma_j^4+2\gamma_j^2-3}{\gamma_j^2-1}\right)\right]e_2\right\}$$

$$\sigma_{111}^{j} = -\left\{\left[K\left(\gamma_j^2-1\right)\left|z_o-z_o^s\right| - \left(\gamma_j^2-2\right)\right]e_1 + \left[-2K^2\left(\gamma_j^2-1\right)z_o z_o^s - K\left(\gamma_j^2+1\right)z_o + 3K\left(\gamma_j^2-1\right)z_o^s + \left(\gamma_j^2+2\right)\right]e_2\right\}$$

$$\sigma_{311}^{j} = -\left\{-e_1 - e_2\right\} \qquad \text{(A3.1)}$$

in which

$$S = \mathrm{sgn}\left(z_o - z_o^s\right), \quad e_1 = \exp\left(-K\left|z_o - z_o^s\right|\right), \quad e_2 = \exp\left(-K\left|z_o + z_o^s\right|\right). \qquad (A.3.2)$$

Introducing the static integrands from Eqs. (A3.1) into Eqs. (4.2) and evaluating the integrals analytically leads to the following expressions for the static integrals (symbolized by $I_n(0)$ in Eq. (4.23)) for a semi-infinite viscoelastic half-space having properties of the j^{th} layer. The $n=0$ components of the displacement and stress fields are given by

$$U^j_{r_o} = \frac{-1}{2c_1}\left\{\frac{\left(\gamma_j^2-1\right)(\delta-\delta_s)}{R_1^3} + \frac{6\left(\gamma_j^2-1\right)\delta\delta_s(\delta+\delta_s)}{R_2^5} - \frac{\left(\gamma_j^2+1\right)(\delta-\delta_s)}{R_2^3} - \left(\frac{2\gamma_j^2}{\gamma_j^2-1}\right)\frac{R_2 - (\delta+\delta_s)}{R_2}\right\}$$

$$U^j_{z_o} = \frac{-1}{2c_1}\left\{\frac{-2(\delta-\delta_s)^2 - \left(\gamma_j^2+1\right)}{R_1^3} + \frac{6\left(\gamma_j^2-1\right)\delta\delta_s(\delta+\delta_s)^2}{R_2^5} - \frac{\left(\gamma_j^2+1\right)(\delta+\delta_s)^2 + 2\left(\gamma_j^2-1\right)\delta\delta_s}{R_2^3} + \left(\frac{\gamma_j^4+1}{\gamma_j^2-1}\right)\frac{1}{R_2}\right\}$$

$$\Sigma^j_{rz_o} = -\left\{\frac{-3\left(\gamma_j^2-1\right)(\delta-\delta_s)^2}{R_1^5} + \frac{\gamma_j^2}{R_1^3} - \frac{30\left(\gamma_j^2-1\right)\delta\delta_s(\delta+\delta_s)^2}{R_2^7} + \frac{3\left(\gamma_j^2+1\right)\delta(\delta+\delta_s) + 3\left(\gamma_j^2-1\right)\delta_s(3\delta+\delta_s)}{R_2^5} - \frac{\gamma_j^2}{R_2^3}\right\}$$

$$\Sigma^j_{rr_0} + \Sigma^j_{\theta\theta_0} = -\left\{\frac{-3\left(\gamma_j^2-1\right)(\delta-\delta_s)}{R_1^5} - \frac{2\delta_j^2(\delta-\delta_s)}{R_1^3} - \frac{30\left(\gamma_j^2-1\right)\delta\delta_s(\delta+\delta_s)}{R_2^7}\right.$$

$$+ \frac{3\left(\gamma_j^2+1\right)(\delta-\delta_s) - 12\gamma_j^2\delta_s(\delta+\delta_s)^2 - 12\left(\gamma_j^2-1\right)\delta_s^2(\delta+\delta_s)}{R_2^5}$$

$$\left. + \frac{2}{\left(\gamma_j^2-1\right)}\,\frac{\gamma_j^4\delta + \left(7\gamma_j^4 - 6\delta_j^2\right)\delta_s}{R_2^3}\right\}$$

$$\Sigma^j_{rr_0} + \frac{2c_j}{d_j r_o}\,U^j_{r_0} = -\left\{\frac{-3\left(\gamma_j^2-1\right)(\delta-\delta_s)}{R_1^3} - \frac{(\delta-\delta_s)}{R_1^3} - \frac{30\left(\gamma_j^2-1\right)\delta\delta_s(\delta+\delta_s)}{R_2^7}\right.$$

$$\left. + \frac{3\left(\gamma_j^2+1\right)(\delta-\delta_s) - 6\gamma_j^2\delta_s(\delta+\delta_s)^2 + 6\left(\delta_j^2-1\right)\delta_s\left(\delta^2-\delta_s^2\right)}{R_2^5} - \frac{(\delta-\delta_s)-8\gamma_j^2\delta_s}{R_2^3}\right\}$$

$$U^j_{\theta_0} = \Sigma^j_{r\theta_0} = \Sigma^j_{\theta r_0} = 0$$

with the corresponding n=1 components given as

$$U^j_{r_1} + U^j_{\theta_1} = \frac{-1}{2c_j}\left\{\frac{\gamma_j^2-1}{R_1^3} - \frac{6\left(\gamma_j^2-1\right)\delta\delta_s}{R_2^5} - \frac{\gamma_j^2+1}{R_2^3} - \left(\frac{2\gamma_j^2}{\gamma_j^2-1}\right)\frac{\left[R_2-(\delta+\delta_s)\right]^2}{R_2}\right\}$$

$$U^j_{r_1} - U^j_{\theta_1} = \frac{+1}{2c_j}\left\{\frac{2\left(\gamma_j^2-1\right)(\delta-\delta_s)^2 + \left(\gamma_j^2+3\right)}{R_1^3} + \frac{6\left(\gamma_j^2-1\right)\delta\delta_s}{R_2^5} + \frac{\left(\gamma_j^2+1\right) - 4\left(\gamma_j^2-1\right)\delta\delta_s}{R_2^3}\right.$$

$$\left. - \frac{2\left(\gamma_j^4-\gamma_j^2+1\right)}{\gamma_j^2-1}\,\frac{1}{R_2}\right\}$$

$$U^j_{z_1} = \frac{-1}{2c_j}\left\{\frac{(\gamma_j^2-1)(\delta-\delta_s)}{R_1^3} - \frac{6(\gamma_j^2-1)\delta\delta_s(\delta+\delta_s)}{R_2^5} - \frac{(\gamma_j^2+1)(\delta-\delta_s)}{R_2^3} + \frac{2\gamma_j^2}{\gamma_j^2-1}\frac{R_2-(\delta+\delta_s)}{R_2}\right\}$$

$$\Sigma^j_{rz_1} + \Sigma^j_{\theta z_1} = -\left\{\frac{-3(\gamma_j^2-1)(\delta-\delta_s)}{R_1^5} + \frac{30(\gamma_j^2-1)\delta\delta_s(\delta+\delta_s)}{R_2^7} + \frac{3\left[(\gamma_j^2+1)\delta-(\gamma_j^2-1)\delta_s\right]}{R_2^5}\right\}$$

$$\Sigma^j_{rz_1} - \Sigma^j_{\theta z_1} = +\left\{\frac{3(\gamma_j^2-1)(\delta-\delta_s)}{R_1^5} - \frac{2\gamma_j^2(\delta-\delta_s)}{R_1^3} - \frac{30(\gamma_j^2-1)\delta\delta_s(\delta+\delta_s)}{R_2^7} - \frac{3\left[(\gamma_j^2+1)\delta-(\gamma_j^2-1)\delta_s\right]-12(\gamma_j^2-1)\delta\delta_s(\delta+\delta_s)}{R_2^5} + \frac{2\gamma_j^2(\delta-\delta_s)}{R_2^3}\right\}$$

$$\Sigma^j_{zz_1} = -\left\{\frac{-3(\gamma_j^2-1)(\delta-\delta_s)^2}{R_1^5} - \frac{\gamma_j^2}{R_1^3} + \frac{30(\gamma_j^2-1)\delta\delta_s(\delta+\delta_s)^2}{R_2^7} + \frac{3(\gamma_j^2+1)\delta(\delta+\delta_s) - 3(\gamma_j^2-1)\delta_s(\delta-\delta_s)}{R_2^5} + \frac{\delta_j^2}{R_2^3}\right\}$$

$$\Sigma^j_{rr_1} + \Sigma^j_{\theta\theta_1} = -\left\{\frac{-3(\gamma_j^2-1)}{R_1^5} + \frac{30(\gamma_j^2-1)\delta\delta_s}{R_2^7} + \frac{3(\gamma_j^2+1) + 24(\gamma_j^2-1)\delta_s^2 + 12\delta_s(\delta+\delta_s)}{R_2^5} + \frac{2\gamma_j^2}{(\gamma_j^2-1)}\frac{1}{R_2^3}\right\}$$

$$\Sigma^j_{rr_1} + \frac{2c_j}{d_j r_o}\left(U^j_{r_1} + U^j_{\theta_1}\right) = -\left\{\frac{-3\left(\gamma_j^2-1\right)}{R_1^5} + \frac{\left(2\gamma_j^2-1\right)}{R_1^3} - \frac{30\left(\gamma_j^2-1\right)\delta\delta_s(\delta+\delta_s)^2}{R_2^7}\right.$$

$$\left. - \frac{3\left(\gamma_j^2+1\right)\delta^2 + \left(5\gamma_j^2-1\right)\delta_s(\delta+\delta_s)}{R_2^5} + \frac{\gamma_j^2+2}{R_2^3}\right\}$$

$$\Sigma^j_{r\theta_1} + \frac{2c_j}{d_j r_o}\left(U^j_{r_1} + U^j_{\theta_1}\right) = -\left\{\frac{-1}{R_1^3} - \frac{1}{R_2^3}\right\} \qquad \text{(A3.3)}$$

in which

$$\delta = \frac{z_o}{r_o} = \frac{z}{r}\,, \quad \delta_s = \frac{z^s_o}{r_o} = \frac{z^s}{r}$$

$$R_1 = \left[(\delta-\delta_s)^2 + 1\right]^{1/2}, \quad R_2 = \left[(\delta+\delta_s)^2 + 1\right]^{1/2}\,. \qquad \text{(A3.4)}$$

APPENDIX IV

MOTION OF THE FREE SURFACE DUE TO A BURIED DISLOCATION USING RECIPROCITY RELATIONS

The displacement field at the free surface resulting from the action of a buried dislocation is derived in terms of the stress tensor solution evaluated at the depth of the dislocation resulting from the action of a point force at the free surface.

As shown in Figure A4.1, the idealized dislocation occurs at a point $\vec{y}$ on surface S in volume V. The receiver is located at point $\vec{x}$ on the free surface of volume V. Volume V may correspond to the viscoelastic layered half-space consistent with previous usage in Chapter 3 of the present work.

The local fault geometry is defined with respect to the unit vectors $\hat{e}_1$, $\hat{e}_2$, $\hat{e}_3$ in the Cartesian coordinate system x_1, x_2, x_3. The x_1 axis is aligned with the strike of the fault (direction of $\hat{e}_1$, which is at an azimuth of β degrees from the receiver). The slip vector $\vec{\delta}(\vec{y})$ is constrained to have a rake of γ degrees in the plane defining surface S (see Figure A4.2):

$$\vec{\delta}(\vec{y}) = \delta_{\infty}(\vec{y})\left[(\cos\gamma)\hat{e}_1 + (\sin\gamma\cos\delta)\hat{e}_2 + (\sin\gamma\sin\delta)\hat{e}_3\right] . \quad (A4.1)$$

In Eq. (A4.1), δ is the dip of the fault plane measured counterclockwise from the x_2 axis, such that the projection of the unit normal to surface S in the x_1, x_2, x_3 system is

$$\vec{\nu}(\vec{y}) = (-\sin\delta)\hat{e}_2 + (\cos\delta)\hat{e}_3 , \quad (A4.2)$$

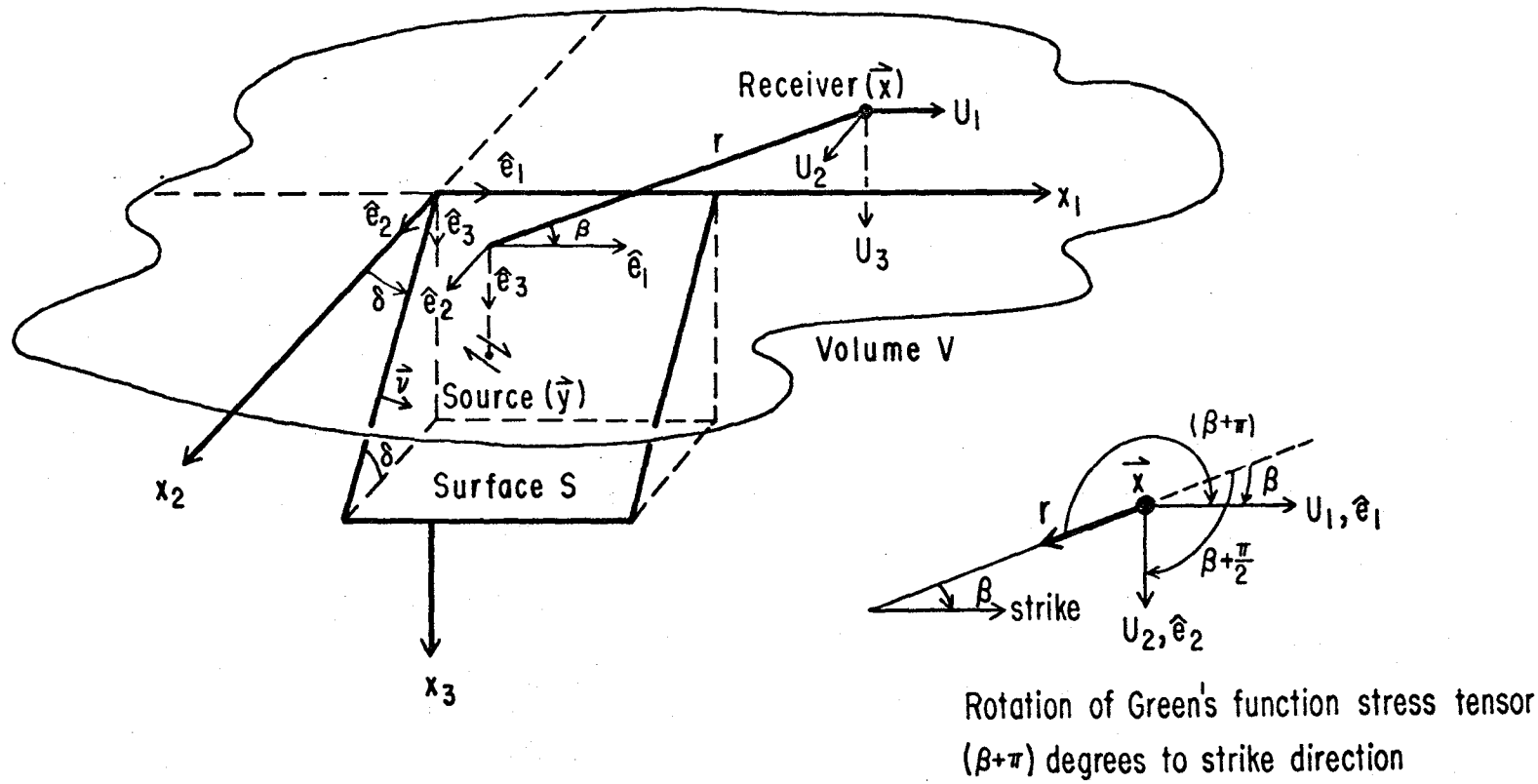

Figure A4.1. Coordinate system and source-receiver geometry for buried point dislocation.

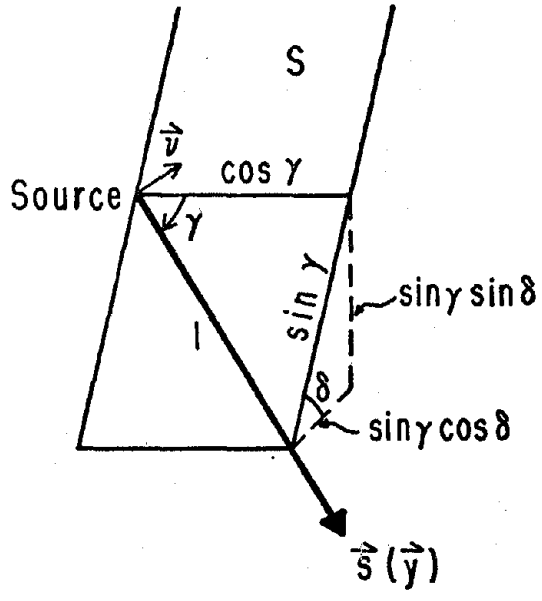

Figure A4.2. Slip vector orientation on surface S.

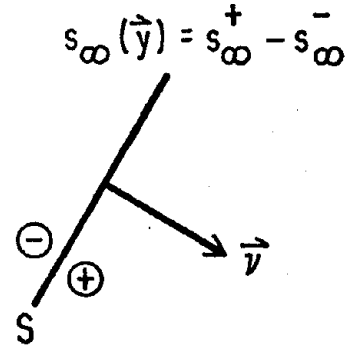

Figure A4.3. Sign convention for slip vector.

and $\delta_\infty(\vec{y})$ is the amplitude of the dislocation, i.e., the displacement of the positive side of the fault relative to the negative side with the unit normal $\vec{\nu}(\vec{y})$ positive pointing from the negative side to the positive side (see Figure A4.3).

Assuming that the displacement and stress components have harmonic time dependence, it is convenient to apply the Knopoff-deHoop (1958) representation theorem to volume V of Figure A4.1. In the absence of body forces in V and assuming continuity of tractions on S, the representation theorem in Cartesian coordinates is written in the frequency domain as

$$U_i(\vec{x};\omega) = -\int_S \overset{\nu}{H}_{ji}(\vec{y},\vec{x};\omega)U_j(\vec{y};\omega)dS(\vec{y}), \qquad (i,j = 1,2,3) \tag{A4.3}$$

in which the point $\vec{x}$ has been specialized to be on the free surface (defined by the plane $x_3 = 0$).

In Eq. (A4.3), the factors $\exp(i\omega t)$ have been omitted and $\overset{\nu}{H}_{ji}(\vec{y},\vec{x};\omega)$ denotes the j-component of the traction vector at $\vec{y} \in S$ due to a concentrated point load at $\vec{x}$ in the i-direction. $U_j(\vec{y};\omega)$ represents the j-component of the displacement vector prescribed at $\vec{y} \in S$, which for this problem is equivalent to the slip vector component $\delta_j(\vec{y})$ as defined in Eq. (A4.1). The summation convention over repeated indices is understood.

The tractions $\overset{\nu}{H}_{ji}(y,x;\omega)$ are expressed in terms of the stresses by

$$\overset{\nu}{H}_{ji}(\vec{y},\vec{x};\omega) = \tau_{kj_i}(\vec{y},\vec{x};\omega)\ \nu_k(\vec{y}) \tag{A4.4}$$

in which $\tau_{kj_i}(\vec{y},\vec{x};\omega)$ denotes the kj-component of the stress tensor at $\vec{y} \in S$ due to a concentrated point load at $\vec{x}$ in the i-direction.

Eq. (A4.4) is introduced into Eq. (A4.3) in conjunction with Eq. (A4.2). Then substituting the slip vector $\vec{a}(\vec{y})$ into the right-hand-side of Eq. (A4.3) leads, after simplification, to the final expression for the displacements at $\vec{x}$ due to the buried point dislocation at $\vec{y} \in S$ (integration over surface S is omitted by not considering an extended source):

$$\begin{aligned} U_i(\vec{x};\omega) = {} & (\cos\gamma\sin\delta)\ \tau_{12_i}(\vec{y},\vec{x};\omega) \\ & - (\cos\gamma\cos\delta)\ \tau_{13_i}(\vec{y},\vec{x};\omega) \\ & - (\sin\gamma\cos 2\delta)\ \tau_{23_i}(\vec{y},\vec{x};\omega) \\ & + (1/2\ \sin\gamma\sin 2\delta)\ \tau_{22_i}(\vec{y},\vec{x};\omega) \\ & - (1/2\ \sin\gamma\sin 2\delta)\ \tau_{33_i}(\vec{y},\vec{x};\omega) \quad . \end{aligned} \tag{A4.5}$$

All that remains is to relate the stresses $\tau_{kj_i}(\vec{y},\vec{x};\omega)$ in the x_1, x_2, x_3 system to the stresses in the system of cylindrical coordinates r, θ, z. Using the notation of Eqs. (3.4), (3.5), the clockwise rotation of $(\beta + \pi)$ degrees from the r, θ, z system to the x_1, x_2, x_3 system (as shown at the bottom of Figure A4.1) is delineated by

$$\tau_{11_i} = \frac{1}{2}\left(\sigma^j_{rr_i} + \sigma^i_{\theta\theta_i}\right) + \frac{1}{2}\left(\sigma^j_{rr_i} - \sigma^j_{\theta\theta_i}\right)\cos 2\beta + \sigma^j_{\theta r_i}\sin 2\beta$$

$$\tau_{22_i} = \frac{1}{2}\left(\sigma^j_{rr_i} + \sigma^j_{\theta\theta_i}\right) - \frac{1}{2}\left(\sigma^j_{rr_i} - \sigma^j_{\theta\theta_i}\right)\cos 2\beta - \sigma^j_{\theta r_i}\sin 2\beta$$

$$\tau_{12_i} = -\frac{1}{2}\left(\sigma^j_{rr_i} - \sigma^j_{\theta\theta_i}\right)\sin 2\beta + \sigma^j_{\theta r_i}\cos 2\beta$$

$$\tau_{13_i} = -\left(\sigma^j_{rz_i}\cos\beta + \sigma^j_{\theta z_i}\sin\beta\right)$$

$$\tau_{23_i} = -\left(-\sigma^j_{rz_i}\sin\beta + \sigma^j_{\theta z_i}\cos\beta\right)$$

$$\tau_{33_i} = \sigma^j_{zz_i} \qquad \text{(A4.6)}$$

where the arguments $(\vec{y}, \vec{x}; \omega)$ have been omitted for brevity and the superscript j indicates the layer in which the stress tensor solution is monitored.

For completeness and consistency with the notation used in Chapter 3, the stresses appearing in the right-hand-side of Eq. (A4.6) are presently listed. The stress components for the $i = 1,2$ terms (concentrated point load at $\vec{x}$ in the $\hat{e}_1$, $\hat{e}_2$ directions, respectively) are given as follows:

$$\begin{Bmatrix} \sigma^j_{r z_i} \\ \sigma^j_{\theta z_i} \\ \sigma^j_{z z_i} \\ \sigma^j_{r r_i} \\ \sigma^j_{\theta\theta_i} \\ \sigma^j_{\theta r_i} \end{Bmatrix}_{(y,x;\omega)} = \frac{r_o^2 Q_1}{4\pi r^2} \begin{Bmatrix} \Sigma^j_{rz_1}(r_o,z_o)\cos(\theta-\theta_{o_i}) \\ \Sigma^j_{\theta z_1}(r_o,z_o)\sin(\theta-\theta_{o_i}) \\ \Sigma^j_{zz_1}(r_o,z_o)\cos(\theta-\theta_{o_i}) \\ \Sigma^j_{rr_1}(r_o,z_o)\cos(\theta-\theta_{oi}) \\ \Sigma^j_{\theta\theta_1}(r_o,z_o)\cos(\theta-\theta_{o_i}) \\ \Sigma^j_{\theta r_1}(r_o,z_o)\sin(\theta-\theta_{o_i}) \end{Bmatrix}, \quad i = 1,2 \tag{A4.7}$$

in which the reference angles $\theta-\theta_{o_i}$ for the direction of the concentrated point force at $\vec{x}$ are determined from Figure A4.1 to be

$$\theta-\theta_{o_i} = \begin{cases} \beta, & \text{for } i = 1 \\ \beta + \frac{\pi}{2}, & \text{for } i = 2 \end{cases}.$$

The stress components for the $i = 3$ terms (concentrated point load at $\vec{x}$ in the $\hat{e}_3$ direction) are given as follows:

$$\begin{Bmatrix} \sigma^j_{rz_3} \\ \sigma^j_{\theta z_3} \\ \sigma^j_{zz_3} \\ \sigma^j_{rr_3} \\ \sigma^j_{\theta\theta_3} \\ \sigma^j_{\theta r_3} \end{Bmatrix}_{(\vec{y},\vec{x};\omega)} = \frac{r_o^2 Q_0}{4\pi r^2} \begin{Bmatrix} \Sigma^j_{rz_0}(r_o,z_o) \\ 0 \\ \Sigma^j_{zz_0}(r_o,z_o) \\ \Sigma^j_{rr_0}(r_o,z_o) \\ \Sigma^j_{\theta\theta_0}(r_o,z_o) \\ 0 \end{Bmatrix} . \qquad \text{(A4.9)}$$

The amplitudes Q_1 and Q_0, of the horizontal and vertical concentrated point loads respectively, in Eqs. (A4.7) and (A4.9), are determined by realizing in Eqs. (A4.3), (A4.4) that $\overset{\nu}{H}$ corresponds to stress if $Q_0 = Q_1 = 1$. Dimensionally, Eq. (A4.3) reveals that

$$U \sim \tau\, \delta_\infty\, A = \frac{\tau}{\mu}\,(\mu\, \delta_\infty\, A) = \tau\, \frac{M_o}{\mu} \qquad \text{(A4.10)}$$

so that if $U \sim \tau$ as in Eq. (A4.5), then

$$Q_0 = Q_1 = \frac{M_o}{\mu} \; . \qquad \text{(A4.11)}$$

In Eqs. (A4.10), (A4.11), A is the area of surface S over which the slippage occurs; δ_∞ is the amplitude of the dislocation at a point on S; M_0 is the source moment; and μ is the shear modulus of the layer containing the point dislocation.

To summarize, in Eq. (A4.5), the displacements at point $\vec{x}$ in the i-direction on the free surface due to a buried dislocation at point $\vec{y} \in S$ are represented in terms of the stress tensor solution at $\vec{y} \in S$ due to a concentrated point load at point $\vec{x}$ in the i-direction on the free surface. The displacements at point $\vec{x}$ in any direction may be obtained from Eq. (A4.5) by appropriately adding vectorially the $U_i(\vec{x};\omega)$, $(i = 1,2,3)$. The displacements for an extended source may be obtained by spatially integrating over surface S the components appearing on the right-hand-side of Eq. (A4.5).

The variables γ and δ represent the local rake and dip of the dislocation and β represents the azimuth of the receiver relative to the strike of the dislocation. The stress tensor components appearing in Eq. (A4.5) are defined in the local coordinates x_1, x_2, x_3 of the dislocation. Eq. (A4.6) relates these local stress components to the stress components in the global cylindrical coordinates r, θ, z. The individual global stress components are listed in Eqs. (A4.7), (A4.9), consistent with the notation used in Chapter 3 of the present work.

CHAPTER 1

INTRODUCTION

1.1 OBJECTIVES AND SCOPE

To analyze the effects of soil-structure interaction on the earthquake response of a structure, it is convenient to partition the soil-structure system at the interface between the superstructure and the foundation-soil system. Thereby, the characterization of the interaction between the foundation and the surrounding soil may be combined with a separate analysis of the overhead structure to determine the aggregate earthquake response of the superstructure.

The complete characterization of the foundation-soil interaction problem involves the evaluation of the dynamic response of the foundation when excited by both external forces and incoming seismic waves. In the complete soil-structure interaction problem, these external forces correspond to the forces and moments that the superstructure exerts on the foundation.

The evaluation of the response of the foundation to external forces and moments reduces to the problem of determining the "impedance matrix" for the foundation-soil system and corresponds to a radiation boundary-value problem. The evaluation of the response of the foundation to seismic waves is associated with the problem of determining the "input motion" matrix for the foundation-soil system and corresponds to a scattering problem. It is important to realize that the only case in which the input motion at the foundation level may be equivalent to the surface

free-field motion is when the foundation is nonembedded and the seismic waves are vertically incident. Otherwise the presence of either foundation embedment or oblique incidence of seismic waves modifies the input motion at the foundation level.

Once the impedance and input motion matrices for the foundation are determined, then the complete soil-structure interaction problem for any configuration of the superstructure can be formulated and solved, since there exist generally accepted techniques for modeling the superstructure. The present work is focussed, however, on the determination of the impedance matrix for various embedded foundation-soil systems.

A limited number of such force-displacement relations (impedance matrices) are available at present, most of which are restricted to a model of the soil corresponding to a homogeneous, non-dissipative, purely elastic half-space. Also, in most studies, the effect of the embedment of the foundation into the surrounding soil is neglected by constraining the analysis to the case of flat foundations.

It is the objective of this study to remove both limitations by representing the soil as a layered viscoelastic medium and by considering the effect of foundation embedment into the soil. Also, two different types of contact between the foundation and the surrounding soil will be considered: 1) welded contact where the soil moves with the foundation; and 2) relaxed contact where various degrees of separation are allowed.

Several previous studies have shown the need for incorporating material damping in the solution, particularly when large strains are involved or when the medium representing the soil is layered. The effects of material or internal damping are automatically incorporated into the

present analysis as well as the radiation damping (geometric energy dissipation).

Although the formulation of the radiation boundary-value problem presented herein is completely general, only numerical results for harmonic forced vertical, torsional, rocking, and horizontal vibrations (i.e., the impedance matrices) of axisymmetric rigid foundations embedded in layered viscoelastic media will be presented.

1.2 REVIEW OF THE LITERATURE

Reissner (1936, 1937) initiated the study of foundation problems when he analyzed the response of a flat circular disc bonded to an elastic half-space and subjected to external harmonic forces and torques. The problem of forced vibrations of a flat rigid foundation resting on an elastic layer supported on a rigid base has been studied by Arnold, Bycroft and Warburton (1955), Bycroft (1956), Warburton (1957), and Kobori, Minai and Suzuki (1966, 1967). In all these studies, the complexity of the mixed boundary value problem was avoided by assuming particular stress distributions under the footing. A circular foundation was considered in the first three studies, while a rectangular foundation was considered in the latter two works.

On the other hand, Collins (1962) and Paul (1967) considered the mixed boundary value problem for a rigid circular disc on a layer supported on a rigid base and presented asymptotic expansions for low frequencies. Kashio (1970), Wei (1971), and Luco (1974) reduced the mathematical formulation of the mixed boundary value problem (for forced vibrations of a rigid circular foundation on a layer welded to an

elastic half-space) to the solution of a set of Fredholm integral equations, by assuming relaxed boundary conditions under the foundation (i.e., no friction exists between the disc and the soil for vertical and rocking vibrations, while the normal component of stress in the contact region is assumed to be zero for horizontal vibrations).

Veletsos and Verbic (1973) were the first to consider the harmonic response of a circular foundation placed on a uniform viscoelastic half-space. They extended solutions obtained numerically for the elastic case to the viscoelastic case through use of the correspondence principle. Unfortunately, such methodology cannot be employed in the analysis of layered media since the impedance coefficients may exhibit strong fluctuations as a function of frequency.

Although more general with respect to the method of incorporating material damping, the studies of Kobori, et al. (1968, 1970, 1971) still avoided the mixed boundary value problem by assuming a stress distribution at the contact between the foundation and the soil. Luco (1976b) extended his previous work (1974) to solve the forced vibration problem of a rigid circular disc on a multilayered viscoelastic half-space by once again reducing the relaxed mixed boundary value problem to the solution of a set of Fredholm integral equations with the material damping introduced at the outset of the formulation.

Finally, Wong and Luco (1977) formulated an analytical method applicable to arbitrarily shaped, rigid, flat foundations undergoing any type of excitation. The numerical solution is based on representing the displacements in terms of integrals of the discrete Green's functions for a uniform viscoelastic half space (similar to present approach for embedded foundations in viscoelastic layered media). When the approach

of Wong and Luco is combined with the Green's functions for a viscoelastic layered half-space as derived in Part I of this dissertation, the complete foundation-soil interaction problem for arbitrarily shaped flat foundation(s) placed on a layered viscoelastic medium may be considered solved.

This leaves only the case of three-dimensional embedded foundations to be discussed. Analytical solutions for embedded foundations are restricted mainly to the cases of antiplane conditions (e.g., Luco, 1969; Thau and Umek, 1973; Wong and Trifunac, 1974; Luco, et al., 1975) and plane-strain conditions (e.g., Thau and Umek, 1974; Dravinsky and Thau, 1976). Analytical solutions for a limited number of problems involving axisymmetric foundations embedded in an elastic half-space have been derived. Luco (1976a) obtained the exact torsional response of a hemispherical foundtion embedded in an elastic half-space when excited by both an external torque and an obliquely incident SH wave and Apsel and Luco (1976) generalized the dynamic torsional response to include foundations of semi-ellipsoidal shape. Finally, Luco (1976c) derived the static torque-twist relation for a rigid cylinder embedded in a layered elastic half-space by reducing the problem to the solution of a system of two integral equations.

A variety of approximate methods have been used to study the response of embedded foundations. The approximate analytical approach of Baranov (1967) has been used with some success to study the dynamic response of a rigid cylindrical foundation embedded in an elastic half-space. Basically, Baranov's method assumes that the soil reactions of the base of the foundation are equal to the reactions of a flat foundation

placed on the surface of the soil while the lateral soil reactions are evaluated independently. When applied to the case of layered soil deposits, it is assumed that the layers of soil surrounding the cylindrical foundation act independently of each other and of the underlying halfspace (Beredugo and Novak, 1972; Novak and Beredugo, 1972, 1973; Novak and Sachs, 1973).

The finite element method (Lysmer and Kuhlemeyer, 1969; Waas, 1972; Lysmer and Waas, 1972; Isenberg and Adham, 1972; Seed and Idriss, 1973) has been used in the past to determine the frequency response of foundations, but was shown to be incapable of reproducing analytical results (Scavuzzo, 1970; Tsai, 1973; Luco, et al., 1974a, 1974b; Hadjian, et al., 1974; Wong, 1975). The ineffectiveness of the finite element analysis was due mainly to the inability of the finite element grid to represent the extended earth. Lysmer and Waas (1972) seemed to have controlled the problems associated with the finite size of the soil model by implementing special nonreflecting boundary conditions at the horizontal extremes of the grid to simulate a horizontally unbounded medium acting in anti-plane strain. Waas (1972) and Kausel, et al. (1975) extended the nonreflecting boundaries to a cylindrical geometry, but to date, no satisfactory conditions have appeared in the literature for allowing energy to radiate through the bottom boundary of the grid. Until the frequency domain finite element treatments include adequate nonreflecting boundaries, such analyses will still be incapable of reproducing certain aspects of analytical solutions, such as the radiation damping at low frequencies (see Kausel and Röesset, 1975).

Day (1977) has studied the embedded foundation problem by performing the finite element analysis in the time domain using the SWIS

program developed by Frazier (see Frazier, et al., 1973; Frazier and Petersen, 1974). The spurious effects due to the finite grid boundaries are eliminated by providing enough grid exterior to the region of interest so that the transient analysis is completed before the boundary reflections blemish the signal (frequency response is obtained through Fourier synthesis). Although Day's results are encouraging, the procedure is limited in that it is difficult to properly model the material damping in the soil over the entire frequency range of interest. Also, it is difficult to include all the reflected energy in a layered half-space (while at the same time eliminating the spurious reflections from the artificial boundaries) without supplying an extremely large grid.

This review clearly indicates the need for alternative methods of solution which are capable of considering foundations of arbitrary shape embedded in layered media. The next section describes a flexible approach which is based on solving an integral equation involving the Green's functions for a layered viscoelastic half-space.

1.3 DESCRIPTION OF PRESENT METHOD

To accomplish the objectives delineated in Section 1.1, it is necessary to devise a method capable of treating arbitrarily shaped three-dimensional foundations embedded in layered soil deposits. It is also a prerequisite that the methodology incorporate material damping (internal dissipation) into the soil as well as radiation damping (geometric energy dissipation). The final requirement is that the procedure be cost-efficient.

In the present approach, the problem of determining the dynamic response of any arbitrarily shaped three-dimensional foundation(s) will

be reduced to the solution of an integral equation. The kernel of the integral equation involves the Green's functions for a layered viscoelastic half-space so that the differential equations of motion are automatically satisfied in the volume comprising the soil conjointly with the continuity conditions at the layer interfaces, the traction-free conditions at the surface of the layered half-space, and the geometric radiation conditions in the underlying half-space. Such Green's functions, which properly represent the material dissipation in the soil medium, are now available as derived in Part I of this dissertation. The boundary conditions at the soil-foundation interface will be approximated very closely by numerically solving the integral equation. The procedure experiences no frequency limitation and the cost is competitive with Day's finite element approach (1977).

In Chapter 2, the general integral equation formulation is presented for axisymmetric as well as fully three-dimensional foundations with relaxed as well as welded type contact assumed at the soil-foundation interface. The integral equations are discretized in Chapter 3 into a form suitable for numerical solution by standard techniques as well as by eigenanalysis. Comparisons with known solutions are presented in Chapter 4 along with several new results including the effects of foundation embedment depth; attenuation in the soil; type of contact between the foundation and the surrounding soil; and layering in the soil deposit.

CHAPTER 2

FORMULATION OF THE RADIATION PROBLEM

2.1 STATEMENT OF THE PROBLEM

The principal objective of the present work is to determine the motion of a foundation embedded in a viscoelastic layered half-space when excited by external forces acting directly on the foundation. These external forces consist of forces and moments that the foundation exerts on the surrounding soil and hence this problem corresponds to a radiation problem. The dynamic response of the foundation can be characterized by the "impedance matrix" for the foundation-soil system (viz., the dynamic force-displacement relations for the embedded foundation undergoing the action of external forces).

Secondly, it would be desirable to obtain the motion of the foundation when excited by incoming seismic waves. This problem corresponds to a diffraction or scattering problem and involves the determination of the "input motion" matrix for the foundation (viz., the motion of the foundation assumed massless and the free from external forces when subjected to the seismic excitation). Since the scattering problem can be separated into the solution of a propagation problem in the absence of the foundation plus the solution of the radiation problem (by determining the external forces and moments necessary to keep the foundation fixed under the action of the incoming waves), it is sufficient to consider only the radiation problem.

With these objectives in mind a general model is considered. The model geometry is depicted in Figure 2.1, where volume V' represents an intrusion, either rigid or flexible in comparison with the surrounding soil medium; volume V represents the soil deposit into which the intrusion is embedded; and surface S (with unit normal $\vec{\nu}$ pointing into the volume V') defines the geometry of the embedded intrusion. In particular, volume V is assumed to be a multilayered viscoelastic half-space composed of N parallel layers overlying a half-space. Each of the layers and the half-space forming volume V is considered to be a homogeneous, isotropic, viscoelastic, horizontally infinite slab characterized by shear and compressional wave velocities, density, energy dissipation factors for shear and compressional waves and layer thickness. Also, the primary concern involves finding the motion of the intrusion when external harmonic forces and moments are applied to it.

The contact at the interfaces between the layers is such that the displacements and tractions are continuous across each interface, while the normal traction components vanish at the surface of the layered half-space and the displacement and stress fields obey the geometric radiation condition for the underlying half-space. Three different types of boundary conditions are plausible at the soil-intrusion interface (i.e., along surface S): 1) displacements prescribed everywhere on S (e.g., for welded contact between a rigid foundation and the surrounding soil); 2) tractions prescribed everywhere on S (e.g., for diffraction by a canyon); or 3) mixed boundary conditions where the displacements are prescribed on a portion S_2 of S while

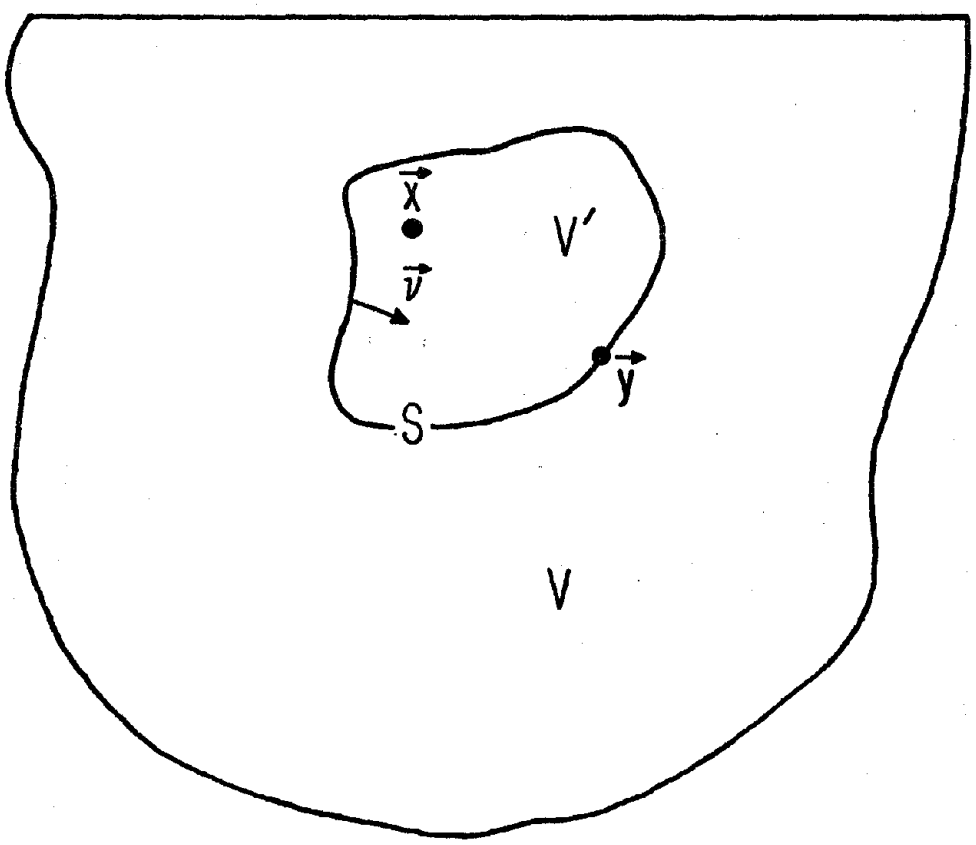

Figure 2.1. Model geometry used to study various radiation and scattering problems in elastodynamics with surface S defining the boundary between volumes V and V′.

the tractions are prescribed on the remaining portion S_1 of S so that the soil is constrained to move with the foundation only on S_2 (e.g., when separation exists along S_1).

The next section reduces the problem to the solution of an integral equation involving the Green's functions for the layered viscoelastic half-space so that the differential equations of motion in volume V are automatically satisfied in compliance with the continuity conditions at the layer interfaces, the traction-free conditions at the surface of the layered half-space, and the geometric radiation conditions in the underlying half-space. The integral equations are obtained by imposing the boundary conditions on surface S (the soil-intrusion interface).

2.2 REDUCTION TO AN INTEGRAL EQUATION

Assuming that the displacement and stress components have harmonic time dependence, it is convenient to apply the Knopoff-deHoop (1958) representation theorem to volume V of Figure 2.1. In the absence of body forces in V, the representation theorem in Cartesian coordinates is written in the frequency domain as

$$\varepsilon(\vec{x})\, U_i(\vec{x}) = \int_S \left[G_{ji}(\vec{y};\, \vec{x})\, \overset{\nu}{T}_j(\vec{y}) - \overset{\nu}{H}_{ji}(\vec{y};\, \vec{x})\, U_j(\vec{y}) \right] dS(\vec{y}) \,, \quad (i,j = 1,2,3) \tag{2.1}$$

in which

$$\varepsilon(\vec{x}) = \begin{cases} 0 , & \vec{x} \in V' \\ 1/2 , & \vec{x} \in S \\ 1 , & \vec{x} \in V \end{cases} .$$

In Eq. (2.1), the factors $\exp(i\omega t)$ have been omitted and $G_{ji}(\vec{y}; \vec{x})$ and $\overset{\nu}{H}_{ji}(\vec{y}; \vec{x})$ denote, respectively, the j-component of the displacement and traction vectors at $\vec{y} \in S$ due to a concentrated point load at $\vec{x}$ in the i-direction, while $U_j(\vec{y})$ and $\overset{\nu}{T}_j(\vec{y})$ represent, respectively, the j-component of displacement and traction at $\vec{y} \in S$. Also, in Eq. (2.1) and in the sequel, the summation convention over repeated indices is understood, and the unit normal $\vec{\nu}$ is defined positive pointing into the volume V'.

Applying Eq. (2.1) to a point $\vec{x}$ in volume V' leads directly to

$$\int_S G_{ji}(\vec{y}; \vec{x}) \overset{\nu}{T}_j(\vec{y}) \, dS(\vec{y}) = \int_S \overset{\nu}{H}_{ji}(\vec{y}; \vec{x}) \, U_j(\vec{y}) \, dS(\vec{y}) \qquad (2.2)$$

where $\vec{x} \in V'$ and $\vec{y} \in S$. For the displacement boundary value problem (welded contact between the intrusion and the surrounding soil), the displacements $U_j(\vec{y})$ are prescribed on S and the integral equation (2.2) must be solved for the unknown tractions $\overset{\nu}{T}_j(\vec{y})$ on S. Modifications to the method of solution for the mixed boundary value problem are discussed in Section 2.3.

The method of solution proposed here is based on considering a set of forces $\vec{F}(\vec{x}')$ distributed over a surface S' located within volume V' (refer to Figure 2.2), selected in such a way that the

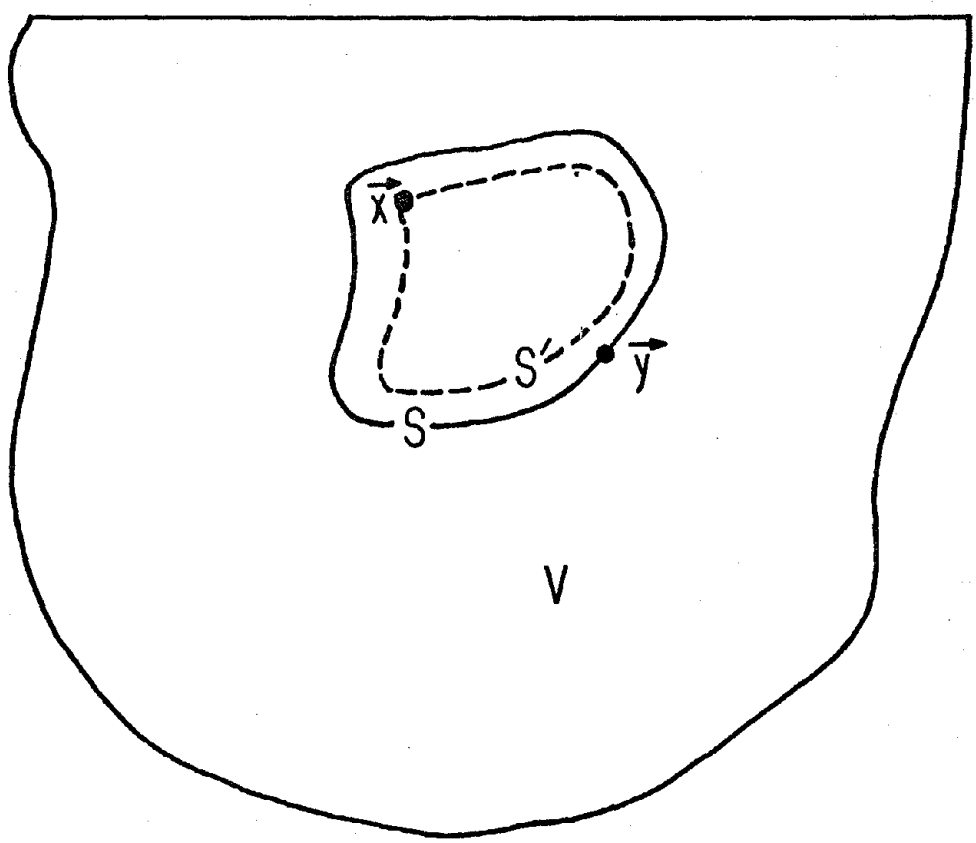

Figure 2.2. Model geometry including internal source surface S' on which the forces $\vec{F}$ are distributed.

unknown tractions can be represented as

$$\int_{S'} \overset{\nu}{H}_{jk}(\vec{y};\ \vec{x}')\ F_k(\vec{x}')\ dS(\vec{x}') = \overset{\nu}{T}_j(\vec{y}) \ , \quad \vec{y} \in S \ . \tag{2.3}$$

Substitution from Eq. (2.3) into the left-hand side of Eq. (2.2) and formally interchanging the order of integration leads to the following integral equation for the distributed forces $\vec{F}(\vec{x}')$:

$$\int_{S'} \hat{G}_{ij}(\vec{x};\ \vec{x}')\ F_j(\vec{x}')\ dS'(\vec{x}') = \int_S \overset{\nu}{H}_{ji}(\vec{y};\ \vec{x})\ U_j(\vec{y})\ dS(\vec{y}) \tag{2.4}$$

in which

$$\hat{G}_{ij}(\vec{x};\ \vec{x}') = \int_S G_{ki}(\vec{y};\ \vec{x})\ \overset{\nu}{H}_{kj}(\vec{y};\ \vec{x}')\ dS(\vec{y}) \tag{2.5}$$

with $\vec{x},\ \vec{x}' \in V$. The function $\hat{G}_{ij}(\vec{x};\ \vec{x}')$ is symmetric, i.e.,

$$\hat{G}_{ij}(\vec{x};\ \vec{x}') = \hat{G}_{ji}(\vec{x}';x) \qquad (\vec{x},\ \vec{x}' \in V) \ , \tag{2.6}$$

as is easily proven by taking

$$U_j(\vec{y}) = G_{jk}(\vec{y};\ \vec{x}') \quad \text{and} \quad \overset{\nu}{T}_j(\vec{y}) = \overset{\nu}{H}_{jk}(\vec{y};\ \vec{x}) \ , \quad \vec{x}' \in V'$$

in Eq. (2.2).

If $\vec{x}$ is taken on S', then Eqs. (2.4) correspond to a system of symmetric Fredholm integral equations of the first kind for $F_j(\vec{x}')$. Once these equations are solved for $F_j(\vec{x}')$, substitution into Eq. (2.3) gives the traction distribution on S from which other quantities of interest are readily obtained. In particular, the displacement field

in V can also be obtained by use of

$$U_j(\vec{x}) = \int_{S'} G_{jk}(\vec{x};\ \vec{x}')\ F_k(\vec{x}')\ dS'(\vec{x}')\ , \quad (\vec{x} \in V)\ . \qquad (2.7)$$

Two other methods of solution will be discussed and compared presently. Kupradze (1963) proposes to directly solve the original integral equations (2.2) for the unknown tractions by choosing the points $\vec{x}$ to be on a surface (such as S') within volume V', so as to avoid the singularities in the Green's functions, G_{ji} and $\overset{\nu}{H}_{ji}$, when the points $\vec{y}$ and $\vec{x}$ coincide. However, the kernel of the resulting integral equations is not symmetric. Ohsaki (1973) proposes to solve the integral equations (2.7) for $\vec{F}(\vec{x}')$ with $\vec{x} \in S$. Given the displacements $U_j(\vec{y})$, the unknown tractions are then obtained by substituting $\vec{F}(\vec{x}')$ back into Eq. (2.3). Formally, Ohsaki's approach in conjunction with a least squares method of solution (on Eq. (2.7) with $\vec{x} \in S$) leads to

$$\int_{S'} G^{o}_{ij}(\vec{x};\ \vec{x}')\ F_j(\vec{x}')\ dS'(\vec{x}') = \int_{S} G_{ji}(\vec{y};\ \vec{x})\ U_j(\vec{y})\ dS(\vec{y})$$

in which

$$G^{o}_{ij}(\vec{x};\ \vec{x}') = \int_{S} G_{ki}(\vec{y};\ \vec{x})\ G_{kj}(\vec{y};\ \vec{x}')\ dS(\vec{y})$$

is symmetric. Thus, Ohsaki's approach is similar to the present approach. However, the advantage of the present method rests in its physical connection with work as discussed below.

To show that the distributed forces $\vec{F}(\vec{x}')$, as a solution to Eq. (2.4), are the optimal solution from a variational standpoint, Eq. (2.4) is multiplied by $F_i(\vec{x})$ and integrated over $dS'(\vec{x})$ to give

$$\int_{S'}\int_{S'} F_i(\vec{x})\, \hat{G}_{ij}(\vec{x};\, \vec{x}')\, F_j(\vec{x}')\, dS'(\vec{x})\, dS'(\vec{x}')$$

$$= \int_S \left[\int_{S'} F_i(\vec{x})\, \overset{\nu}{H}_{ji}(\vec{y};\, \vec{x})\, dS'(\vec{x})\right] U_j(\vec{y})\, dS(\vec{y})$$

$$= \int_S \overset{\nu}{T}_j(\vec{y})\, U_j(\vec{y})\, dS(\vec{y}) \qquad (2.8)$$

where Eq. (2.3) has been used to show that the right-hand side of Eq. (2.8) corresponds to the work done by the tractions on the displacements. The form of Eq. (2.8) suggests that Eq. (2.4) may be obtained as the condition for an extremal of the following functional:

$$\Pi(\vec{F}) = -\int_{S'}\int_{S'} F_i(\vec{x})\, \hat{G}_{ij}(\vec{x};\, \vec{x}')\, F_j(\vec{x}')\, dS'(\vec{x})\, dS'(\vec{x}')$$

$$+ 2\int_S\int_{S'} F_i(\vec{x})\, \overset{\nu}{H}_{ji}(\vec{y};\, \vec{x})\, U_j(\vec{y})\, dS'(\vec{x})\, dS(\vec{y}) \,. \qquad (2.9)$$

Then, the extremal of $\Pi(\vec{F})$ corresponds to the work done by the tractions on the displacements when $\vec{F}$ is a solution of Eq. (2.4), that is to say

$$\Pi(\vec{F})\Big|_{\text{extreme}} = \int_S \overset{\nu}{T}_j(\vec{y})\, U_j(\vec{y})\, dS(\vec{y}) \,. \qquad (2.10)$$

The procedures used to obtain approximate solutions to the integral equations (2.4) are presented in the following chapter.

2.3 CASE OF MIXED BOUNDARY CONDITIONS

For the mixed boundary-value problem, displacements are prescribed on S_2 and tractions are prescribed on S_1 (refer to Figure 2.3). An example is the case in which separation is allowed to exist between the embedded foundation and the surrounding soil. Equation (2.2) is then written more conveniently for the case of mixed boundary conditions as

$$\int_{S_2} G_{ji}(\vec{y};\ \vec{x})\ \overset{\nu}{T}_j(\vec{y})\ dS_2(\vec{y}) - \int_{S_1} \overset{\nu}{H}_{ji}(\vec{y};\ \vec{x})\ U_j(\vec{y})\ dS_1(\vec{y})$$

$$= \int_{S_2} \overset{\nu}{H}_{ji}(\vec{y};\ \vec{x})\ U_j(\vec{y})\ dS_2(y) - \int_{S_1} G_{ji}(\vec{y};\ \vec{x})\ \overset{\nu}{T}_j(\vec{y})\ dS_1(\vec{y}) \tag{2.11}$$

in which $\overset{\nu}{T}_j$ is unknown on S_2 with U_j prescribed there, while U_j is unknown on S_1 with $\overset{\nu}{T}_j$ prescribed there, and $\vec{x} \in V'$.

Again, the set of forces $\vec{F}(\vec{x}')$ are selected according to Eqs. (2.3), (2.7) as in the displacement boundary-value problem for the case of welded contact. Then, introducing Eqs. (2.3), (2.7) into Eq. (2.11) permits the reduction of the integral equation for the distributed forces to the form

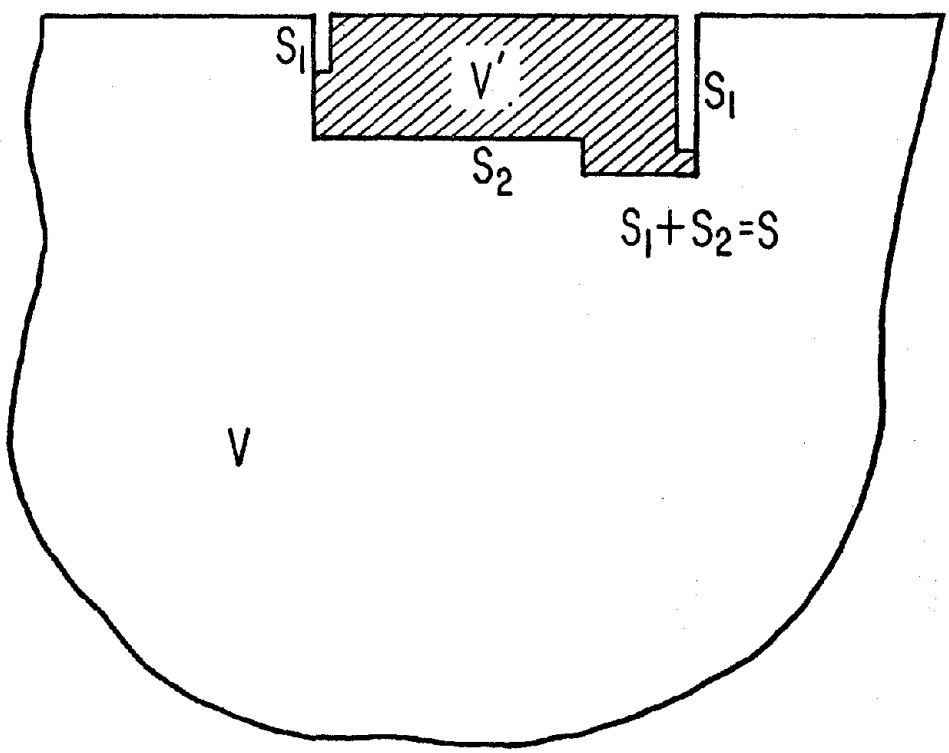

Figure 2.3. Model geometry for mixed boundary problem in which displacements are prescribed on S_2 and tractions are prescribed on S_1.

$$\int_{S'} \hat{\hat{G}}_{ij}(\vec{x};\, \vec{x}')\, F_j(\vec{x}')\, dS'(\vec{x}') = \int_{S_2} \overset{\nu}{H}_{ji}(\vec{y};\, \vec{x})\, U_j(\vec{y})\, dS_2(\vec{y})$$

$$- \int_{S_1} G_{ji}(\vec{y};\, \vec{x})\, T_j(\vec{y})\, dS_1(\vec{y}) \qquad (2.12)$$

in which

$$\hat{\hat{G}}_{ij}(\vec{x};\, \vec{x}') = \int_{S_2} G_{ki}(\vec{y};\, \vec{x})\, \overset{\nu}{H}_{kj}(\vec{y};\, \vec{x}')\, dS_2(\vec{y})$$

$$- \int_{S_1} \overset{\nu}{H}_{ki}(\vec{y};\, \vec{x})\, G_{kj}(\vec{y};\, \vec{x}')\, dS_1(\vec{y}) \qquad (2.13)$$

with $\vec{x}$, $x' \in V'$ (in particular, on surface S'). As before, once the integral equation (2.12) is solved for the distributed forces $\vec{F}(\vec{x}')$, then Eq. (2.3) determines the traction distribution for points $y \in S_2$, and Eq. (2.7) determines the displacement field for points $x \in V$ and S_1. Also, since the symmetry relation $\hat{\hat{G}}_{ij}(\vec{x};\, \vec{x}') = \hat{\hat{G}}_{ji}(\vec{x}';x)$ is readily proven, it can once again be shown that the distributed forces $\vec{F}(\vec{x}')$, as a solution to Eq. (2.12), are the optimal solutions in the sense of variational principles.

2.4 RESPONSE OF RIGID INTRUSIONS — THE IMPEDANCE MATRIX

The response of rigid foundations to the excitation of external forces and moments involves the determination of the "impedance matrix" (i.e., the dynamic force-displacement relations) for the foundation-soil system. In deriving the force-displacement relations for harmonic motion

(with angular frequency ω) of a rigid foundation occupying volume V', the displacement vector

$$\{u(\vec{y})\}e^{i\omega t} = \left(u_x(\vec{y}),\ u_y(\vec{y}),\ u_z(\vec{y})\right)^T e^{i\omega t} \quad , \quad \vec{y} \in S$$

is expressed in terms of the "generalized displacement", $\{\Delta\}e^{i\omega t}$, as

$$\{u(\vec{y})\} = [\alpha(\vec{y})]\{\Delta\} \quad . \tag{2.14}$$

In Eq. (2.14), $\{\Delta\}$ is the 6x1 vector including the three translational and three rotational degrees of freedom for the rigid foundation as is illustrated in Figure 2.4, such that

$$\{\Delta\} = (\Delta_x,\ \Delta_y,\ \Delta_z,\ \phi_x,\ \phi_y,\ \phi_z)^T \quad , \tag{2.15}$$

and $[\alpha(\vec{y})]$ is the 3x6 influence matrix relating the six components of rigid body motion $\{\Delta\}$ to the three components of the displacement $\{u\}$. For small rotations about the origin of the coordinate system, one finds that

$$[\alpha(\vec{y})] = \begin{bmatrix} 1 & 0 & 0 & 0 & z & -y \\ 0 & 1 & 0 & -z & 0 & x \\ 0 & 0 & 1 & y & -x & 0 \end{bmatrix} \quad . \tag{2.16}$$

The "generalized force" $\{\Gamma(\omega)\}e^{i\omega t}$ is defined as

$$\{\Gamma(\omega)\}e^{i\omega t} = (F_x,\ F_y,\ F_z,\ M_x,\ M_y,\ M_z)^T e^{i\omega t} \tag{2.17}$$

consisting of the six forces and moments associated with the "generalized displacement". The "generalized force" that the rigid foundation exerts on the soil is obtained for the welded contact problem by

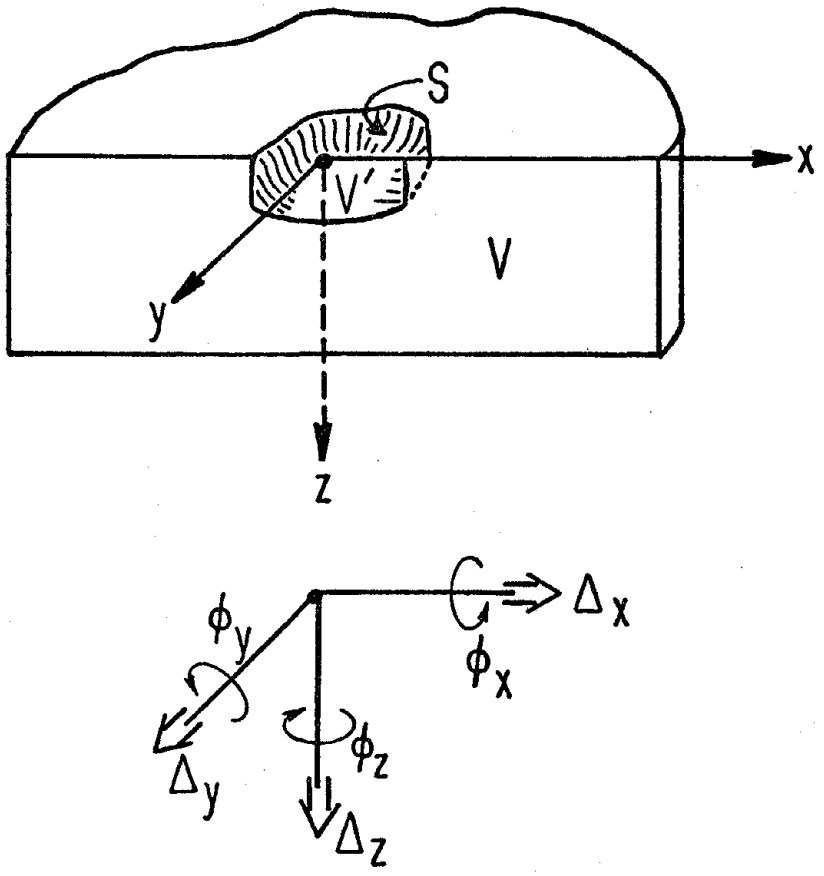

Figure 2.4. Model geometry and coordinate system for studying the response of rigid intrusions to the excitation of external forces and moments.

$$\{\Gamma(\omega)\} = \int_S [\alpha(\vec{y})]^T \left\{ {}^{\nu}T(\vec{y}) \right\} dS(\vec{y}) \qquad (2.18)$$

in which $\left\{ {}^{\nu}T(\vec{y}) \right\}$ is the 3x1 vector of traction components distributed on S as a solution of equations (2.4), (2.3) with $\{u(\vec{y})\}$ given by Eq. (2.14).

Since the integral equations for the distributed forces on S' depend linearly on the displacements prescribed on S and since the tractions on S are linear functions of the distributed forces, then the tractions on S will depend linearly on the displacements on S. Formally, this relation can be written in the form

$$\left\{ {}^{\nu}T(\vec{y}) \right\} = \int_S [\hat{k}(\vec{y}; \vec{y}')]\{u(\vec{y}')\} dS(\vec{y}') , \quad \vec{y}, \vec{y}' \in S . \qquad (2.19)$$

Substitution from Eqs. (2.19) and (2.14) into Eq. (2.18) leads to

$$\{\Gamma(\omega)\} = \int_S \int_S [\alpha(\vec{y})]^T [\hat{k}(\vec{y}; \vec{y}')][\alpha(\vec{y}')]\{\Delta\} dS(\vec{y}') dS(\vec{y}) \qquad (2.20)$$

or

$$\{\Gamma(\omega)\} = [k(\omega)]\{\Delta\}$$

where the 6x6 impedance matrix $[k(\omega)]$ is given by

$$[k(\omega)] = \int_S \int_S [\alpha(\vec{y})]^T [\hat{k}(\vec{y}; \vec{y}')][\alpha(\vec{y}')] dS(\vec{y}') dS(\vec{y}) . \qquad (2.21)$$

2.5 CASE OF AXISYMMETRIC GEOMETRIES

For axially symmetric geometries with respect to the z axis (refer to Figure 2.5), it will prove convenient to modify the integral equation formulation of the previous three sections to take advantage of the geometric symmetry of the problem. It is important to realize that the form of the integral equations remains the same in cylindrical coordinates provided that the components associated with indices 1, 2, 3 are taken to be the radial, azimuthal and vertical components, respectively.

The objective here is to specialize the integral equations to a form most suitable for axially symmetric geometries by analytically integrating over the azimuthal coordinate (index 2). In Eq. (2.2), let (r, θ, z) be the cylindrical coordinates at $\vec{y} \in S$, and let (r', θ', z') be the cylindrical coordinates at $\vec{x} \in V'$. Then, defining the function $\Theta^{(i)}$ (superscript (i) is used to signify no summation in the indicial notation) as

$$\Theta^{(i)}(m\phi) = \begin{cases} \begin{matrix}\cos \\ \sin\end{matrix}(m\phi) , & i=1,3 \\ \\ \begin{matrix}\sin \\ -\cos\end{matrix}(m\phi) , & i=2 \end{cases} , \qquad (2.22)$$

multiplying Eq. (2.2) by $\Theta^{(i)}(m\theta')$, integrating over θ' between the limits 0 and 2π, and formally changing the order of integration leads to (with ω omitted as argument in variables for brevity)

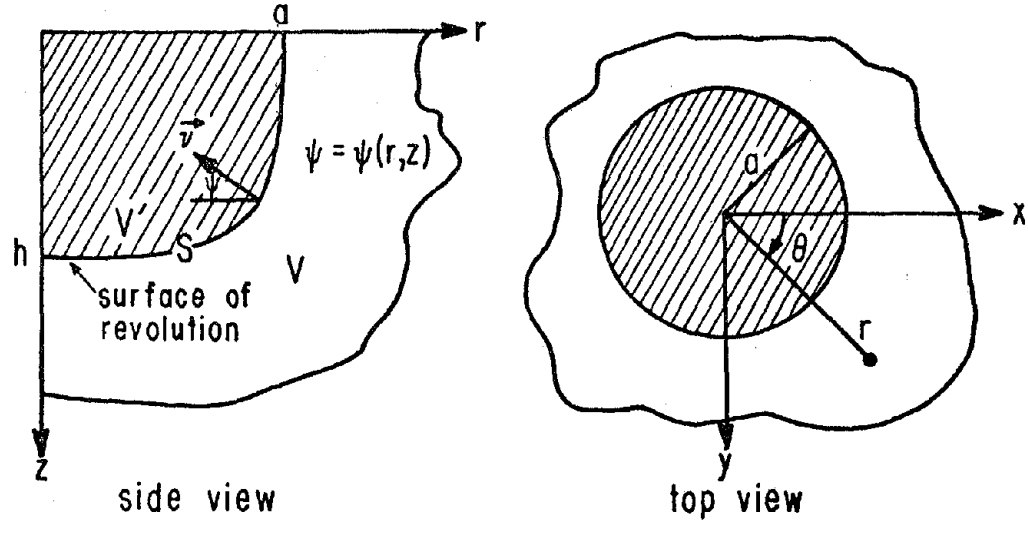

Figure 2.5. Model geometry and coordinate system for studying problems involving axially symmetric geometries with respect to a vertical axis.

$$\int_S \bar{G}^m_{ji}(r, \theta, z; r', z') \overset{\nu}{T}_j(r, \theta, z)\, dS(r, \theta, z)$$

$$= \int_S \bar{H}^m_{ji}(r, \theta, z; r', z')\, U_j(r, \theta, z)\, dS(r, \theta, z) \ . \qquad (2.23)$$

In Eq. (2.23), $i,j = 1$ corresponds to the radial direction while $i,j = 2,3$ corresponds to the azimuthal and vertical directions, respectively, and

$$\bar{G}^j_{ji}(r, \theta, z; r', z') = \frac{1}{2\pi r'} \int_0^{2\pi} G_{ji}(r, \theta, z; r', \theta', z')\, \Theta^{(i)}(m\theta')d\theta',$$

$$(i = 1,2,3) \qquad (2.24)$$

is the j-component (radial, azimuthal or vertical) of the displacement vector at $\vec{y}(r, \theta, z)$ due to a concentrated ring load (per unit arc-length) of radius r' and azimuthal dependence $\Theta^{(i)}(m\theta')$ acting in the i-direction through (r', θ', z') (i=1 for radial ring; i=2 for tangential ring; and i=3 for vertical ring), and

$$\overset{\nu}{\bar{H}}^m_{ji}(r, \theta, z; r', z') = \frac{1}{2\pi r'} \int_0^{2\pi} \overset{\nu}{H}_{ji}(r, \theta, z; r', \theta', z')\, \Theta^{(i)}(m\theta')d\theta' \ ,$$

$$(i = 1,2,3) \qquad (2.25)$$

is the corresponding traction at $\vec{y}(r, \theta, z)$ in the j-direction acting on a plane defined by $\vec{\nu}$ (normal pointing into volume V' enclosed by a surface of revolution S) due to a concentrated ring load at (r', θ', z') acting in the i-direction with azimuthal dependence $\Theta^{(i)}(m\theta')$.

Finally, noting that

$$\left.\begin{aligned} \bar{G}^{j}_{ji}(r, \theta, z; r', z') &= G^{m}_{ji}(r, z; r', z')\ \Theta^{(j)}(m\theta) \\ \overset{\nu}{\bar{H}}{}^{j}_{ji}(r, \theta, z; r', z') &= H^{m}_{ji}(r, z; r', z')\ \Theta^{(j)}(m\theta) \end{aligned}\right\} (j = 1,2,3), \tag{2.26}$$

substituting from Eq. (2.26) back into Eq. (2.23), and carrying out the integration over θ results in

$$\int_L G^{m}_{ji}(r, z; r', z')\ \overset{\nu}{T}{}^{m}_{j}(r, z)\ \pi\varepsilon_m r\ dL(r, z)$$

$$= \int_L \overset{\nu}{H}{}^{m}_{ji}(r, z; r', z')\ U^{m}_{j}(r, z)\ \pi\varepsilon_m r\ dL(r, z) \tag{2.27}$$

in which

$$\left.\begin{aligned} \pi\varepsilon_m\ U^{m}_{j}(r, z) &= \int_0^{2\pi} U_j(r, \theta, z)\ \Theta^{(j)}(m\theta)\ d\theta \\ \pi\varepsilon_m\ \overset{\nu}{T}{}^{m}_{j}(r, z) &= \int_0^{2\pi} \overset{\nu}{T}_{j}(r, \theta, z)\ \Theta^{(j)}(m\theta)\ d\theta \end{aligned}\right\} (j = 1,2,3) \tag{2.28}$$

with

$$\varepsilon_m = \begin{cases} 2 & \text{for} \quad m = 0 \\ 1 & \text{for} \quad m = 1,2, \ldots \end{cases} . \tag{2.29}$$

The method of solution of integral equation (2.27) exactly parallels that for the fully 3-D case in integral equation (2.2), except that now the integrals are carried out along a line L on surface S rather than over the entire surface S.

The set of forces $\vec{F}^m(\vec{x}')$ distributed along a line L' on a surface S' located within volume V' are required to satisfy

$$\int_{L'} \overset{\nu}{H}{}^m_{jk}(\vec{y};\ \vec{x}')\ F^m_k(\vec{x}')\ \pi\epsilon_m r'\ dL'(\vec{x}') = \overset{\nu}{T}{}^m_j(\vec{y}) \ , \tag{2.30}$$

in which $\vec{y}(r,\ z) \in L$ and $\vec{x}\ (r',\ z') \in L'$. Then introducing $\overset{\nu}{T}{}^m_j(\vec{y})$, as defined in Eq. (2.30), into the left-hand side of Eq. (2.27) and changing the order of integration, the integral equation for the distributed forces $\vec{F}^m(\vec{x}')$ for the axially symmetric, three-dimensional, welded contact foundation problem becomes

$$\int_{L'} \hat{G}^m_{ij}(\vec{x};\ \vec{x}')\ F^m_j(\vec{x}')\ \pi\epsilon_m r'\ dL'(\vec{x}') = \int_L \overset{\nu}{H}{}^m_{ji}(\vec{y};\ \vec{x})\ U_j(\vec{y})\ r\ dL(\vec{y}) \tag{2.31}$$

in which $\vec{U}(\vec{y})$ is prescribed along all of L and

$$\hat{G}^m_{ij}(\vec{x};\ \vec{x}') = \int_L G^m_{ki}(\vec{y};\ \vec{x})\ \overset{\nu}{H}{}^m_{kj}(\vec{y};\ \vec{x}')\ r\ dL(\vec{y}) \tag{2.32}$$

with $\vec{x},\ \vec{x}' \in S'$. In particular, $\vec{x}$ can be chosen on L' as well as $\vec{x}'$ once again, and all the reciprocity relations and variational principles are proven as indicated in Section 2.2. Once the integral equations

(2.31) have been solved for the distributed forces $\vec{F}^m(\vec{x}')$, the traction distribution along L can be determined by use of Eq. (2.30).

For the mixed boundary-value problem, where separation is allowed to exist along L_1, the analogous integral equation to Eq. (2.12) for three-dimensional axisymmetric foundations is found to be

$$\int_{L'} \hat{G}^m_{ij}(\vec{x};\ \vec{x}')F^m_j(\vec{x}')\pi\epsilon_m r' dL'(x') = \int_{L_2} \overset{\nu}{H}{}^m_{ji}(\vec{y};\ \vec{x})\ U_j(\vec{y})\ r\ dL_2(\vec{y}) - \int_{L_1} G^m_{ji}(\vec{y};\ \vec{x})\ \overset{\nu}{T}_j(\vec{y})\ r\ dL_1(\vec{y}) \tag{2.33}$$

in which $\vec{U}(\vec{y})$ is prescribed along L_2, $\overset{\nu}{\vec{T}}(\vec{y})$ is prescribed along L_1 and

$$\hat{G}^m_{ij}(\vec{x};\ \vec{x}') = \int_{L_2} G^m_{ki}(\vec{y};\ \vec{x})\ \overset{\nu}{H}{}^m_{kj}(\vec{y};\ \vec{x}')\ r\ dL_2(\vec{y}) - \int_{L_1} \overset{\nu}{H}{}^m_{ki}(\vec{y};\ \vec{x})\ G^m_{kj}(\vec{y};\ \vec{x}')\ r\ dL_1(\vec{y}) \tag{2.34}$$

with $\vec{x}, \vec{x}' \in S'$ (in particular, on line L').

Finally, once the traction distribution is found along L from Eq. (2.30) with the distributed forces $F^m(x')$ determined by solving integral Eq. (2.31) for the displacement boundary-value problem or Eq. (2.33) for the mixed boundary problem, then the impedance matrix for the axisymmetric foundation may be formed as in Section 2.4 by

employing the appropriate cylindrical coordinates.

The problem of determining the 6x6 impedance matrix separates into two subproblems for the axisymmetric foundation: 1) when torsional or vertical motions are prescribed); and 2) when rocking about a horizontal axis or horizontal motions are prescribed. The displacement vector

$$\{u(\vec{y})\}e^{i\omega t} = \left(u_r(\vec{y}),\ u_\theta(\vec{y}),\ u_z(\vec{y})\right)^T e^{i\omega t} \quad , \quad \vec{y} \in L$$

for the first subproblem is expressed in terms of the 2x1 "generalized displacement", $\{\Delta^0\}e^{i\omega t}$, according to

$$\begin{Bmatrix} u_r^0 \\ u_\theta^0 \\ u_z^0 \end{Bmatrix} = \begin{bmatrix} 0 & 0 \\ 0 & r \\ 1 & 0 \end{bmatrix} \begin{Bmatrix} \Delta_z \\ \phi_z \end{Bmatrix} = [\alpha^0]\{\Delta^0\} \quad . \tag{2.35}$$

Similarly for the second problem, the displacement vector is expressed in terms of the 2x1 "generalized displacement", $\{\Delta^1\}e^{i\omega t}$, according to

$$\begin{Bmatrix} u_r^1 \\ u_\theta^1 \\ u_z^1 \end{Bmatrix} = \begin{bmatrix} 1 & (z-h) \\ -1 & -(z-h) \\ 0 & -r \end{bmatrix} \begin{Bmatrix} \Delta_x \\ \phi_y \end{Bmatrix} = [\alpha^1]\{\Delta^1\} \tag{2.36}$$

where the embedment depth, h, has been introduced to later refer the rocking and coupled rocking-horizontal impedance functions to the bottom of the foundation.

The force-displacement relations are given in this case by

$$\begin{Bmatrix} F_z \\ M_z \end{Bmatrix} = [k^0(\omega)] \begin{Bmatrix} \Delta_z \\ \phi_z \end{Bmatrix}$$

$$\begin{Bmatrix} F_x \\ M_y \end{Bmatrix} = [k^1(\omega)] \begin{Bmatrix} \Delta_z \\ \phi_y \end{Bmatrix} , \quad \begin{Bmatrix} F_y \\ -M_x \end{Bmatrix} = [k^1(\omega)] \begin{Bmatrix} \Delta_y \\ -\phi_x \end{Bmatrix} \tag{2.37}$$

where $[k^0(\omega)]$ and $[k^1(\omega)]$ are the 2x2 impedance matrices for the first and second subproblems, respectively.

Analogous to Eq. (2.19), the traction distribution on L will formally depend linearly on the displacements there for each order m, i.e.,

$$\left\{ \overset{\nu}{T}{}^m(\vec{y}) \right\} = \int_L [\hat{K}^m(\vec{y}; \vec{y}')]\{U^m(\vec{y}')\}\, dL(\vec{y}') , \quad \vec{y}, \vec{y}' \in L . \tag{2.38}$$

Then, the 2x2 impedance matrices $[k^m(\omega)]$ for each subproblem are determined by

$$[k^m(\omega)] = \int_L \int_L [\alpha^m(\vec{y})]^T [\hat{k}^m(\vec{y}; \vec{y}')][\alpha^m(\vec{y}')]\, \pi\varepsilon_m r'\, dL(\vec{y}')\, dL(\vec{y}) , \tag{2.39}$$

in which the 3x2 influence matrices $[\alpha^m]$ are defined from Eqs. (2.35), (2.36) for subproblems 1 and 2, respectively.

The individual terms in the 2x2 impedance matrices are denoted as follows:

$$[k^0(\omega)] = \begin{bmatrix} K_{VV} & 0 \\ 0 & K_{TT} \end{bmatrix}, \quad [k^1(\omega)] = \begin{bmatrix} K_{HH} & K_{HM} \\ K_{MH} & K_{MM} \end{bmatrix} \tag{2.40}$$

in which K_{VV} and K_{TT} are the uncoupled vertical and torsional impedance functions for subproblem 1; and K_{HH} and K_{MM} are the horizontal and rocking impedance functions for subproblem 2, coupled through the so-called coupling impedances K_{HM}, K_{MH}. The coupling impedances are equal due to the symmetry of $[\hat{k}^m]$, whose symmetry is in turn due to the symmetry of $[\hat{G}^m]$ or $[\hat{\bar{G}}^m]$ depending on the boundary-value problem under consideration. All other impedance functions are zero in the full 6x6 impedance matrix due to the geometric symmetry with respect to the z-axis.

It will be convenient for later use in graphically displaying the impedance coefficients as a function of frequency for axisymmetric foundations to introduce the following real and dimensionless stiffness coefficients k_{VV}, k_{TT}, k_{HH}, k_{MM}, k_{HM} and damping coefficients c_{VV}, c_{TT}, c_{HH}, c_{MM}, c_{HM} according to

$$\begin{aligned} K_{VV} &= \bar{\mu} a (k_{VV} + i a_o c_{VV}) \\ K_{TT} &= \bar{\mu} a^3 (k_{TT} + i a_o c_{TT}) \\ K_{HH} &= \bar{\mu} a (k_{HH} + i a_o c_{HH}) \\ K_{MM} &= \bar{\mu} a^3 (k_{MM} + i a_o c_{MM}) \\ K_{HM} &= K_{MH} = \bar{\mu} a^2 (k_{HM} + i a_o c_{HM}) \end{aligned} \tag{2.41}$$

in which "$\bar{\mu}$" is a reference shear modulus, "a" is the surface radius of the axisymmetric foundation, and "a_o" is the dimensionless frequency $\omega a/\bar{\beta}$, with $\bar{\beta}$ being a reference shear wave velocity.

Finally, it will be useful to express the 3x3 Green's function traction matrix $\overset{\nu}{H}{}^{m}_{ji}(\vec{y};\ \vec{x})$ in terms of the stresses caused by the concentrated ring sources. Referring to Figure 2.5, the unit normal pointing into the volume of revolution V' is given by

$$\vec{\nu}(\vec{y}) = (\nu_1,\ \nu_2,\ \nu_3) = \left(-\cos\psi(\vec{y})\ ,\ 0\ ,\ -\sin\psi(\vec{y})\right)\ . \qquad (2.42)$$

Using Eq. (2.42) in conjunction with

$$\overset{\nu}{H}{}^{m}_{ji}(\vec{y};\ \vec{x}) = \left(\frac{2\pi r'}{r^2}\right) \Sigma^{i}_{kj}\ (\vec{y};\ \vec{x})\ \nu_k(\vec{y}) \qquad (2.43)$$

leads directly to

$$\begin{bmatrix} \overset{\nu}{H}{}^{m}_{11} & \overset{\nu}{H}{}^{m}_{12} & \overset{\nu}{H}{}^{m}_{13} \\ \overset{\nu}{H}{}^{m}_{21} & \overset{\nu}{H}{}^{m}_{22} & \overset{\nu}{H}{}^{m}_{23} \\ \overset{\nu}{H}{}^{m}_{31} & \overset{\nu}{H}{}^{m}_{32} & \overset{\nu}{H}{}^{m}_{33} \end{bmatrix}_{(\vec{y};\ \vec{x})} = -\left(\frac{2\pi r'}{r^2}\right)\cos\psi(\vec{y}) \begin{bmatrix} \Sigma^{R}_{rr} & \Sigma^{T}_{rr} & \Sigma^{V}_{rr} \\ \Sigma^{R}_{r\theta} & \Sigma^{T}_{r\theta} & \Sigma^{V}_{r\theta} \\ \Sigma^{R}_{rz} & \Sigma^{T}_{rz} & \Sigma^{V}_{rz} \end{bmatrix}_{(\vec{y};\ \vec{x})}$$

$$-\left(\frac{2\pi r'}{r^2}\right)\sin\psi(\vec{y}) \begin{bmatrix} \Sigma^{R}_{zr} & \Sigma^{T}_{zr} & \Sigma^{V}_{zr} \\ \Sigma^{R}_{z\theta} & \Sigma^{T}_{z\theta} & \Sigma^{V}_{z\theta} \\ \Sigma^{R}_{zz} & \Sigma^{T}_{zz} & \Sigma^{V}_{zz} \end{bmatrix}_{(\vec{y};\ \vec{x})} \qquad (2.44)$$

in which the superscripts i ($i = 1,2,3$) on the individual stress components Σ^i_{kj} refer to the stress components resulting from radial, tangential and vertical concentrated ring loads, respectively, of azimuthal order m. The factor of $2\pi r'/r^2$ was introduced into Eqs. (2.43), (2.44) in order to be consistent with the notation used in Part I, Section 2.4, where the individual stress components Σ^i_{kj} are derived.

CHAPTER 3

METHOD OF ANALYSIS

3.1 DISCRETIZATION

Even for the simplest geometries, the integral equations for the distributed forces $\vec{F}(\vec{x})$ in Chapter 2 must be solved numerically by discretizing the formulation. The problem would thereby reduce to the solution of a set of simultaneous, complex, linear, algebraic equations. The discretization consists of three basic steps for any three-dimensional or axisymmetric problem having displacement or mixed boundary conditions. Therefore, analogous to the integral formulation in Chapter 2, the radiation problem involving a three-dimensional foundation in welded contact with the surrounding soil (Section 2.2) will be used to exemplify the discretized formulation.

The first step in the discretization is to replace the surface integrals appearing in Eq. (2.4) with formulae of quadrature. Letting A_n, (n=1,N) and B_m, (m=1,M) represent the quadrature coefficients for integration over surfaces S' and S, respectively, then Eq. (2.4) may be written in the following form:

$$\sum_{n=1}^{N} \hat{G}_{ij}(\vec{x}; \vec{x}_n)F_j(\vec{x}_n)A_n = \sum_{m=1}^{M} {}^{\nu}H_{ji}(\vec{y}_m; \vec{x})u_j(\vec{y}_m)B_m \quad . \tag{3.1}$$

The second step in the discretization is to impose the integral equation for the discrete set of forces $\vec{F}(\vec{x}_n)$ in Eq. (3.1) to a set of discrete points on S' which are the same as those used in the quadrature over S':

$$\sum_{n=1}^{N} \hat{G}_{ij}(\vec{x}_\ell; \vec{x}_n)F_j(\vec{x}_n)A_n = \sum_{m=1}^{M} \overset{\nu}{H}_{ji}(\vec{y}_m; \vec{x}_\ell)U_j(\vec{y}_m)B_m, \quad (\ell=1,N). \tag{3.2}$$

The third step in the discretization is to write the integral defining $\hat{G}_{ij}$ in terms of the B_m quadrature formula:

$$\hat{G}_{ij}(\vec{x}_\ell; \vec{x}_n) = \sum_{m=1}^{M} G_{ki}(\vec{y}_m; \vec{x}_\ell)\overset{\nu}{H}_{kj}(\vec{y}_m; \vec{x}_n)B_m \ . \tag{3.3}$$

Now, once the N simultaneous, complex, linear, algebraic equations in Eq. (3.2) are solved for the N discrete forces $\vec{F}(\vec{x}_n)$, the discrete traction distribution on S is determined from Eq. (2.3) as

$$\overset{\nu}{T}_j(\vec{y}_m) = \sum_{n=1}^{N} \overset{\nu}{H}_{jk}(\vec{y}_m; \vec{x}_n)F_k(\vec{x}_n)A_n \ , \tag{3.4}$$

from which other quantities of interest may be obtained.

The Green's functions, $G_{ji}(\vec{y}_m; \vec{x}_\ell)$ and $\overset{\nu}{H}_{ji}(\vec{y}_m; \vec{x}_\ell)$, become singular in the limit as the point $\vec{x}_\ell$ approaches the point $\vec{y}_m$, so it would be convenient to insure that no source point $\vec{x}_\ell$, $(\ell=1,N)$ ever coincides with any receiver point $\vec{y}_m$, $(m=1,M)$. This is most easily accomplished by requiring that the entire surface S' be sufficiently offset from the surface S so as to avoid the unnecessary problems associated with integrals of singular functions. Details of how to choose the optimum location of surface S' as well as the number of quadrature points (N on surface S' and M on surface S) will be discussed in Sections 3.2 and 3.3.

At this point, it is advantageous to introduce the following matrices (composed of 3 x 3 submatrices) and vectors (composed of 3 x 1 subvectors) in order to cast the discretization into matrix formalism:

$$\left[G\right] = \left[\begin{array}{c|c|c|c} \left[G_{ij}(\vec{y}_1, \vec{x}_1)\right] & \left[G_{ij}(\vec{y}_1, \vec{x}_2)\right] & \cdots & \left[G_{ij}(\vec{y}_1, \vec{x}_N)\right] \\ \hline \left[G_{ij}(\vec{y}_2, \vec{x}_1)\right] & \left[G_{ij}(\vec{y}_2, \vec{x}_2)\right] & & \left[G_{ij}(\vec{y}_2, \vec{x}_N)\right] \\ \hline \vdots & & \ddots & \\ \hline \left[G_{ij}(\vec{y}_m, \vec{x}_1)\right] & \left[G_{ij}(\vec{y}_m, \vec{x}_2)\right] & & \left[G_{ij}(\vec{y}_M, \vec{x}_N)\right] \end{array}\right]_{3M \times 3N} \tag{3.5}$$

$$\left[\overset{\nu}{H}\right] = \left[\begin{array}{c|c|c|c} \left[\overset{\nu}{H}_{ij}(\vec{y}_1, \vec{x}_1)\right] & \left[\overset{\nu}{H}_{ij}(\vec{y}_1, \vec{x}_2)\right] & \cdots & \left[\overset{\nu}{H}_{ij}(\vec{y}_1, \vec{x}_N)\right] \\ \hline \left[\overset{\nu}{H}_{ij}(\vec{y}_2, \vec{x}_1)\right] & \left[\overset{\nu}{H}_{ij}(\vec{y}_2, \vec{x}_2)\right] & & \left[\overset{\nu}{H}_{ij}(\vec{y}_2, \vec{x}_N)\right] \\ \hline \vdots & & \ddots & \\ \hline \left[\overset{\nu}{H}_{ij}(\vec{y}_m, \vec{x}_1)\right] & \left[\overset{\nu}{H}_{ij}(\vec{y}_2, \vec{x}_2)\right] & & \left[\overset{\nu}{H}_{ij}(\vec{y}_M, \vec{x}_N)\right] \end{array}\right]_{3M \times 3N} \tag{3.6}$$

$$\left[\diagdown A \diagdown\right] = \begin{bmatrix} \begin{bmatrix} A_1 & 0 & \\ 0 & A_1 & \\ & 0 & A_1 \end{bmatrix} & \begin{bmatrix} 0 \end{bmatrix} & \cdots & \begin{bmatrix} 0 \end{bmatrix} \\ \begin{bmatrix} 0 \end{bmatrix} & \begin{bmatrix} A_2 & 0 & \\ 0 & A_2 & \\ & 0 & A_2 \end{bmatrix} & & \begin{bmatrix} 0 \end{bmatrix} \\ \vdots & & \ddots & \\ \begin{bmatrix} 0 \end{bmatrix} & \begin{bmatrix} 0 \end{bmatrix} & & \begin{bmatrix} A_N & 0 & \\ 0 & A_N & \\ & 0 & A_N \end{bmatrix} \end{bmatrix}$$

$3N \times 3N$

(3.7)

$$\left[\diagdown B \diagdown\right] = \begin{bmatrix} \begin{bmatrix} B_1 & 0 & \\ 0 & B_1 & \\ & 0 & B_1 \end{bmatrix} & \begin{bmatrix} 0 \end{bmatrix} & \cdots & \begin{bmatrix} 0 \end{bmatrix} \\ \begin{bmatrix} 0 \end{bmatrix} & \begin{bmatrix} B_2 & 0 & \\ 0 & B_2 & \\ & 0 & B_2 \end{bmatrix} & & \begin{bmatrix} 0 \end{bmatrix} \\ \vdots & & \ddots & \\ \begin{bmatrix} 0 \end{bmatrix} & \begin{bmatrix} 0 \end{bmatrix} & & \begin{bmatrix} B_M & B_M & B_M \end{bmatrix} \end{bmatrix}$$

$3M \times 3M$

(3.8)

$$\{F\} = \begin{Bmatrix} \{F_i(\vec{x}_1)\} \\ \{F_i(\vec{x}_2)\} \\ \vdots \\ \{F_i(\vec{x}_N)\} \end{Bmatrix}, \quad \{U\} = \begin{Bmatrix} \{U_i(\vec{y}_1)\} \\ \{U_i(\vec{y}_2)\} \\ \vdots \\ \{U_i(\vec{y}_M)\} \end{Bmatrix}, \quad \{\overset{\nu}{T}\} = \begin{Bmatrix} \{\overset{\nu}{T}_i(\vec{y}_1)\} \\ \{\overset{\nu}{T}_i(\vec{y}_2)\} \\ \vdots \\ \{\overset{\nu}{T}_i(\vec{y}_M)\} \end{Bmatrix} \qquad \begin{matrix} (3.9) \\ (3.10) \\ (3.11) \end{matrix}$$

$3Nx1 \qquad 3Mx1 \qquad 3Mx1$

in which $[G]$ and $[\overset{\nu}{H}]$ are the Green's function displacement and traction matrices, respectively; A_n $(n = 1,N)$ and B_m $(m = 1,M)$ are the quadrature coefficients for integration over S' and S, respectively (e.g., coefficients from Simpson's integration rule); $\{F\}$ are the unknown discrete forces on S'; $\{U\}$ are the displacements prescribed on S; and $\{\overset{\nu}{T}\}$ are the tractions on S caused by the displacements $\{U\}$ from which other information may be obtained.

Once discretized, Eq. (2.4) may be written in the form

$$\left[\hat{G}\right]\{F_A\} = \left[\overset{\nu}{H}_B\right]^T\{U\} \tag{3.12}$$

in which

$$\left[\hat{G}\right] = \left[G\right]^T\left[\overset{\nu}{H}_B\right] \tag{3.13}$$

is numerically symmetric and

$$\left[\overset{\nu}{H}_B\right] = \left[\diagdown B \diagdown\right]\left[\overset{\nu}{H}\right], \tag{3.14}$$

$$\{F_A\} = [A]\{F\} . \tag{3.15}$$

It is important to realize that the formulation is completely general in that the prescribed displacements $\{U\}$ on S can represent, for example, the excitation caused by external forces and moments, incoming seismic waves, shock waves from nuclear explosions, etc.

Inverting the symmetric $3N \times 3N$ matrix $[\overset{\nu}{G}]$, and multiplying through Eq. (3.12) yields the $3N$ complex amplitudes of the N unknown force vectors:

$$\{F_A\} = [\hat{G}]^{-1}[\overset{\nu}{H}_B]^T\{U\} . \tag{3.16}$$

Now, the traction distribution on S is given in discretized form by

$$\{\overset{\nu}{T}\} = [\overset{\nu}{H}]\{F_A\} \tag{3.17}$$

so that substitution from Eq. (3.16) into Eq. (3.17) results in

$$\{\overset{\nu}{T}\} = [\overset{\nu}{H}][\hat{G}]^{-1}[H_B]^T\{U\} . \tag{3.18}$$

Assuming that the nodal forces $\mathcal{F}_i(\vec{y}_K)$, $(K = 1,2, \ldots, M)$ are obtained from the tractions by the B_i quadrature

$$\{\mathcal{F}\} = [B]\{\overset{\nu}{T}\}$$

where

$$\left\{\mathcal{F}\right\} = \begin{Bmatrix} \left\{\mathcal{F}_i(\vec{y}_1)\right\} \\ \left\{\mathcal{F}_i(\vec{y}_2)\right\} \\ \vdots \\ \left\{\mathcal{F}_i(\vec{y}_M)\right\} \end{Bmatrix} \tag{3.20}$$

then, introducing Eq. (3.18) for the tractions leads to

$$\left\{\mathcal{F}\right\} = \left[\hat{K}\right]\left\{U\right\} \tag{3.21}$$

in which

$$\left[\hat{K}\right] = \left[{}^{\nu}_{H_B}\right]\left[\hat{G}\right]^{-1}\left[H_B\right]^{T} . \tag{3.22}$$

The 3Mx3M matrix $[\hat{K}]$ in Eq. (3.21) corresponds to the stiffness matrix representing the viscoelastic material outside the volume V'. Since the stiffness matrix $[\hat{K}]$ connects the nodal forces on S with the displacements there, the individual components of $[\hat{K}]$ can be utilized as nonreflecting boundary conditions on S -- a major breakthrough for finite element modelling of region V'.

Of immediate concern for the present work, however, is that the 6x6 impedance matrix $[K]$ can be written in terms of the stiffness matrix $[\hat{K}]$, as insinuated in Section 2.4. Consider the total work done by the discrete set of tractions on the rigid body displacements which are defined by Eq. (2.14) for a point $\vec{y}_K$, (k = 1,2,...,M) on S:

$$\int_S \left\{ \overset{\nu}{T}(\vec{y}) \right\}^T \left\{ U(\vec{y}) \right\} dS(\vec{y}) = \left\{ \overset{\nu}{T} \right\}^T \left[\overset{\nu}{B} \right] \{ U \}$$

$$= \{ \Delta \}^T [\alpha]^T [\hat{K}] [\alpha] \{ \Delta \}$$

$$= \{ \Delta \}^T [K] \{ \Delta \} \tag{3.23}$$

in which $[\alpha]$ is now the $3M \times 6$ influence matrix. It is clear from Eq. (3.23) that the impedance matrix is related to the stiffness matrix by

$$[K] = [\alpha]^T [\hat{K}] [\alpha] \tag{3.24}$$

in which $[\hat{K}]$ depends upon the frequency of excitation, the geometry of volume V', the boundary conditions on S (welded or relaxed), and the material comprising volume V. In addition to depending on $[\hat{K}]$, the impedance matrix $[K]$ is also a function of whether or not the foundation is rigid or flexible through the influence matrix $[\alpha]$.

For the case of mixed boundary conditions, the integral equations of Section 2.3 are discretized using M_1 points on surface S_1 (where tractions are prescribed) and M_2 points on surface S_2 (where displacements are prescribed) such that $M_1 + M_2 = M$. The Green's function matrices $[G]$ and $\overset{\nu}{[H]}$, the integration coefficient matrix $\left[\overset{\nu}{B} \right]$, and the displacement and traction vectors $\{U\}$ and $\overset{\nu}{\{T\}}$ must all be partitioned in Eqs. (3.5), (3.6), (3.8), (3.10) and (3.11), respectively.

Since the integrals over S_1 are carried out to the boundary of S_2, then the point(s) separating S_1 from S_2 must be treated as a double point(s) insofar as the last three rows of the $3(M_1+1) \times 3N$

matrices $[G_1(\vec{y}_k;\vec{x}_\ell)]$ and $[H_1(\vec{y}_k;\vec{x}_\ell)]$ for $(k=1,2,\ldots,M_1+1)$, $(\ell=1,2,\ldots, N)$ are the same as the first three rows of the $3M_2 \times 3N$ matrices $[G_2(\vec{y}_k;\vec{x}_\ell)]$ and $[\overset{\nu}{H}_2(\vec{y}_k;\vec{x}_\ell)]$, respectively, for $(k-M_1+1, M_1+2, \ldots, M)$, $(\ell=1,2,\ldots, N)$. Also, the $3(M_1+1) \times 3(M_1+1)$ diagonal matrix $\left[\diagdown B_1 \diagup\right]$ includes the integration coefficient B_{M_1+1} as the end point for integration over S_1 and could be different from the coefficient B_{M_1+1} used as the end point for integration over S_2 appearing in the first three diagonal locations of the $3M_2 \times 3M_2$ diagonal matrix $\left[\diagdown B_2 \diagup\right]$. The subscripts $\underline{1}$ and $\underline{2}$ appearing in the subsequent matrix analysis refer to observation points $\vec{y} \in S_1$ and $\vec{y} \in S_2$, respectively.

Therewith, Eq. (2.12) appears in discretized form as

$$\left[\hat{G}\right]\{F_A\} = \left[\overset{\nu}{H}_{B_2}\right]^T\{U_2\} - \left[G_1\right]^T\{\overset{\nu}{T}_{B_1}\} \tag{3.25}$$

in which

$$\left[\hat{G}\right] = \left[G_2\right]^T\left[\overset{\nu}{H}_{B_2}\right] - \left[\overset{\nu}{H}_{B_1}\right]^T\left[G_1\right] \tag{3.26}$$

is numerically symmetric, $\{F_A\}$ is defined previously in Eq. (3.15), and

$$\left[\overset{\nu}{H}_{B_1}\right] = \left[\diagdown B_1 \diagup\right]\left[\overset{\nu}{H}_1\right] \quad , \quad \left[\overset{\nu}{H}_{B_2}\right] = \left[\diagdown B_2 \diagup\right]\left[\overset{\nu}{H}_2\right] \tag{3.27}$$

$$\{\overset{\nu}{T}_{B_1}\} = \left[\diagdown B_1 \diagup\right]\{\overset{\nu}{T}_1\} \quad . \tag{3.28}$$

Now, the discrete traction distribution on S_2 and displacement distribution on S_1 are written as

$$\left\{ \begin{matrix} \nu \\ T_2 \end{matrix} \right\} = \left[\begin{matrix} \nu \\ H_2 \end{matrix} \right] \left\{ F_A \right\} \quad , \quad \left\{ U_1 \right\} = \left[G_1 \right] \left\{ F_A \right\} \quad , \tag{3.29}$$

which, after solving Eq. (3.25) for the $3N$ complex amplitudes of the N unknown force vectors, appear in the final form as

$$\left\{ \begin{matrix} \nu \\ T_2 \end{matrix} \right\} = \left[\begin{matrix} \nu \\ H_2 \end{matrix} \right] \left[\hat{\hat{G}} \right]^{-1} \left(\left[\begin{matrix} \nu \\ H_{B_2} \end{matrix} \right] \left\{ U_2 \right\} - \left[G_1 \right] \left\{ \begin{matrix} \nu \\ T_{B_1} \end{matrix} \right\} \right) \tag{3.30}$$

$$\left\{ U_1 \right\} = \left[G_1 \right] \left[\hat{\hat{G}} \right]^{-1} \left(\left[\begin{matrix} \nu \\ H_{B_2} \end{matrix} \right] \left\{ U_2 \right\} - \left[G_1 \right] \left\{ \begin{matrix} \nu \\ T_{B_1} \end{matrix} \right\} \right) \quad . \tag{3.31}$$

Assuming for the moment that the prescribed tractions $\{ \overset{\nu}{T}_1 \}$ are zero, then the total work results from the tractions acting on the displacements as prescribed on S_2. Thereby, the only nonzero terms in the stiffness matrix for the mixed boundary conditions are those appearing in the $3M_2 \times 3M_2$ submatrix

$$\left[\hat{\hat{K}} \right] = \left[\begin{matrix} \nu \\ H_{B_2} \end{matrix} \right] \left[\hat{\hat{G}} \right]^{-1} \left[\begin{matrix} \nu \\ H_{B_2} \end{matrix} \right]^{T} \tag{3.32}$$

and the 6×6 impedance matrix is determined from

$$\left[K \right] = \left[\alpha_2 \right]^{T} \left[\hat{\hat{K}} \right] \left[\alpha_2 \right] \tag{3.33}$$

in which $[\alpha_2]$ is the $3M_2 \times 6$ influence matrix relating the "generalized displacement" to the rigid body displacments at all M_2 points on S_2.

Finally, for three-dimensional volumes V' having axial symmetry with respect to the vertical axis, the discretization of the integral equations appearing in Section 2.5 exactly parallels the procedure

outlined above with the following changes: 1) the components of the Green's function matrices defined in Eqs. (3.5) and (3.6) involve ring source functions of order m rather than point forces; 2) the components of all matrices are expressed in cylindrical coordinates along cylindrical directions instead of in rectangular coordinates along rectangular directions; 3) the integration coefficients A_i ($i = 1,2, \ldots, N$) and B_i ($i = 1,2, \ldots, M$) appearing in Eqs. (3.7) and (3.8), respectively, must include the factors $\varepsilon_m \pi r'$ and $\varepsilon_m \pi r$, respectively, when calculating the quadrature formulae for integration over S' and S, respectively; and 4) the surfaces S and S' are actually lines (L and L') in the axisymmetric formulation and must be treated as such.

Therefore, writing out the discretized equations for axisymmetric geometries would be inconsequential since the discretization for the fully 3-D case may be directly employed by keeping in mind the aforementioned alterations. The only significant difference, as was discussed in Section 2.5, is the determination of the impedance matrix in two steps: 1) $m=0$ ring load order for torsional and vertical impedances; and 2) $m=1$ ring load order for horizontal, rocking and coupling impedances. In both subproblems, the influence matrix $[\alpha^m]$ will be $3M \times 2$ instead of $3M \times 6$.

The following two sections discuss in detail how to numerically implement the discretization analysis of the radiation problem with applications to axisymmetric geometries in particular.

3.2 SOLUTION BY STANDARD INVERSION

All that remains to complete the discretization analysis is to devise a set of rules governing how many observation points to use on S and how many source points to use on S', as well as where to locate surface S' relative to surface S. The number of observation points, M, on surface S necessary to numerically perform the discretized integrals in Eqs. (3.12) through (3.33) to a certain accuracy depends not only on the shortest wavelength considered in the radiation problem, but also depends largely on the location of the internal surface S'. This is due to the fact that the closer S' is to S, the more pronounced the Green's functions become, thus requiring more observation points to evaluate the integrals properly. The minimum requirement for the number of observation points, M, on surface S is that the matrix $[\hat{G}]$ in Eq. (3.13) (or $[\hat{\hat{G}}]$ in Eq. (3.26) for mixed boundary conditions) be numerically symmetric.

Yet, if any portion of surface S' is so far removed from surface S that the Green's functions on S resulting from neighboring sources on S' become too similar, then the matrix $[\hat{G}]$ becomes poorly conditioned even though the symmetry of the individual elements of $[\hat{G}]$ may be excellent. Also, requiring that the matrix $[\hat{G}]$ be numerically symmetric and well-conditioned is a necessary but not sufficient prescription for achieving accurate displacements and tractions on S. What also must be fathomed is the number of sources, N, to employ on surface S'.

To properly represent the displacements and tractions on S, it is sometimes necessary to utilize a large number of sources on S'

(e.g., if mixed boundary conditions are imposed or if corners exist on S), in which case the surface S' must be situated closer to the surface S (to avoid the conditioning problem in $[\hat{G}]$). This in turn means increasing the number of observation points, M, on S so as to enable the numerical integrations in Eqs. (3.12) through (3.33) to be performed within a desired error tolerance.

The impact of the errors associated with choosing the number of observation points, M, on S, the number of source points, N, on S', and the location of S' will be discussed presently, after which some general rules will be summized for numerical implementation of the discretization analysis presented in Section 3.1.

Assuming that the number of observation points, M, on S is chosen sufficiently large (with source surface S' specified) to accurately perform the numerical integrations, then the real question becomes how to balance the tradeoff between number of sources, N, needed on surface S' with the actual location of surface S' interior to surface S. To help resolve this question, the response of a rigid circular cylinder embedded in a viscoelastic half-space is examined when excited by external forces and moments.

The axisymmetric cylindrical foundation to be studied has a ratio of embedment depth $\underline{h}$ to radius $\underline{a}$ equal to 2.0 and three different surfaces S' are considered on which various numbers of ring sources are located, as shown in Figure 3.1. The spacing of the observation points on surface S (surface of the cylinder) is sufficiently fine (h/40) to insure that the numerical integrations are accurate to three significant digits for any of the internal source surfaces S'_a, S'_b, S'_c.

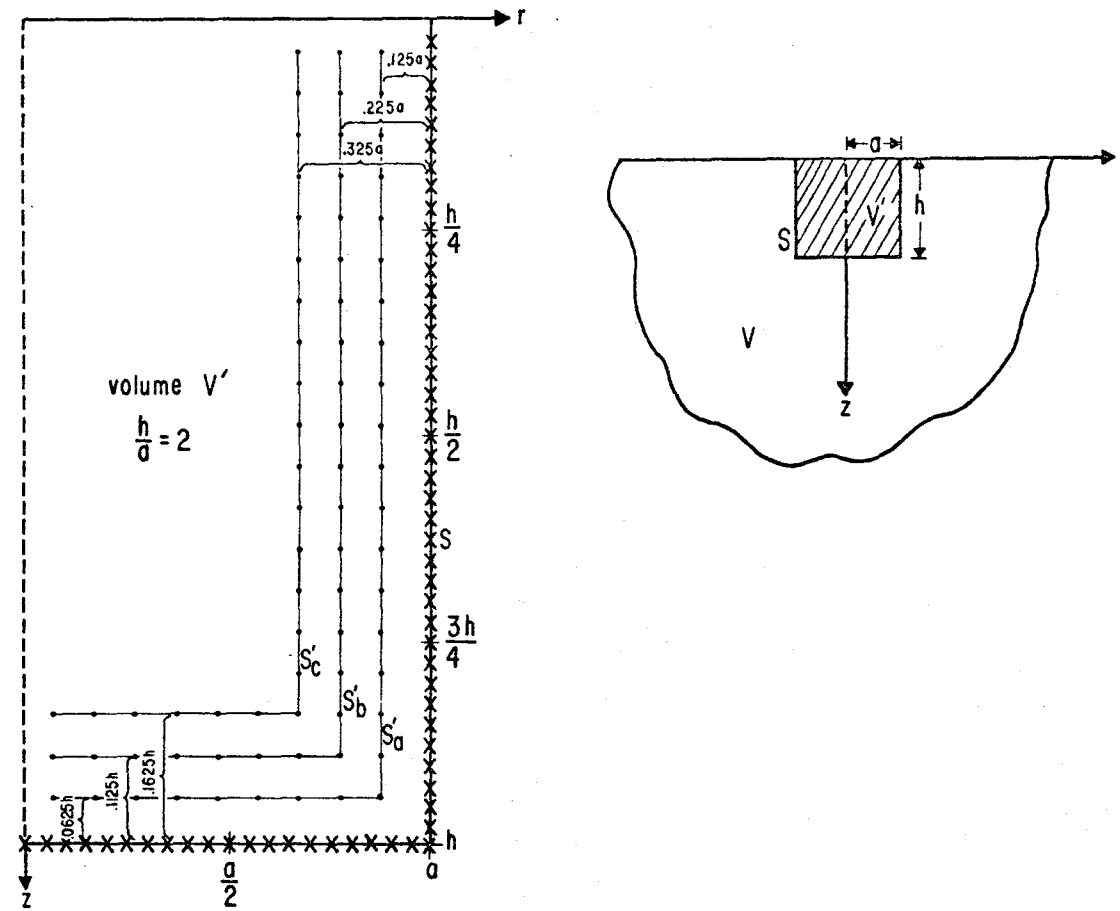

Figure 3.1. Boundary geometry, coordinate system and numerical grid used to study the tradeoff between the number of sources on surface S´ and the location of surface S´ interior to surface S. The rigid cylindrical foundation has an embedment ratio of h/a = 2.

It is important to realize that the Green's function traction components as defined in Eq. (2.44) will be identically zero on the portion of S which coincides with the free surface of the half-space. Thereby, the integrals along this portion of S may be disgarded from the analysis for this particular problem. Also, due to the symmetry about the vertical axis, only half of the axisymmetric problem need be considered. The viscoelastic half-space representing volume V is characterized by a reference shear wave velocity $\bar{\beta}$, a compressional wave velocity $\alpha = \sqrt{3}\ \bar{\beta}$, and specific attenuation factors $Q_\beta = 50$, $Q_\alpha = 100$ for the shear and compressional waves, respectively.

The foundation impedance coefficients provide a synopsis of the overall accuracy of the method. Therefore, much of the discussion embraces the behavior of the impedance coefficients as a function of number of ring sources used on S' as well as the precise location of S' interior to surface S of the cylinder. The dependence on frequency, embedment ratio, material damping and layering of soil deposit will be studied exclusively in Chapter 4.

In Figure 3.2, the real parts of the torsional and vertical impedance coefficients at dimensionless frequency $a_o = \omega a/\bar{\beta} = 0.1$ for the rigid cylindrical foundation modeled in Figure 3.1 are plotted versus the number of ring sources used on each of the internal surfaces S'_a, S'_b, S'_c. The impedance coefficients are normalized in Figure 3.2 by their "exact" values, which were calculated using an extremely refined mesh with the source surface S' located closer to the foundation surface S.

It is encouraging to find that for all three source surfaces, the impedance coefficients fall within three percent of the "exact"

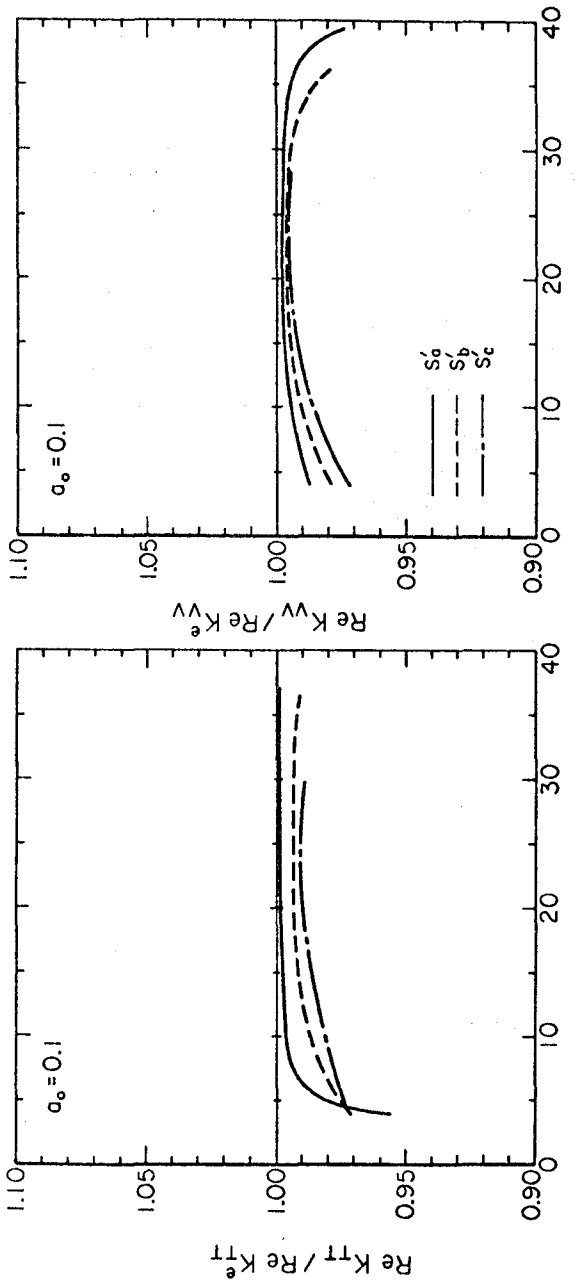

Figure 3.2. Real parts of the tortional and vertical impedance coefficients displayed at dimensionless frequency $a_o = 0.1$ as a function of number of sources used on each of the internal source surfaces shown in Figure 3.1. The impedance coefficients are normalized by their "exact" values.

values over an astoundingly wide range of number of sources (from N=5 to N=38). Also, as the number of sources is increased from N=1 to N=20, the general trend is to approach the "exact" impedances.

However, depending on the location of the source surface S', there exists a certain number of sources, after which the impedances begin to diverge when using the standard inversion formulation. This phenomenon is related to the conditioning problem in reference to the proximity of the sources on S'. Further substantiation is possible by noticing that the divergent trend occurs sooner for the source surfaces further removed from the surface of the cylinder (since the effective separation of the sources is smaller relative to the distance from S' to S). Similar behavior is exhibited in Figure 3.3 for the torsional impedance coefficient at dimensionless frequencies $a_0 = 0.5$, 1, 2 and 5.

To summarize thus far, impedances consistently within one percent of the "exact" value are obtainable at all frequencies of practical interest by utilizing the source surface S'_a with the sources separated by approximately a distance $h/20$. If, for some reason, a more refined source spacing is required, then the standard inversion technique may lead to conditioning problems associated with the proximity of the sources on S'. For such a problem, two alternatives are plausible: 1) resort to solving the discretized equations with eigenanalysis instead of standard inversion (e.g., Gaussian elimination) as will be discussed in Section 3.3; 2) locate the source surface S' nearer to the foundation surface S, which is by far the inferior countermeasure since the number of observation points on S would then have to be drastically increased (since the kernels of the integral equations would be more pronounced).

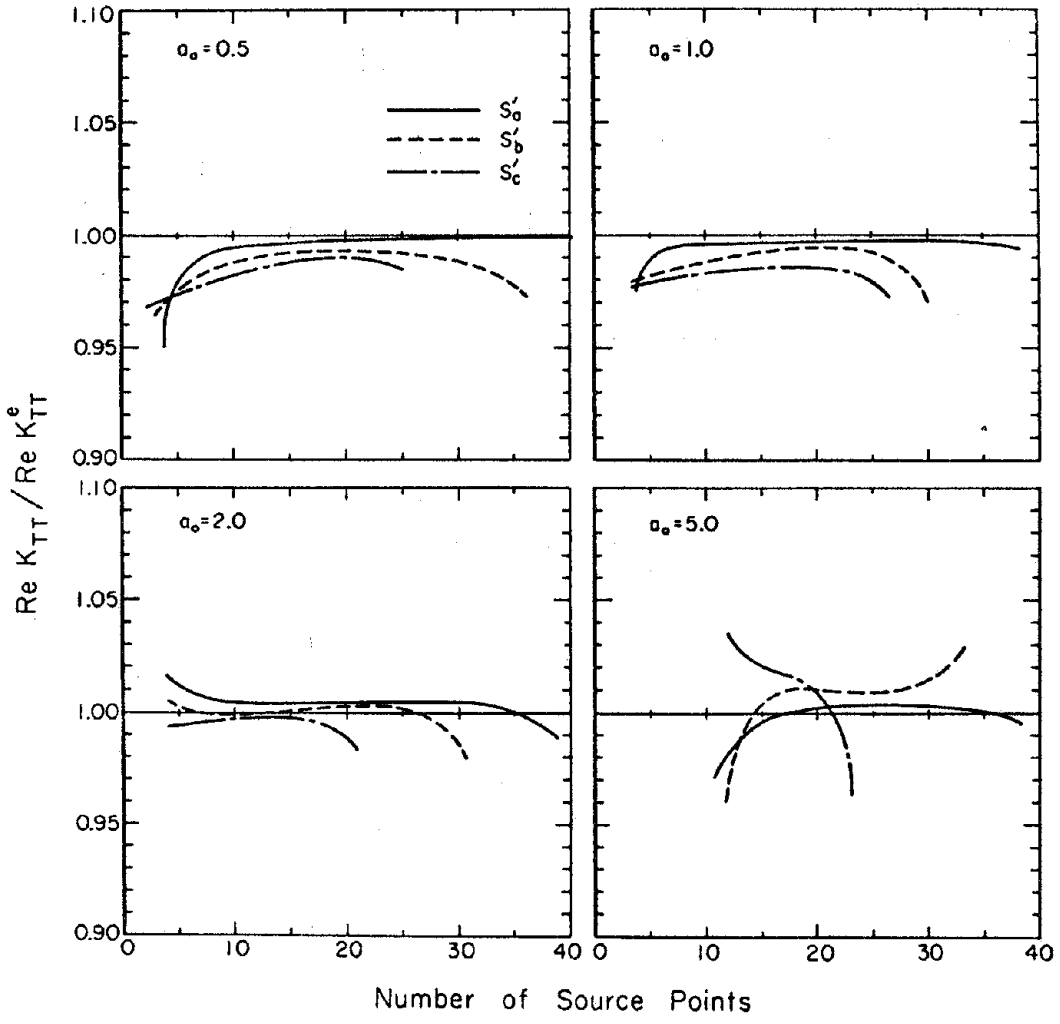

Figure 3.3. Corresponding results to Figure 3.2 for the real part of the normalized torsional impedance coefficient at dimensionless frequencies a_0 = .5, 1, 2 and 5.

To verify that source surface S_a' is the most practical choice, it would be convenient to compare the computed displacements and tractions on S caused by the rigid body movements of the foundation for the different internal source surfaces. It should be mentioned that closing a source surface other than by uniformly shrinking the surface S causes the matrix $[\hat{G}]$ to become nearly singular since one or more columns would be small relative to the others. Also, the trend in Figures 3.2 and 3.3 to obtain more accurate results when the source surface is located nearer to the foundation surface is actually a general prescription. However, the gain in accuracy is found to be minimal compared to the increased computational effort required.

In Figure 3.4, the real parts of the vertical displacement along the mantle of the cylinder are displayed at four representative frequencies $a_0 = .1, .5, 2, 5$ (from left to right). The displacements calculated using the three internal source surfaces S_a', S_b', S_c' of Figure 3.1 are compared on each plot. Since the contact between the foundation and soil is of welded type, the forced vertical vibrations of the rigid cylinder (viz., the "generalized displacement" $\Delta_z = 1$; all other components equal zero) should cause the entire foundation to move rigidly downward an amount unity. Therefore, a heavy line representing the exact response is drawn down the center of each graph at unity (imaginary part of response is zero).

The vertical axis in each plot in Figure 3.4 corresponds to the observation depth along the mantle of the cylinder (measured from the free surface); the horizontal axis corresponds to the amplitude of the real part of the vertical component of displacement. The horizontal

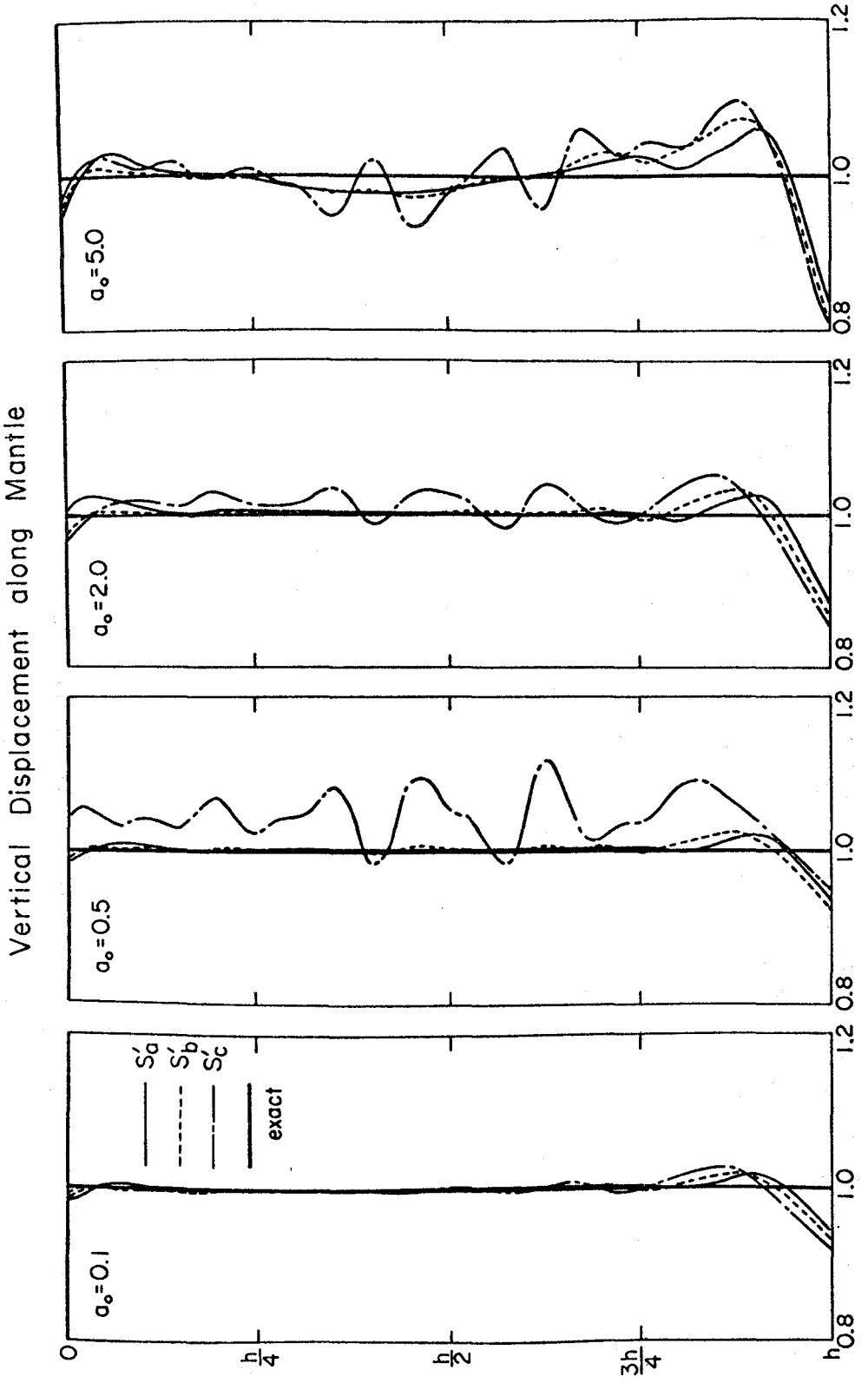

Figure 3.4. Vertical displacement along the mantle of the cylinder from Figure 3.1 displayed at dimensionless frequencies a_o = .1, .5, 2 and 5 and calculated using each of the internal source surfaces depicted in Figure 3.1.

scale is magnified around values within 20 percent of the exact amplitude to more easily distinguish the numerical oscillations associated with the location of the internal source surface. The number of sources used (27, 25, 23) and their locations on the three internal source surfaces (S_a', S_b', S_c', respectively) is depicted by the dots on S_a', S_b', S_c' in Figure 3.1 and corresponds to the optimum number of sources to exploit on the respective source surfaces, as insinuated in Figures 3.2 and 3.3 (for the standard inversion solution technique).

Proceeding with the discussion of Figure 3.4, it should be first pointed out that all frequencies considered, the displacements most consistently near the exact response are those obtained using source surface S_a'. The largest deviation from the exact value of unity is 0.25 percent except near the bottom corner of the cylinder. At the corner, the displacements are deficient because the observation points are furthest from the source surface by virtue of uniformly offsetting the source surface away from a corner (such an issue is nonexistent for surfaces S smoothly defined). The displacements associated with source surface S_c' are of subordinate accuracy compared to the results obtained with source surfaces S_a', S_b', similar to the impedance coefficients in Figures 3.2 and 3.3. The results are still reliable, however, to within 10 percent of the exact value.

Various attempts were made at overcoming the deficiency at the corner such as considering alternative combinations of sources in the vicinity of the corner in order to suitably modify the radiation pattern from the sources there. However, new problems were introduced into the analysis whenever sources were positioned on more than one internal source

surface simultaneously. The most effective remedy is to reduce the spacing of the sources near the corner (and near any other special points) with a possibly larger source spacing elsewhere. For example, displacements just as accurate as those corresponding to 27 equally spaced ring sources on S_a' as displayed in Figure 3.4 were obtained using 20 unequally spaced ring sources on S_a' with finer spacing near the corner of S_a' (comparison not presented). It is impossible to totally eliminate the deficiency at the corner so long as the source surface is internal to the observation surface, but later in this section, improved results will be presented using a refined mesh with the source surface located nearer to the observation surface.

Before elucidating on the computed traction distribution, one should be aware that the computed displacement distribution along the base of the cylinder behaves similarly to the distribution along the mantle as just discussed. The real parts of the vertical displacement along the base of the cylinder are shown in Figure 3.5, with the three internal source surfaces S_a', S_b', S_c' compared on each plot. The exact response of unity is once again represented by a heavy line at each of the four frequencies. The horizontal axes correspond to the observation radius along the base of the cylinder (measured from the axis of the cylinder) while the vertical axes correspond to the magnified amplitudes.

The computed traction components on the surface of the cylinder sketched in Figure 3.1 are shown in Figures 3.6 and 3.7 for forced torsional and vertical vibrations at frequency $a_o = 1$. The traction distribution in Figure 3.6 is determined with the S_b' source surface while the corresponding curves in Figure 3.7 are determined with the S_a'

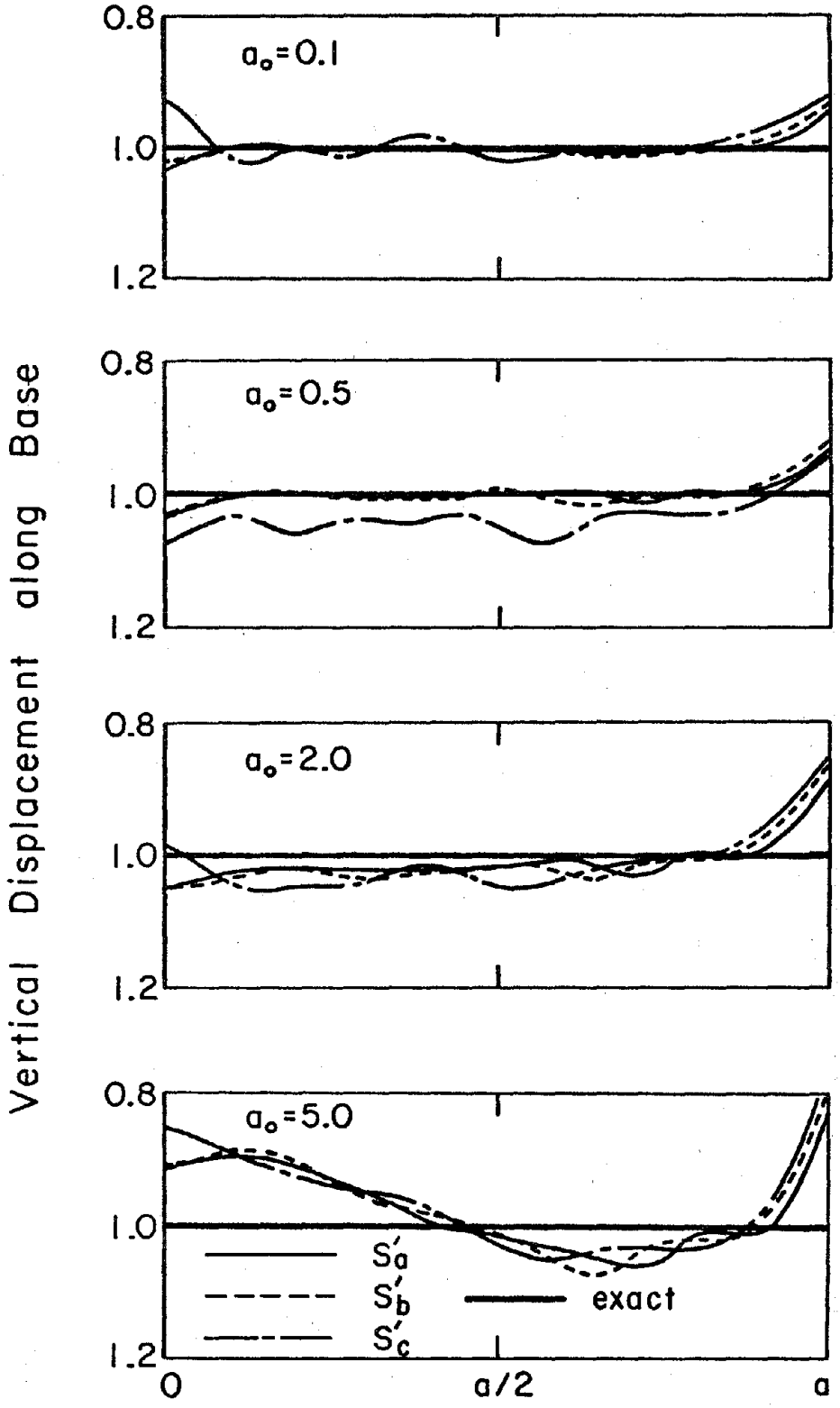

Figure 3.5. Corresponding results to Figure 3.4 for the vertical displacement along the base of the cylinder.

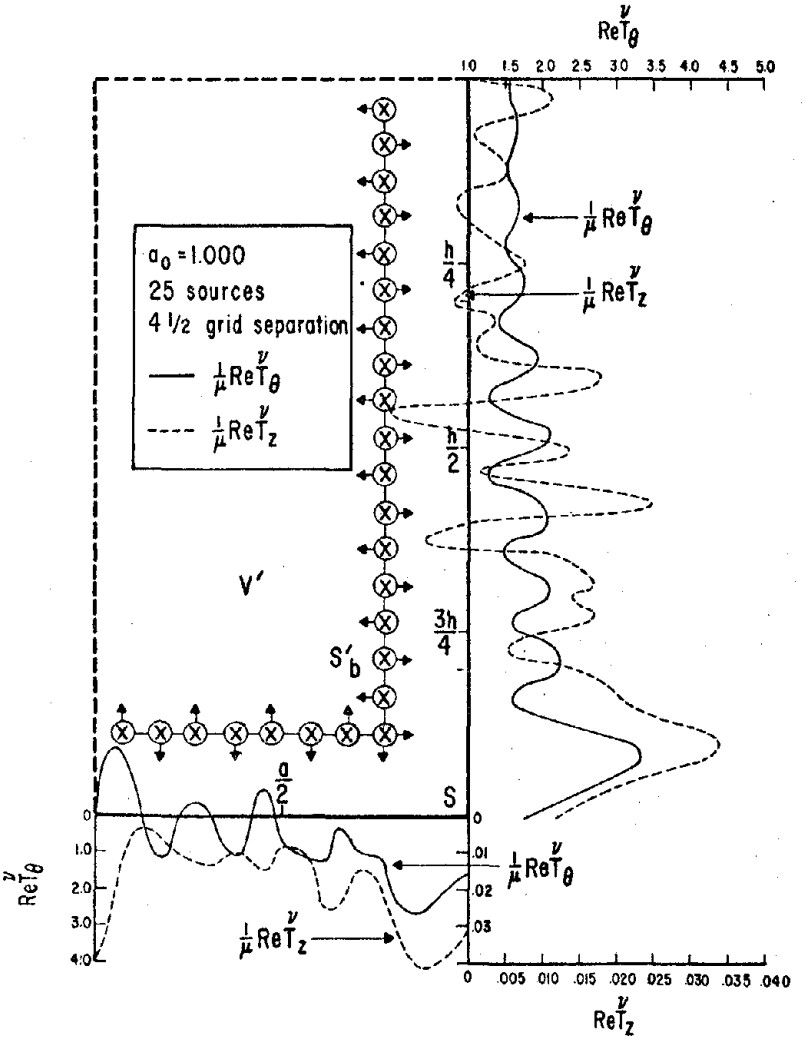

Figure 3.6. Traction distribution on the surface of the cylinder shown in Figure 3.1 for forced torsional and vertical vibrations at dimensionless frequency $a_0 = 1$, calculated using source surface S'_b.

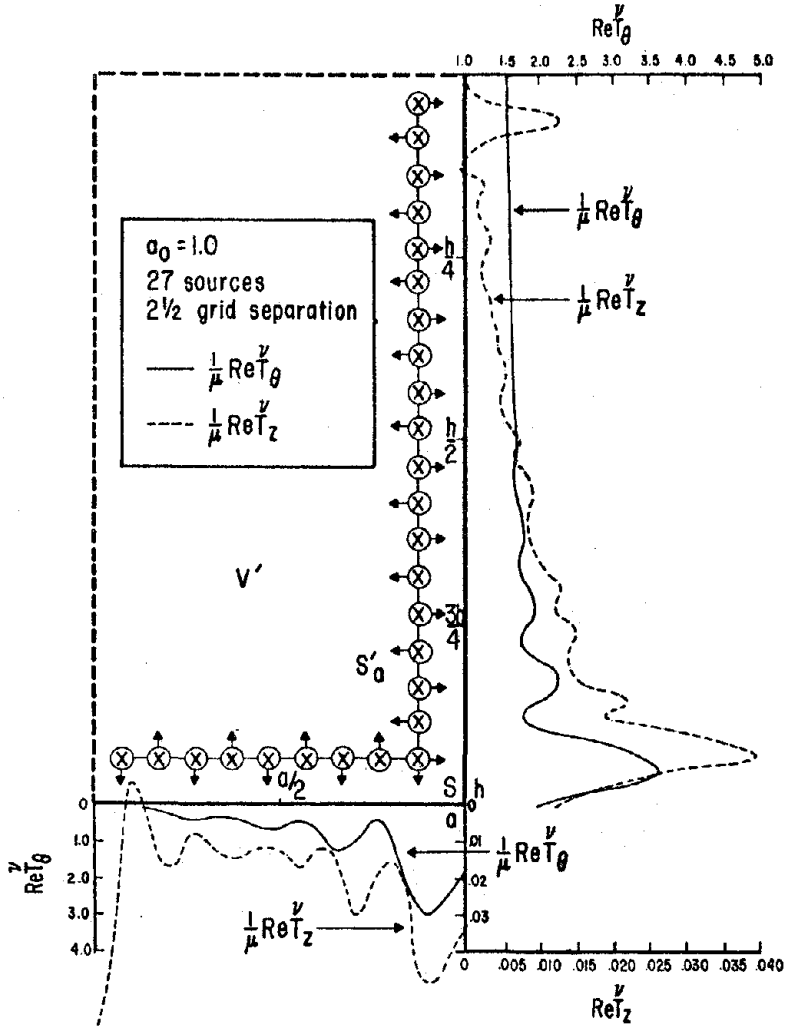

Figure 3.7. Corresponding results to Figure 3.6 when using source surface S'_a.

source surface. The placement of the sources is the same as for the displacements in Figures 3.4, 3.5 and their exact location on S_b', S_a' interior to surface S of the cylinder has been repeated in Figures 3.6 and 3.7, respectively, for illustrative purposes.

One striking feature, that was not quite so obvious when studying the displacements, is the marked effect of the discrete set of forces on the fluctuations in the traction components. Consider $\overset{\nu}{T}_\theta$, the traction due to the forced torsional oscillations of the rigid cylinder, since there is but one discrete force component per ring source. As portrayed by the arrows on the radiation patterns of the sources, the discrete force components alternate signs going from source to source. This phenomenon is an attempt to adjust for the singularity in the tractions at the corner. This is clearly the justification in Figure 3.7, since $\overset{\nu}{T}_\theta$ is smoothly behaved far away from the corner, but starts oscillating in phase with the discrete forces near the corner. On the other hand, in Figure 3.6, the oscillations linger much further away from the corner, which is additional motivation for declaring source surface S_a' to be the most effective choice of those surfaces considered.

Even for a surface in absence of a corner, there would inevitably be spurious fluctuations in the more sensitive traction components due to the discretization of surface S', but they would probably be minimal. If for some reason, it becomes desirable to obtain more accurate displacements and tractions, a refined source spacing is required with the source surface S' situated as close as possible to the foundation surface S. As previously mentioned, such an undertaking involves increased computational effort since more observation points would be required on S due

to the more pronounced kernels in the integral equations. Irregardless, such a refined result will now be presented, after which the general rules will finally be summized for the standard inversion method of solution.

The internal source surface used for the refined results in Figures 3.8 through 3.10 is situated halfway between the foundation surface and internal source surface S_a' of the previous studies. To ensure that the discretization analysis be performed at least as accurately as for source surface S_a', twice the number of observation points on S are used ($M=121$) since the kernels of the integral equations are more distinctive. Both $N=29$ and $N=57$ ring sources are considered on the internal source surface and the refined results are displayed at dimensionless frequency $a_o=1$.

The vertical displacements along the mantle and the base of the cylinder in Figure 3.8 are improved over the corresponding results using source surface S_a' as shown in Figures 3.4 and 3.5, respectively. The improvement is experienced with approximately the same number of source points ($N=29$), revealing the importance of the location of the internal source surface. Furthermore, noticing the insignificant improvement with $N=57$ source points compared to $N=29$ source points, it may be concluded that additional refinements in the results are best obtained by continuing to move the source surface closer to the foundation surface (and at the same time, increasing the number of observation points to impractical extremes). Similar conclusions may be drawn when comparing the refined traction distributions in Figure 3.9 ($N=29$) and in Figure 3.10 ($N=57$) to the corresponding traction distributions in Figure 3.7 (surface S_a').

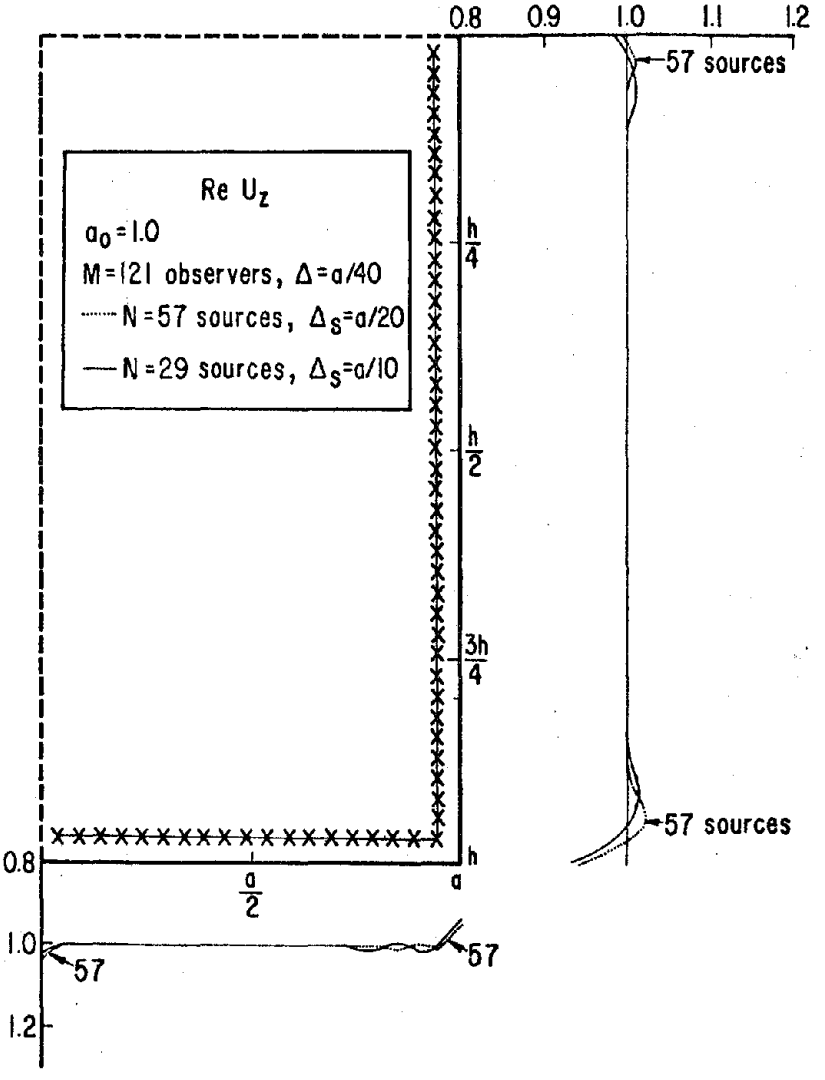

Figure 3.8. Corresponding results to Figures 3.4 and 3.5 at dimensionless frequency $a_0 = 1$, calculated using a highly refined mesh for a source surface twice as close to the observation surface as source surface S'_a.

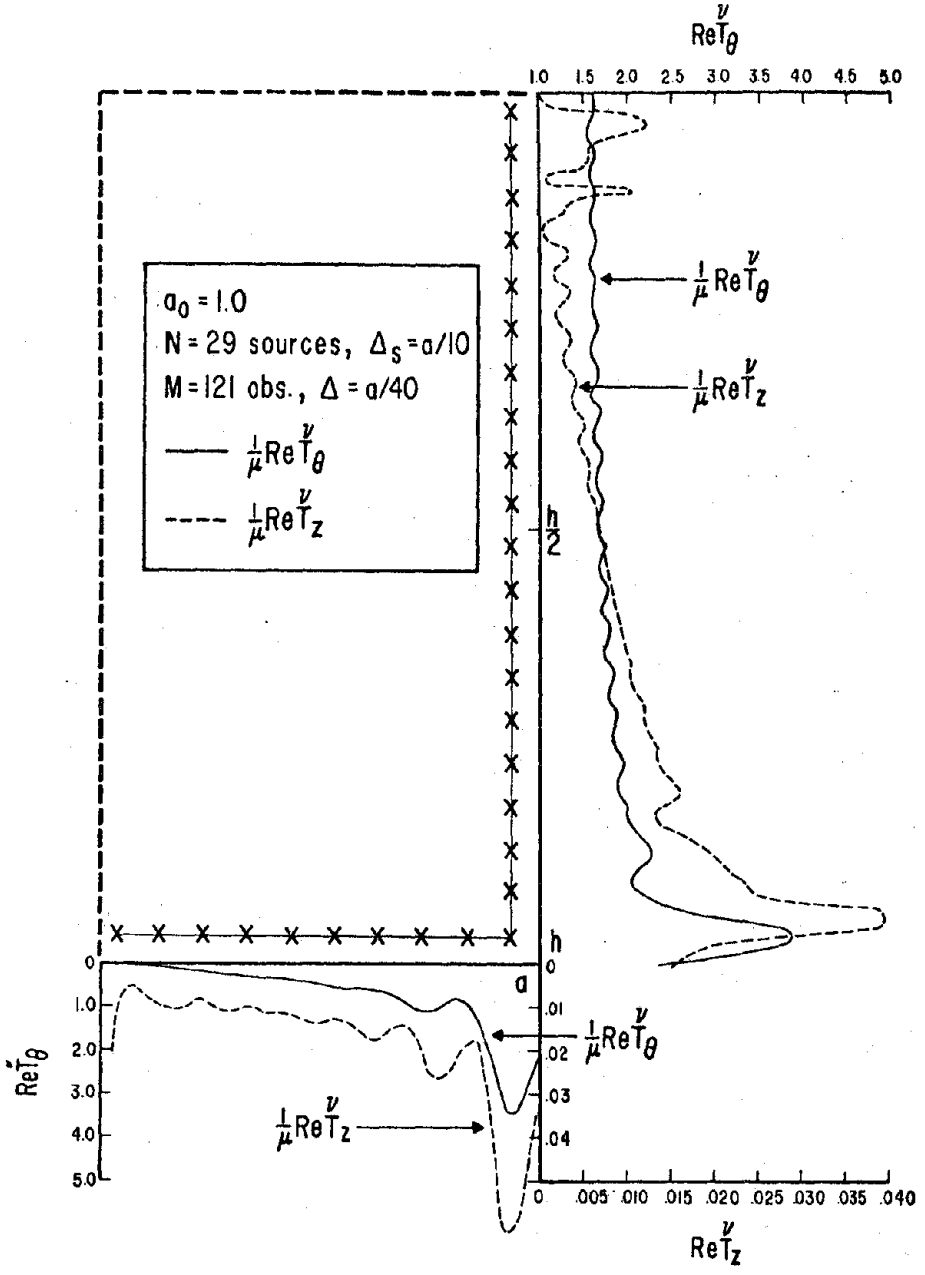

Figure 3.9. Corresponding results to Figure 3.7 calculated using a slightly refined mesh for a source surface twice as close to the observation surface $S_{a'}$.

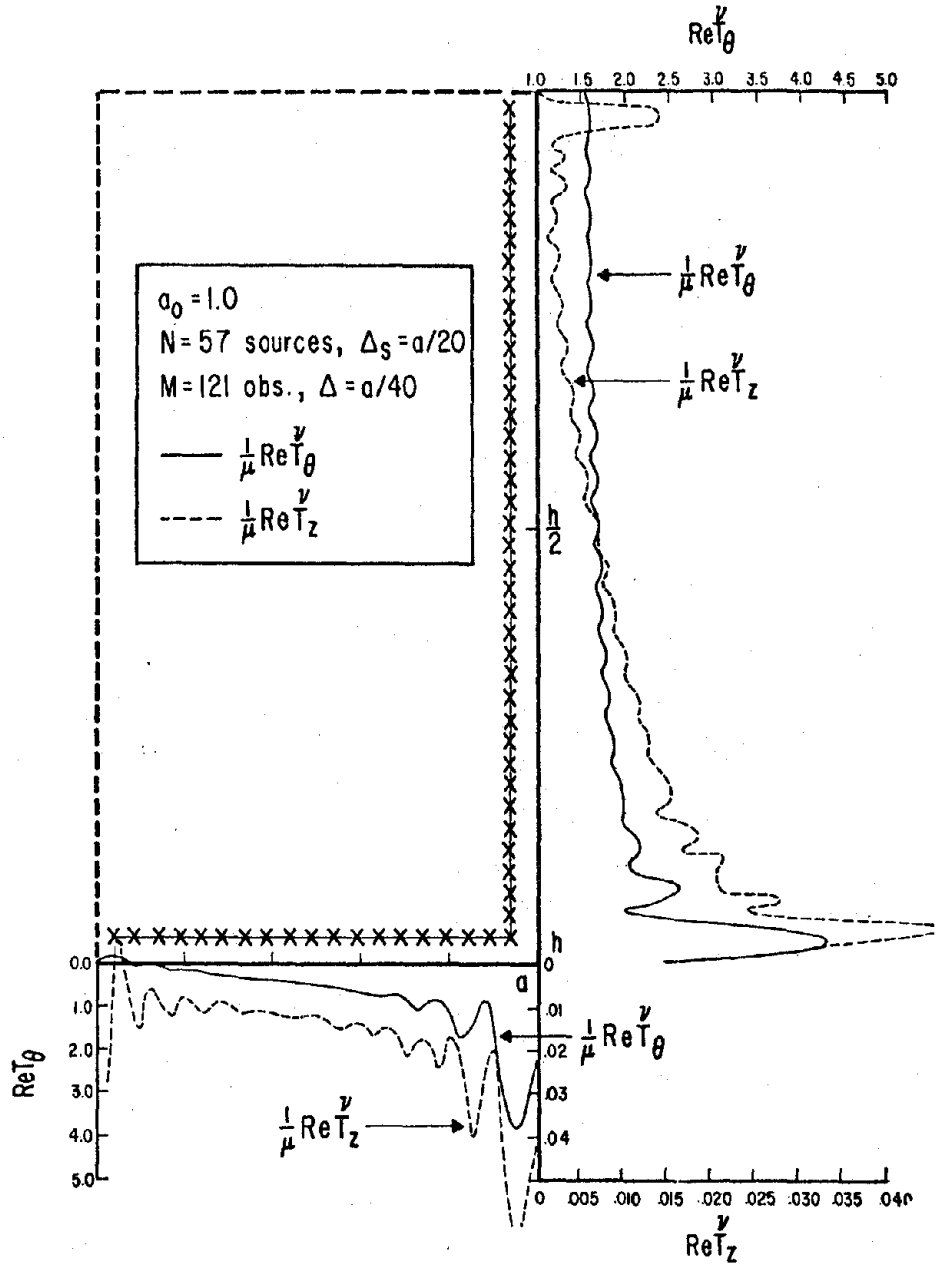

Figure 3.10. Corresponding results to Figure 3.7 calculated using a highly refined mesh for a source surface twice as close to the observation surface as source surface S_a'.

In summary of the method of solution by standard inversion, the following general rules will be stated as suggestions for solving axisymmetric radiation problems:

(1) First, the number of sources, N, is chosen to provide a sufficient number of discrete forces to accurately represent the displacements and tractions on S (normally 10 or 15 ring sources, unless separation conditions are imposed or if corners exist on S in which case additional sources would then be inserted on the source surface near the special points).

(2) Then, the location of internal source surface S′ is selected as close to surface S as is economically feasible considering that the spacing ΔS of the M observation points on S must be reduced as the distance separating the two surfaces decreases. For most practical applications, the surface S′ should be offset from surface S a distance equal to $2.5\ \Delta S$ (by uniformly shrinking surface S) in order to insure good symmetry in the matrix $[\hat{G}]$. The rationale for locating the source surface S′ close to the observation surface S is not only to avoid the possibility of a poorly conditioned matrix $[\hat{G}]$, but also to increase the accuracy of the discretization analysis as described in Figures 3.2 through 3.10.

(3) As a final check, the M observation points must be spaced finely enough to provide at least six points within the smallest wavelength of interest for the problem. Also, the spacing ΔS on surface S should be at most half the spacing of the nearest sources on surface S', so that the calculated displacement and traction distributions appear reasonably smooth on surface S.

3.3 SOLUTION BY EIGENANALYSIS

As was mentioned in the previous section, there are two reasons why an alternative to the "standard inversion" solution technique is sought. First is the problem of convergence when the number of sources exceeds a certain number depending on the location of surface S'. The second problem deals with the need to suppress the spurious oscillations in the computed tractions on surface S which result from representing the traction components directly in terms of the discrete forces. The second problem was found to be soluble by moving the internal source surface S' in toward the observation surface S, but is not a practical solution in the sense that an excessive number of observation points on surface S may then be required to adequately evaluate the numerical integrals. On the other hand, the first problem of showing convergence for any number of sources was determined to be untractable with the standard inversion approach.

The alternative approach proposed here aspires to solve both of the aforementioned problems. Basically, using eigenanalysis, the quantities of interest will be represented in terms of combinations of the discrete forces (corresponding to a modal analysis of the problem) rather than in terms of the discrete forces, themselves. Then by suitably discarding the combinations of forces associated with the higher modes, convergence for any number of sources on a given internal source surface can be proven. In addition, the artificial oscillations observed in the traction distributions in Section 2.2 may be reduced. This is under the assumption that the remaining modes have already converged to the correct response, so that the higher modes contribute nothing but spurious information.

Proceeding with the eigenanalysis, a solution to the eigenvalue problem

$$\left(\left[\underset{\sim}{A}^{1/2}\right]\left[\hat{G}\right]\left[\underset{\sim}{A}^{1/2}\right]\right)\left[\Phi\right] = \left[\Phi\right]\left[\underset{\sim}{\lambda}\right] \tag{3.34}$$

is sought, in which the j^{th} column of the $3N \times 3N$ matrix $[\Phi]$ corresponds to the eigenvector associated with the eigenvalue appearing in the j^{th} diagonal location of the $3N \times 3N$ diagonal matrix $\left[\underset{\sim}{\lambda}\right]$. The $3N \times 3N$ diagonal matrices $\left[\underset{\sim}{A}^{1/2}\right]$ containing the square roots of the quadrature coefficients A_n have been introduced in order to properly normalize the eigenvalues associated with each mode.

Since the matrix $[G]$ is symmetric and since the matrix $\left[\underset{\sim}{A}^{1/2}\right]$ is diagonal, then the matrix $\left(\left[\underset{\sim}{A}^{1/2}\right]\left[\hat{G}\right]\left[\underset{\sim}{A}^{1/2}\right]\right)$ is also symmetric. Therefore, the corresponding eigenvectors of this matrix appearing in Eq. (3.34) form an orthogonal basis, which allows the

eigenvector matrix $[\Phi]$ to be normalized as

$$\left[\Phi\right]\left[\Phi\right]^{T} = \left[I\right] \tag{3.35}$$

where $[I]$ is the $3N \times 3N$ identity matrix.

Post-multiplying Eq. (3.34) by $[\Phi]^T$ and utilizing Eq. (3.35) leads to the following decomposition for the matrix $[\hat{G}]$:

$$\left[\hat{G}\right] = \left[\underset{\sim}{A}^{-1/2}\right]\left[\Phi\right]\left[\underset{\sim}{\lambda}\right]\left[\Phi\right]^{T}\left[\underset{\sim}{A}^{-1/2}\right] \quad . \tag{3.36}$$

Introducing this decomposition into Eq. (3.16) results in an alternative expression for the $3N$ complex amplitudes of the N discrete force vectors:

$$\left\{F_A\right\} = \left[\Phi'\right]\left\{\eta_u\right\} \quad , \tag{3.37}$$

in which the $3N \times 3N$ matrix $[\Phi']$ is defined by

$$\left[\Phi'\right] = \left[\underset{\sim}{A}^{1/2}\right]\left[\Phi\right] \tag{3.38}$$

and the $3N \times 1$ vector $\{\eta_u\}$ is determined from

$$\left\{\eta_u\right\} = \left[\underset{\sim}{\lambda}^{-1}\right]\left[\Phi_{H_B}\right]^{T}\left\{U\right\} \quad . \tag{3.39}$$

The $3M \times 3N$ matrix $[\Phi_{H_B}]$ appearing in Eq. (3.39) is given by

$$\left[\Phi_{H_B}\right] = \left[\overset{\nu}{H}_B\right]\left[\Phi'\right] \quad , \tag{3.40}$$

and the diagonal matrix $\left[\underset{\sim}{\lambda}^{-1}\right]$ contains the inverse of the j^{th} eigenvalue in the j^{th} diagonal location ($j = 1, 2, \ldots, 3N$).

Substitution from Eq. (3.37) into Eq. (3.17) yields an expression for the discrete traction distribution on S

$$\begin{Bmatrix} \nu \\ T \end{Bmatrix} = \begin{bmatrix} \Phi_H \end{bmatrix} \{ \eta_u \} \tag{3.41}$$

with the corresponding displacement distribution calculated according to

$$\{ U \} = \begin{bmatrix} \Phi_G \end{bmatrix} \{ \eta_u \} \tag{3.42}$$

in which

$$\begin{bmatrix} \Phi_G \end{bmatrix} = \begin{bmatrix} G \end{bmatrix} \begin{bmatrix} \Phi^{-} \end{bmatrix} \quad , \quad \begin{bmatrix} \Phi_H \end{bmatrix} = \begin{bmatrix} \nu \\ H \end{bmatrix} \begin{bmatrix} \Phi^{-} \end{bmatrix} \quad . \tag{3.43}$$

The nodal forces are obtained by introducing the tractions from Eq. (3.41) into Eq. (3.19) and making use of Eq. (3.39):

$$\begin{aligned} \{ \mathcal{F} \} &= \begin{bmatrix} \Phi_{H_B} \end{bmatrix} \{ \eta_u \} \\ &= \left(\begin{bmatrix} \Phi_{H_B} \end{bmatrix} \begin{bmatrix} \lambda^{-1} \end{bmatrix} \begin{bmatrix} \Phi_{H_B} \end{bmatrix}^T \right) \{ U \} \quad . \end{aligned} \tag{3.44}$$

Comparison of Eqs. (3.44) and (3.21) permits the stiffness matrix $[\hat{K}]$ to be written in the form

$$\begin{bmatrix} \hat{K} \end{bmatrix} = \begin{bmatrix} \Phi_{H_B} \end{bmatrix} \begin{bmatrix} \lambda^{-1} \end{bmatrix} \begin{bmatrix} \Phi_{H_B} \end{bmatrix}^T \quad . \tag{3.45}$$

Finally, substitution from Eq. (3.45) into Eq. (3.24) gives the 6 x 6 foundation impedance matrix $[K]$ in terms of the eigenformulation

$$\begin{bmatrix} K \end{bmatrix} = \begin{bmatrix} \eta_\alpha \end{bmatrix}^T \begin{bmatrix} \lambda \end{bmatrix} \begin{bmatrix} \eta_\alpha \end{bmatrix} \quad , \tag{3.46}$$

in which

$$\begin{bmatrix} \eta_\alpha \end{bmatrix} = \begin{bmatrix} \lambda^{-1} \end{bmatrix} \begin{bmatrix} \Phi_{H_B} \end{bmatrix}^T \begin{bmatrix} \alpha \end{bmatrix} \tag{3.47}$$

It should be pointed out that the j^{th} element of the vector $\{\eta_u\}$ corresponds to the participation factor for the j^{th} mode, as represented in Eq. (3.39). Similar interpretations are possible for the elements of the matrix $[\eta_\alpha]$, as defined in Eq. (3.47). Therewith, a procedure for discarding the higher modes (that inflict spurious oscillations into the numerical results) may be devised. Namely, for any eigenvalue having modulus less than some specified value, the participation factors corresponding to that particular eigenvalue are set to zero. This effectively eliminates the spurious contributions from the modes associated with the "smallest" eigenvalues in Eqs. (3.37) through (3.47).

The eigenformulation for the case of mixed boundary conditions proceeds in the same manner and hence will be omitted for brevity. The remainder of this section is focussed at presenting results similar to those of Section 3.2 as a function of number of modes used. As in Section 3.2, the demonstrational foundation is a circular cylinder of radius $\underline{a}$ embedded a depth of $h = 2a$ into a viscoelastic half-space.

The internal source surface is chosen to be S_a' (see Figure 3.1), on which 35 ring sources are available. Thereby, the first 35 torsional modes, 70 vertical modes, or 105 horizontal-rocking-coupling modes may be scrutinized in an attempt to understand when and why the higher modes introduce artificial undulations into the calculated displacement and traction distributions.

Before analyzing the dependence of the foundation impedances, and the displacement and traction distributions on the number of modes, it is instructive to examine the behavior of the eigenvalues as

catalogued in Tables 3.1 through 3.4. The five columns represent the real parts of the eigenvalues as calculated when respectively using 35, 27, 14, 9 and 5 ring sources on the internal source surface S_a'. The torsional eigenvalues are depicted in Tables 3.1, 3.2 and 3.3 at dimensionless frequencies $a_0 = .1$, 1 and 5, respectively, while the vertical eigenvalues are displayed only at $a_0 = 1$ in Table 3.4.

The normalization of the eigenvalues is verified by observing in Table 3.1 that the eigenvalue corresponding to the first torsional mode may be obtained by utilizing anywhere from 5 to 35 ring sources. Of course, only N modes are determined for torsion by N ring sources, and hence the void locations. By comparing across the columns, it is not surprising to find that the eigenvalues corresponding to the highest modes are predicted less accurately than the lower mode eigenvalues. This is explained by realizing that more than j number of sources is required to accurately represent the eigenvalue corresponding to the j^{th} torsional mode (or $2 \times j^{th}$ vertical mode). Such a phenomenon, which is common to most modal analyses, becomes more striking at higher frequencies, as is evidenced in Table 3.3.

Of equal significance in deciding which modes to discard during a computation are the relative amplitudes of the corresponding eigenvalues. For cases $N=5$ or 9, the amplitudes diminish with number of modes by only two orders of magnitude and therefore, the contribution from the highest modes may be required. Yet, as was previously pointed out, the highest modes are necessarily less accurate than the lower modes. For the case $N = 35$, one can discard the last few modes without rejecting any essential information. The suite of 35 ring sources will be utilized in the remainder of this section for discussion of the effects of number

Torsional Mode	N = 35	N = 27	N = 14	N = 9	N = 5
1	.215E+01	.214E+01	.212E+01	.211E+01	.209E+01
2	.920E+00	.904E+00	.880E+00	.859E+00	.724E+00
3	.356E+00	.349E+00	.342E+00	.342E+00	.314E+00
4	.156E+00	.158E+00	.155E+00	.157E+00	.254E+00
5	.101E+00	.101E+00	.978E-01	.820E-01	.566E-01
6	.667E-01	.656E-01	.607E-01	.561E-01	
7	.376E-01	.375E-01	.457E-01	.400E-01	
8	.256E-01	.253E-01	.277E-01	.307E-01	
9	.182E-01	.175E-01	.169E-01	.164E-01	
10	.110E-01	.111E-01	.116E-01		
11	.770E-02	.774E-02	.806E-02		
12	.577E-02	.547E-02	.688E-02		
13	.360E-02	.399E-02	.547E-02		
14	.234E-02	.223E-02	.567E-02		
15	.203E-02	.177E-02			
16	.113E-02	.114E-02			
17	.813E-03	.765E-03			
18	.573E-03	.610E-03			
19	.423E-03	.422E-03			
20	.295E-03	.277E-03			
21	.237E-03	.227E-03			
22	.160E-03	.162E-03			
23	.112E-03	.105E-03			
24	.851E-04	.853E-04			
25	.563E-04	.689E-04			
26	.451E-04	.512E-04			
27	.324E-04	.300E-04			
28	.205E-04				
29	.135E-04				
30	.271E-05				
31	.185E-05				
32	.405E-06				
33	.286E-06				
34	.430E-07				
35	.318E-07				

Table 3.1

Real part of the torsional eigenvalues using N ring sources on the internal source surface S_a' at dimensionless frequency $a_o = 0.1$.

Torsional Mode	N = 35	N = 27	N= 14	N = 9	N = 5
1	.304E+01	.304E+01	.301E+01	.299E+01	.296E+01
2	.118E+01	.116E+01	.113E+01	.110E+01	.902E+00
3	.393E+00	.386E+00	.378E+00	.376E+00	.346E+00
4	.165E+00	.167E+00	.163E+00	.164E+00	.272E+00
5	.105E+00	.106E+00	.102E+00	.858E-01	.589E-01
6	.690E-01	.679E-01	.628E-01	.582E-01	
7	.385E-01	.384E-01	.468E-01	.411E-01	
8	.261E-01	.258E-01	.232E-01	.313E-01	
9	.185E-01	.178E-01	.173E-01	.168E-01	
10	.112E-01	.113E-01	.118E-01		
11	.781E-02	.785E-02	.817E-02		
12	.585E-02	.554E-02	.698E-02		
13	.363E-02	.403E-02	.553E-02		
14	.236E-02	.226E-02	.572E-03		
15	.205E-02	.179E-02			
16	.114E-02	.115E-02			
17	.820E-02	.771E-03			
18	.578E-03	.615E-03			
19	.426E-03	.425E-03			
20	.297E-03	.279E-03			
21	.238E-03	.228E-03			
22	.161E-03	.163E-03			
23	.113E-03	.106E-03			
24	.855E-04	.858E-04			
25	.566E-04	.693E-04			
26	.454E-04	.514E-04			
27	.326E-04	.302E-04			
28	.206E-04				
29	.136E-04				
30	.272E-05				
31	.185E-05				
32	.407E-06				
33	.287E-06				
34	.431E-07				
35	.316E-07				

Table 3.2

Real part of the torsional eigenvalues using N ring sources on the internal source surface S_a' at dimensionless frequency $a_o = 1.0$.

Torsional Mode	N = 35	N = 27	N = 14	N = 9	N = 5
1	-.801E+00	-.799E+00	-.777E+00	-.745E+00	-.293E+00
2	.608E+00	.606E+00	.586E+00	.484E+00	.984E+00
3	.521E+00	.518E+00	.488E+00	.415E+00	.253E+00
4	.219E+00	.213E+00	.194E+00	.190E+00	.238E+00
5	.164E+00	.164E+00	.167E+00	.179E+00	.657E-01
6	.795E-01	.791E-01	.947E-01	.869E-01	
7	.474E-01	.467E-01	.436E-01	.520E-01	
8	.310E-01	.297E-01	.297E-01	.331E-01	
9	.169E-01	.170E-01	.178E-01		
10	.112E-01	.113E-01	.115E-01		
11	.810E-02	.765E-02	.960E-02		
12	.478E-02	.529E-02	.757E-02		
13	.315E-02	.304E-02	-.123E-02		
14	.267E-02	.231E-02	.722E-03		
15	.142E-02	.143E-02			
16	-.133E-02	-.135E-02			
17	.100E-02	.945E-03			
18	.701E-03	.746E-03			
19	.510E-03	.507E-03			
20	.350E-03	.329E-03			
21	.280E-03	.267E-03			
22	.186E-03	.189E-03			
23	.130E-03	.121E-03			
24	.973E-04	.980E-04			
25	.637E-04	.783E-04			
26	.516E-04	.576E-04			
27	.367E-04	.339E-04			
28	.229E-04				
29	.151E-04				
30	.299E-05				
31	.213E-05				
32	.440E-06				
33	.310E-06				
34	.456E-07				
35	.334E-07				

Table 3.3

Real part of the torsional eigenvalues using N ring sources on the internal source surface S_a' at dimensionless frequency $a_o = 5.0$.

Vertical Mode	N = 35	N = 27	N = 14	N = 9	N = 5
1	-.293E+01	-.292E+01	-.288E+01	-.279E+01	-.251E+01
2	.862E+00	.859E+00	.848E+00	.820E+00	.721E+00
3	.459E+00	.446E+00	.432E+00	.428E+00	.451E+00
4	.322E+00	.328E+00	.322E+00	.304E+00	.401E+00
5	.278E+00	.275E+00	.275E+00	.293E+00	.261E+00
6	.229E+00	.229E+00	.231E+00	.204E+00	.210E+00
7	.146E+00	.146E+00	.148E+00	.122E+00	.157E+00
8	.127E+00	.125E+00	.127E+00	.101E+00	.117E+00
9	.943E-01	.944E-01	.888E-01	.975E-01	.701E-01
10	.767E-01	.771E-01	.815E-01	.751E-01	.168E-01
11	.613E-01	.619E-01	.560E-01	.657E-01	
12	.457E-01	.462E-01	.432E-01	.584E-01	
13	.404E-01	.401E-01	.354E-01	.306E-01	
14	.326E-01	.326E-01	.330E-01	.224E-01	
15	.295E-01	.288E-01	.284E-01	.174E-01	
16	.263E-01	.256E-01	.259E-01	.108E-01	
17	.196E-01	.193E-01	.212E-01	.855E-02	
18	.171E-01	.176E-01	.191E-01	.431E-02	
19	.123E-01	.122E-01	.164E-01		
20	.116E-01	.109E-01	.132E-01		
21	.935E-02	.933E-02	.838E-02		
22	.727E-02	.694E-02	.620E-02		
23	.627E-02	.660E-02	.396E-02		
24	.571E-02	.562E-02	.340E-02		
25	.487E-02	.492E-02	.312E-02		
26	.393E-02	.388E-02	.307E-02		
27	.366E-02	.351E-02	.277E-02		
28	.309E-02	.306E-02	.354E-03		
29	.252E-02	.223E-02			
30	.208E-02	.210E-02			
31	.157E-02	.163E-02			
32	.141E-02	.141E-02			
33	.122E-02	.115E-02			
34	.109E-02	.107E-02			
35	.918E-03	.859E-03			

Table 3.4

Real part of the vertical eigenvalues using N ring sources on the internal source surface S_a' at dimensionless frequency $a_o = 1.0$.

Vertical Mode	N = 35	N = 27	N = 14	N = 9	N = 5
36	.786E-03	.746E-03			
37	.658E-03	.711E-03			
38	.558E-03	.576E-03			
39	.536E-03	.557E-03			
40	.387E-03	.387E-03			
41	.275E-03	.270E-03			
42	.252E-03	.222E-03			
43	.223E-03	.165E-03			
44	.166E-03	.156E-03			
45	.155E-03	.149E-03			
46	.123E-03	.113E-03			
47	.118E-03	.105E-03			
48	.950E-04	.858E-04			
49	.861E-04	.745E-04			
50	.791E-04	.712E-04			
51	.572E-04	.673E-04			
52	.557E-04	.527E-04			
53	.451E-04	.519E-04			
54	.329E-04	.286E-04			
55	.174E-04				
56	.122E-04				
57	.105E-04				
58	.783E-05				
59	.381E-05				
60	.298E-05				
61	.194E-05				
62	.137E-05				
63	.479E-06				
64	.343E-06				
65	.271E-06				
66	.142E-06				
67	.444E-07				
68	.435E-07				
69	.408E-07				
70	-.101E-07				

Table 3.4 (continued)

of modes on the foundation impedance functions as well as on the displacement and traction distributions.

The torsional and vertical stiffness coefficients are displayed as a function of number of modes utilized in Figures 3.11 and 3.12. respectively. The different curves represent the five dimensionless frequencies $a_0 = .1, .5, 1, 2, 5$. In accordance with the decrease in amplitude of the eigenvalues, convergence is achieved as more modes are added at all frequencies. Of particular interest is naturally the larger number of modes necessary at high frequency to achieve the same degree of convergence experienced at low frequency. Of major importance, however, is the divergent trend beginning around 33 modes for the torsional stiffness and around 60 modes (35 sources used) for the vertical stiffness. This is precisely the conditioning problem due to the proximity of the individual sources on the internal source surface, as discussed in Section 3.2. Such a conditioning problem was determined to be insurmountable with the "standard inversion" method of solution in the previous section. On the other hand, the eigenanalysis offers an immediate solution to the problem with no limitation on the proximity of sources. The resolution is to use as many sources as desired and then truncate the modal summation after a specified convergence is achieved, before including any possibly spurious higher modes.

In Figure 3.13, the real parts of the vertical displacement along the mantle of the cylinder are displayed at three representative frequencies $a_0 = .1, 1, 5$ (from left to right). The different curves on each plot correspond to various numbers of modes used, as indicated. Comparing the displacement distribution at $a_0 = 5$ (using 52 out of 70

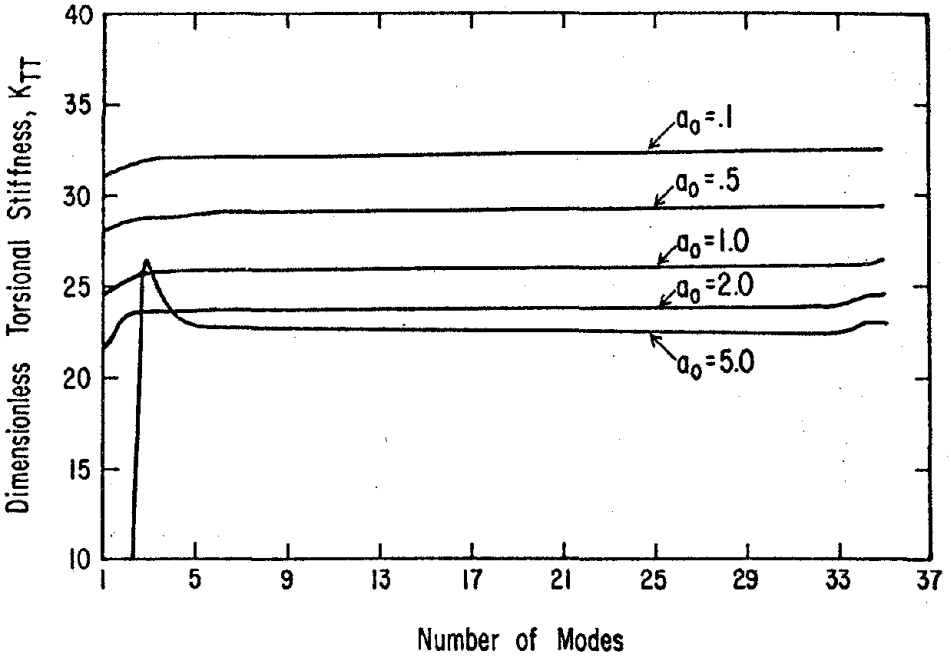

Figure 3.11. Effect of number of modes utilized (out of a possible 35 modes) on the torsional stiffness coefficient for a cylinder with embedment ratio h/a = 2.0 and internal source surface S_a'.

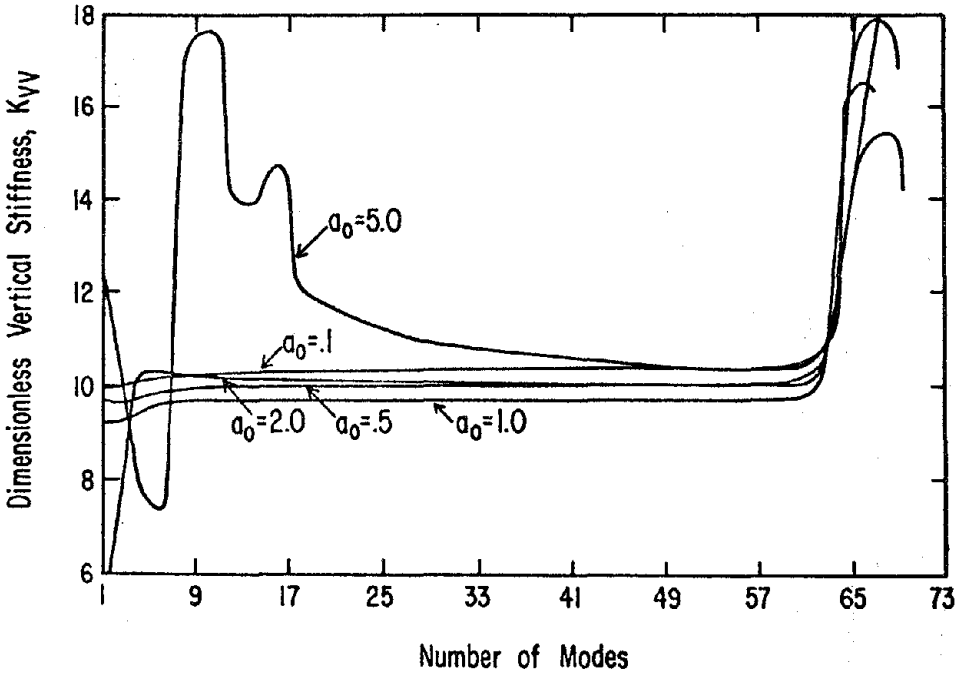

Figure 3.12. Effect of number of modes utilized (out of a possible 70 modes) on the vertical stiffness coefficient for a cylinder with embedment ratio h/a = 2.0 and internal source surface S_a'.

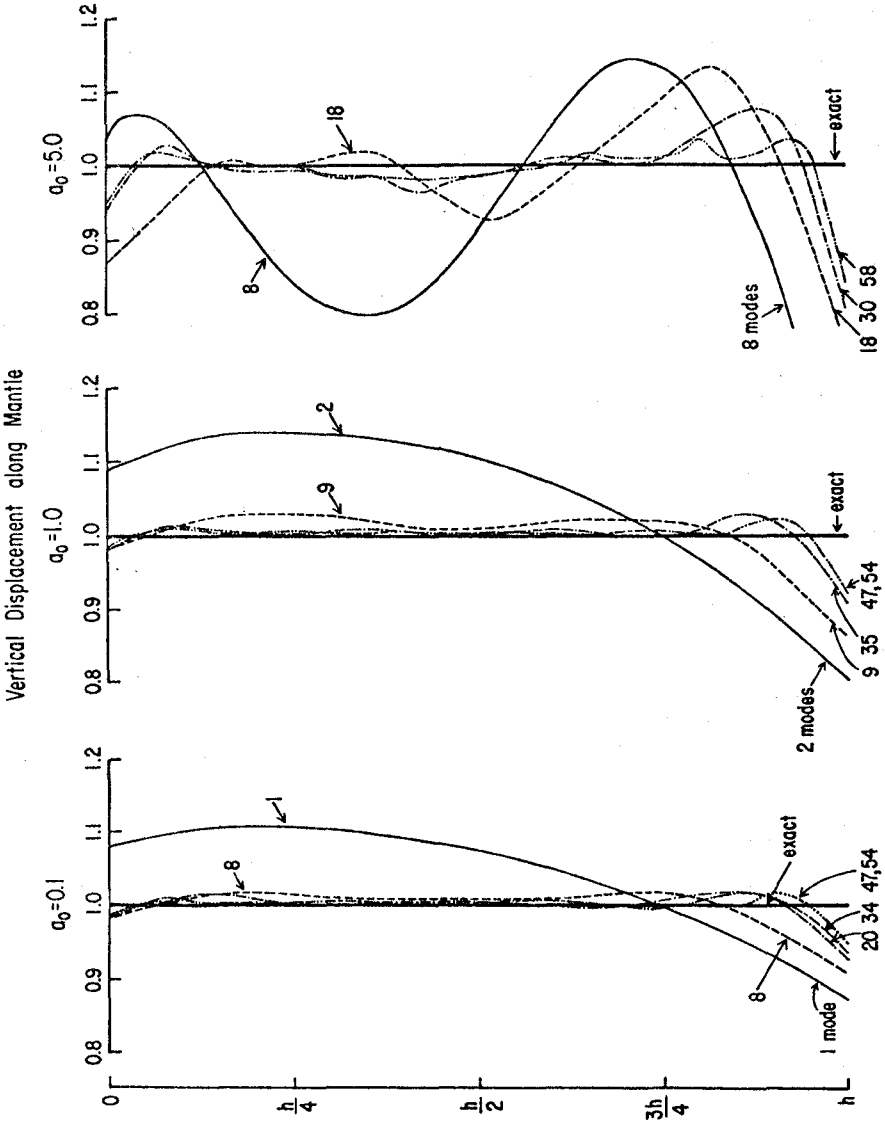

Figure 3.13. Vertical displacement distribution calculated along mantle utilizing various numbers of modes.

modes) to the corresponding displacement distribution in Figure 3.4 (standard inversion with 27 sources) reveals that the eigen generated displacements are consistently closer to the exact response of unity, although the differences are on the order of only one percent. Similar comparisons can be made between the torsional traction distribution along the mantle in Figure 3.14 with the analogous distribution displayed in Figure 3.7 at dimensionless frequency $a_o = 1.0$.

In summary, an alternative to the "standard inversion" formulation has been presented in which all the quantities of interest are expressed in terms of modal summations, with each mode corresponding to a unique combination of the discrete forces. The limitation on the number (or proximity) of sources evidenced in the "standard inversion" method of solution has been eliminated by truncating the modal summation when convergence is achieved. Although one may thereby utilize as many sources as desired on a given internal source surface, the numerical oscillations in the displacement and traction components near a corner of the foundation surface may be reduced more effectively by locating the internal source surface closer to the foundation surface.

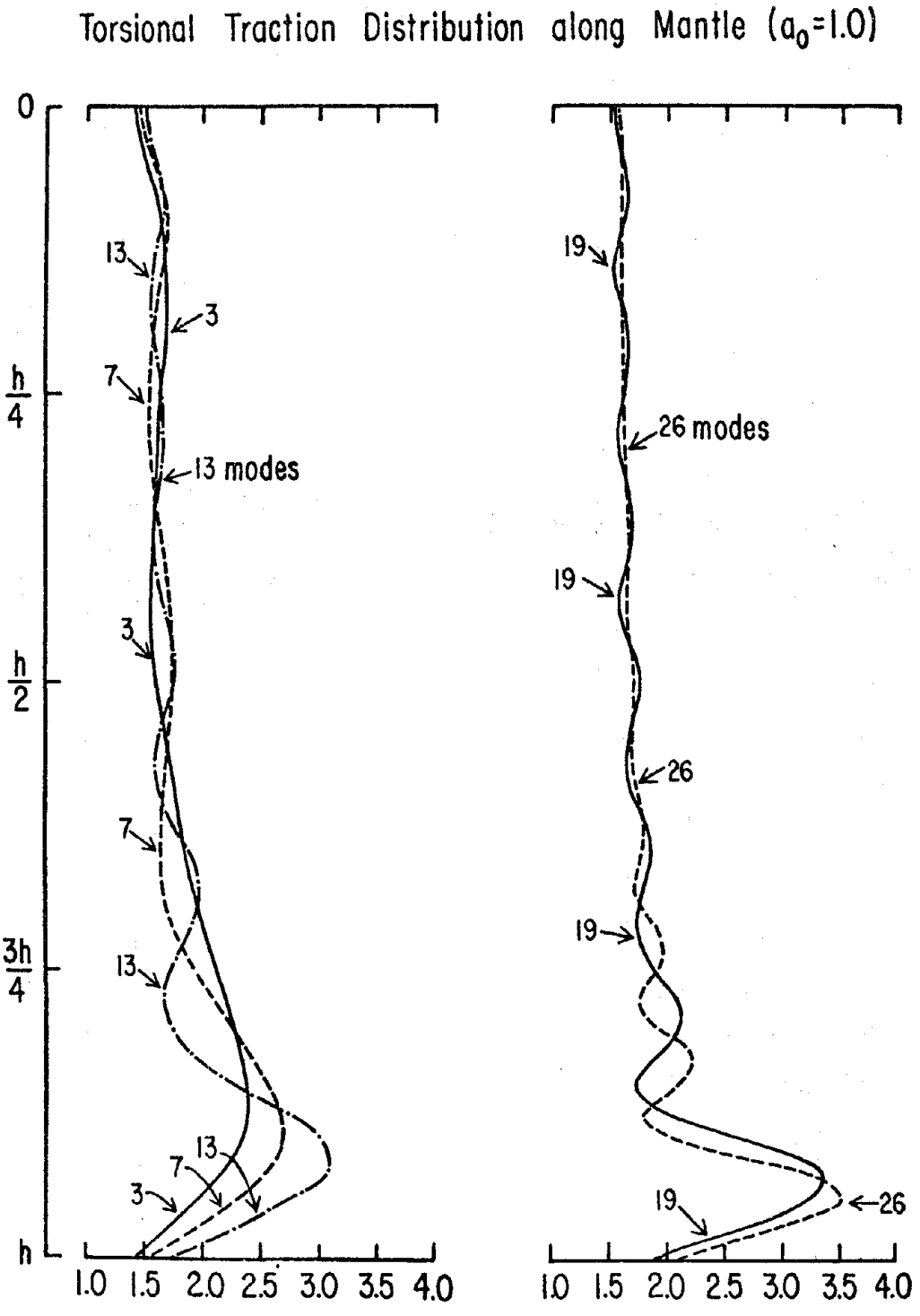

Figure 3.14. Torsional traction distribution calculated along mantle utilizing various numbers of modes.

CHAPTER 4

RESULTS AND COMPARISONS

4.1 IMPEDANCE FUNCTIONS FOR EMBEDDED FOUNDATIONS

As an application of the method described in the previous chapters, the impedance functions for rigid cylindrical foundations embedded in a uniform viscoelastic half-space are calculated. The effects on the impedance functions of the embedment depth, the type of contact between the foundation and the surrounding soil, and the attenuation in the soil are studied. In addition, the consequences of introducing layering into the soil deposit are examined, and a number of comparisons with results obtained by other methods are presented.

In this section, a study is made on the effects of embedment depth for cylindrical foundations having embedment ratios h/a (embedment depth h to foundation radius a) equal to 0.25, 0.5, 1.0, and 2.0, as shown in Figure 4.1. In each case, the cylindrical foundation is embedded in a uniform viscoelastic half-space and the impedance functions are referred to the center of the bottom of the foundation. The viscoelastic half-space represents the soil medium comprising volume V and is characterized by a shear wave velocity β, a compressional wave velocity $\alpha = \sqrt{3}\,\beta$, and specific attenuation factors for shear and compressional waves, $Q_\beta = 50$ and $Q_\alpha = 100$, respectively (i.e., material damping ratios of 0.01 and 0.005 for shear waves and compressional waves, respectively.

The discretization of the line L' (on the surface of revolution S' containing the concentrated ring sources) and the line L (on the

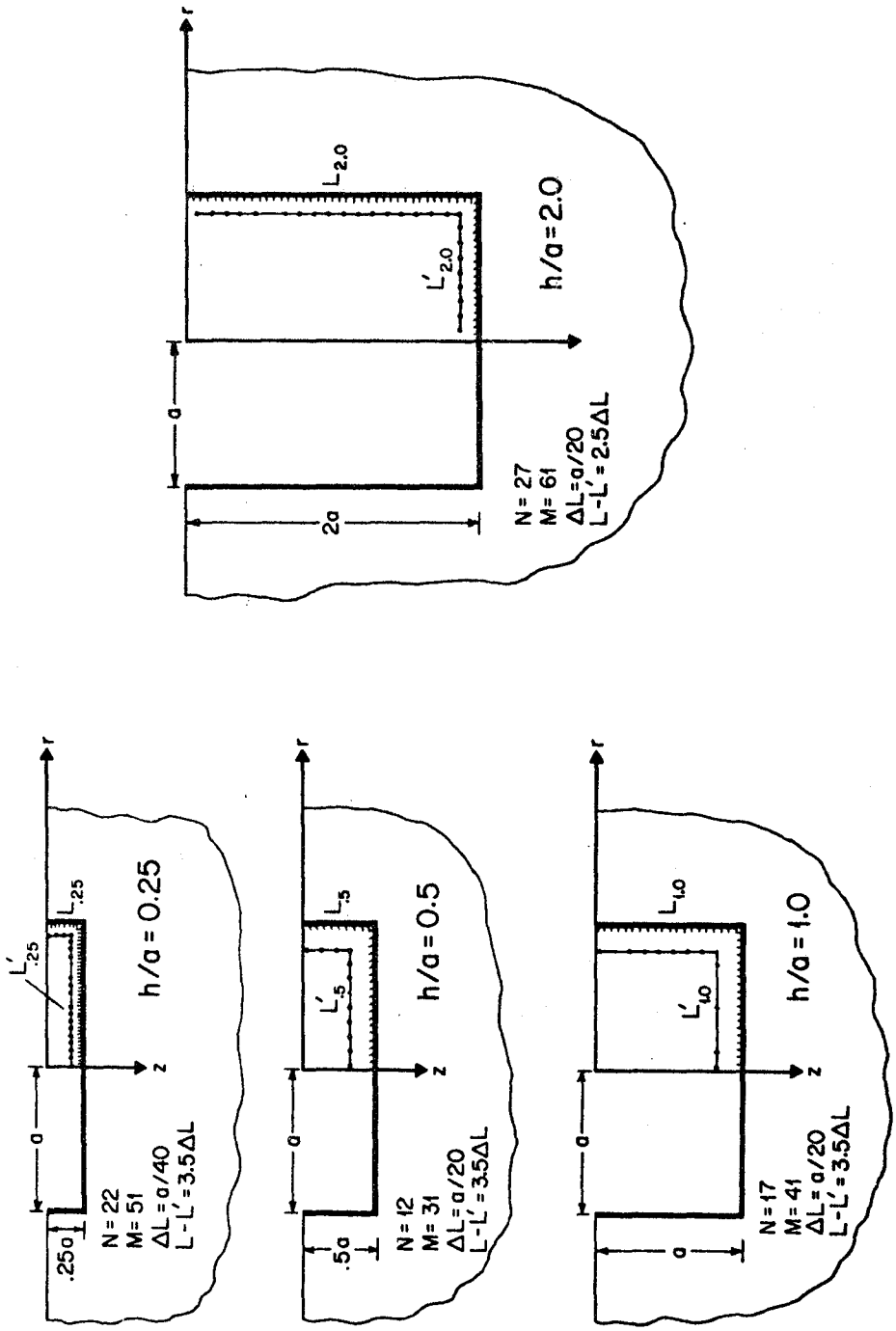

Figure 4.1. Boundary geometries, coordinate systems and discretization used for analysis of various cylindrical foundations embedded in a uniform half-space.

periphery of the foundation defined by surface of revolution S containing the observation points) is shown graphically in Figure 4.1 for the various cylinders. Also, the number of source points, N, on L', the number of observation points, M, on L, the spacing ΔL of points on L, and the offset of L-L' of internal line L' relative to L can be found as subcaptions below each foundation displayed. Accuracy tests such as these presented in Section 3.2 confirm that the discretizations in Figure 4.1 are extremely conservative, especially since only the foundation impedance functions are to be studied in this section.

In addition to analyzing the effects of varying the embedment ratios, the results will serve another important purpose. Recently, Day (1977) was able to accurately obtain the same impedance functions for the welded contact problem using the finite element method as discussed in Section 1.2. Therefore, the reliability of both methods will be established through comparison of the impedance functions for cylinders embedded in a uniform half-space.

The five complex impedance functions normalized as in Eq. (2.41) are plotted against dimensionless frequency $a_0 = \omega a/\beta$ in Figures 4.2 through 4.11, for the various embedment ratios. The real parts of the impedance functions will be referred to as stiffness coefficients while the corresponding imaginary parts divided by the dimensionless frequency will be referred to as damping coefficients. In each figure, the dimensionless stiffness or damping coefficients are compared to those obtained by Day (1977) for embedment ratios of 0.5, 1.0, and 2.0 in the range of dimensionless frequency between zero and six. The results obtained with the present method are distinguished by solid lines while Day's results

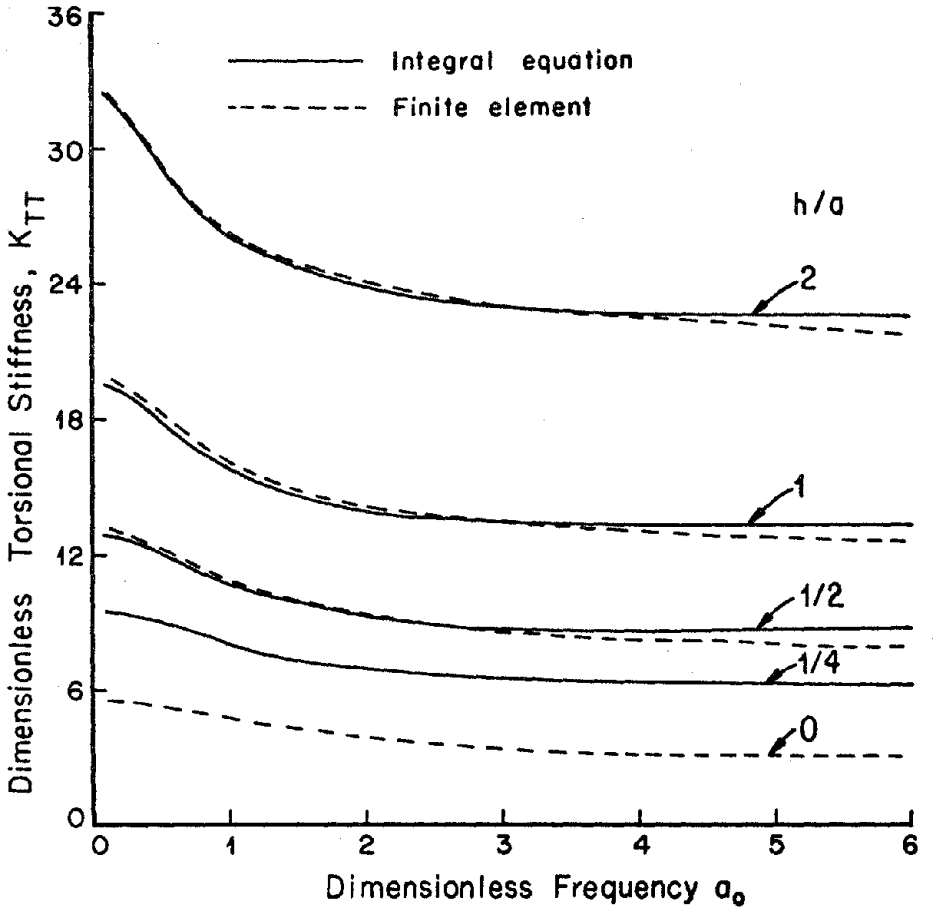

Figure 4.2. Effects of embedment on the torsional stiffness coefficient and comparison to finite element solution.

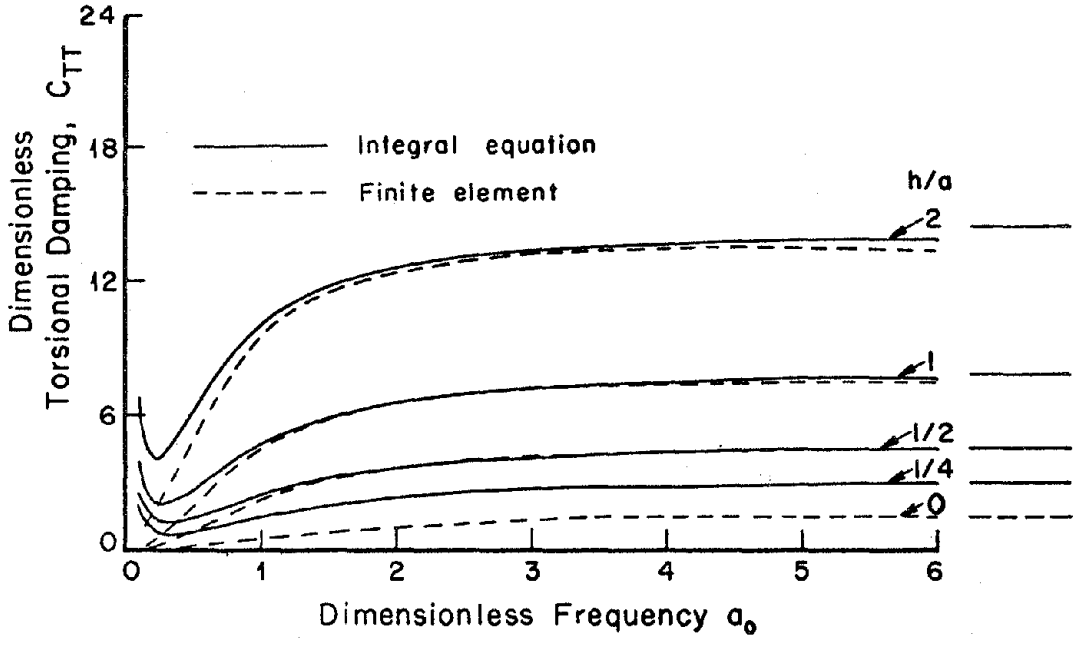

Figure 4.3. Effects of embedment on the torsional damping coefficient and comparison to finite element solution.

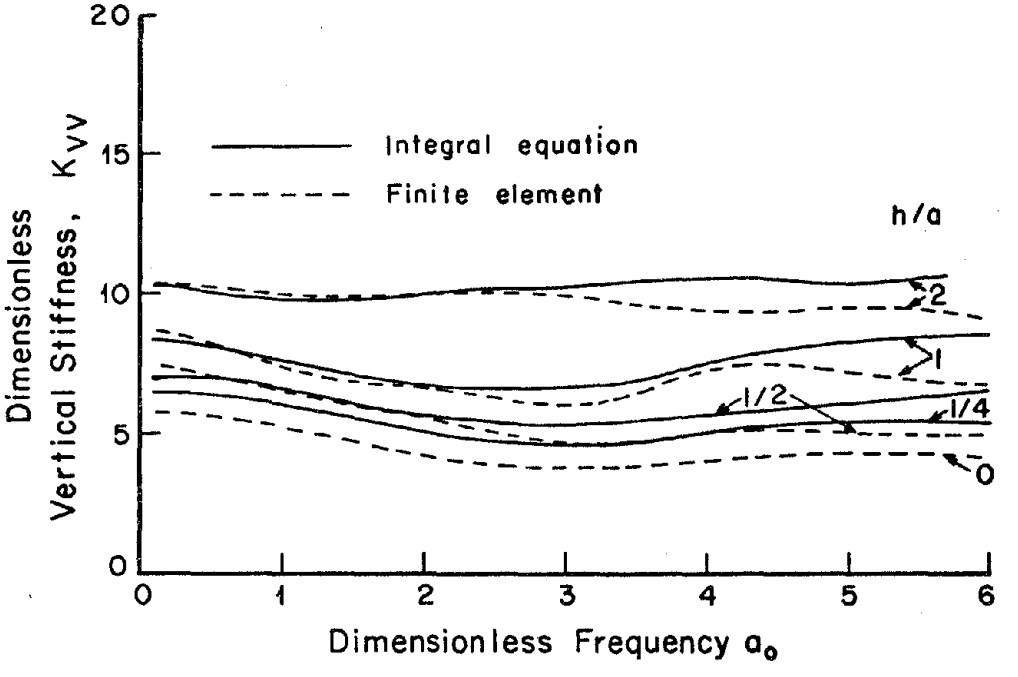

Figure 4.4. Effects of embedment on the vertical stiffness coefficient and comparison to finite element solution.

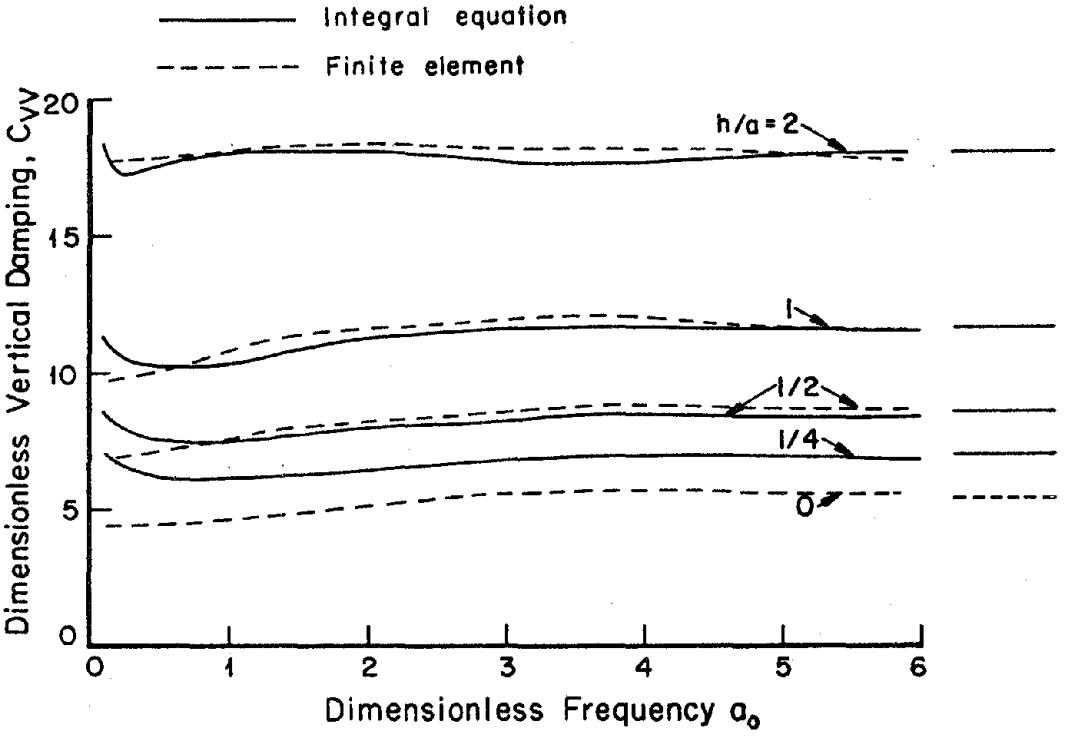

Figure 4.5. Effects of embedment on the vertical damping coefficient and comparison to finite element solution.

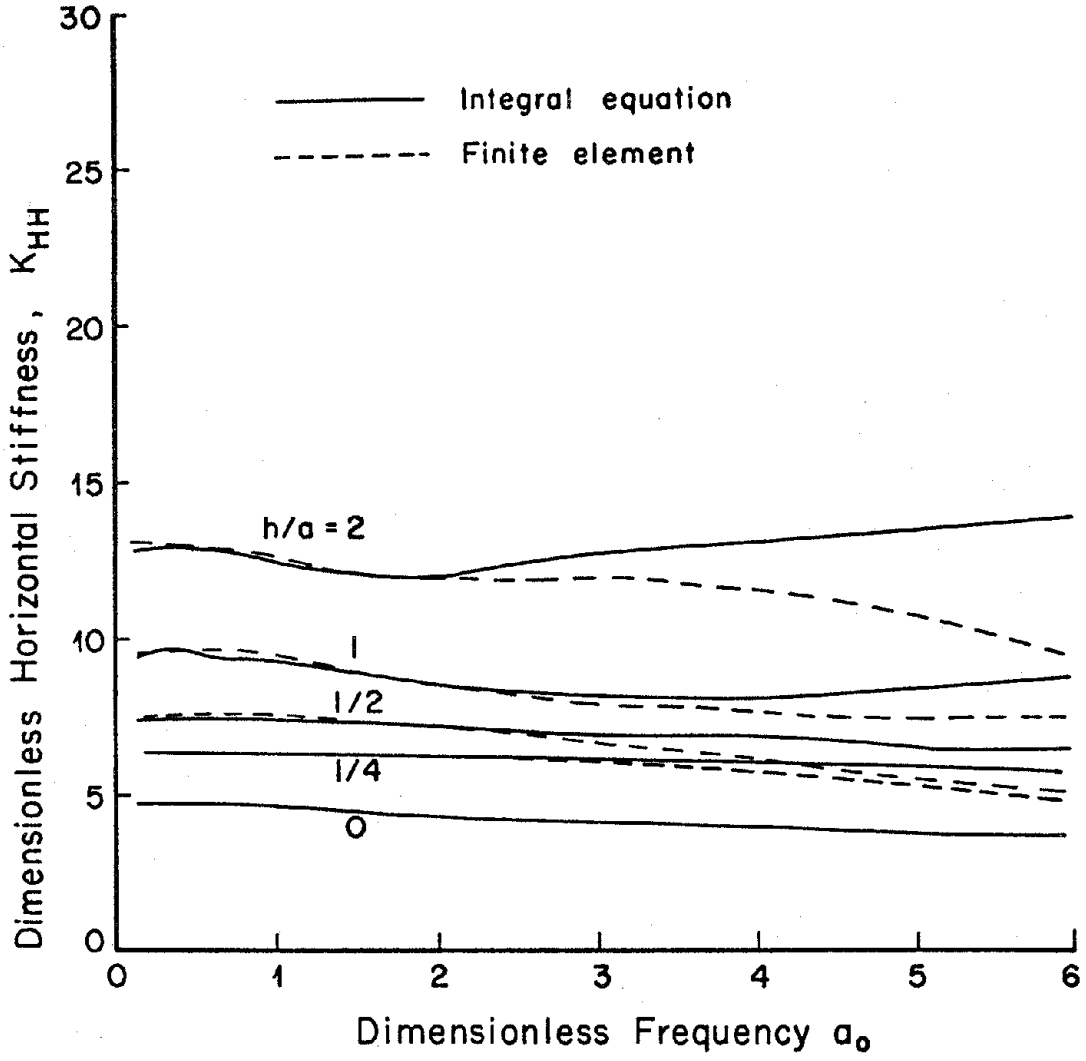

Figure 4.6. Effects of embedment on the horizontal stiffness coefficient and comparison to finite element solution.

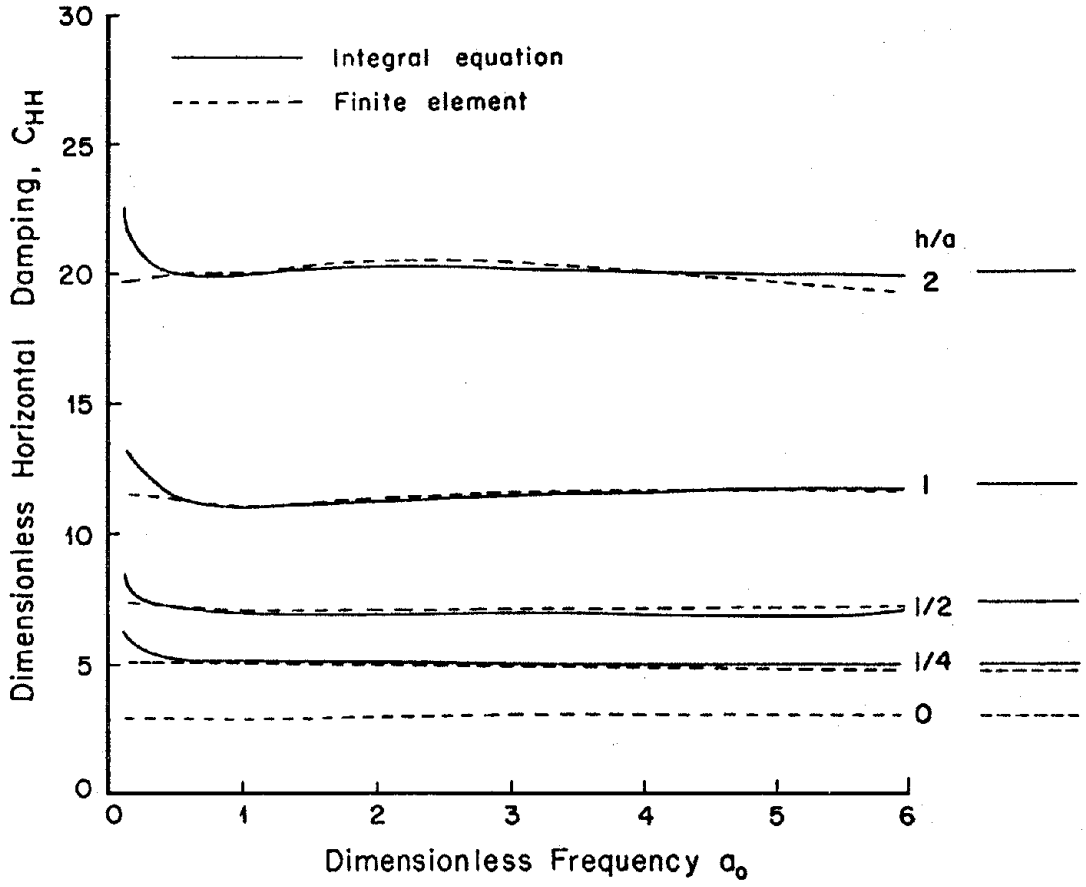

Figure 4.7. Effects of embedment on the horizontal damping coefficient and comparison to finite element solution.

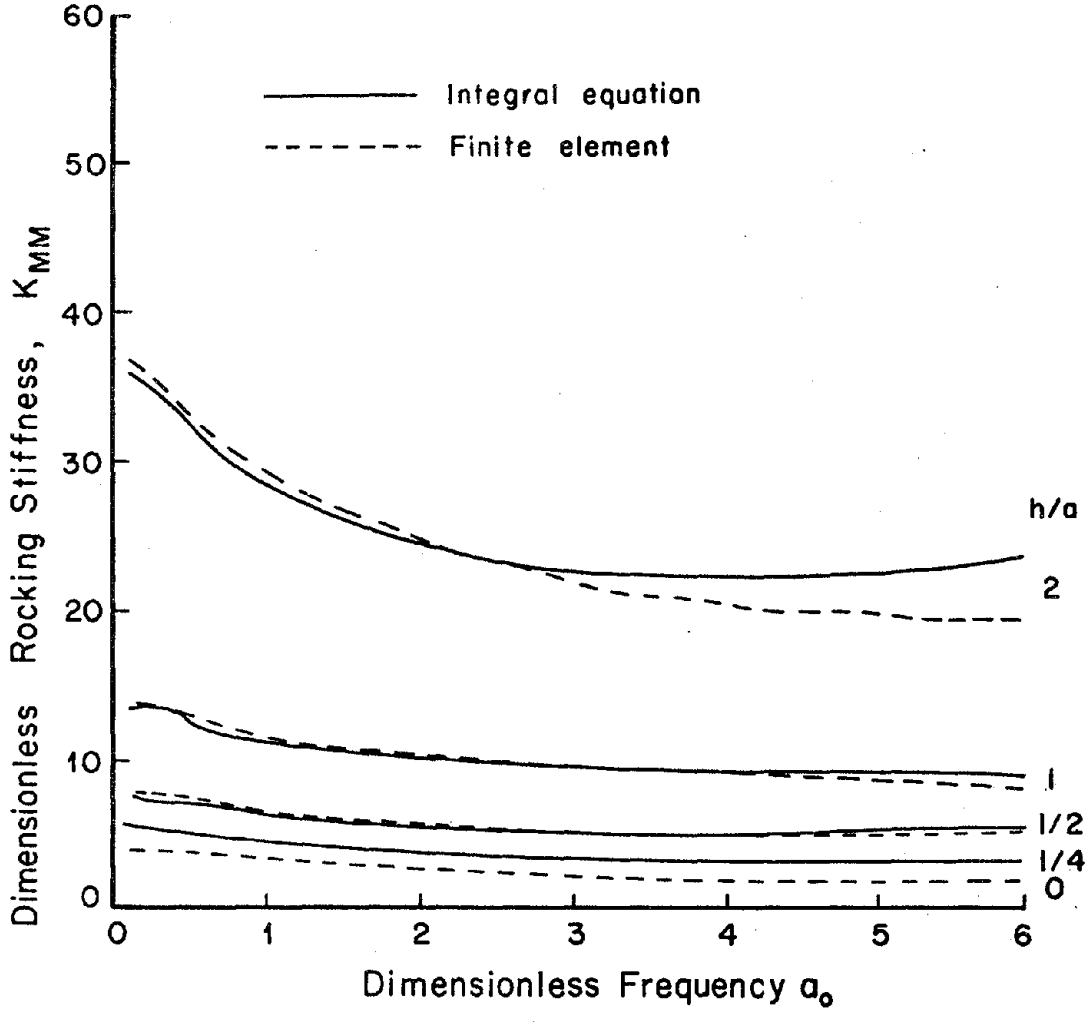

Figure 4.8. Effects of embedment on the rocking stiffness coefficient and comparison to finite element solution.

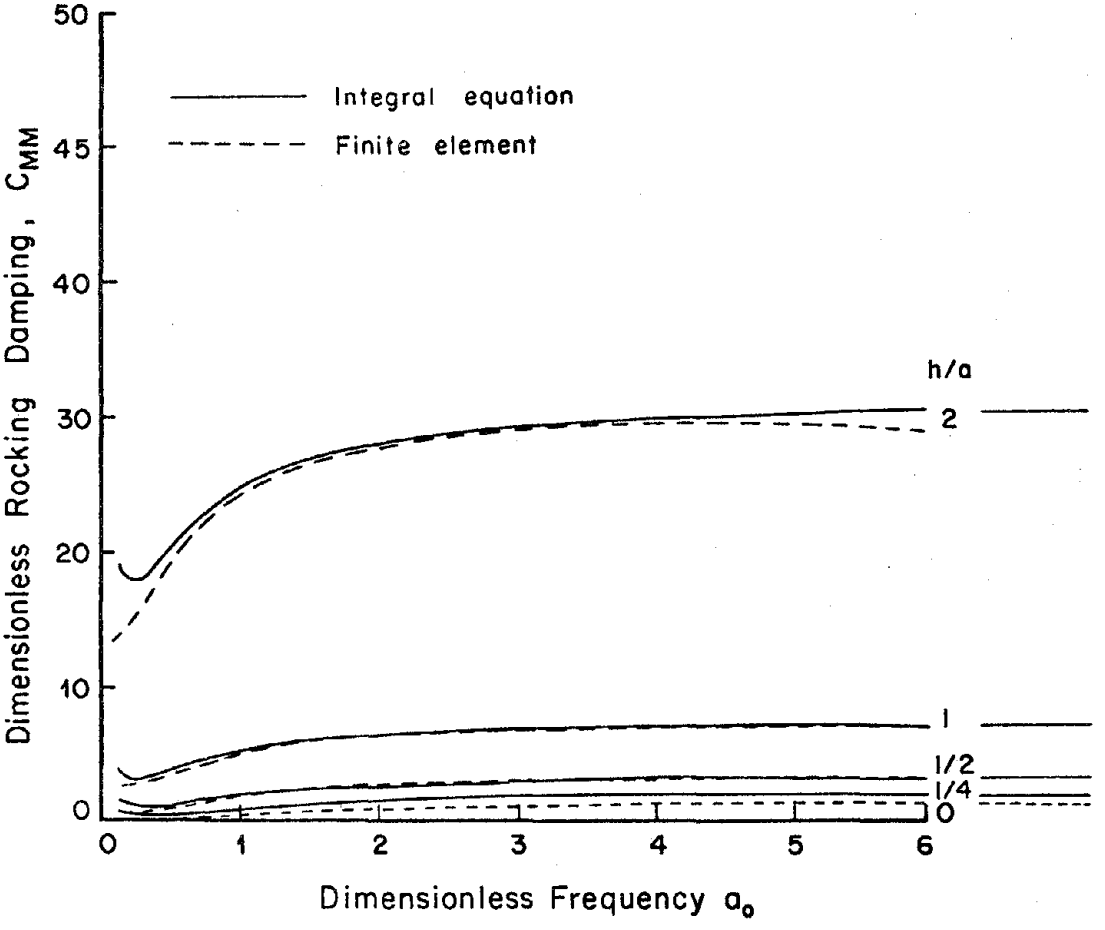

Figure 4.9. Effects of embedment on the rocking damping coefficient and comparison to finite element solution.

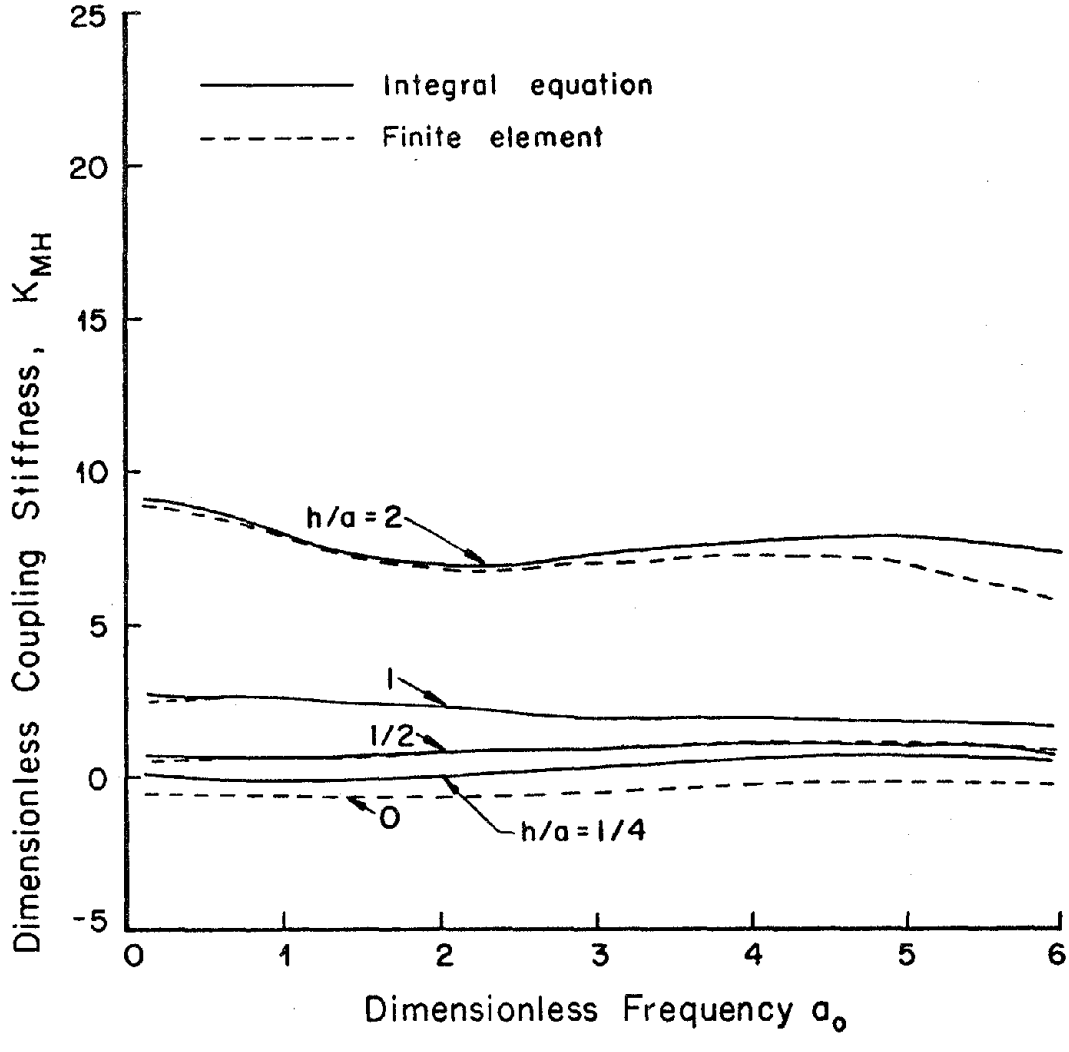

Figure 4.10. Effects of embedment on the coupling stiffness coefficient and comparison to finite element solution.

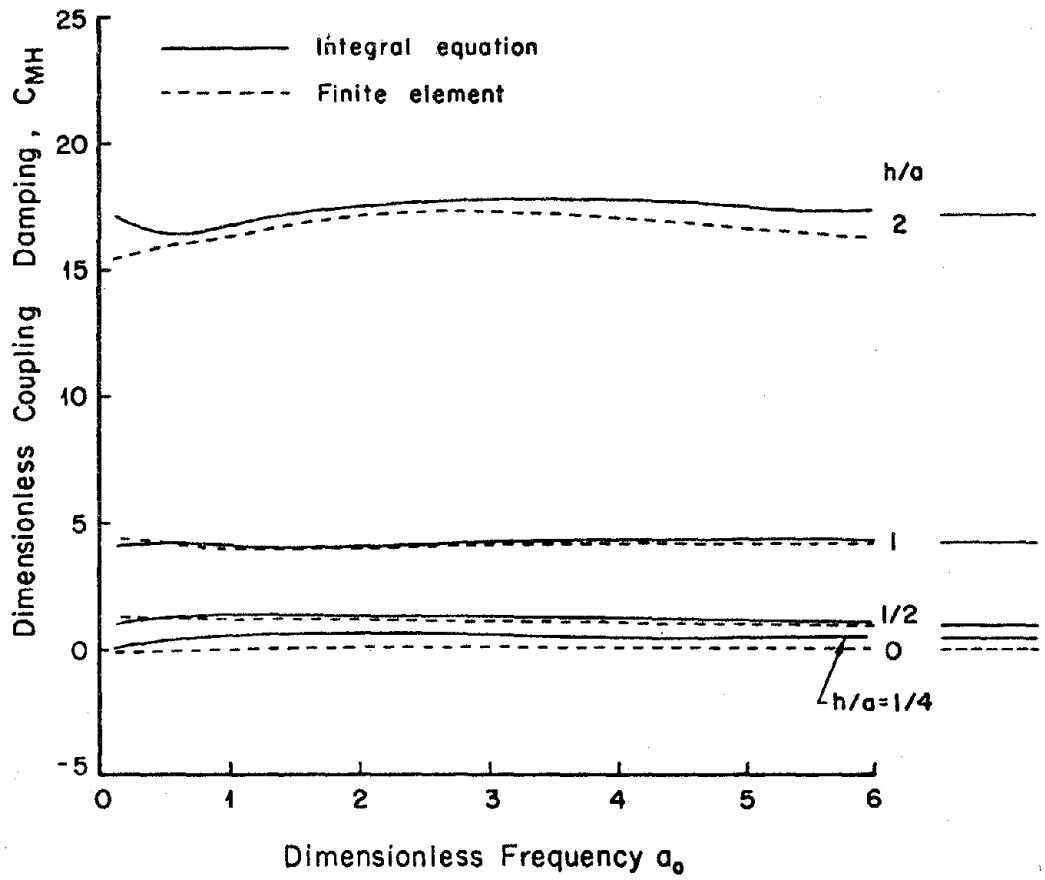

Figure 4.11. Effects of embedment on the coupling damping coefficient and comparison to finite element solution.

are displayed with dashed lines. In interpreting these comparisons, it must be kept in mind that Day's transient finite element results were obtained for a perfectly elastic soil deposit (no material attenuation) while the present integral equation results include a small amount of material damping.

It may be observed that the embedment ratio (h/a) has a marked effect on the torsional stiffness coefficients (Figure 4.2) -- an increase in the embedment ratio leads to an increase in the stiffness k_{TT} at all frequencies. In particular, the torsional stiffness increases almost linearly with embedment ratio for a fixed dimensionless frequency a_o. Also, the torsional stiffness is a decreasing function of frequency until it approaches an asymptotic value for each embedment ratio.

It may be seen in Figure 4.2 that there is close agreement between the finite element and integral equation results. The only significant differences appear at high frequencies where the finite element results are slightly lower than the corresponding results obtained by the present method. The difference at high frequency is proportional to a_o^2 indicating that the discrepancy is due to the finite element approximation of the mass distribution of the soil model adjacent to the foundation surface. There are several indications that this discrepancy at large a_o is associated with errors in the finite element results. Firstly, the material damping introduced in the integral equation method tends to slightly reduce the stiffness coefficients at high frequency (as will be discussed in more detail in Section 4.2). Since the transient finite element results do not incorporate material damping into the

analysis, then the finite element stiffnesses should be higher than those obtained by the present method as the frequency is increased. Secondly, a comparison of Day's finite element results for the torsional impedance of a hemispherical foundation to the analytical solution obtained by Luco (1976) reveals that the finite element method tends to underestimate the stiffness at high frequencies with the error proportional to $0.12\ a_0^2$ (see Day, 1977, pp. 76-77). Finally, there are similar discrepancies at high frequencies in the tortional damping coefficients (Figure 4.3), but it is the integral equation results that appear to more closely approach the exact asymptotic values at high frequencies for the rigid cylinders embedded in a uniform half-space.

The torsional damping coefficients (Figure 4.3) increase almost linearly with (h/a) for a fixed a_0. In particular, it may be shown for high values of a_0, that the radiation damping for different embedment ratios is in the ratio of the moments of inertia about the vertical axis of the corresponding soil-foundation contact areas. In general, the torsional damping coefficients are increasing functions of frequency until the asymptotic values are reached. The asymptotic values are shown in Figure 4.3 by lines adjacent to the results for different embedment ratios. An exception to this behavior may be seen at low frequencies where material damping causes an increase in the values of the damping coefficients (see Section 4.2 for more details).

In summary for the torsional stiffness k_{TT} and torsional damping coefficients c_{TT}, excellent agreement with Day's transient finite element results has been achieved with the slight discrepancies completely accounted for. Both the torsional stiffness and damping

coefficients are approximately linear functions of embedment ratio for a given frequency. Also, both are frequency dependent and consequently, the soil reaction may not be represented accurately by a constant spring-dashpot system even for a uniform half-space (the frequency dependence will naturally be even more pronounced when considering layered media).

The comparisons for the other impedance functions further establish the reliability of both methods. The most significant differences occur for the vertical and horizontal stiffness coefficients at high frequencies and are probably associated once again with shortcomings of the finite element method for small wavelengths.

Unlike the torsional impedances, the vertical impedances (Figures 4.4, 4.5) are relatively independent of frequency for all embedment ratios except for the broad minimum in the stiffness coefficients occurring in the vicinity of $a_0 = 3$ for embedment ratios less than unity. The vertical damping coefficients (Figure 4.5) increase linearly and strongly with embedment ratio while the effect of embedment on the vertical stiffness is not as marked. Once again, the agreement with Day is good with the largest differences related to the frequency limitation of the finite element approach.

The behavior of the horizontal impedances shown in Figures 4.6 and 4.7 is similar to that of the vertical impedances shown in Figures 4.4 and 4.5. The dependence on frequency is minimal and the horizontal damping coefficients increase more strongly with embedment ratio than the horizontal stiffness coefficients.

For the rocking and coupling impedances shown in Figures 4.8-4.11, it must be stated that the point of reference is at the center of the base of the cylinder. The behavior of the rocking impedance coefficients presented in Figures 4.8 and 4.9 as a function of frequency closely resembles the frequency dependence of the torsional impedance functions. The coupling impedances illustrated in Figures 4.10 and 4.11 are virtually frequency independent. One distinguishing feature for the rocking and coupling impedances is that the increase with embedment ratio is stronger than linear.

The computed values for the five damping coefficients are compared to the exact asymptotic values for a_o approaching infinity in Table 4.1. Day's finite element results calculated at $a_o = 6$ are displayed in column two for each radiation damping coefficient. The present integral equation results calculated at $a_o = 10$ are displayed in column three for each damping coefficient. The results shown in Table 4.1 indicate that both the transient finite element method and the integral equation method provide sufficiently accurate results (less than 10% error at high frequency) for most practical applications. These results also confirm that the integral equation method of solution leads to slightly better accuracy.

Values for the impedance functions calculated by the present integral equation method are tabulated in Appendix I. Results are presented at ten representative dimensionless frequencies for each of the four cylindrical foundations studied with the integral equation method in Figures 4.2 through 4.11 (embedment ratios of 0.25, 0.5, 1.0, 2.0).

	c_{TT}			c_{VV}			c_{HH}			c_{MM}			c_{MN}		
	Asy.	F.E.	I.E.	Asy.	F.E.	I.E.	Asy.	F.E.	I.E.	Asy.	F.E.	I.E.	Asy.	F.E.	I.E.
h/a	$a_o \to \infty$	$a_o = 6$	$a_o = 10$	$a_o \to \infty$	$a_o = 6$	$a_o = 10$	$a_o \to \infty$	$a_o = 6$	$a_o = 10$	$a_o \to \infty$	$a_o = 6$	$a_o = 10$	$a_o \to \infty$	$a_o = 6$	$a_o = 10$
2.0	14.14	13.34	13.98	18.01	17.54	17.81	20.30	19.85	20.08	30.53	28.81	30.26	17.17		17.45
1.0	7.85	7.40	7.67	11.73	11.49	11.52	11.73	11.54	11.54	7.36	7.01	7.22	4.29		4.43
0.5	4.71	4.44	4.53	8.58	8.59	8.37	7.43	7.18	7.25	3.29	3.27	3.13	1.07		1.18
0.25	3.14	--	3.04	7.01	--	6.88	5.29	--	5.10	2.19	--	2.12	0.27	--	0.34
0.0	1.57	1.51	--	5.44	5.52	--	3.14	3.12	--	1.36	1.43	--	0.00		--

Table 4.1

Comparison of integral equation solution with finite element solution and with asymptotic solution for the high frequency values of the damping coefficients for cylindrical foundations embedded in a uniform half-space.

The next section analyzes the effects of varying the amount of material damping in the soil, while Section 4.3 considers the effects of lateral separation on the impedance functions for cylindrical foundations.

4.2 EFFECTS OF MATERIAL ATTENUATION ON THE IMPEDANCE FUNCTIONS

It is the purpose of this section to describe in detail the effects of including physically realizable material attenuation into the soil model. The effects of material damping on the impedance functions are investigated by considering the cylindrical foundation with an embedment ratio of 0.25 as modelled in Figure 4.1 and by calculating the impedance functions for various degrees of material damping in the soil. The material damping in the viscoelastic half-space is assumed to be of the hysteretic type.

The impedance functions are evaluated for shear wave material damping ratios of 1, 5 and 10 percent, corresponding to specific attenuation factors for shear waves, Q_β, of 50, 10 and 5, respectively (specific attenuation factors for compressional waves, Q_α, are 100, 20, and 10 for the three cases considered). The five complex impedances normalized as in Eq. (2.41) are presented in Figures 4.12 through 4.21 as a function of dimensionless frequency, a_0, for the three different values of material damping.

In general, the results obtained indicate that material damping tends to reduce the stiffness coefficients at high frequencies. This trend begins at moderate frequencies and broadens as the frequency is increased. At low frequencies, the degree of material damping has negligible influence on the stiffness coefficients (Figures 4.12, 4.14, 4.16, 4.18, 4.20).

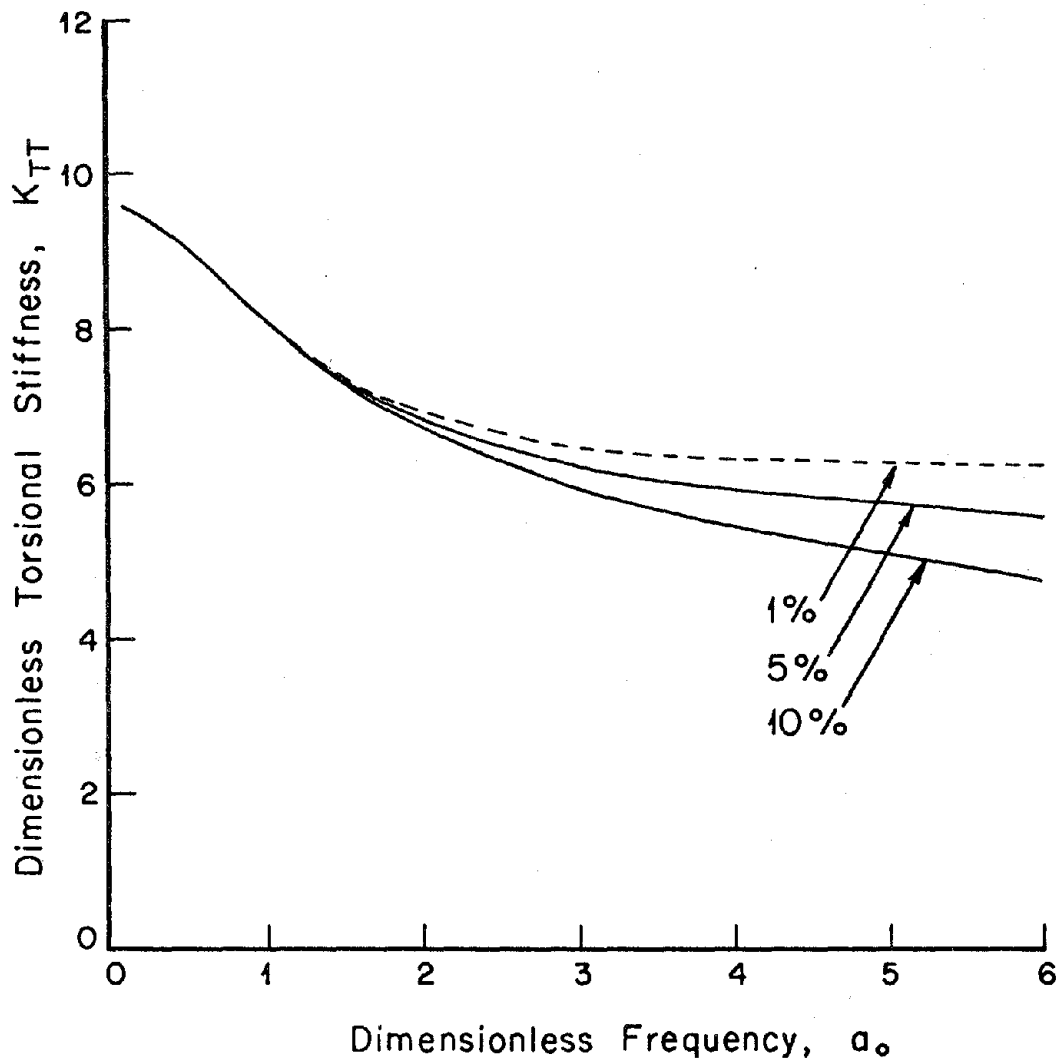

Figure 4.12. Effects of material attenuation on the torsional stiffness coefficients.

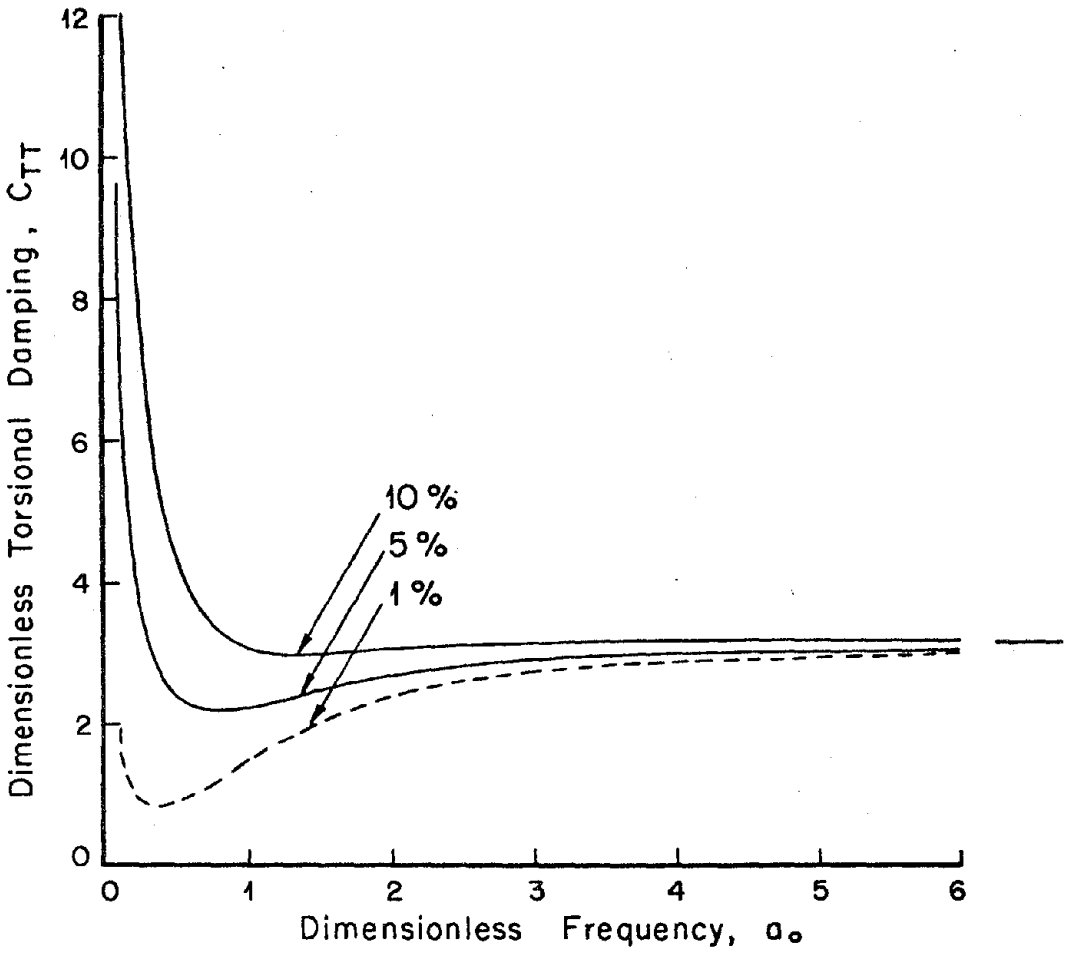

Figure 4.13. Effects of material attenuation on the torsional damping coefficients.

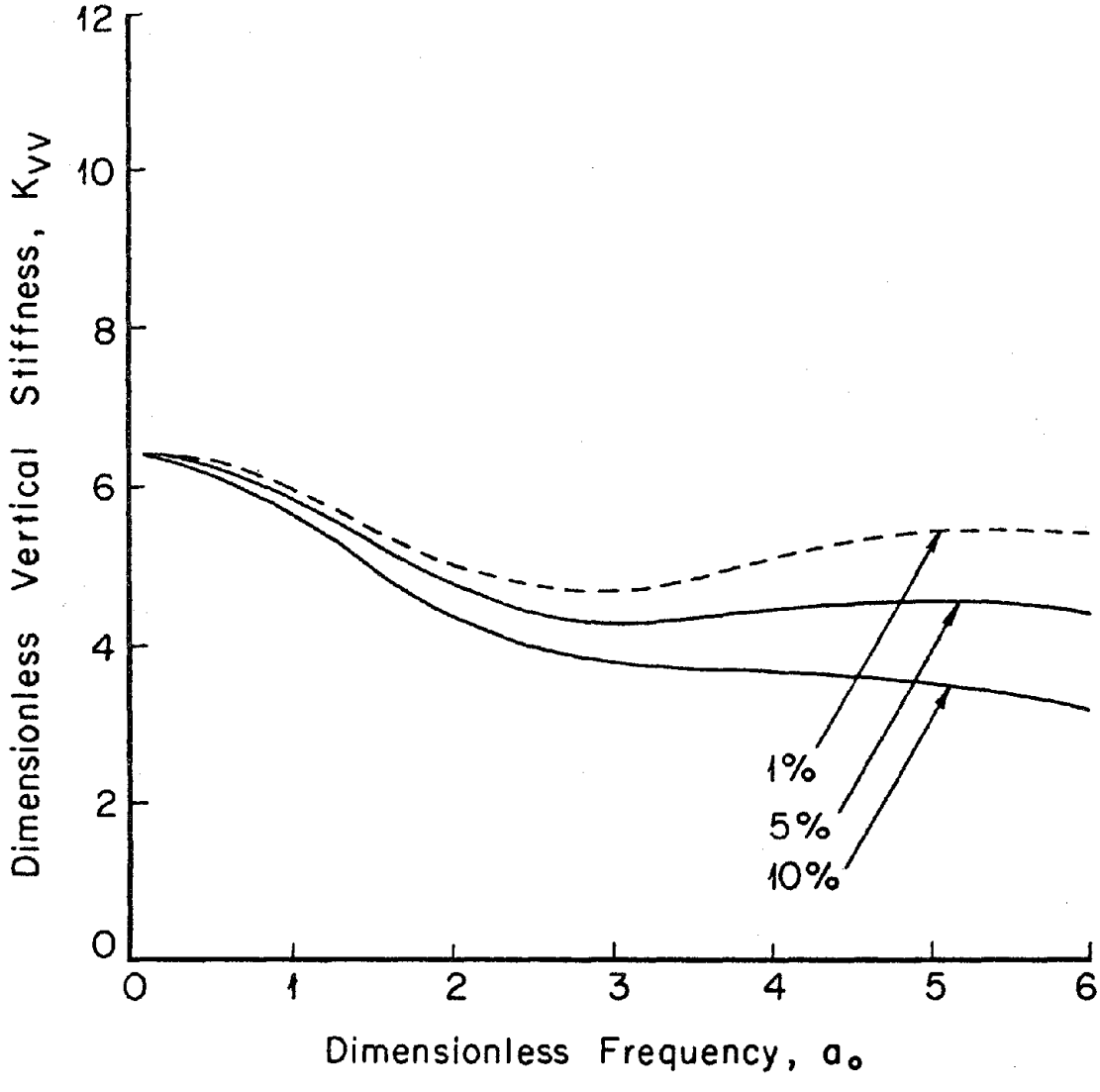

Figure 4.14. Effects of material attenuation on the vertical stiffness coefficients.

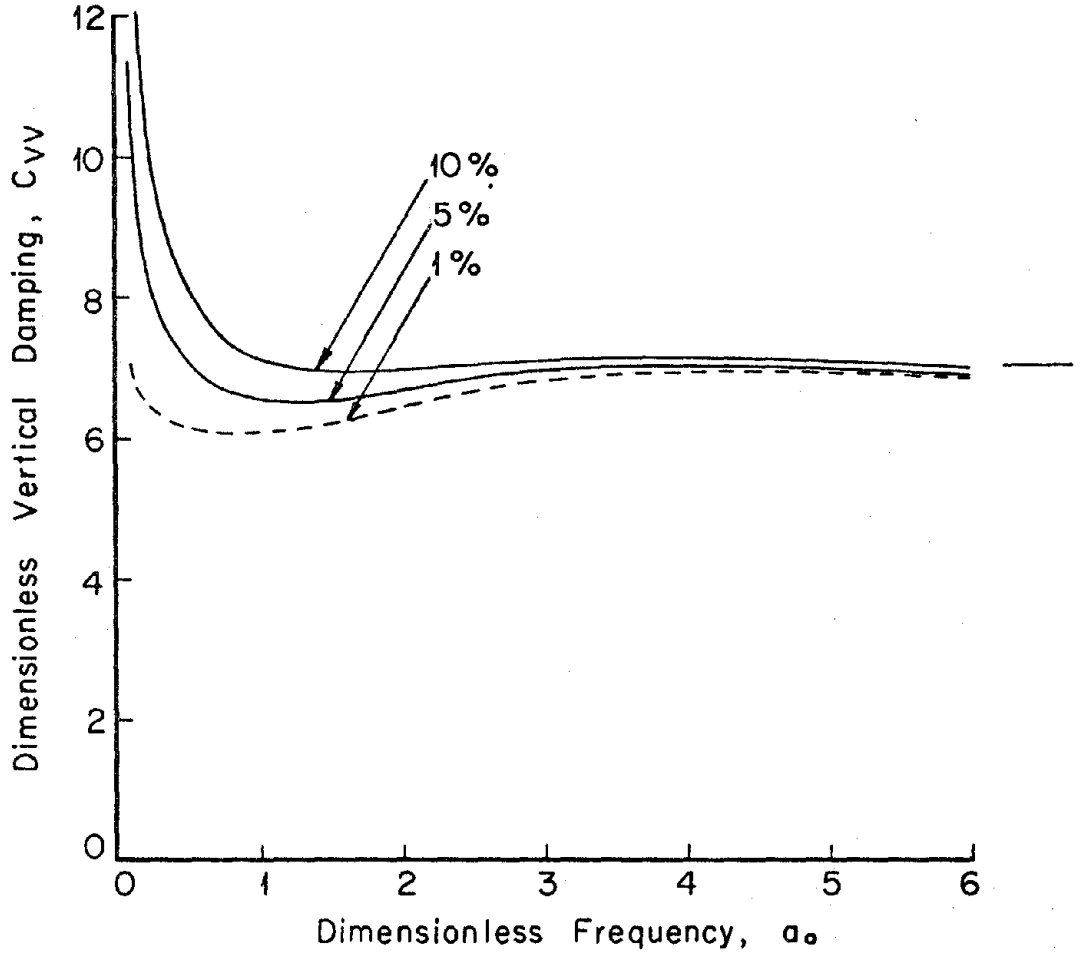

Figure 4.15. Effects of material attenuation on the vertical damping coefficients.

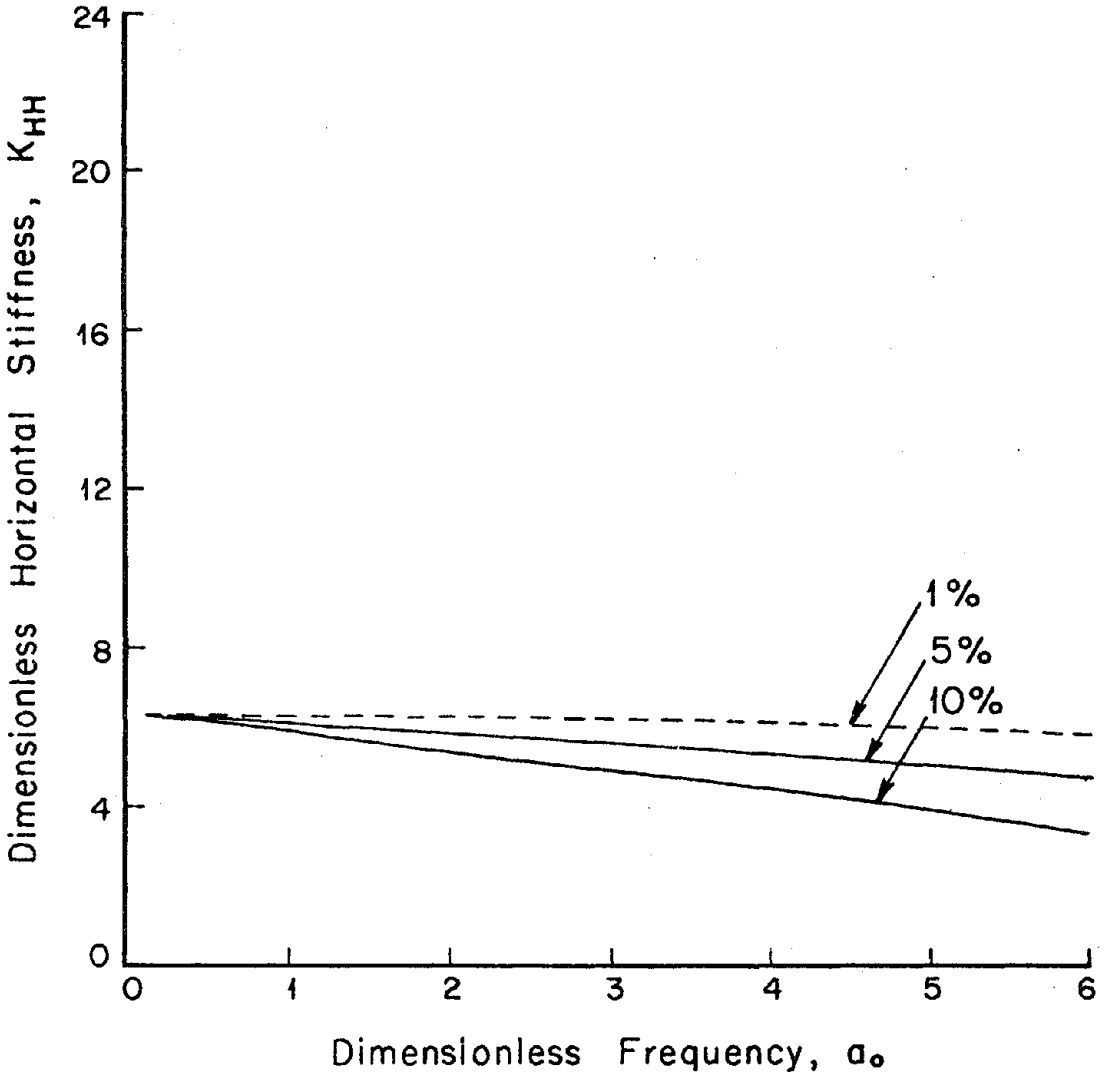

Figure 4.16. Effects of material attenuation on the horizontal stiffness coefficients.

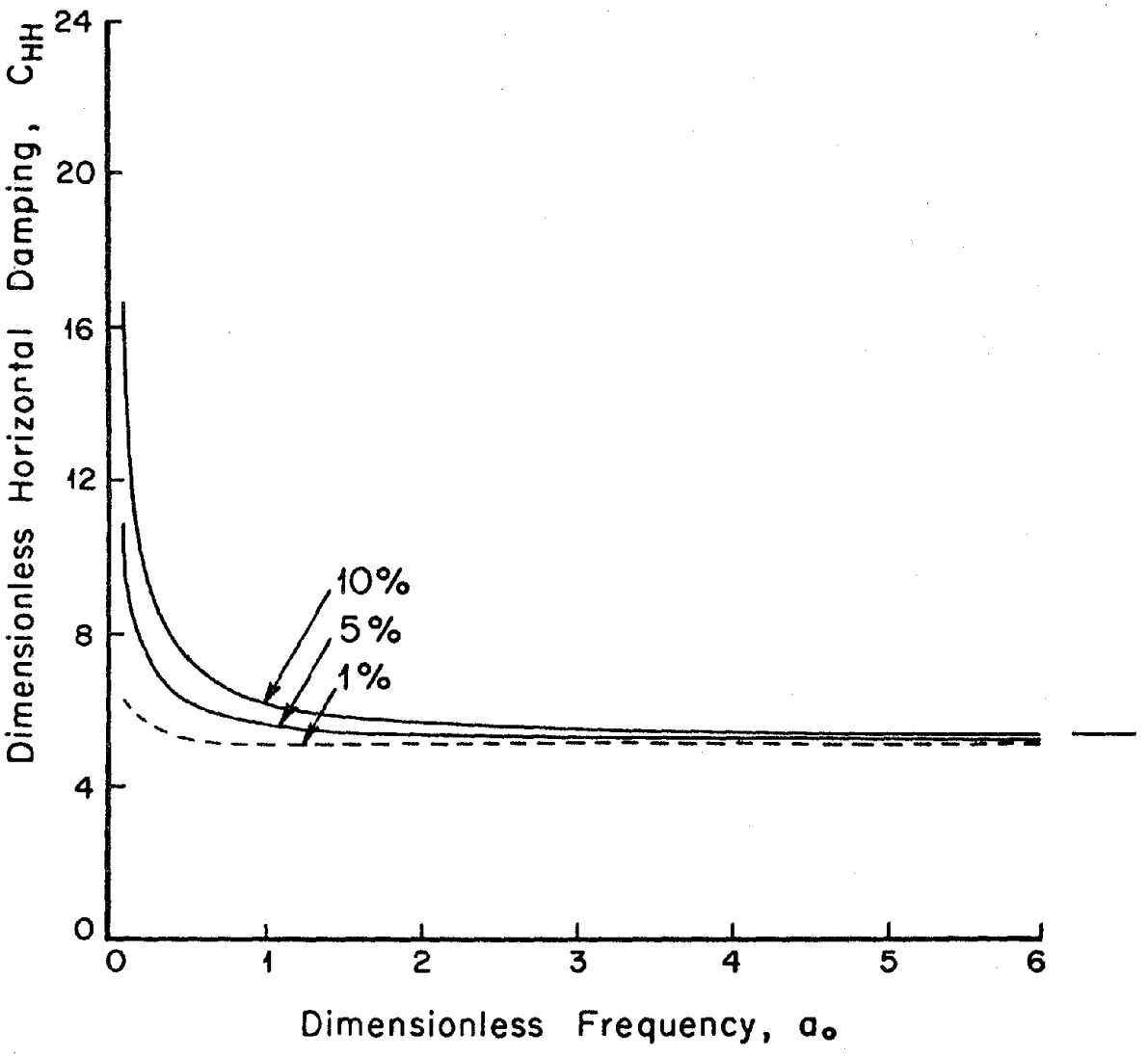

Figure 4.17. Effects of material attenuation on the horizontal damping coefficients.

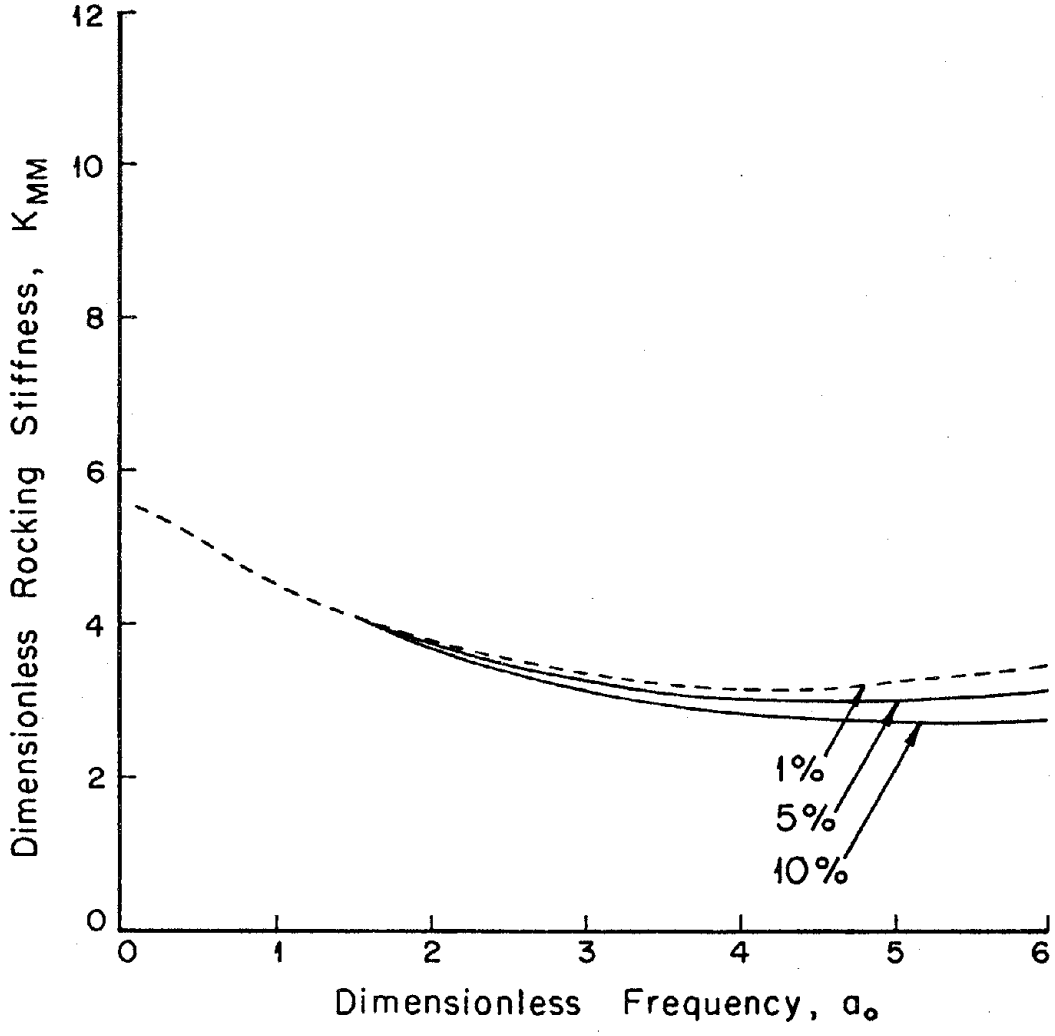

Figure 4.18. Effects of material attenuation on the rocking stiffness coefficients.

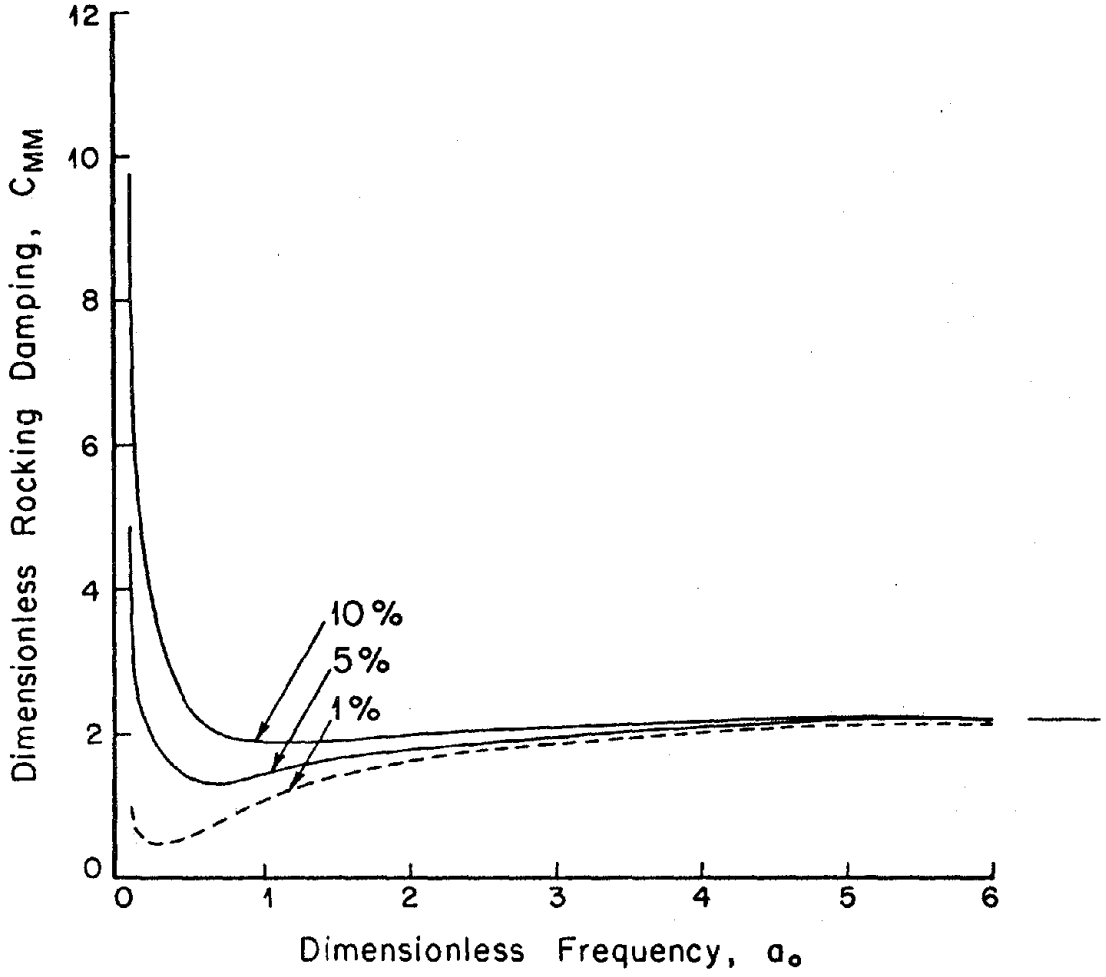

Figure 4.19. Effects of material attenuation on the rocking damping coefficients.

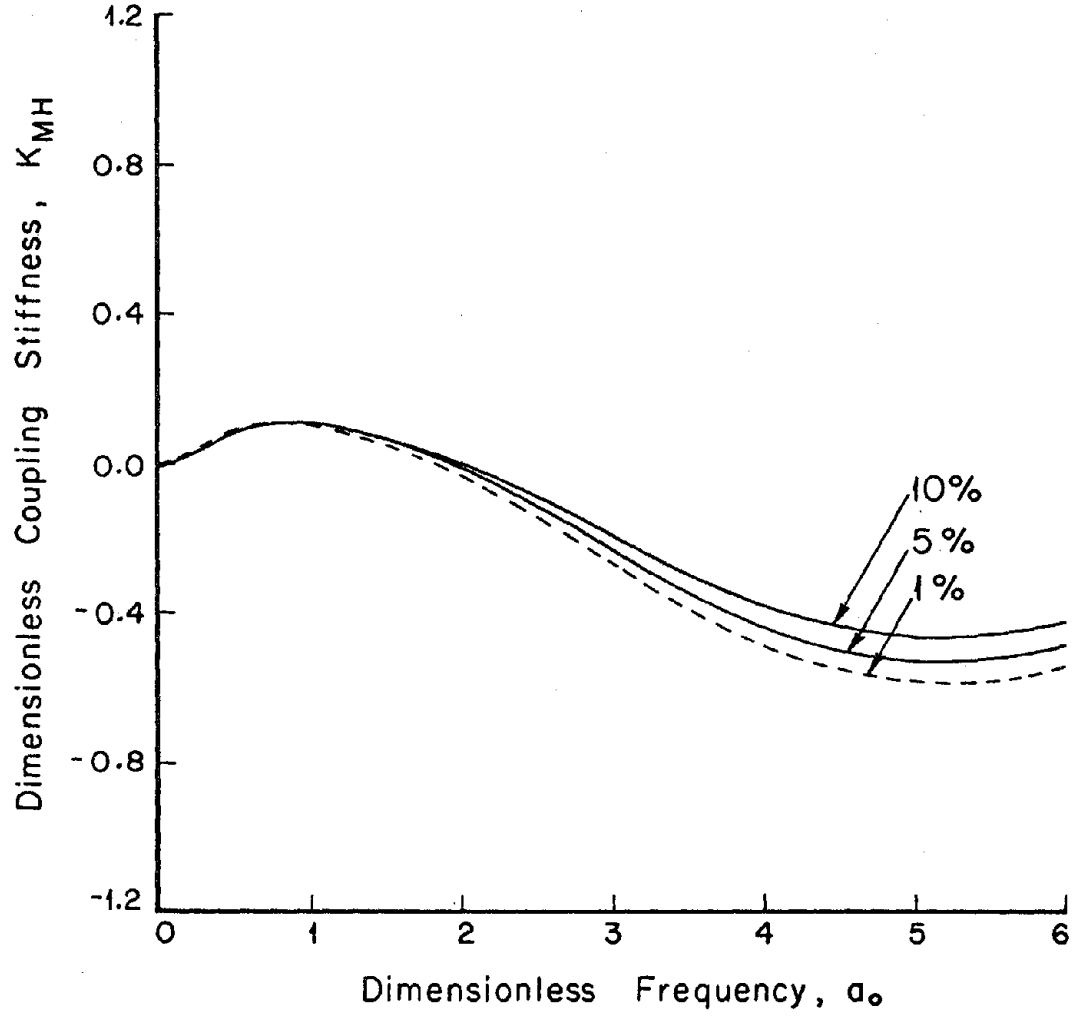

Figure 4.20. Effects of material attenuation on the coupling stiffness coefficients.

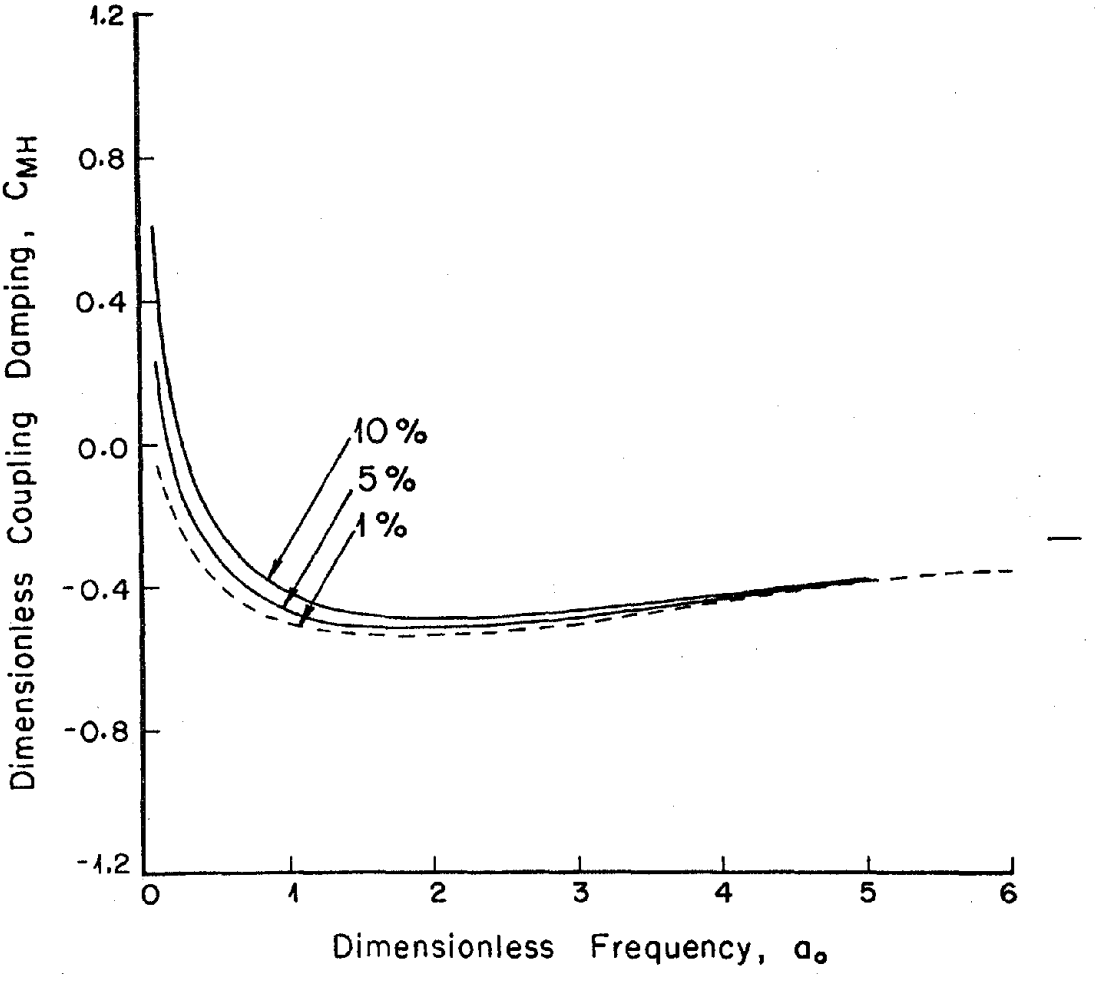

Figure 4.21. Effects of material attenuation on the coupling damping coefficients.

Conversely, the effects of material damping on the damping coefficients are quite marked at low frequencies and decrease as the frequency increases (Figures 4.13, 4.15, 4.17, 4.19, 4.21). The trend in the radiation damping coefficients is an increase in amplitude as the material damping is increased.

For hysteretic type material damping, the damping ratio, $\xi_\beta = \frac{1}{2Q_\beta}$, is independent of frequency and is analogous to the precentage of critical damping under resonant conditions, or during free vibrations. For this type of material damping, it can be shown that the damping coefficients tend to $2\xi_\beta/a_o$ as a_o approaches zero (see Luco, 1976b). To give a rough idea of the practical ranges of ξ_β and hence Q_β, one should realize that the hysteretic damping constant ξ_β is strain dependent: values for low strain may be less than 0.02, while for high strains ξ_β may reach values of 0.15 or 0.20.

It is important to mention that the integral formulation employed can also be used to investigate other attenuation mechanisms in addition to the hysteretic type just described.

4.3 EFFECTS OF CONTACT CONDITIONS ON THE IMPEDANCE FUNCTIONS

In many situations, it is not realistic to assume that the foundation is in welded contact with the surrounding soil. The presence of backfill or the possible inelastic deformation of the top soil layers suggest that a more realistic model for the contact conditions must allow for the lateral separation between the foundation and the soil. The effects of lateral separation are investigated by considering various degrees of contact between a cylindrical foundation of embedment ratio

2.0 and the surrounding soil represented by a uniform viscoelastic half-space ($\xi_\beta = 0.01$, $\alpha/\beta = \sqrt{3}$). Four cases are considered: in the first case, the foundation is perfectly welded to the surrounding soil (0% separation); in the second case, the top 25% of the lateral boundary of the foundation acts independently from the soil while the rest of the foundation remains in welded contact (25% separation); the third and fourth cases correspond to 50% and 75% separation, respectively.

The torsional stiffness and torsional damping coefficients plotted versus dimensionless frequency are shown in Figures 4.22 and 4.23, respectively, for the four different degrees of contact. The torsional stiffness, k_{TT} (Figure 4.22), undergoes a dramatic reduction in amplitude at all frequencies as the percentage of lateral separation is increased. Another interesting feature is the fluctuations introduced by the separation conditions. Both the reduction in amplitude and the fluctuations are easily interpretted by considering the physics of the separation problem. The separation zone acts as if the soil surrounding the foundation in this region were extremely soft so that the stiffness of the soil to the rigid body movements is effectively zero in this region. Therefore, the separation condition could be approximated by considering a soft layer instead of the separation zone and carrying out the analysis as if welded contact were prescribed.

Similar reductions in amplitude and appearances of fluctuations as a function of frequency are exhibited in Figure 4.23 for the torsional damping coefficient, c_{TT}. At high frequencies, it appears as though the reduction is linearly proportional to the percentage of separation. It is interesting to notice that the damping coefficients

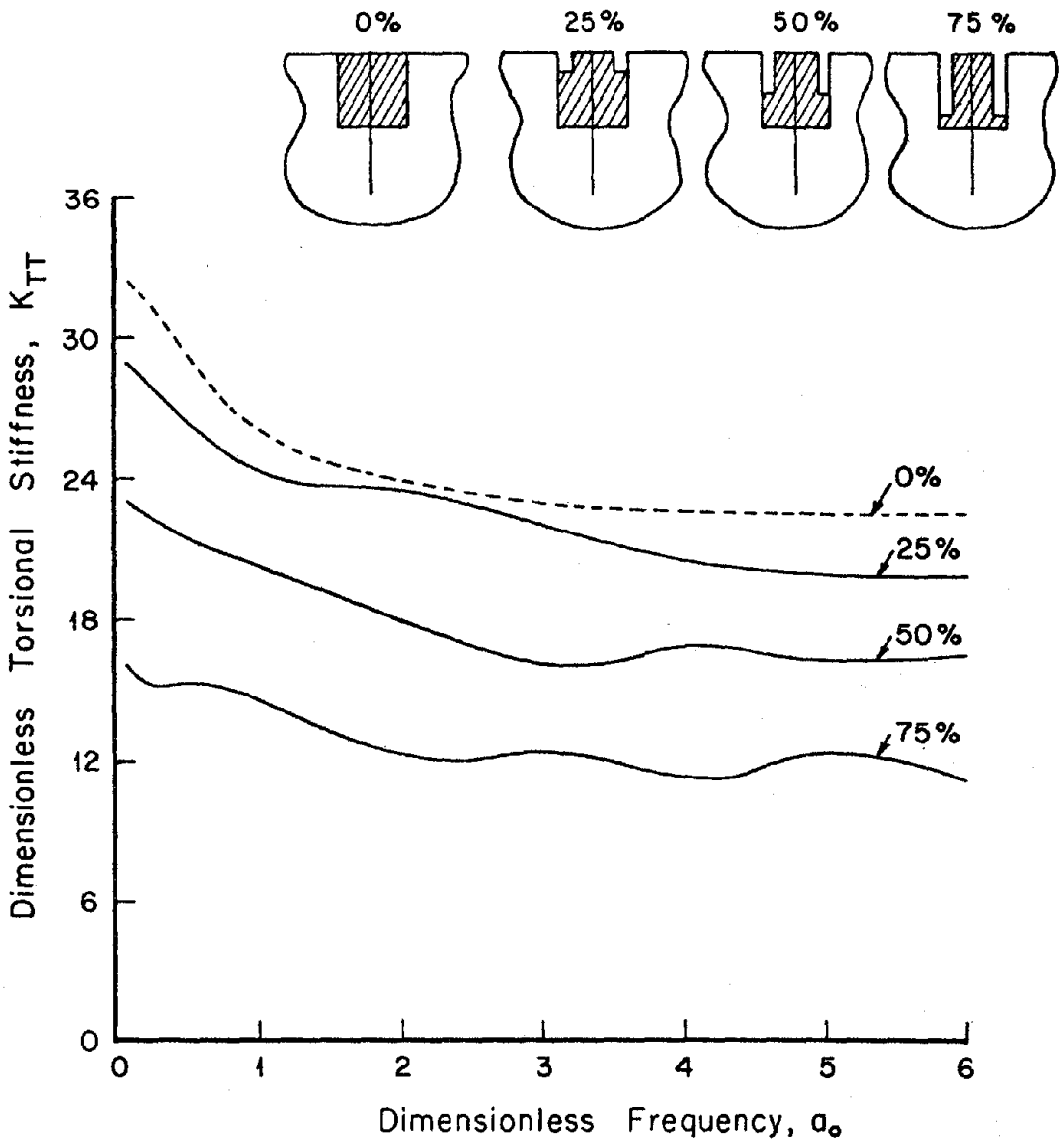

Figure 4.22. Effects of contact conditions on the torsional stiffness coefficient. The parameter is the percentage of separation of the lateral boundary of the cylinder.

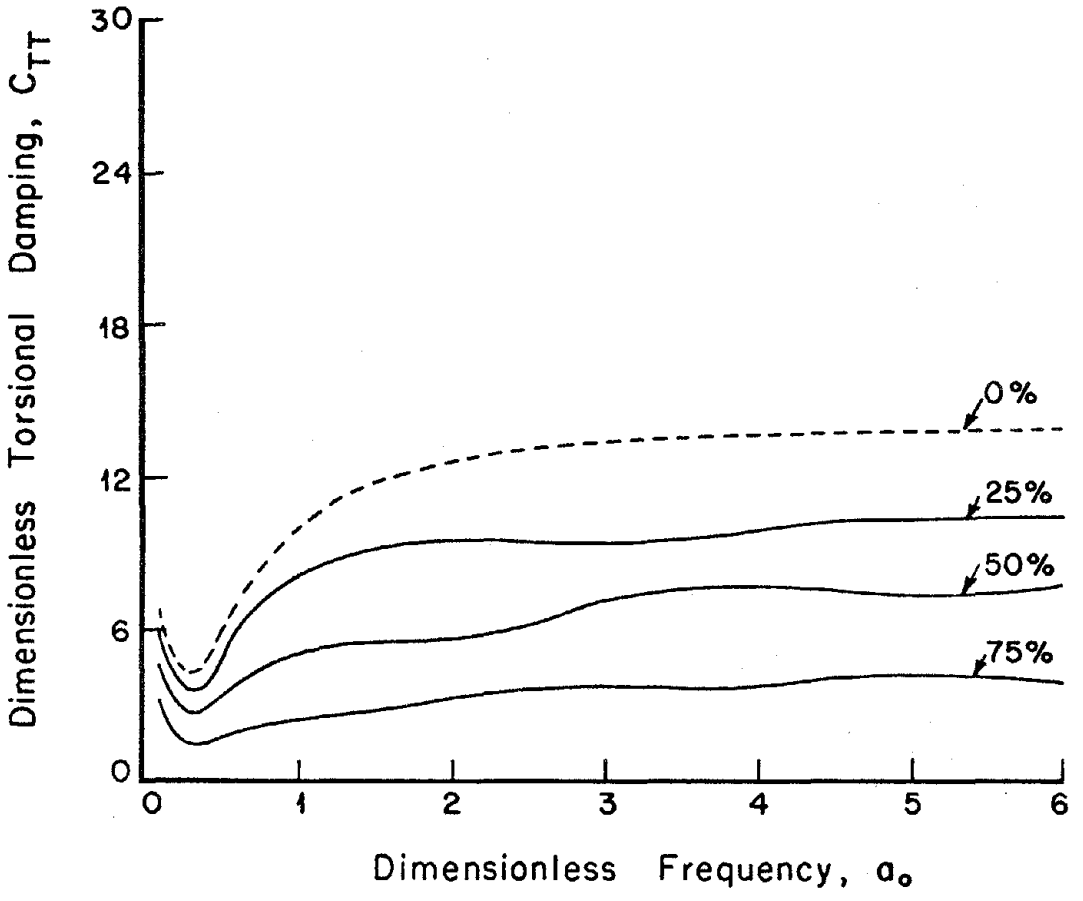

Figure 4.23. Effects of contact conditions on the torsional damping coefficient. The parameter is the percentage of separation of the lateral boundary of the cylinder.

for a cylindrical foundation with an embedment ratio of $h/a = 2.0$ and with lateral separation on the top 50% of the mantle are very close to the corresponding damping coefficients for a cylindrical foundation welded to the soil and with an "effective" embedment ratio of $h/a = 1.0$ (refer to Figures 4.23 and 4.3).

To summarize, with the torsional impedances serving as typical results, the reduction in amplitude is directly attributable to the reduced contact area on which the soil resists the movements of the foundation. The fluctuations as a function of frequency appear analogously to problems in which the soil deposit is layered. If not for the fluctuations, the lateral separation conditions would lead to results similar to those for foundations less deeply embedded ("effective" embedment would be approximately the total embedment depth h minus the depth of the separation zone).

4.4 COMPARISON WITH FINITE ELEMENT FOR LAYERED CASE

Until this section, all the results presented were for foundations embedded in uniform semi-infinite media. Now, the case of a rigid cylindrical foundation of radius $a = 40$ feet embedded to a depth $h = 16$ feet in a layered soil deposit is to be considered. The soil deposit consists of two parallel viscoelastic layers overlying a uniform viscoelastic half-space and the soil properties are listed in Table 4.2.

Both the time domain finite element method and the present integral equation method were used to solve the radiation problem. Since the present method is based on solving integral equations involving the Green's functions, there is virtually no additional effort required to

Layer	β ft/sec	α ft/sec	ρ lb/ft^3	Q_β	Q_α	Thickness ft
1	980	2400	133	100	200	16
2	1270	2540	133	100	200	16
3	1380	2760	133	150	300	∞

Table 4.2

Material properties for the earth structure used in comparison with finite element solution for simple layered problem.

include the layers in the model because the Green's functions for the viscoelastic layered half-space are readily obtainable as in Part I of this dissertation.

The rigid cylindrical foundation considered has an embedment ratio of 16/40 as shown in Figure 4.24 and is assumed to be in welded contact with the sourrounding soil. Relatively large specific attenuation factors (Q_β = 100 corresponding to a material damping ratio of 0.5) were chosen for the comparisons since the finite element results correspond to the case of no material damping.

The horizontal, rocking and coupling impedance functions, referred to the center of the base of the foundation, are tabulated in Table 4.3 at seven representative frequencies. The stiffness and damping coefficients have been normalized as in Eq. (2.41) by the shear modulus and shear wave velocity of the top layer. Comparing the results obtained in Table 4.3, good agreement is found particularly at low frequencies. Realizing how vastly different are the two solution techniques, considerable confidence should be given to the results of both methods for such a complex problem.

In the next section, a more complex layering profile extending to a depth of 20 times the foundation embedment is considered.

4.5 OTHER RESULTS

In this section, the present method (numerical solution to integral equations involving the dynamic Green's functions for layered viscoelastic media) is applied to a typical foundation embedded in a typical soil medium. In particular, the soil-foundation system to be

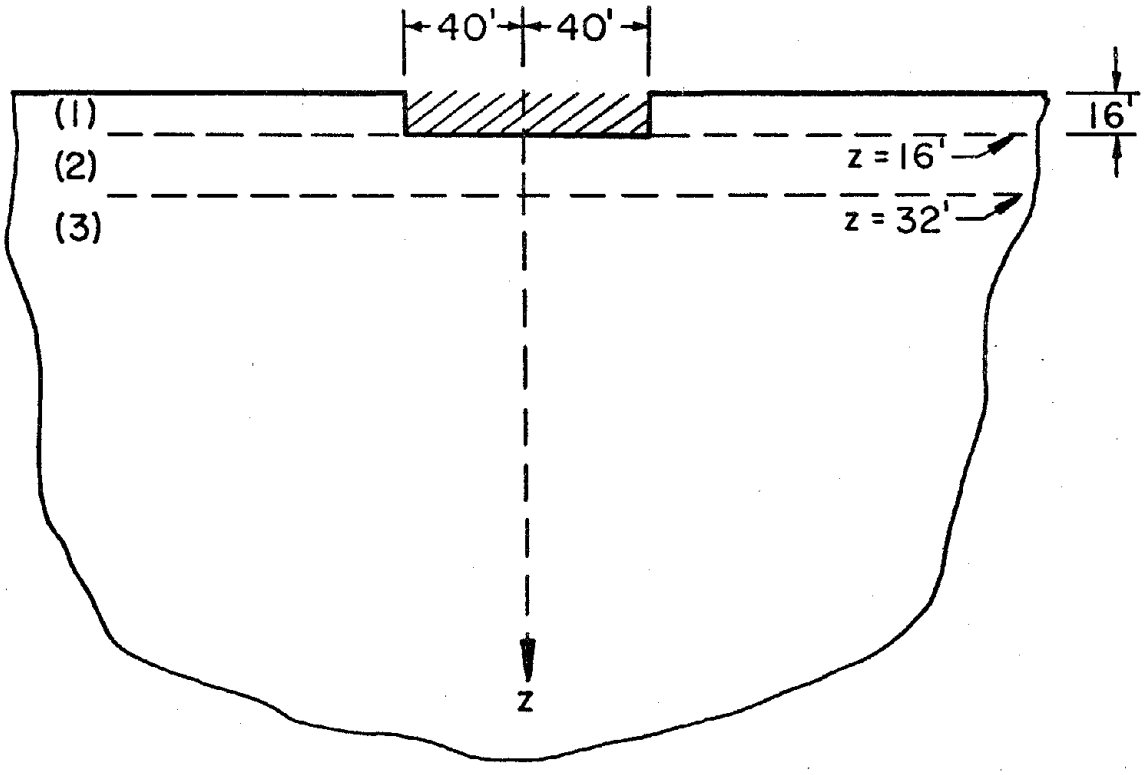

Figure 4.24. Problem geometry for comparison to finite element solution involving a simple layered earth model.

a_o	k_{HH}	k^*_{HH}	c_{HH}	c^*_{HH}	k_{MM}	k^*_{MM}	c_{MM}	c^*_{MM}	k_{MH}	k^*_{MH}	c_{MH}	c^*_{MH}
.40906	11.747	11.86	6.661	6.679	10.990	11.51	0.505	0.475	-0.628	-0.534	-0.740	-0.803
1.02265	11.359	11.45	6.766	6.802	9.879	10.36	1.149	1.087	-0.522	-0.447	-0.961	-0.881
2.0453	10.587	10.51	6.991	7.094	8.363	8.565	2.008	2.132	-0.534	-0.475	-1.027	-0.982
3.06795	9.884	9.536	7.140	7.236	7.220	7.394	2.425	2.546	-0.612	-0.607	-1.043	-0.967
4.0906	9.126	8.437	7.248	7.339	6.182	5.988	2.716	2.861	-0.759	-0.793	-1.052	-0.976
4.90872	8.490	7.445	7.301	7.348	5.517	5.239	2.922	3.098	-0.997	-1.101	-1.049	-0.950
5.93137	6.865	5.681	7.388	7.363	5.188	4.731	3.145	3.297	-1.468	-1.459	-1.027	-0.889

* is finite elements (Steve Day)

Table 4.3

Comparison of integral equation solution with finite element solution for the horizontal, rocking and coupling impedance functions for cylinder embedded in layered half-space with material properties defined in Table 4.2.

analyzed is shown in Figure 4.25 where the foundation is a rigid (in comparison with the surrounding soil) circular cylinder of radius 40 feet and embedment depth 18 feet. The soil deposit consists of six parallel viscoelastic layers overlying a uniform viscoelastic half-space with the layer properties given in Table 4.4.

The foundation is discretized as in Figure 4.26 according to the suggestions presented at the end of Section 3.2. First, the number of ring sources, N, to be used on the internal source surface is chosen conservatively to be 26. The location of the source surface S' is chosen to be offset from the observation surface S by 2.5 feet and the spacing ΔL on a line on surface S is taken to be 1.0 feet (so that $M = 59$). Thereby, accurate final results (impedance functions) as well as accurate intermediate results (displacement and traction distribution on S) are insured.

The horizontal, rocking and coupling impedances, normalized as in Eq. (2.41) by the shear modulus and shear wave velocity of the top layer, are displayed in Figure 4.27. The impedances are referred to the center of the base of the foundation and welded contact is assumed at the boundary between the foundation and the surrounding soil. As a general observation, one should notice the strong dependence on frequency in all the stiffness and damping coefficients, so that the soil reaction can in no way be represented by a constant spring-dashpot system.

Of particular distinction is the considerable reduction of the damping coefficients c_{HH}, c_{MM}, c_{MH}, especially at low frequencies, compared to the respective stiffness coefficients k_{HH}, k_{MM}, k_{MH}. This reduction is explained by the fact that the layers underyling the

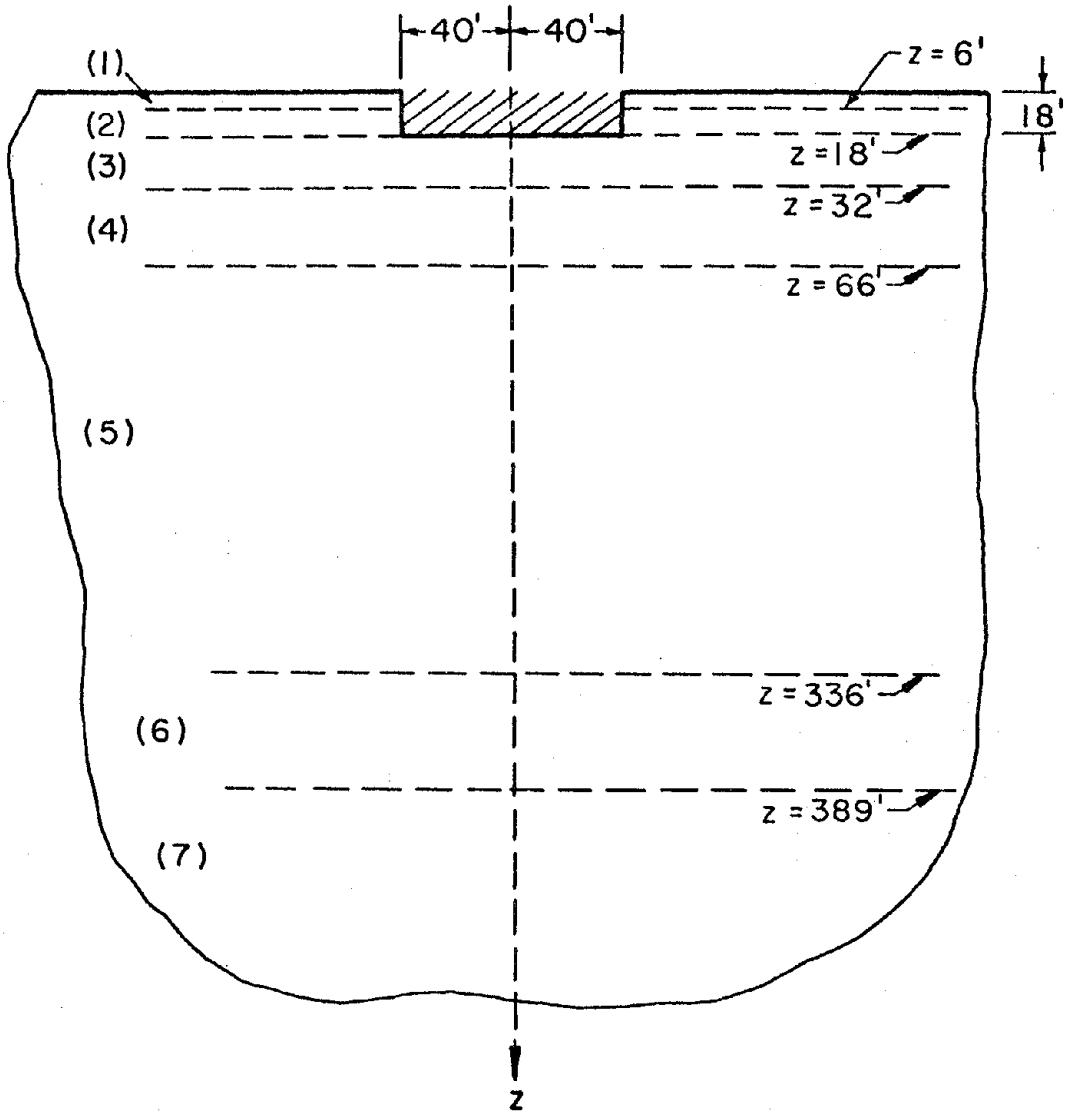

Figure 4.25. Problem geometry and a 7-layer model for analysis of the embedded foundation of the Millikan Library at California Institute of Technology.

Layer	β ft/sec	α ft/sec	ρ lb/ft^3	Q_β	Q_α	Thickness ft
1	630	1260	133	50	100	6
2	1110	2220	133	50	100	12
3	1380	2760	133	50	100	14
4	1600	3200	133	50	100	34
5	2000	4000	133	50	100	270
6	2500	5000	133	50	100	53
7	3100	6200	133	50	100	∞

Table 4.4

Material properties for a 7-layer model of the Millikan Library geologic site at California Institute of Technology.

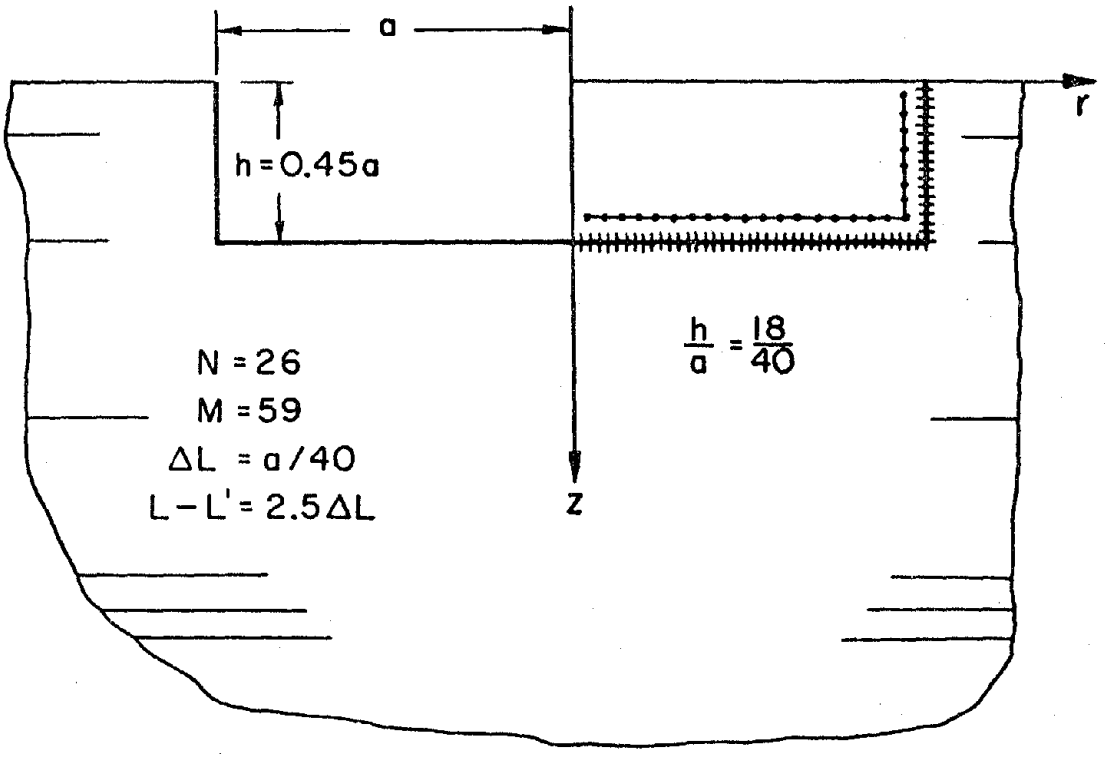

Figure 4.26. Boundary geometry, coordinate system and discretization used for analysis of model described in Figure 4.25.

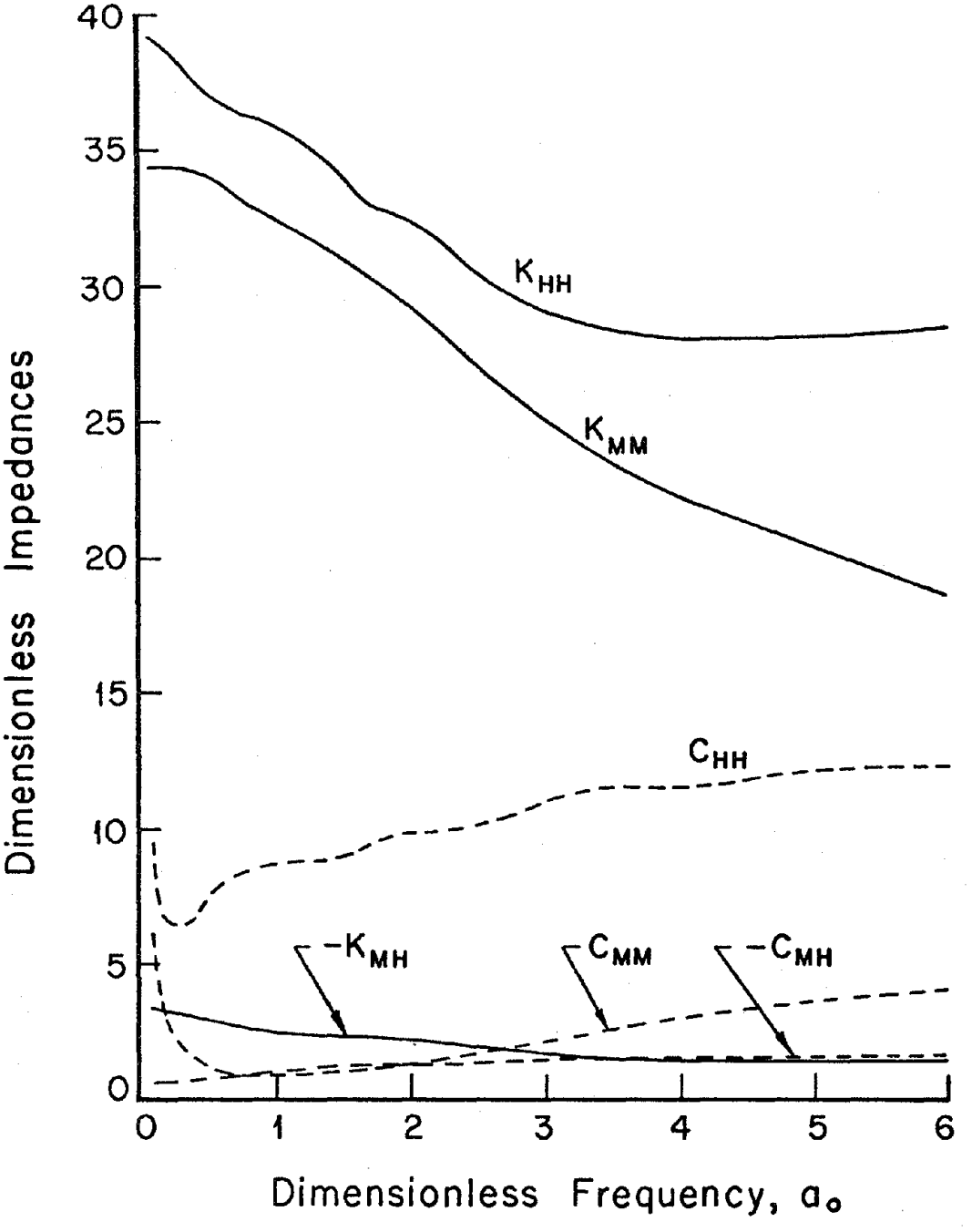

Figure 4.27. Dimensionless impedance coefficients for cylindrical foundation embedded in layered viscoelastic half-space as depicted in Table 4.4 and Figures 4.25 and 4.26.

foundation are stiffer than the surface layers, retarding the radiation of energy away from the foundation at low frequencies.

The behavior of the damping coefficients at low frequency and the behavior of the stiffness coefficients at high frequency offers no surprises in light of the discussion concerning material damping in Section 4.2. The frequency dependence of the horizontal and rocking stiffnesses are quite similar and the coupling stiffness is rather insignificant.

These results indicate that the present integral equation formulation used in conjunction with the Green's functions for layered viscoelastic media provides an excellent technique to obtain the response of foundations embedded in layered viscoelastic media.

CHAPTER 5

SUMMARY AND CONCLUSIONS

The integral equation formulation used in conjunction with the Green's functions for layered viscoelastic media provides an accurate and effective method for studying the response of foundations embedded in layered viscoelastic media. Such an analysis resolves two prevailing shortcomings in the present state-of-the-art: 1) the practice of restricting the soil model to a homogeneous, non-dissipative, purely elastic half-space; and 2) the practice of constraining the analysis to the case of flat foundations. The flexibility of the integral equation method permits its application to a wide variety of problems such as the generation of nonreflecting boundary conditions for use in properly modeling the extended earth with finite elements; the response of valleys and canyons to incoming waves; and the equivalent source representation for propagation purposes.

Extensive internal checks and comparisons with available results were presented in Chapters 3 and 4, respectively, to document the accuracy of the method. Guidelines for efficient implementation of the discretization and subsequent numerical solution of the integral equations were also enumerated.

Basically, to accurately represent the displacements and tractions on the surface of the foundation, the number of sources chosen on the internal source surface must be sufficient for the problem considered (more sources necessary when corners exist on the foundation surface or

when mixed boundary conditions are imposed). For axisymmetric foundations, it is demonstrated that 10 or 15 ring sources are adequate. The location of the internal source surface is selected as close to the surface of the foundation as is economically feasible considering that the closer the internal surface, the more pronounced the Green's functions become, thus requiring more observation points to accurately evaluate the numerical integrals. For axisymmetric foundations, it is suggested to demarcate the internal source surface by uniformly shrinking the foundation surface an amount 2 1/2 times the spacing of the observation points on the foundation surface.

The effects of embedment on the impedance functions for cylindrical foundations reveal that embedment has a marked influence on the response. Both the stiffness and damping coefficients (real and imaginary part of the impedance, respectively) increase with increasing embedment at all frequencies and for all components. In general, the damping coefficients are more strongly influenced by the embedment than the corresponding stiffness coefficients. However, as a function of frequency, the various impedance functions tend to preserve their shape as the embedment is changed. Yet, the impedance functions are frequency dependent and consequently, the soil reaction may not be accurately modeled with a constant spring-dashpot system.

The effects of material damping on the impedance functions are to reduce the stiffness coefficients at high frequencies and to increase the damping coefficients at low frequencies. Hysteretic type material damping was assumed in all the results, but the integral equation analysis can also be used to investigate other attenuation mechanisms.

The effects of considering various degrees of lateral separation at the contact between cylindrical foundations and the surrounding soil lead to the conclusion that the reduction in amplitude of the impedance functions is directly ascribable to the reduced contact area on which the soil resists the movements of the foundation. Also, the fluctuations introduced into the impedances as a function of frequency are attributable to the lateral zone of separation where the stiffness of the soil to the foundation movements is effectively zero (similar to imposing an extremely soft layer in place of the separation zone).

With the ever increasing speed and capacity of the modern computer, the present integral equation method should be capable of performing three-dimensional analysis of nonaxisymmetric problems. Also, once the input motion for the foundation-soil system is determined by this same integral equation approach, then the complete soil-structure interaction problem may be solved with the foundations embedded in layered viscoelastic media.

REFERENCES

Apsel, R. J. and Luco, J. E., 1976. Torsional response of rigid embedded foundations, Journal of the Engineering Mechanics Division, ASCE, 102, 957-970.

Arnold, R. N., Bycroft, G. N. and Warburton, G. B., 1955. Forced vibration of a body on an infinite elastic solid, Journal of Applied Mechanics, ASME, 22, No. 3, 391-400.

Baranov, V. A., 1967. On the calculation of excited vibrations of an embedded foundation, (in Russian), Voprosy Dynamiki i Prochnocti, No. 14, Polytechnical Institute of Riga, 195-209.

Beredugo, Y. O. and Novak, M., 1972. Coupled horizontal and rocking vibration of embedded footings, Canadian Geotechnical Journal, 9, 477-497.

Bielak, J., 1971. Earthquake response of building-foundation systems, Report EERL-71-04, Earthquake Engineering Research Laboratory, California Institute of Technology, Pasadena, California.

Bycroft, G. N., 1956. Forced vibrations of a rigid circular plate on a semi-infinite elastic space or on an elastic stratum, Phil. Trans., Royal Soc. of London, 248, 327-368.

Collins, W. D., 1962. The forced torsional oscillations of an elastic half-space and an elastic stratum, Proc. London Math. Soc., 12, No. 46, 226-244.

Day, S. M., 1977. Finite Element Analysis of Seismic Scattering Problems, Ph.D. Thesis, University of California, San Diego, California.

deHoop, A. T., 1958. Representation theorems for the displacement in an elastic solid and their application to elastodynamic diffraction theory, D.Sc. Thesis, Technische Hogeschool, Delft.

Dravinski, M. and Thau, S. A., 1976. Multiple diffractions of elastic waves by a rigid rectangular foundation: plane-strain model, Journal of Applied Mechanics, ASME, 43, 291-294.

Frazier, G. A., Alexander, J. H. and Petersen, C. M., 1973. 3-D seismic code for ILLIAC IV, Systems, Science and Software Report SSS-R-73-1506.

Frazier, G. A. and Petersen, C. M., 1974. 3-D stress wave code for the ILLIAC IV, Systems, Science and Software Report SSS-R-74-2103.

Hadjian, A. H., Luco, J. E. and Tsai, N. C., 1974. Soil-structure interaction: Continuum or finite element ?, Nucl. Eng. Des., 31, 151-167.

Isenberg, J. and Adham, S. A., 1972. Interaction of soil and power plants in earthquakes, Journal of the Power Division, ASCE, 98, 273-291.

Kashio, J., 1970. Steady State Response of a Circular Disk Resting on a Layered Medium, Ph.D. Thesis, Rice University.

Kausel, E. R. and Roësset, J. M., 1975. Dynamic stiffness of circular foundations, Journal of the Engineering Mechanics Division, ASCE, 101, 771-785.

Kausel, E. R., Roësset, J. M. and Waas, G., 1975. Dynamic analysis of footings on layered media, Journal of the Engineering Mechanics Division, ASCE, 101, 679-693.

Kobori, T., Minai, R. and Suzuki, T., 1966. Dynamic ground compliance of rectangular foundation on an elastic stratum, Proc. 2nd Japan National Symposium on Earthquake Engrg. Cont., Japan, 261-266.

Kobori, T., Minai, R. and Suzuki, T., 1967. Dynamic ground compliance of rectangular foundation on an elastic stratum over a semi-infinite rigid medium, Annual Report, Disaster Prevention Research Institute of Kyoto University, No. 10A, 315-341.

Kobori, T., Minai, R. and Suzuki, T., 1968. Dynamic ground compliance of rectangular foundation on an elastic stratum over a semi-infinite viscoelastic medium, Annual Report, Disaster Prevention Research Institute of Kyoto University, No. 11A, 349-367.

Kobori, T. and Suzuki, T., 1970. Foundation vibrations on a viscoelastic multilayered medium, Proc. Third Japan Earthquake Engineering Symposium, Tokyo, 493-499.

Kobori, T., Minai, R. and Suzuki, T., 1971. The dynamic ground compliance of a rectangular foundation on a viscoelastic stratum, Bull. Disaster Prev. Res. Inst., Kyoto University, 20, March, 389-429.

Kupratze, V. D., 1963. Dynamical Problems in Elasticity, Progress in Solid Mechanics, III, North-Holland Publishing Company, Amsterdam, Holland.

Luco, J. E., 1969. Dynamic interaction of a shear wall with the soil, Journal of the Engineering Mechanics Division, ASCE, 95, 333-346.

Luco, J. E. and Westmann, R. A., 1971. Dynamic response of circular footings, Journal of the Engineering Mechanics Division, ASCE, 97, 1381-1395.

Luco, J. E. and Westmann, R. A., 1972. Dynamic response of a rigid footing bonded to an elastic half-space, Journal of Applied Mechanics, ASME, 39, No. 2, 527-534.

Luco, J. E. and Hadjian, A. H., 1974. Two dimensional approximations to the three-dimensional soil-structure interaction problem, Nucl. Eng. Des., 31, 195-203.

Luco, J. E. Hadjian, A. H. and Bos, H. D., 1974. The dynamic modeling of the half-plane by finite elements, Nucl. Eng. Des., 31, 184-194.

Luco, J. E., Wong, H. L. and Trifunac, M. D., 1975. A note on the dynamic response of rigid embedded foundations, International Journal of Earthquake Engineering and Structural Dynamics, 4, No. 2, 119-128.

Luco, J. E., 1976a. Torsional response of structures for SH waves: the case of hemispherical foundations, Bull. Seism. Soc. Am., 66, 109-123.

Luco, J. E., 1976b. Torsional response of structures to obliquely incident seismic waves, International Journal of Earthquake Engrg. and Struct. Dyn., 4, 207-219.

Luco, J. E., 1976c. Torsion of a rigid cylinder embedded in an elastic half-space, Journal of Applied Mechanics, ASME, 43, 419-423.

Lysmer, J. and Kuhlemeyer, R. L., 1969. Finite dynamic model for infinite media, Journal of the Engineering Mechanics Division, ASCE, 95, 859-877.

Lysmer, J. and Waas, G., 1972. Shear waves in plane infinite structures, Journal of the Engineering Mechanics Division, ASCE, 98, 85-105.

Novak, M. and Beredugo, Y. O., 1972. Vertical vibrations of embedded footings, Journal of the Soil Mechanics and Foundations Division, ASCE, 98, 1291-1310.

Novak, M. and Beredugo, Y. O., 1973. The effect of embedment of footing vibrations, Proceedings of the First Canadian Conference on Earthquake Engineering Research, University of British Columbia, Vancouver, B. C., 111-125.

Novak, M. and Sachs, K., 1973. Torsional and coupled vibration of embedded footings, International Journal of Earthquake Engineering and Structural Dynamics, 2, 11-33.

Ohsaki, Y., 1973. On movements of a rigid body in semi-infinite elastic medium, Proceedings of the Japan Earthquake Engineering Symposium, Tokyo, 245-252.

Paul, H. S., 1967. Vibration of a rigid circular disc on an infinite elastic plate, Journal of Acoustical Soc. of Am., 42, 412-416.

Reissner, E., 1936. Stationäre, axialsymmetrische, durch eine schüttelnde Masse erregte Schwingungen eines homogenen elastischen halbraumes, Ingenieur-Archiv., 7, 381-396.

Reissner, E., 1937. Freie and erzwungene torsionschwingungen des elastischen halbraumes, Ingenieur-Archiv., 9, 229-245.

Reissner, E. and Sagoci, H. F., 1944. Forced torsional oscillations of an elastic half-space, Journal of Applied Physics, 15, 652-654.

Richard, F. E., Hall, J. R. and Woods, R. D., 1970. Vibration of Soils and Foundations, Prentice-Hall, New York.

Scavuzzo, R. J., 1970. Structure-foundation of nuclear power plants -- Phase I final report, The Research Foundation, University of Toledo, Ohio.

Seed, H. B. and Idriss, I. M., 1973. Soil structure interaction of massive embedded structures during earthquakes, Fifth World Conference on Earthquake Engineering, Rome.

Shah, P. M., 1968. On the Dynamic Response of Foundation Systems, Ph.D. Thesis, Rice University, Houston, Texas.

Takaso, H., Uchida, K. and Masuda, K., 1969. Stresses and deformations in the vicinity of building foundation, stress analysis by finite element method, Institute of Structural Mechanics, Muto.

Thau, S. A. and Umek, A., 1973. A transient response of a buried foundation to antiplane shear waves, Journal of Applied Mechanics, ASME, 40, 1061-1066.

Thau, S. A. and Umek, A., 1974. Coupled rocking and translating vibrations of a buried foundation, Journal of Applied Mechanics, ASME, 41, 697-702.

Thomas, D. P., 1968. A note on the torsional oscillations of an elastic half-space, International Journal of Engineering Science, 6, 565-570.

Thomas, D. P., 1968. Torsional oscillations of an elastic half-space, Quarterly Journal of Mechanics and Applied Mathematics, 21, 51-65.

Tsai, N. C., 1973. Discussion of report by P. K. Agrawal, Comparative study for soil structure interaction effect by the soil spring and finite element method (Sargent and Lundy Engineers, Report SAD-082), Bechtel Power Coproration, San Francisco, October Technical Report.

Ufliand, I. S., 1961. On torsional vibrations of half-space, Physics of Metals and Metallography, 25, 228-233.

Veletsos, A. S. and Verbic, B., 1973. Vibration of viscoelastic foundations, Report 18, Department of Civil Engineering, Rice University, Houston, Texas.

Veletsos, A. S. and Nair, V.V.D., 1974. Torsional vibration of viscoelastic foundation, Journal of the Geotechnical Engineering Division, ASCE, 100, 225-246.

Waas, G., 1972. Linear Two-Dimensional Analysis of Soil Dynamics Problems in Semi-Infinite Layered Media, Ph.D. Thesis, University of California, Berkeley, California.

Waas, G. and Lysmer, J., 1972. Vibrations of footings embedded in layered media, Symposium on Applied Finite Element Method in Geotechnical Engineering, U. S. Army Engineer Waterways Experiment Station, Vicksburg, Miss., 1-24.

Warburton, G. B., 1957. Forced vibrations of a body on an elastic stratum, Journal of Applied Mechanics, Trans. ASME, 24 55-58.

Wei, Y., 1971. Steady State Response of Certain Foundation Systems, Ph.D. Thesis, Rice University, Houston, Texas.

Wong, H. L. and Trifunac, M. D., 1974. Interaction of a shear wall with the soil for incident plane SH waves: Elliptical Rigid foundation, Bull. Seism. Soc. Am., 64, 1825-1842.

Wong, H. L., 1975. Dynamic Soil-Structure Interaction, Report EERL 75-01, Earthquake Engineering Research Laboratory, California Institute of Technology, Pasadena, California.

Wong, H. L. and Luco, J. E., 1978. Dynamic response of rectangular foundations to obliquely incident seismic waves, Earthquake Engineering and Structural Dynamics, 6, 3-16.

APPENDIX I

TABLES OF IMPEDANCE FUNCTIONS FOR CYLINDRICAL FOUNDATIONS EMBEDDED IN VISCOELASTIC HALF-SPACE

Table I.1

Impedance Functions for Cylindrical Foundation (h/a = 0.25)

Embedded in Viscoelastic Half-Space ($\alpha = \sqrt{3}\,\beta$, $Q_\alpha = 100$, $Q_\beta = 50$)

a_o	K_{TT}	C_{TT}	K_{VV}	C_{VV}	K_{HH}	C_{HH}	K_{MM}	C_{MM}	K_{MH}	C_{MH}
					h/a = 0.25					
.1	9.55	1.94	6.40	7.09	6.31	6.29	5.51	0.99	0.00	-0.05
.3	9.35	0.84	6.38	6.34	6.32	5.46	5.36	0.49	0.05	-0.27
.5	9.01	0.88	6.33	6.17	6.32	5.27	5.13	0.60	0.09	-0.38
1.0	8.08	1.51	6.01	6.09	6.27	5.12	4.52	1.09	0.10	-0.50
2.0	6.92	2.36	5.01	6.43	6.18	5.11	3.79	1.63	-0.03	-0.53
3.0	6.44	2.72	4.67	6.81	6.19	5.10	3.35	1.87	-0.27	-0.50
4.0	6.30	2.88	5.05	6.91	6.13	5.07	3.16	2.02	-0.49	-0.44
5.0	6.27	2.94	5.37	6.86	5.98	5.06	3.24	2.10	-0.59	-0.39
6.0	6.21	2.97	5.34	6.81	5.85	5.07	3.44	2.12	-0.54	-0.35
10.0	6.22	3.04	5.34	6.88	5.51	5.10	3.61	2.12	-0.43	-0.34

Table I.2

Impedance Functions for Cylindrical Foundation (h/a = 0.5)

Embedded in Viscoelastic Half-Space ($\alpha = \sqrt{3}\ \beta$, $Q_\alpha = 100$, $Q_\beta = 50$)

a_o	K_{TT}	C_{TT}	K_{VV}	C_{VV}	K_{HH}	C_{HH}	K_{MM}	C_{MM}	K_{MH}	C_{MH}
					h/a = 0.5					
.1	12.88	2.63	7.05	8.53	7.47	8.51	7.50	1.50	-0.77	-0.99
.3	12.56	1.22	7.03	7.70	7.49	7.46	7.26	0.91	-0.71	-1.17
.5	12.04	1.39	6.96	7.52	7.50	7.20	6.90	1.16	-0.69	-1.28
1.0	10.71	2.44	6.62	7.45	7.45	6.99	6.12	1.93	-0.72	-1.35
2.0	9.27	3.64	5.65	7.81	7.25	6.95	5.37	2.60	-0.84	-1.31
3.0	8.68	4.09	5.29	8.17	7.05	6.98	4.96	2.86	-0.92	-1.27
4.0	8.51	4.31	5.66	8.33	6.88	7.01	4.83	3.03	-1.00	-1.23
5.0	8.60	4.41	6.13	8.33	6.68	7.06	5.04	3.11	-0.95	-1.18
6.0	8.74	4.46	6.53	8.33	6.66	7.10	5.33	3.13	-0.75	-1.17
10.0	9.41	4.53	8.23	8.37	7.42	7.25	6.07	3.13	-0.04	-1.18

Table I.3

Impedance Functions for Cylindrical Foundation (h/a = 1.0)
Embedded in Viscoelastic Half-Space ($\alpha = \sqrt{3}\,\beta$, $Q_\alpha = 100$, $Q_\beta = 50$)

a_o	K_{TT}	C_{TT}	K_{VV}	C_{VV}	K_{HH}	C_{HH}	K_{MM}	C_{MM}	K_{MH}	C_{MH}
					h/a = 1.0					
.1	19.53	4.02	8.29	11.68	9.51	13.15	13.67	3.82	-2.80	-4.17
.3	18.91	2.12	8.22	10.76	9.55	11.66	13.13	3.10	-2.73	-4.21
.5	17.97	2.68	8.10	10.61	9.53	11.28	12.45	3.80	-2.71	-4.26
1.0	15.83	4.71	7.61	10.66	9.30	11.03	11.20	5.27	-2.68	-4.21
2.0	13.94	6.60	6.57	11.19	8.57	11.19	10.02	6.32	-2.34	-4.22
3.0	13.37	7.19	6.51	11.62	8.26	11.41	9.42	6.71	-2.01	-4.34
4.0	13.25	7.42	7.49	11.69	8.21	11.51	9.20	6.90	-1.94	-4.40
5.0	13.23	7.52	8.26	11.56	8.38	11.58	9.08	6.98	-1.87	-4.41
6.0	13.29	7.58	8.54	11.54	8.89	11.61	8.92	7.04	-1.70	-4.43
10.0	13.85	7.67	9.39	11.52	10.32	11.54	9.08	7.22	-1.54	-4.43

Table I.4

Impedance Functions for Cylindrical Foundation (h/a = 2.0)

Embedded in Viscoelastic Half-Space ($\alpha = \sqrt{3}\,\beta$, $Q_\alpha = 100$, $Q_\beta = 50$)

a_o	K_{TT}	C_{TT}	K_{VV}	C_{VV}	K_{HH}	C_{HH}	K_{MM}	C_{MM}	K_{MH}	C_{MH}
					h/a = 2.0					
.1	32.40	6.80	10.42	18.44	12.87	22.81	35.82	19.00	-9.12	-17.18
.3	30.91	4.28	10.22	17.33	12.92	20.53	34.11	18.27	-8.98	-16.48
.5	29.29	5.99	10.04	17.55	12.83	20.03	32.20	20.54	-8.77	-16.40
1.0	26.07	10.00	9.69	17.95	12.45	19.92	28.48	24.65	-8.04	-16.71
2.0	23.79	12.56	10.00	18.04	12.10	20.28	24.57	27.89	-7.06	-17.48
3.0	22.85	13.24	10.19	17.64	12.76	20.31	22.63	29.20	-7.35	-17.73
4.0	22.57	13.55	10.58	17.64	13.21	20.19	22.51	29.83	-7.85	-17.66
5.0	22.42	13.80	10.44	17.88	13.65	20.05	22.69	30.20	-8.03	-17.51
6.0	22.65	13.77	12.05	17.67	13.87	20.06	23.40	30.26	-7.53	-17.45
10.0	22.33	13.98	11.24	17.81	17.04	20.08	24.84	30.26	-6.06	-17.45